The Paleostress History

of the Central European Basin System

Judith Sippel

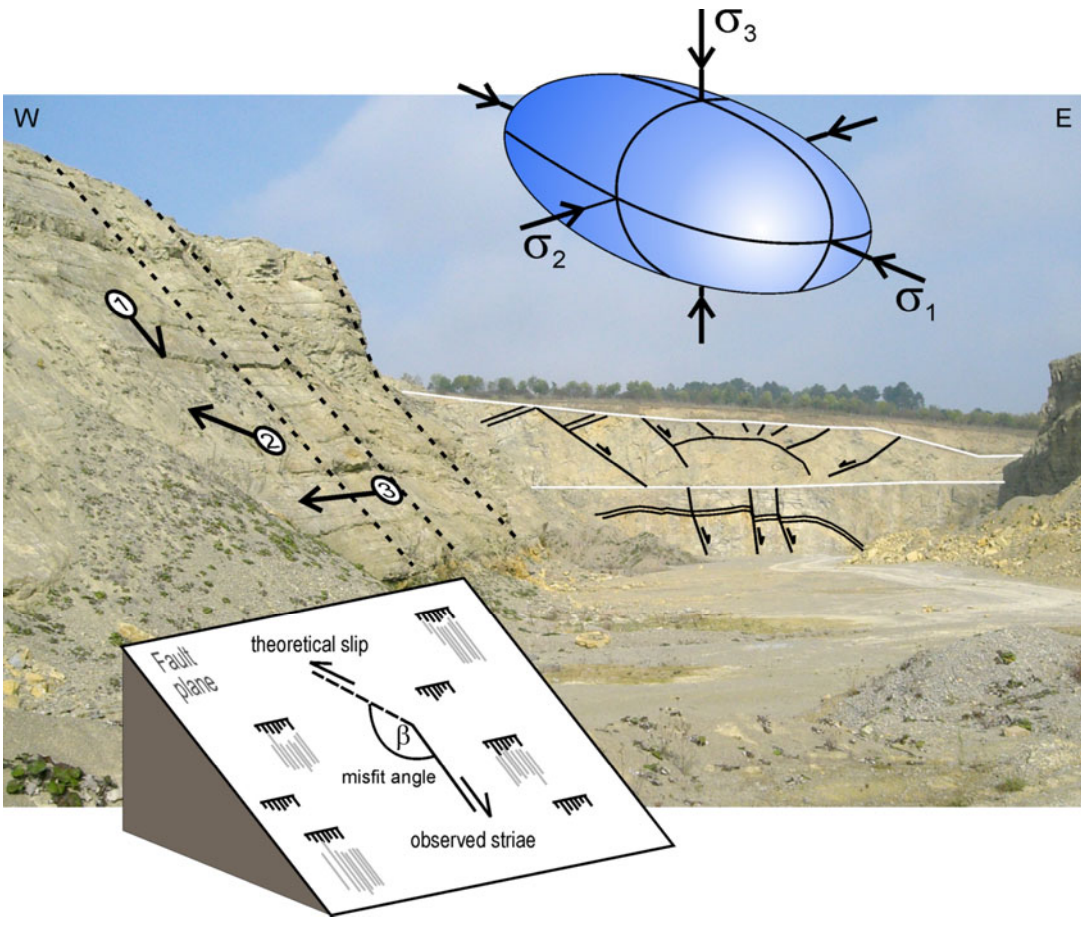

The Paleostress History

of the Central European Basin System

Dissertation

zur Erlangung des akademischen Grades

doctor rerum naturalium (Dr. rer. nat.)

dem Fachbereich Geowissenschaften

der Freien Universität Berlin

vorgelegt von

Judith Sippel

Berlin, 2009

1. Gutachter: Prof. Dr. Onno Oncken
Freie Universität Berlin
Helmholtz-Zentrum Potsdam Deutsches GeoForschungsZentrum – GFZ

2. Gutachter: Prof. Dr. Klaus Reicherter
Rheinisch-Westfälische Technische Hochschule Aachen (RWTH)

Tag der Disputation: 13.02.2009

Eidesstattliche Erklärung

Hiermit versichere ich, dass die vorliegende Dissertation ohne unzulässige Hilfe Dritter und ohne Benutzung anderer als der angegebenen Literatur angefertigt wurde. Die Stellen der Arbeit, die anderen Werken wörtlich oder inhaltlich entnommen sind, wurden durch entsprechende Angaben der Quellen kenntlich gemacht. Diese Arbeit hat in gleicher oder ähnlicher Form noch keiner Prüfungsbehörde vorgelegen.

Potsdam, November 2008

to my family

Contents

Abstract

Zusammenfassung

1 Introduction **5**
1.1 Paleostress analysis 7
1.2 Geological Setting of the CEBS 8
1.3 Study areas 11
1.3.1 The southern margin of the CEBS 11
1.3.2 The Oslo Graben area 16

2 Fault-slip analysis and paleostress reconstruction **20**
2.1 Basics 20
2.1.1 Multiple Inverse Method (MIM; Yamaji, 2000) 23
2.1.2 PBT-axes Method (PBT; Sperner et al., 1993) 24
2.2 A new strategy for stress inversion from (heterogeneous) fault-slip data 25
2.2.1 Stress Inversion Via Simulation (SVS) 25
2.2.2 Stress inversion by MIM and simulation - a comparative test 29
2.2.3 Discussion 31
2.2.4 Summary 32
2.3 From local fault-slip data to regional stress fields 35
2.3.1 Data acquisition 35
2.3.2 Data presentation 36
2.3.3 Data correction 36
2.3.4 Stress inversion 36
2.3.5 Constraints on the chronology of stress states 37

3 Structural evolution of the CEBS – state of the art **42**
3.1 Initial rift phase 42
3.2 Post-rift phase of thermal subsidence 43
3.3 Mid-Triassic – Jurassic phase of E-W extension 45
3.4 Mid-Jurassic phase of uplift 46
3.5 Late Jurassic – Early Cretaceous phase of localized subsidence 47
3.6 Late Cretaceous – Early Tertiary phase of inversion 48
3.7 Cenozoic subsidence and transition to present-day stress conditions 50
3.8 Salt tectonics 51

4 The southern margin of the CEBS **53**
4.1 Estimated paleostress tensors 53
4.2 Analysis of chronological indicators 62
4.2.1 Faulting vs. folding 63
4.2.2 Stress states vs. large-scale structures - the Osning Lineament area 71
4.2.3 Oblique stress states 72
4.3 Cross-outcrop correlation of paleostress states 77
4.3.1 Consistencies between folding and faulting 77
4.3.2 Locally estimated chronologies of paleostress states 78
4.3.3 Consistencies in the directions of principal axes 81
4.4 Regional vs. local phenomena 84
4.4.1 Compressional stress states 84

4.4.2 Strike-slip stress states with a N- to NE-directed maximum compression 86
4.4.3 Strike-slip stress states with a W- to NNW-directed maximum compression 88
4.4.4 Tensional stress states postdating compressional or strike-slip stress states 90
4.4.5 Local phenomena 91
4.5 Discussion 93
4.5.1 Chronology 93
4.5.2 Mechanisms 96
4.6 Summary and conclusions 100

5 The Oslo Graben area 101
5.1 The Oslo Graben as part of the Oslo Rift System 101
5.1.1 Geometry and structure of the Oslo Rift System 101
5.1.2 Permo-Carboniferous rift evolution 102
5.1.3 Post-rift evolution 103
5.2 Estimated paleostress states 103
5.2.1 Direct constraints on the relative timing of stress states 109
5.2.2 Regional implications 109
5.3 Discussion 123
5.3.1 Chronology 123
5.3.2 Mechanisms 124
5.4 Conclusions 127

6 Synthesis 129

7 References 135

8 Acknowledgements 149

Parts of Chapters 2 and 4 are already in press in the following journal:

Paleostress states at the south-western margin of the Central European Basin System - application of fault-slip analysis to unravel a polyphase deformation pattern
Sippel, J., Scheck-Wenderoth, M., Reicherter, K. and Mazur, S.
Tectonophysics (in press), available online since April 2008,
DOI: 10.1016/j.tecto.2008.04.010

Abstract

The Central European Basin System (CEBS) in North Central Europe is a complex intracontinental system of sedimentary basins that evolved through several geodynamic phases since Late Carboniferous times. At present, the basin system is framed by the Tornquist Zone in the north and the Elbe Fault System in the south. The main structural configuration of the basin system is well established due to decades of scientific research and intense industrial exploration for mineral resources. The scope of this PhD thesis is to assess which paleostress fields controlled the evolution of the basin system.

The base for the present study is provided by fault-slip data (striated fault planes with known sense of slip) measured in outcrops of two structural domains: along the Elbe Fault System as part of the inverted southern margin of the CEBS (906 fault-slip data) and in the Oslo Graben area located north of the Tornquist Zone (2191 data). The first part of this thesis (Chapter 2) introduces a new strategy for estimating paleostress states from heterogeneous sets of fault-slip data (Stress Inversion Via Simulation, SVS). This stepwise technique combines two well established methods, the PBT-axes-Method (Sperner et al., 1993) and the Multiple Inverse Method (Yamaji, 2000), with a final simulation of stress states (Yamaji & Sato, 2005). The simulation allows interactively fitting the parameters of a 'reduced stress tensor' comprising (1) the directions of the principal stress axes, σ_1, σ_2, σ_3 (with $\sigma_1 \geq \sigma_2 \geq \sigma_3$) and (2) the ratio of principal stress differences, $R=(\sigma_2-\sigma_3)/(\sigma_1-\sigma_3)$, to a set of fault-slip data. One improvement of SVS compared to former stress inversion techniques is that an estimated stress tensor fulfils both the criterion of low misfit angles (Wallace-Bott slip criterion) and that of high shear-to-normal-stress ratios (Mohr-Coulomb criterion) for the associated faults.

In the second part of this thesis (Chapters 4 and 5), estimated paleostress tensors – 77 tensors from the Elbe Fault System area and 194 tensors from the Oslo Graben area – are presented. It is demonstrated, that based on occurrences of stress states in different stratigraphic formations, chronological constraints derived from field observations, and consistencies in the reduced stress tensors, most of the locally estimated stress states can be related to a small number of regionally traceable stress fields.

A compressional stress field with a horizontal NW-SE-directed maximum compression (σ_1) characterises the Caledonian imprint in the Oslo Graben area. The most prominent regional stress field reconstructed in the Oslo Graben area is tensional in character with a horizontal WNW-ESE-directed σ_3 and related to the stages of Permo-Carboniferous rifting. The youngest stress states detected correspond to a wrench regime with a roughly N-S-directed σ_1 and a maximum age of Permian. The absolute timing of this stress field is poorly constrained because of the lack of any exposed rocks younger than Permian. Possibly, the Oslo Graben area remained widely unaffected by any major tectonic activity during much of the Mesozoic and Cenozoic.

The oldest and predominant regional stress fields reconstructed for the Elbe Fault System area are related to the Late Cretaceous - Early Tertiary phase of inversion that affected much of the CEBS. The phase of inversion was controlled by a horizontal N-S- to NE-SW-directed σ_1 which characterised both an older compressional stress field as well as a younger strike-slip stress field. Strike-slip stress states with horizontal E-W- to NW-SE-directed σ_1-axes, on the other hand, might be interpreted as indicating a separate regional stress field that postdated the inversion or as being related to permutations of principal axes still under the N-S- to NE-SW-directed strike-slip stress field of inversion. The youngest reconstructed stress regime in the Elbe Fault System area is tensional in character combining various directions of horizontal extension. The associated stress states locally reveal low stress ratios indicating vertical flattening which partly can be related to the occurrence and potential movements of salt structures underneath. The scarcity of pre-Late Cretaceous signs of faulting in the Elbe Fault System area indicates that the inversion-related deformation widely overprinted potential

traces of earlier deformation which corresponds to an extensive “reprogramming” of the observable strain patterns along the inverted southern margin of the CEBS.
Finally, the last part of this thesis presents implications drawn from a synthesis of various studies on paleostresses and recent stresses in North Central Europe. Since the stress fields from the two study areas cannot be correlated temporally, conclusions on the Permo-Carboniferous to recent evolution of stress fields affecting the entire Central European Basin System are strongly limited. The lack of any indications of Late Cretaceous - Early Tertiary inversion tectonics in the Oslo Graben area might be related to the N-S trend of this fault-bounded block which like other N-S-trending domains in the CEBS was in line with the N-S-directed contraction during inversion. Another explanation may be provided by strain localisation along the Tornquist Zone due to which the Oslo Graben area has been shielded from inversion-related far field stresses. Strain localisation along the Elbe Fault System and the Tornquist Zone exposes the special role of these pre-existing zones of crustal weakness for the spatial variation of stresses and strain patterns.

Zusammenfassung

Das Zentraleuropäische Beckensystem (CEBS) im nördlichen Zentraleuropa ist ein komplexes intrakontinentales System sedimentärer Becken, das sich seit dem spätesten Karbon im Zuge verschiedener geodynamischer Phasen entwickelt hat. Die gegenwärtige Struktur dieses Beckensystems wird entscheidend durch die Tornquist Störungszone im Norden und das Elbe-Störungssystem im Süden geprägt. Das strukturelle Inventar dieses Beckensystems ist weitgehend bekannt, was eine Folge jahrzehntelanger wissenschaftlicher Aktivitäten und industrieller Untersuchungen zur Exploration mineralischer Rohstoffe im Gebiet ist. Im Rahmen dieser Dissertation zu Erlangung des akademischen Grades Dr. rer. nat. soll rekonstruiert werden, welche tektonischen Paläospannungsfelder die Entwicklung des CEBS kontrollierten.

Die vorliegende Studie basiert auf Harnischflächen-Daten (gestriemte Störungsflächen mit bekanntem Bewegungssinn), die in Aufschlüssen zweier struktureller Einheiten eingemessen wurden: zum einen entlang des Elbe-Störungssystems am invertierten Südrand des CEBS (906 Daten), zum anderen im Gebiet des Oslograbens nördlich der Tornquist Störungszone (2191 Daten). Im ersten Teil dieser Arbeit wird eine neue Strategie zur Ermittlung von Paläospannungszuständen aus heterogenen und polyphasen Harnischflächen-Datensätzen vorgestellt (Spannungsinversion mittels Simulation, SVS). Dieses schrittweise Verfahren kombiniert zwei bereits bewährte Methoden, die PBT-Achsenmethode (Sperner et al., 1993) und die Multiple Inversionsmethode (Yamaji, 2000), mit einer abschließenden Spannungssimulation (Yamaji & Sato, 2005). Mittels Spannungssimulation können die Parameter des ‚reduzierten Spannungstensors', d.h. die Richtungen der Hauptspannungsachsen σ_1, σ_2, σ_3 (mit $\sigma_1 \geq \sigma_2 \geq \sigma_3$) und der Spannungsdifferenzenquotient, $R=(\sigma_2-\sigma_3)/(\sigma_1-\sigma_3)$, variiert und interaktiv an einen Harnischflächen-Datensatz angepasst werden. Eine Optimierung, die SVS gegenüber früheren Inversionsmethoden auszeichnet, betrifft die Qualität der ermittelten Spannungstensoren: sie passen optimal zu den betrachteten Harnischflächen-Daten, da sie nicht nur die beobachteten Scherrichtungen herbeiführen, sondern auch ein großes Verhältnis zwischen Scher- und Normalspannung auf den Flächen induzieren würden (Wallace-Bott-Scherbewegungskriterium <u>und</u> Reibungskriterium erfüllt).

Im zweiten Teil dieser Dissertation werden die ermittelten Paläospannungstensoren präsentiert: 77 Tensoren aus dem Gebiet des Elbe-Störungssystems und 194 Tensoren aus dem Gebiet des Oslo Grabens. Es wird gezeigt, dass sich diese lokal ermittelten Paläospannungen aufgrund ihre Auftretens in verschieden alten Gesteinsformationen, aufgrund von Geländebefunden zu relativen Altersbeziehungen und aufgrund von Übereinstimmungen in den Parametern der ‚reduzierten Spannungstensoren' zu wenigen regional wirkenden Spannungsfeldern vereinen lassen.

Ein kompressionales Spannungsfeld mit horizontaler NW-SE-gerichteter maximaler Kompression (σ_1) charakterisiert die Einflüsse der Kaledonischen Orogenese im Gebiet des Oslograbens. Das am stärksten ausgeprägte regionale Paläospannungsfeld im Oslograbengebiet entspricht einem extensionalen Regime mit horizontaler WNW-ESE-gerichteter σ_3-Achse. Dieses Paläospannungsfeld kann zeitlich der Hauptphase der permo-karbonen Riftentstehung im Gebiet zugeordnet werden. Die jüngsten rekonstruierten Paläospannungstensoren im Oslograbengebiet entsprechen einem Seitenverschiebungsregime mit etwa N-S-gerichteter σ_1-Achse. Diese Paläospannungen sind maximal permischen Alters, wobei sich ihr absolutes Alter aufgrund des Fehlens mesozoischer und känozoischer Gesteinsformationen nicht weiter spezifizieren lässt. Es ist möglich, dass das Oslograbengebiet über weite Zeiträume des Mesozoikums und Känozoikums nicht von stärkeren tektonischen Aktivitäten erfasst wurde.

Die ältesten und zugleich am deutlichsten erkennbaren regionalen Paläospannungsfelder, die für das Gebiet des Elbe-Störungssystems ermittelt wurden, lassen sich mit der spätkretazisch-frühtertiären Phase der Beckeninversion in weiten Teilen des CEBS in Verbindung bringen. Diese Phase der Inversion wurde von einer horizontalen N-S- bis NE-SW-gerichteten σ_1-Achse beherrscht, die sowohl ein älteres Kompressions- als auch ein jüngeres Seitenverschiebungsfeld charakterisiert. Lokal auftretende Seitenverschiebungsspannungen mit horizontal E-W- bis NW-SE-gerichteter σ_1-Achse können zum einen als ein separates, nach der Inversion eintretendes Spannungsfeld interpretiert werden. Zum anderen lassen sie sich auch durch lokale Permutationen von Hauptspannungsachsen während der Seitenverschiebungsphase der Inversion erklären. Die jüngsten Paläospannungen im Elbe-Störungssystem entsprechen einem extensionalen Regime, das durch eine große Variation lokaler Extensionsrichtungen (σ_3) gekennzeichnet ist. Verbreitet sind diese Spannungen mit niedrigen Spannungsdifferenzenquotienten verbunden, die zum Teil mit dem Auftreten und den potentiellen Bewegungen von Salzstrukturen im Untergrund in Verbindung gebracht werden können. Die seltene Nachweisbarkeit von prä-spätkretazischer Störungsaktivität im Gebiet des Elbe-Störungssystems ist ein Indiz dafür, dass Spuren älterer Deformationsphasen im Zuge der Inversion großflächig überprägt wurden, was einer weitgehenden „Neuprogrammierung" der beobachtbaren Deformationsmuster gleichkommt.

Im abschließenden Teil dieser Arbeit werden Schlussfolgerungen formuliert, die auf einer Synthese verschiedener Studien zu Paläospannungen und rezenten Spannungsfeldern im nördlichen Zentraleuropa basieren. Da eine zeitliche Korrelation der in den zwei Untersuchungsgebieten ermittelten Paläospannungen nicht möglich ist, sind Schlussfolgerungen, die die permo-karbone bis rezente Entwicklung von Paläospannungen im gesamten Zentraleuropäischen Beckensystem betreffen, stark eingeschränkt. Das Fehlen jeglicher Indikationen für eine spätkretazisch-frühtertiäre Deformation im Oslograbengebiet könnte Folge der N-S-Ausrichtung dieser strukturellen Einheit sein, die somit (ähnlich wie andere N-S-gerichtete Strukturen im CEBS) für eine Reaktivierung durch N-S-gerichtete Kontraktion und Inversion nicht geeignet war. Ein alternatives Szenario berücksichtigt die starke Konzentration von Deformation auf Gebiete der Tornquist Störungszone, durch die das Oslograbengebiet gegen die Fernwirkung inversionssteuernder Spannungen eventuell abgeschirmt wurde. Die Lokalisation von Deformation auf die Gebiete des Elbe-Störungssystems und der Tornquist Störungszone spiegelt den Einfluss präexistierender krustaler Schwächezonen auf die räumliche Variation und den örtlichen Wirkungsgrad von Spannungsfeldern wider.

1 Introduction

Understanding sedimentary basins is of great and ever growing importance for society as these geological archives provide great amounts of economic recourses as oil and water while at the same time they are getting in the focus for waste disposal and the usage of geothermal energy. To understand the present configuration of a basin system and to potentially forecast its future evolution requires comprehending as much as possible of its development through the past. Under changing external forces, a sedimentary basin may become complex in terms of geometry of sub-basins, distribution of sedimentary products, or heat flux, for instance. Accordingly, successive deformation phases are often related to a complex pattern of superposing structures archived in the stratigraphic sequence of a basin. The base for the present study is provided by structures of brittle deformation accessible in outcrops of the Central European Basin System. The goal of the study, finally, is to assess which paleostress fields had controlled the evolution of this complex system of basins.

The Central European Basin System (CEBS) in North Central Europe is a complex intracontinental sedimentary basin system that evolved through a series of Late Carboniferous to Cenozoic deformation phases (Fig. 1; Scheck-Wenderoth and Lamarche, 2005). The CEBS has been extensively explored over the past decades, not least for the sake of its economically important resources of hydrocarbons. As a result, the sedimentary fill and the present crustal structure of the basin system are well constrained by geophysical and geological data acquired in particular during seismic experiments like DEKORP Basin '96, MONA LISA, or BABEL.

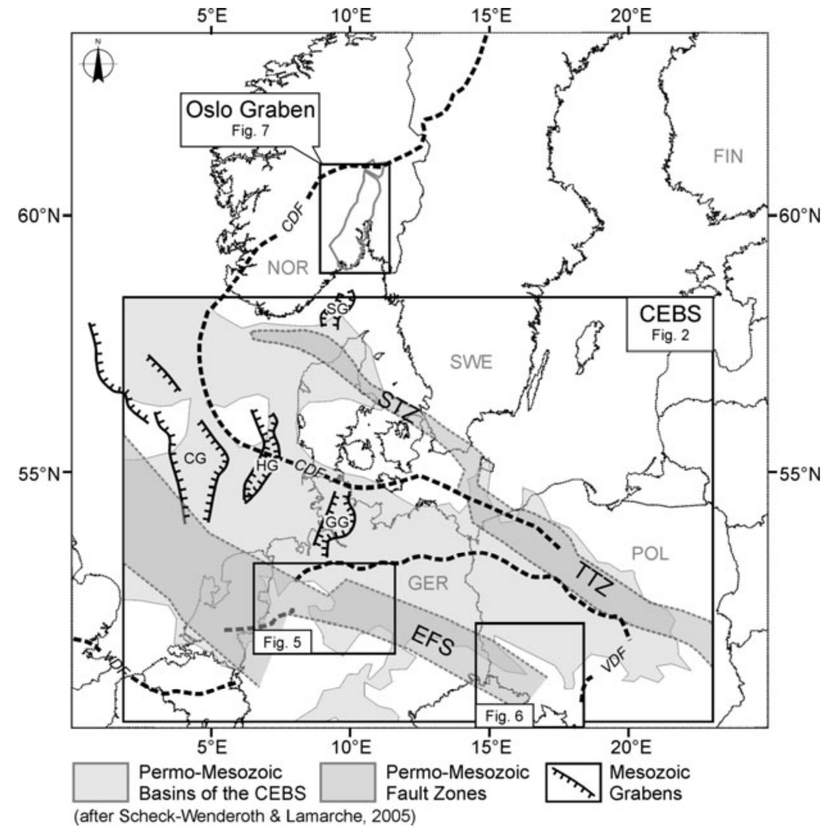

Figure 1: Sketch map of the main structural elements and the location of the Central European Basin System. The present study focuses on two areas along the Elbe Fault System (Fig. 5, 6) and an area structured by the Permo-Carboniferous Oslo Graben (Fig. 7).

CDF – Caledonian Deformation Front (EUGENO-S Working Group, 1988), VDF – Variscan Deformation Front (Lokhorst, 1998), CG – Central Graben, EFS – Elbe Fault System, GG – Glücksstadt Graben, HG – Horn Graben, SG – Skagerrak Graben, STZ – Sorgenfrei-Tornquist Zone, TTZ – Teisseyre-Tornquist Zone (all after Scheck-Wenderoth & Lamarche, 2005).

The CEBS is framed by two major NW-SE-oriented fault systems: the Elbe Fault System (EFS) in the south and the Tornquist Zone (TZ) comprising the elements of the Sorgenfrei-Tornquist Zone and the Teisseyre-Tornquist Zone in the north (Fig. 2). Between these major fault zones, several sub-basins are arranged with NW-SE-trending axes like the Norwegian-Danish Basin, the North German Basin, and the Polish Basin which, in turn, are separated by the structural highs of the Mid-North-Sea-High and the Ringkøbing-Fyn-High. Beside this prominent NW-SE trend of structures, there are also elements with N-S-oriented axes, such as the Central Graben, the Horn Graben, and the Glückstadt Graben. Despite having developed above a puzzle of different crustal domains with Precambrian, Caledonian and Variscan consolidation ages, the different sub-basins are characterised by partially correlating subsidence histories since Late Carboniferous times – consistencies in their development that unite them to a collective system of basins, the CEBS.

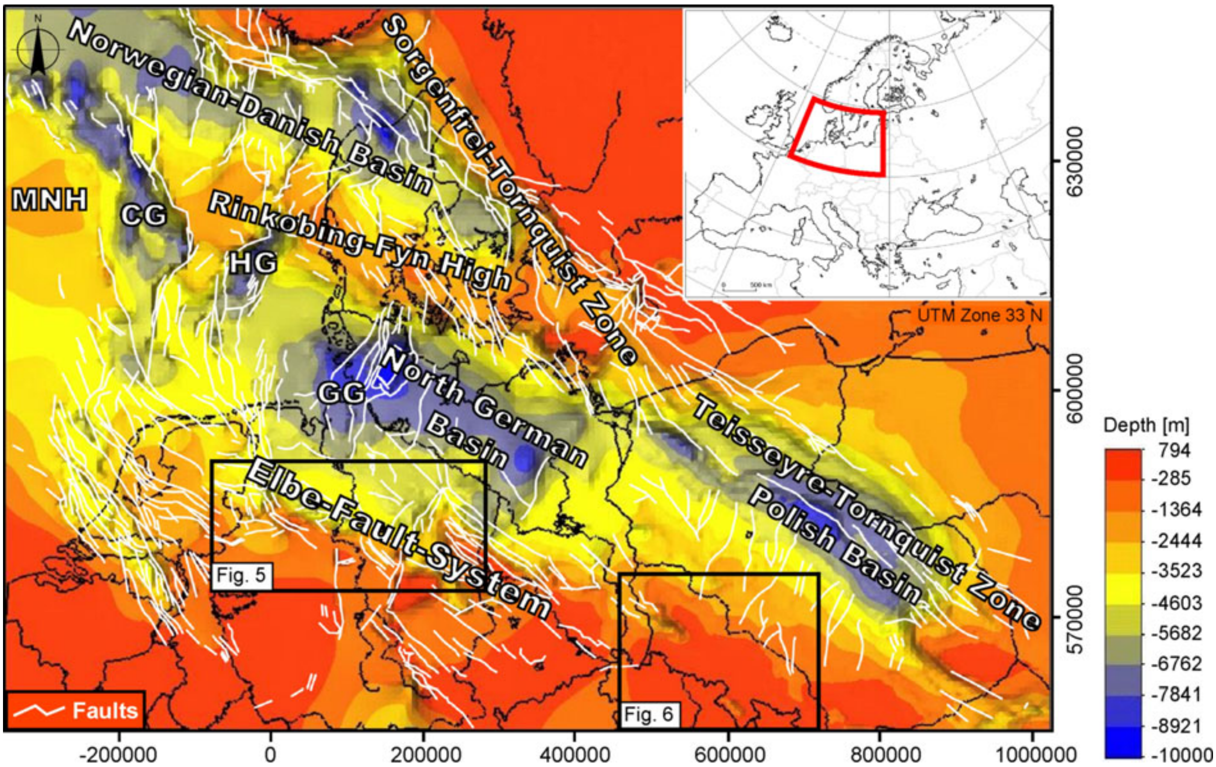

Figure 2: Depth to top pre-Permian in the Central European Basin System (modified after Scheck-Wenderoth & Lamarche, 2005). The major structural elements strike NW-SE as the Elbe Fault System, the Mid-North-Sea High (MNH), the Ringkøbing Fyn High, and the Sorgenfrei- and Teisseyre-Tornquist Zone. A second set of structures trends N-S as the Glücksstadt Graben (GG), the Horn Graben (HG), and the Central Graben (CG). The locations of the studied areas within the Elbe Fault System are indicated (Fig. 5, 6).

Whereas the main structural configuration of the basin system is well known and the documented temporal and spatial variations of depositional and erosional centres provide extensive constraints on the tectonic evolution of the entire CEBS (Chapter 3), to date, the perceptions on the deformation-controlling stress fields are rather qualitatively. Ideas of this kind have evolved from studies that investigate the structural evolution of the CEBS on a basin scale (Scheck-Wenderoth & Lamarche, 2005) or on the scale of sub-basins (Clausen & Pedersen, 1999; Scheck & Bayer, 1999; Hansen et al., 2000; Baldschuhn et al., 2001; Scheck et al., 2002a,b; Evans et al., 2003; Lamarche, et al. 2003). For instance, recurrent changes of the basin-wide stress field can be derived from the fact that two major types of structural elements, striking NW-SE and N-S, respectively, experienced repeated and selective reactivation during basin evolution. The specific orientations of such elements are the key for any reconstruction of the orientations of related paleostress fields.

A state of stress - fully defined by the orientations and magnitudes of the three mutually perpendicular principal stress axes, $\sigma_1 \geq \sigma_2 \geq \sigma_3$ (Fig. 3) - is a body's instantaneous internal distribution of force per area deriving from external applied loads. By reason of the immediate relationship between stress release and deformation, it is not possible to measure paleostress states directly. However, a base for the reconstruction of paleostress states is yielded by strain which is the detectable product of deviatoric stresses. One very effective link between strain and stress is provided by fault kinematics. The orientation of a fault plane complemented by the direction and sense of slip derived from kinematic indicators such as slickensides forms a 'fault-slip datum'. By considering various fault-slip data and well-known principles of fracturing and faulting in the brittle regime of the crust, certain parameters of the stress state responsible for faulting can be estimated.
As part of this thesis, a new strategy for the inversion of stress states from fault-slip data is introduced (Chapter 2). This new approach is applied to data sampled from outcrops along the southern margin of the CEBS (Chapter 4) and from outcrops in the Oslo Graben area (Chapter 5). The results derived from these study areas deliver new insights into the evolution of paleostress fields that controlled the development of the entire CEBS.

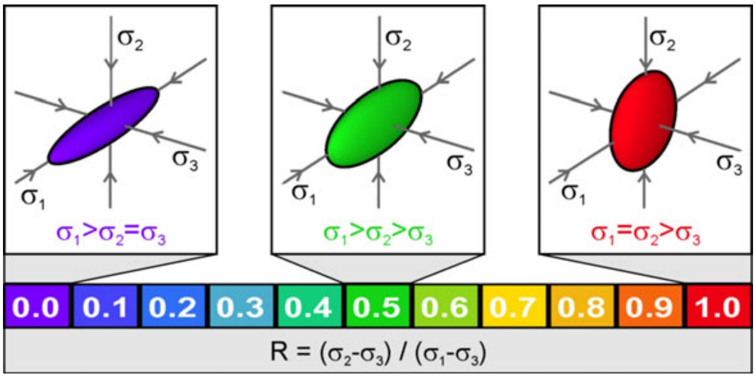

Figure 3: Different stress states illustrated as stress ellipsoids which are spanned by the three mutually perpendicular principal stress axes, $\sigma_1 \geq \sigma_2 \geq \sigma_3$. The relative magnitudes of stress in the directions of σ_1, σ_2, and σ_3 are expressed by the ratio of principal stress differences, R, which corresponds with $\Phi=(\sigma_2-\sigma_3)/(\sigma_1-\sigma_3)$ as defined by Bishop (1966). From R=0.0 which indicates the magnitudes of σ_2 and σ_3 to be equal to R=1 expressing σ_1 and σ_2 to be equal in magnitude, the shape of the ellipsoid changes from prolate to oblate. The presented colour code for different values of R is used throughout the present study.

1.1 Paleostress analysis

The reconstruction of a state of stress from an observed pattern of strain requires a direct cause-and-effect relationship between stress and strain. Stress inversion based on kinematic analysis of faults has become a widely used tool in structural geology since the 1950s; comprehensive reviews on various stress inversion techniques are provided by Angelier (1994) and Ramsay & Lisle (2000). The underlying assumptions of fault-slip analysis, however, give good reasons for a critical handling of data, software tools and results. For discussions on the limitations of fault-slip analysis it shall be referred to Pollard et al. (1993), Dupin et al. (1993), Twiss & Unruh (1998), and Marrett & Peacock (1999).
One of the first to formulate basic conceptions on fault kinematics and related stress states was Anderson (1942) whose hypothesis connects two main aspects: Firstly, as a result of

gravity and the absence of shear stresses parallel to the Earth's surface, one principal stress axis is constrained to be vertical, while the other two axes are horizontal. Secondly, both the orientation and the shear sense of a newly-fractured fault plane depend on the orientations of the principal stress axes with respect to the Earth's surface (Fig. 4).

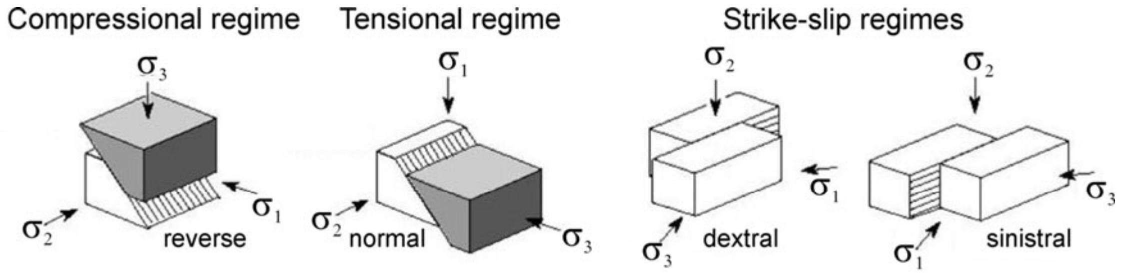

Figure 4: Stress regimes and associated fault-slip modes according to Anderson (1942): A newly-formed fault plane is oriented parallel to the σ_2. The sense of shear along the faults is normal, strike-slip, or reverse, depending on which of the principal stress axes, σ_1, σ_2, or σ_3, respectively, is vertical. The dip angle between the fault plane and the σ_1-axis depends on material properties.

Of course, the Andersonian concept on fault mechanics is only valid for certain situations in the Earth's crust, as it considers only newly-fractured faults with pure dip-slip or pure strike-slip movements. Slip, however, may also take place along pre-existing discontinuities, of which the orientations do not depend on the acting stress state. Considering both newly-formed and reactivated faults, the majority of techniques on fault-slip analysis is based on the assumption that slip direction, inferred from features such as slickenside lineations, is indicative of the shear stress component resolved along the respective fault plane (Wallace, 1951; Bott, 1959). Assuming, in addition, the shear stresses on many faults (i) to be induced by a homogeneous stress field within the volume of rock, (ii) to be resolved independently from movements along other faults, and (iii) to be resolved coevally in response to the same deviatoric stress, a "bulk" stress tensor can be estimated explaining the activation of all faults considered. The last aspect regarding synchronous activation of faults corresponds to one of the greatest challenges of fault-slip analysis: the separation and inversion of heterogeneous fault-slip data which originate from a succession of different paleostress states (Etchecopar et al., 1981; Huang, 1988; Nemcok & Lisle, 1995; Nemcok et el., 1999; Yamaji, 2000; Shan et al., 2003, 2004; Liesa & Lisle, 2004; Žalohar & Vrabec, 2007). The new concept presented in Chapter 2 has especially been developed to solve the problem of mixed data sets.

1.2 Geological setting of the CEBS

Figure 1 compiles the most important structural elements of North Central Europe together with the different areas investigated in the course of this study. As one of the basement structures below the Late Carboniferous to Cenozoic basin fill, the Caledonian Deformation Front spaciously pervades the area. This basement structure corresponds to the western and southern borders of the Baltic Craton which in turn constitutes the Precambrian fraction of Europe from where the continent episodically grew to its recent configuration (Ziegler, 1990; Bertelsen, 1992). The NE-SW-striking part of this suture, the so-called Scandinavian Caledonian Deformation Front, has been initiated during Silurian and Devonian times when it marked the collision zone between `Baltica´ and the North American-Greenland continent `Laurentia´. At almost the same time, a terrane commonly referred to as `Avalonia´ (Meissner et al., 1994, Pharaoh, 1999) is supposed to have collided with Baltica from the South, thus forming the English-North-German-Polish segment of the Caledonian Deformation Front. The southern limit of Avalonia, on the other hand, is formed by the Variscan Deformation

Front which developed during Devonian to Late Carboniferous times when other Gondwana-related terranes were docked on Variscan Europe. The evolution of the CEBS as an entity was initiated at the end of this orogenic phase, at times when the compressional stresses induced by collision-related tectonics were fading and the break-up of supercontinent Pangea was thenceforward controlled by extensional tectonics.

Post-Variscan evolution of the CEBS

The Early Mesozoic tectonic evolution of Central Europe was controlled by its position between the stable Baltic-East European Craton in the north and northeast, the Arctic-North Atlantic rift systems in the northwest and west, and the Tethyan and Central Atlantic rifts in the south. The interrelation of the respective geodynamic processes led to stress changes in the Central European lithosphere which caused, in turn, a complex post-Variscan geodynamic history for which seven main phases can be distinguished (Scheck-Wenderoth et al., 2008a; Scheck-Wenderoth & Lamarche, 2005; Chapter 3):

(1) *Initial rift phase*: During Latest Carboniferous to Early Permian times, the area of the CEBS was tectonically controlled by the latest pulses of the Variscan Orogeny. It is assumed that during this period a dextral mega-shear system developed in Central Europe. This transtrensional system was located between the ongoing subduction in the Urals and the onset of orogenic collapse in both the Appalachians and the European Variscides (Arthaud & Matte, 1977). The dominant products of this initial rift period are large amounts of igneous rocks. These rocks are the expression of a regional thermal destabilization and crustal thinning which are suggested to be related to back-arc extension as a consequence of continued subduction of the Paleotethys (Ziegler, 1990; Stampfli & Borel, 2002; Golonka, 2004). Subsequent to this magmatic stage, a thick succession of Lower Permian continental clastics, the *Rotliegend* sediments, have been deposited within the oldest basins of the CEBS.

(2) *Post-rift phase of thermal subsidence*: From the latest Early Permian until the Mid-Triassic, north Central Europe was mainly affected by a phase of thermal subsidence. The initial N-S trending graben-like depocentres began to join and form two large NW-SE- to WNW-ESE-oriented basins (Ziegler, 1990): the ‘Northern Permian Basin’ which coincides with the Norwegian-Danish Basin and the ‘Southern Permian Basin’ which comprises the southern North Sea, the North German Basin and the Polish Basin (Fig. 2). Between the Northern and Southern Permian Basin, the Mid-North Sea-Ringkøbing-Fyn chain of highs evolved. The phase of thermal subsidence was a period of reduced tectonic activity in the CEBS, while the area of the collapsing Variscan orogen to the south was affected by localised graben formation and active faulting. The tectonic quiescence in the CEBS is remarkable, since Central Europe was surrounded by active plate boundaries and affected coevally by subduction of the Paleotethys, opening of the Neotethys (Ziegler at al., 1988; Decourt et al., 2000; Stampfli et al., 2001; Stampfli & Borel, 2002, 2004) and rifting in the future Central Atlantic domain (Steiner et al., 1998; Zühlke et al., 2004) and in the Norwegian-Greenland Sea (Torsvik et al., 2002). The phase of thermal subsidence was accompanied by the successive deposition of the latest *Rotliegend* clastic sediments, followed by the Upper Permian *Zechstein* evaporites, the Lower Triassic continental clastics of the *Buntsandstein*, and the marine carbonates of the *Muschelkalk*. Due to special rheological properties, the *Zechstein* salt layers have thenceforward recurrently been activated thus modifying later deformation patterns.

(3) *Mid-Triassic – Jurassic phase of E-W extension*: During this period, the tectonic activity in the CEBS was controlled by ongoing rifting processes in the Tethyan and the Arctic-North

Atlantic areas (Scheck-Wenderoth et al., 2008a). A north-directed subduction of the Paleotethys led to the collision of ‘Cimmerian’ terranes with the southern margin of Eurasia (Stampfli & Borel, 2002). In the CEBS, however, roughly E-W oriented extension prevailed. This is indicated by N-S-trending axes of depocentres that partly dissect the Mid-North Sea-Ringkøbing-Fyn High (Scheck-Wenderoth & Lamarche, 2005). For many of these basins, such as the Central Graben, the Horn Graben, and the Glücksstadt Graben, it was recorded that syndepositional normal faulting was accompanied by a mobilization of the underlying *Zechstein* salt layers. Considering the locally increased thickness of lacustrine *Keuper* sediments within the Glücksstadt Graben, maximum extension can be dated back to Mid-Late Triassic times (Maystrenko et al., 2005).

(4) *Mid-Jurassic phase of uplift*: During the Mid-Jurassic, the structural framework of Central Europe was constituted by the start of oceanic spreading in the Alpine Tethys and in the central Atlantic (Stampfli & Borel, 2002) as well as by the development of the central North Sea rift system. The latter is believed to have been initiated by a deep-seated thermal anomaly beneath the Mid-North Sea High and related up-doming of the central North Sea (Underhill & Partington, 1993). The uplift of the central North Sea was strongest at the triple-junction between the Viking Graben, the Moray Firth Basin, and the Central Graben where rift-related processes generated basaltic lavas. Considering that also large parts of north Central Europe successively have been elevated during this period, the whole range of interacting processes which could be regarded responsible for the regional uplift is still enigmatic (Scheck-Wenderoth et al., 2008a). As a result of this uplift, the Jurassic formations in the CEBS widely reflect a development from deep to shallower water conditions.

(5) *Late Jurassic – Early Cretaceous phase of basin differentiation*: During this period, Central Europe was mainly influenced by far-field stresses produced by the northward propagation of the central Atlantic spreading centre (Stampfli & Borel, 2002) and extensive rifting in the Norwegian Sea (Pascal et al., 2002; Torsvik et al., 2002). In the CEBS, Late Jurassic to Early Cretaceous subsidence was restricted to NW-SE trending depocentres along the margins of the basin system, i.e. along the Sorgenfrei-Tornquist Zone (Surlyk, 2003), in the Polish Basin along the Teisseyre-Tornquist Zone (Dadlez et al., 1995, 1998), and in numerous NW-SE-oriented basins along the southern margin where localized subsidence was accompanied by the mobilisation of *Zechstein* salt (Scheck et al., 2002a; Scheck-Wenderoth & Lamarche, 2005). In contrast, areas in the central parts of the CEBS such as the Ringkøbing-Fyn High or the northern parts of the North German Basin experienced uplift (Walter et al., 1995; Kossow & Krawczyk, 2002).

(6) *Late Cretaceous – Early Tertiary phase of inversion*: Though the large-scale plate-tectonic framework of Central Europe was still controlled by earlier commencing processes such as rifting within the Norwegian-Greenland Sea, successive northward propagation of the North Atlantic spreading, and closure of the Tethys, the Late Cretaceous was marked by a grave change in the style of intra-plate deformation from an extensional and transtensional towards a compressional and transpressional mode. Areas which once had subsided during the Late Jurassic to Early Cretaceous now experienced uplift and inversion (Voigt, 1962). This CEBS-wide inversion mainly affected WNW- and NW-striking blocks (Scheck-Wenderoth & Lamarche, 2005), whereas former N-S-striking depocentres as the Glücksstadt Graben generally do not show inversion-related signs of compression or uplift (Maystrenko et al., 2005).

(7) *Cenozoic subsidence*: From the Eocene on, when seafloor spreading reached the North Atlantic, the CEBS experienced continuous sag-like subsidence with little faulting and

renewed salt rise (Scheck-Wenderoth & Lamarche, 2005). It is assumed that either thermal relaxation (Ziegler, 1990) or flexural bending of the North Sea lithosphere (Hansen & Nielsen, 2003; Van Wees & Beekman, 2000) is responsible for this subsidence. Whatever the reason, mainly N-S striking subsidence axes with a major depocentre in the Central North Sea have been created during this stage. This preferred orientation of subsidence centres indicates an interrelation of the Cenozoic subsidence and the build-up of the present-day stress field in Central Europe which is characterised by a predominantly NW-SE-directed maximum horizontal stress, S_{Hmax} (Heidbach et al., 2008).

1.3 Study areas

Since this study is based on field investigations, the distribution of analysed subareas is highly dependent on the availability and suitability of outcrops. The central parts of the CEBS are widely covered by unconsolidated sediments and water so that field studies are generally restricted to the marginal parts of the basin system. Along the southern margin of the CEBS, where Late Paleozoic to Mesozoic rocks are exposed as a consequence of inversion-related uplift and erosion, main focus was laid upon the eastern parts of the Elbe Fault System between western Germany and southwestern Poland (Fig. 5, 6). Thus, a spatial gap is closed between two subareas along the southern margin of the CEBS for which paleostress states already have been reconstructed, i.e. between an area covering parts of southern England, northern France, and Belgium (Vandycke, 2002) and an area in southeastern Poland (Lamarche et al., 1999, 2002). To obtain comparable insights into the development of the northern margin of the CEBS, the study reaches even beyond the Tornquist Zone into the Oslo Graben area, where excellent outcrops of Precambrian to Permian rocks are available (Fig. 7). To potentially detect differently-aged paleostress states and, if possible, infer a paleostress stratigraphy (Kleinspehn et al, 1989), the investigated sites of each subarea were selected so as to cover a broad range of differently-aged rocks (Tab. 1, 2).

1.3.1 The southern margin of the CEBS

The southern margin of the CEBS is structured by the Elbe Fault System (EFS), a NW- to WNW-striking, *en echelon* fault zone extending from the southeastern North Sea to southwestern Poland along the present southern margin of the North German Basin and the northern margin of the Sudetes Mountains (Fig. 2). As a result of a weak, stress-sensitive zone in the lower crust which repeatedly supported strain localisation, this fault zone has been recurrently activated in response to variations in the tectonic regime since Late Carboniferous times (Scheck et al., 2002a). In general, the kinematic interpretation of the EFS still remains a matter of debate; some authors favour pure compressional, respective pure extensional, regimes for different periods and places (Kockel, 2003; Franzke et al., 2007), whereas others postulate recurring phases of wrench tectonics (Betz et al., 1987; Wrede, 1988; Drozdzewski, 1988).
During the Late Carboniferous to Early Permian *initial rift phase*, the EFS is suggested to have acted as the southern boundary fault of a great wrench fault system in north Central Europe, in the centre of which the Northern and the Southern Permian Basin, respectively, developed (Bachmann & Hoffmann, 1997; Mattern, 1996; Ziegler, 1990; Scheck-Wenderoth & Lamarche, 2005). Accordingly, during the Permian to Triassic, the EFS formed the southern margin of the thermally subsiding areas of the North German Basin and the Polish Basin. The phase of *Mid-Triassic – Jurassic E-W extension* which initiated the large N-S-trending grabens of the CEBS had only minor influence on the EFS except for a partial

dissection of the NW-SE-trending structures into smaller segments (Betz et a., 1987). For the *Late Jurassic – Early Cretaceous phase of basin differentiation*, dextral translation along the EFS caused localized subsidence in numerous NW-SE-trending basins including the Lower Saxony Basin and the Subhercynian Basin (Ziegler, 1990; Betz et al., 1987; Scheck & Bayer, 1999) as well as the Cretaceous Münsterland Basin which developed directly above Variscan basement faults (Baldschuhn et al., 2001). Due to their orientation, the numerous NW- and WNW-striking faults of the EFS appear to have been very prone to the phase of *Late Cretaceous – Early Tertiary inversion* which is indicated by thrust and transpressional movements as well as uplift of adjacent sub-basins during this period.

As a consequence of inversion-related uplift and erosion of the southern margin of the CEBS, some of the major structural elements of the EFS are exposed and accessible where Late Paleozoic and Mesozoic rocks crop out. Along the southern margin of the Lower Saxony Basin, the Osning Lineament is exposed as a zone of intensely deformed Upper Cretaceous rocks (Fig. 5). The Northern Harz Boundary Fault, on the other hand, separates the Variscan deformed blocks of the Harz Mountains from the Mesozoic to Cenozoic rocks of the Subhercynian Basin. The Osning Lineament and the Northern Harz Boundary Fault, in turn, are separated by the N-S-trending Hessian Depression providing several outcrops of Triassic rocks. The Subhercynian Basin is bordered to the north by the Allertal Fault Zone which marks the transition towards the mainly Paleozoic rocks of the Flechtingen structural high. The major faults structuring southeastern Poland are the Main Intra-Sudetic Fault and the Sudetic Marginal Fault which differentiate the Sudetic Block into parts with different tectonic histories (Fig. 6).
Whereas the present-day stress configurations in the southern parts of the CEBS are well known (Roth and Fleckenstein, 2001; Kaiser et al., 2005; Heidbach et al., 2008), there are only few studies on the evolution of paleostress fields (Lamarche et al., 1999, 2002; Vandycke, 2002; Franzke et al., 2007). For the reconstruction of paleostress states in the German and Polish parts of the EFS, a total number of 65 outcrops have been investigated (Tab. 1). These outcrops cover rocks of Late Carboniferous, Late Permian, Middle Triassic, Late Jurassic, and Late Cretaceous ages. Most of the investigated sites correspond to active or abandoned quarries, while the area otherwise is widely covered by Cenozoic sediments. At most of the studied locations (#1-37, #55-57), the number and the quality of measured fault-slip data are adequate for applying the stress inversion method introduced in Chapter 2.

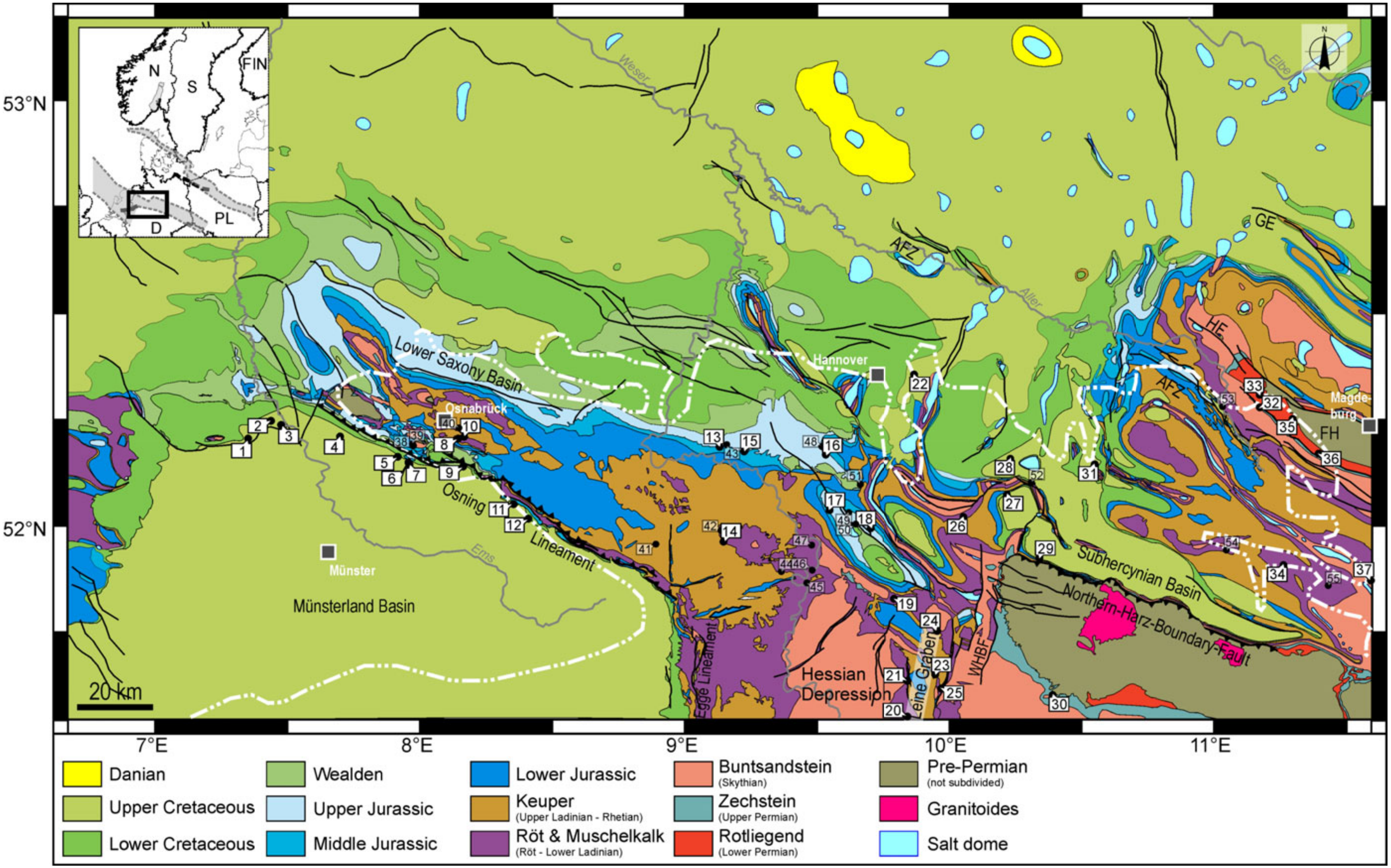

Figure 5: German parts of the Elbe Fault System presented as a geological subcrop map of the base of Cenozoic units (modified after Baldschuhn & Kockel, 1996). Due to inversion-related uplift and erosion, Upper Paleozoic and Mesozoic rocks have been elevated to the level of Upper Cretaceous rocks. The main structural elements strike WNW-ESE. Areas north of the dotted white line are widely covered by Cenozoic sediments. Numbers indicate investigated outcrops. Larger numbers represent sites where the fault-slip data have been adequate for a stress inversion (Tab. 1).
AFZ – Allertal Fault Zone, FH – Flechtingen High, GE – Gardelegen Escarpment, HF – Haldensleben Fault, WHBF – Western Harz Boundary Fault.

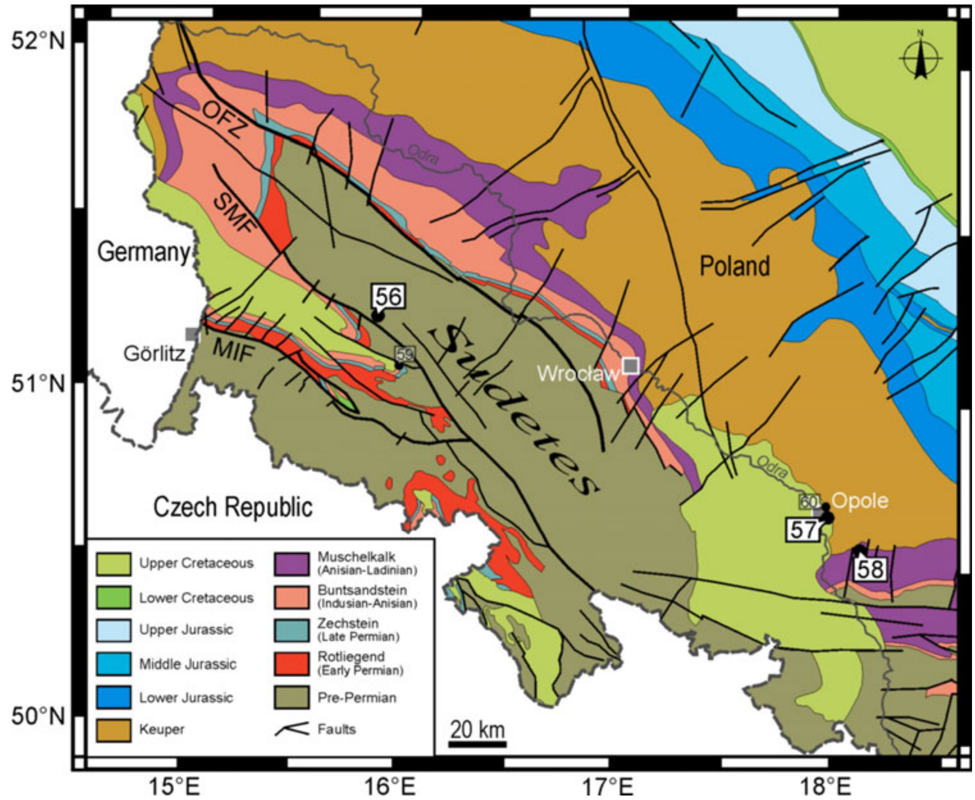

Figure 6: Polish parts of the EFS presented as a geological subcrop map of the base of Cenozoic units (modified after Dadlez et al., 2000). Major faults structuring the Sudetic Block in southeastern Poland strike WNW- to NW such as the Odra Fault Zone (OFZ), the Sudetic Marginal fault (SMF), and the Main Intra-Sudetic Fault (MIF). Dots with numbers indicate investigated outcrops. Larger numbers represent sites where the fault-slip data have been adequate for a stress inversion (Tab. 1).

Table 1: List of outcrops investigated along the southern margin of the CEBS. Shaded numbers indicate sites where the fault-slip data have been adequate for estimating paleostress states.

No.	Name	Latitude [°N]	Longitude [°E]	Lithology	Rock age / Period	Rock age (stratigraphy)
1	Wettringen	52.218	7.321	limestone	Late Cretaceous	Cenomanian-Turonian
2	Rheine	52.262	7.402	limestone	Late Cretaceous	Cenomanian-Turonian
3	Middel	52.256	7.438	limestone	Late Cretaceous	Cenomanian-Turonian
4	Dörenthe	52.227	7.673	limestone	Late Cretaceous	Cenomanian
5	Lengerich	52.182	7.896	limestone	Late Cretaceous	Cenomanian-Turonian
6	Höste	52.167	7.938	limestone	Late Cretaceous	Cenomanian
7	Lienen	52.164	7.942	limestone	Late Cretaceous	Cenomanian
8	Holsten	52.228	8.128	limestone	Middle Triassic	Anisian-Ladinian (Muschelkalk)
9	Hilter	52.161	8.149	limestone	Late Cretaceous	Cenomanian
10	Bissendorf	52.231	8.150	limestone	Middle Triassic	Anisian-Ladinian (Muschelkalk)
11	Halle	52.074	8.345	limestone	Late Cretaceous	Turonian-Coniacian
12	Künsebeck	52.040	8.404	limestone	Late Cretaceous	Cenomanian-Turonian
13	Steinbergen	52.217	9.137	limestone	Late Jurassic	Oxfordian (Malm)
14	Barntrup	51.996	9.154	limestone	Middle Triassic	Anisian-Ladinian (Muschelkalk)
15	Rohden	52.206	9.234	limestone	Late Jurassic	Oxfordian (Malm)
16	Hamelspringe	52.194	9.537	limestone	Late Jurassic	Oxfordian (Malm)
17	Lauenstein	52.068	9.543	limestone	Late Jurassic	Oxfordian (Malm)
18	Marienhagen	52.021	9.704	limestone	Late Jurassic	Oxfordian (Malm)
19	Avendshausen	51.851	9.791	limestone	Middle Triassic	Anisian (Muschelkalk)
20	Emmenhausen	51.576	9.835	limestone	Middle Triassic	Anisian (Muschelkalk)
21	Hardegsen	51.660	9.836	limestone	Middle Triassic	Anisian (Muschelkalk)
22	Misburg	52.384	9.884	limestone	Late Cretaceous	Cenomanian-Turonian
23	Elvese	51.674	9.938	limestone	Middle Triassic	Anisian (Muschelkalk)
24	Vogelbeck	51.775	9.950	limestone	Middle Triassic	Anisian (Muschelkalk)
25	Papenberg	51.643	9.961	limestone	Middle Triassic	Anisian (Muschelkalk)
26	Upstedt	52.042	10.059	limestone	Middle Triassic	Anisian-Ladinian (Muschelkalk)
27	Baddeckenstedt	52.092	10.230	limestone	Late Cretaceous	Cenomanian-Turonian
28	Söhlde	52.182	10.245	limestone	Late Cretaceous	Cenomanian-Turonian
29	Langelsheim	51.939	10.352	limestone	Late Cretaceous	Cenomanian-Turonian
30	Scharzfeld	51.619	10.391	dolomite	Late Permian	Zechstein (Z2)
31	Wendessen	52.161	10.568	limestone	Late Cretaceous	Cenomanian-Turonian
32	Bodendorf	52.279	11.210	andesite	Late Carboniferous	Stephanian
33	Flechtingen	52.315	11.210	rhyolite	Late Carboniferous	Stephanian
34	Kroppenstedt	51.915	11.290	limestone	Middle Triassic	Anisian (Muschelkalk)
35	Dönstedt	52.259	11.333	andesite	Late Carboniferous	Stephanian
36	Mammendorf	52.178	11.435	andesite	Late Carboniferous	Stephanian
37	Förderstedt	51.875	11.629	limestone	Middle Triassic	Anisian (Muschelkalk)
38	Silberberg	52.211	7.945	dolomite	Late Permian	Zechstein
39	Heidberg	52.217	7.949	sandstone	Early Cretaceous	Valanginian-Aptian
40	Natbergen	52.253	8.126	limestone	Middle Triassic	Anisian-Ladinian (Muschelkalk)
41	Detmold-Bentrup	51.988	8.891	limestone	Middle Triassic	Anisian-Ladinian (Muschelkalk)
42	Alverdissen	52.020	9.139	limestone	Middle Triassic	Anisian-Ladinian (Muschelkalk)
43	Bernsen	52.214	9.159	limestone	Late Jurassic	Oxfordian (Malm)
44	Vahlbruch	51.924	9.362	limestone	Middle Triassic	Anisian-Ladinian (Muschelkalk)
45	Straße Forst-Polle	51.887	9.453	limestone	Middle Triassic	Anisian-Ladinian (Muschelkalk)
46	Straße Rühle-Dölme	51.930	9.457	limestone	Middle Triassic	Anisian-Ladinian (Muschelkalk)
47	Hehlen	51.982	9.458	limestone	Middle Triassic	Anisian-Ladinian (Muschelkalk)
48	Springe	52.216	9.527	limestone	Late Jurassic	Oxfordian (Malm)
49	Salzhemmendorf	52.056	9.608	dolomitic limestone	Late Jurassic	Oxfordian (Malm)
50	Thüste	52.022	9.653	limestone	Late Jurassic	Oxfordian (Malm)
51	Wülfinghausen	52.137	9.655	limestone	Late Jurassic	Oxfordian (Malm)
52	Salder	52.124	10.330	limestone	Late Cretaceous	Turonian-Coniacian
53	Walbeck	52.295	11.068	limestone	Middle Triassic	Anisian (Muschelkalk)
54	Schwanebeck	51.955	11.076	limestone	Middle Triassic	Anisian (Muschelkalk)
55	Groß Börnecke	51.866	11.467	limestone	Middle Triassic	Anisian (Muschelkalk)
56	Raciborovice	51.192	15.709	limestone	Middle Triassic	Anisian (Muschelkalk)
57	Folwark	50.612	17.909	limestone	Upper Cretaceous	Cenomanian-Turonian
58	Gorazdze	50.526	18.029	limestone	Middle Triassic	Anisian (Muschelkalk)
59	Forrest	51.121	15.868	sandstone	Lower Triassic	Skythian (Buntsandstein)
60	Opole	50.686	17.931	marl	Upper Cretaceous	Cenomanian-Turonian

1.3.2 The Oslo Graben area

The Oslo Graben in southern Norway is a N-S-trending, 200 km long and 35-65 km wide, down-faulted crustal block that exposes Palaeozoic rocks in contrast to the surrounding Precambrian high-grade metamorphic rocks of Fennoscandia (Fig. 7). The graben is the highly volcanic onshore segment of the Oslo paleorift system, while the Skagerrak Graben to the south forms its offshore counterpart which terminates in the Sorgenfrei-Tornquist Zone (Fig. 1).

The Precambrian basement surrounding the Oslo Graben area formed between 1800 Ma and 1550 Ma and was metamorphosed during the Sveconorwegian orogeny between 1100 Ma and 950 Ma (Berthelsen, 1980, 1992; Skjernaa & Pedersen, 1982). During early Paleozoic times the area was part of an extensive shelf where Cambro-Silurian marine sediments and Silurian to Devonian red bed successions have been deposited (Neumann et al., 1992). During the Silurian and Devonian the entire succession was folded in the course of the Caledonian orogeny and afterwards eroded to a peneplane. A hiatus spanning Devonian (Ludlowian) to early-Middle Carboniferous (Moscovian) rock ages suggests that the Oslo Graben area probably was exposed above sea-level during these times. In Late Carboniferous times, the Variscan Orogeny caused a reorganisation of Pangea involving the transformation of the Variscan fold belt under N-S-directed compression into a wrench system and probably also the development of the intracontinental Oslo Rift system (Ziegler, 1990; Olaussen et al., 1994). According to Larsen et al. (2008), the evolution of the Oslo Rift can be subdivided into 6 progression phases commencing in Late Carboniferous times and spanning about 65 million years (Chapter 5). It is suggested that this period of extensive rifting was followed by a long-lasting period of tectonic quiescence with no major tectonic or magmatic activity (Sundvoll & Larsen, 1994). However, two phases of rapid uplift during Triassic-Jurassic and Neogene times, respectively, caused high rates of erosion (Rohrman et al., 1995) so that presently, there is a great lack in the stratigraphic record encompassing the whole Mesozoic and Cenozoic. Hence, any field-based study in the area relies on the preserved sedimentary and magmatic rocks comprising Precambrian, Cambro-Silurian and Permian rock ages (Fig. 7).

Considering the post-Permo-Carboniferous evolution of the CEBS, even the youngest of exposed rocks in the Oslo Graben area do not provide close constraints on the maximum age of faults and associated stress states therein. However, several authors have suggested that the initiation of the Oslo Rift has been closely tied to concurrent tectonics within the STZ (Glennie, 1984; Ziegler, 1990; Veevers et al., 1994) which, in turn, played a decisive role in the Mesozoic-Cenozoic evolution of the CEBS (Vejbaek, 1990; Scheck-Wenderoth et al., 2008a). In light of these interrelations, fault-slip data from the Oslo Graben area sampled and published by Heeremans et al. (1996) are re-evaluated in this study (Chapter 5) by subjecting them to the new stress inversion procedure introduced in Chapter 2. Beside these data, a second set of unpublished fault-slip data from the graben area is interpreted (sampled and provided by Aline Saintot, Geological Survey of Norway, NGU). Taken together, the total number of 101 investigated locations covers large parts of the graben area and a wide range of exposed rock ages (Tab. 2). Existing studies on the evolution of paleostress fields within the STZ (Bergerat et al., 2007) and on the present-day stress field in Norway (Gregersen, 1992; Lindholm et al., 2000; Heidbach et al., 2008) widen the framework within which the locally inferred paleostress states finally can be discussed.

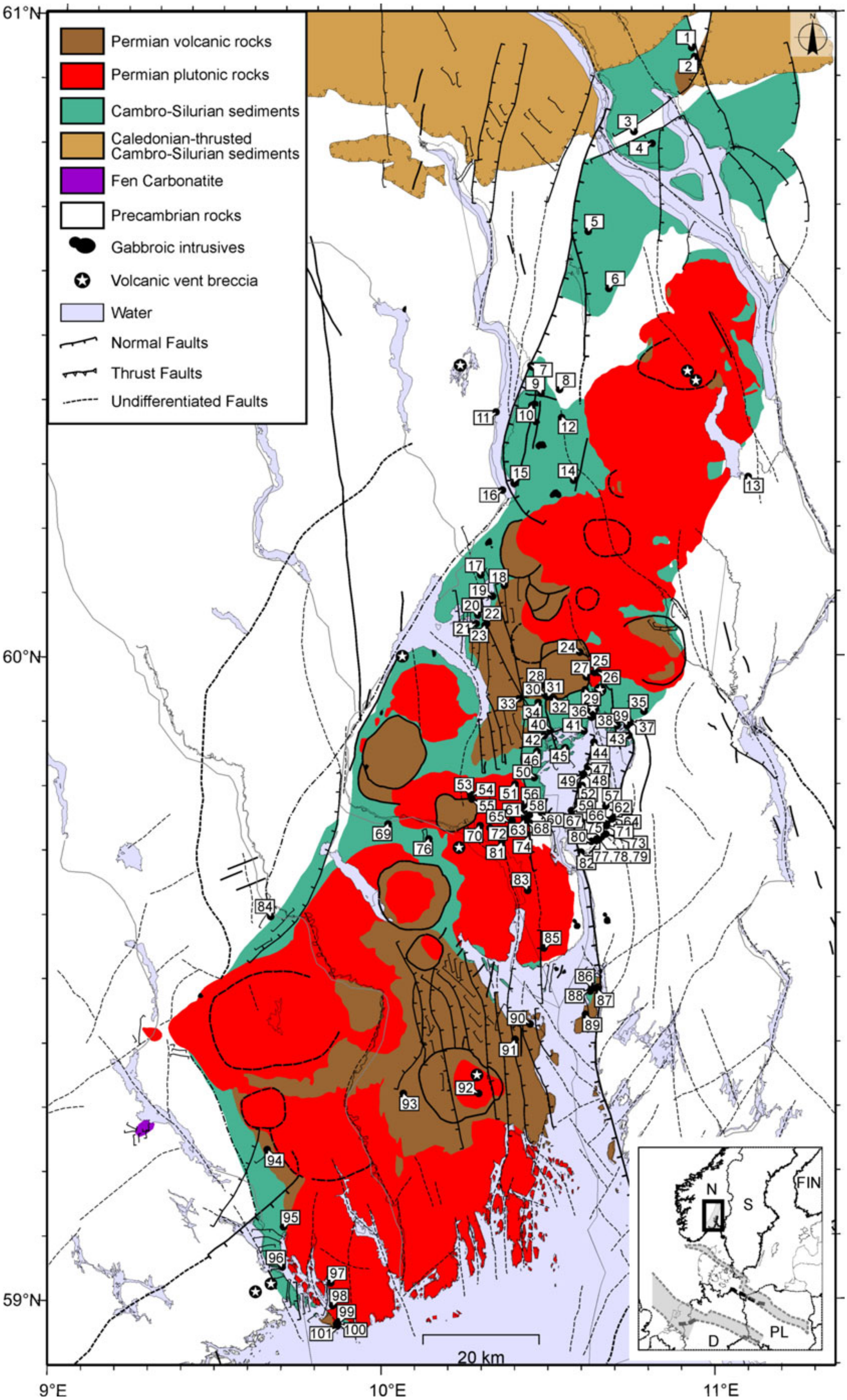

Figure 7: The Oslo Graben area presented as a tectonomagmatic map (modified after Ramberg & Larsen, 1978). The investigated sites are numbered as in Table 2. Note the numerous roughly N-S-striking faults as well as the ring faults that flank caldera structures.

Table 2: List of outcrops investigated in the Oslo Graben area.

No.	Name	Latitude [°N]	Longitude [°E]	Lithology	Rock age	Source
1	Torunstad Mælum	60.9473	10.9899	Shale, Sandstone	Silurian	M. Heeremans
2	Brummunddal	60.9332	10.9984	Sandstone	Permian	M. Heeremans
3	Hellerud	60.8179	10.8027	Gneisse	Precambrian	M. Heeremans
4	Gorum	60.7992	10.8595	Limestone	Lower Ordovician	M. Heeremans
5	Bøverbu	60.664	10.6541	Limestone	Cambro-Silurian	M. Heeremans
6	Korslia	60.5747	10.7171	Limestone, marl	Ordovician-Silurian	M. Heeremans
7	Skari	60.456	10.4708	Gneiss	Precambrian	M. Heeremans
8	Moen	60.4186	10.5599	Gneiss	Precambrian	M. Heeremans
9	Brandbu	60.413	10.5015	Limestone	Ordovician-Silurian	M. Heeremans
10	Tingelstad	60.394	10.4725	Limestone	Ordovician-Silurian	M. Heeremans
11	Engnes	60.3844	10.3596	Gneiss	Precambrian	M. Heeremans
12	Jaren	60.375	10.5651	Maenaite	Permian	M. Heeremans
13	Råholt	60.2793	11.1456	Gneiss	Precambrian	M. Heeremans
14	Roa	60.2771	10.6011	Limestone	Ordovician-Silurian	M. Heeremans
15	Grymyr	60.2725	10.4173	Limestone	Ordovician-Silurian	M. Heeremans
16	Jevnaker	60.2627	10.3787	Gneiss	Precambrian	M. Heeremans
17	Åsa	60.1315	10.3098	Carbonate	Upper Silurian	M. Heeremans
18	Stubdalskampen	60.1148	10.3836	Sandstone, Quartzite (Ringerike Group)	Ordovician-Silurian	M. Heeremans
19	Åsaveien	60.0977	10.3466	Sandstone	Silurian	A. Saintot
20	Kroksund	60.0689	10.2999	Sandstone, Limestone, Marl	Silurian	M. Heeremans
21	Sundvollen 3	60.0556	10.2948	Sandstone (Ringerike)	Silurian	M. Heeremans
22	Sundvollen 2	60.0552	10.3275	Sandstone (PZ1)	Cambro-Silurian	A. Saintot
23	Sundvollen 1	60.0528	10.3221	Rhomb porphyry with sedimentary layers	Permian	A. Saintot
24	Sørkedal	60.0101	10.6152	Volcanics, eruptive and sedimentary breccia	Permian	A. Saintot
25	Holmenkollen	59.9785	10.6601	Granite	Permian	A. Saintot
26	Frognerseteren	59.9782	10.6741	Syenite	Permian	A. Saintot
27	Bogstad	59.9714	10.6348	Syenite, Granite	Permian	A. Saintot
28	Burudveien	59.9596	10.4967	Basalt	Permian	A. Saintot
29	Grinibru	59.9516	10.6309	Limestone, shale, Sandstone	Early Silurian	A. Saintot
30	Skollerudveien	59.9438	10.5087	Basalt	Permian	A. Saintot
31	Bærums Verk	59.9409	10.5133	Rhomb porphyry lava	Permian	A. Saintot
32	Gamle Ringeriksvei	59.9389	10.5328	Basalt	Permian	A. Saintot
33	Hvile	59.9383	10.4254	Rhomb porphyry basalt	Permian	M. Heeremans
34	Rykkinn	59.9325	10.4848	Sandstone (Ringerike group)	Upper Silurian	A. Saintot
35	Sinsen	59.917	10.8118	Marl, Limestone	Cambro-Silurian	M. Heeremans
36	Vækerø	59.9088	10.6504	Limestone, Black shale	Cambro-Silurian	M. Heeremans
37	Ekeberg	59.8996	10.7697	Granite, Gneiss	Precambrian	M. Heeremans
38	Hovedøya	59.8952	10.7283	marl, Limestone, Sandstone	Cambro-Silurian	M. Heeremans
39	Kongshavn	59.8948	10.7587	Gneiss	Precambrian	M. Heeremans
40	Sandvika	59.8883	10.5216	Black shale	Cambro-Silurian	M. Heeremans
41	Fornebru	59.8875	10.6261	Limestone, Marl	Cambro-Silurian	M. Heeremans
42	Gryssestad	59.8808	10.5032	Syenite	Permian	M. Heeremans
43	Malmøya	59.8799	10.7642	Limestone, Marl	Cambro-Silurian	M. Heeremans
44	Nesoddtangen	59.8699	10.6564	Gneiss	Precambrian	A. Saintot
45	Ostøya	59.8617	10.5677	Limestone	Ordovician-Silurian	M. Heeremans
46	Hvalstad	59.8564	10.4808	Black shale, Limestone	Cambro-Silurian	M. Heeremans
47	Bjørnemyr	59.8319	10.6367	Gneiss	Precambrian	A. Saintot
48	Alværn Brygge 2	59.8208	10.6233	Shaly, marly slate, Limestone	Ordovician	A. Saintot
49	Alværn Brygge 1	59.8189	10.6193	Shaly, marly slate, Limestone	Ordovician	A. Saintot
50	Blakstad	59.8157	10.4713	Limestone, Shale (PZ1)	Ordovician	A. Saintot
51	Hauger	59.8061	10.4123	Granite	Permian	A. Saintot
52	Fjellstrand	59.8029	10.6187	Gneiss	Precambrian	A. Saintot
53	Utsikten	59.7905	10.2757	Granite	Permian	A. Saintot
54	Stokke	59.788	10.2768	Granite	Permian	A. Saintot
55	Reistad	59.7832	10.2797	Granite	Permian	A. Saintot
56	Bøveien	59.7722	10.439	Limestone, Shale (PZ1)	Ordovician	A. Saintot
57	Hasle	59.771	10.691	Mica-rich gneiss	Precambrian	A. Saintot
58	Mølleveien	59.7651	10.4377	Slates, Sandstone, Conglomerate	Cambrian	A. Saintot
59	Spro	59.7638	10.5853	Gneiss	Precambrian	A. Saintot
60	Nærsnes	59.7632	10.4964	Gneiss	Precambrian	A. Saintot
61	Slemmestadveien	59.7573	10.4557	Shaly, Marly slates and Limestone	Ordovician	A. Saintot
62	Brevik	59.7522	10.7147	Gneiss	Precambrian	A. Saintot

Table 2: (continued).

No.	Name	Latitude [°N]	Longitude [°E]	Lithology	Rock age	Source
63	Brynsholmen	59.751	10.4408	Gneiss	Precambrian	A. Saintot
64	Dalbanen	59.7504	10.7102	Gneiss	Precambrian	A. Saintot
65	Røyken	59.7488	10.4023	Granite	Permian	A. Saintot
66	Nordre Dal	59.7478	10.6968	Gneiss	Precambrian	A. Saintot
67	Alværn Brygge 3	59.7472	10.6144	Granodiorite, Tonalite	Precambrian	A. Saintot
68	Gunnerud	59.7453	10.4552	Granite	Precambrian	A. Saintot
69	Mjøndalen	59.7441	10.0221	Limestone	Ordovician-Silurian	M. Heeremans
70	Gullaugfjellet	59.7412	10.304	Granite	Permian	A. Saintot
71	Søndre Dal	59.7397	10.6927	Gneiss	Precambrian	A. Saintot
72	Ovnerudveien	59.7378	10.3345	Granite	Permian	A. Saintot
73	Tusse	59.7269	10.6898	Gneiss	Precambrian	A. Saintot
74	Krokodden	59.7264	10.4486	Granite	Permian	A. Saintot
75	Fagerstrandveien	59.7224	10.6759	Gneiss	Precambrian	A. Saintot
76	Konnerud	59.721	10.1468	Limestone	Cambro-Silurian	M. Heeremans
77	Holtbråten 3	59.7204	10.6642	Gneiss, Pegmatite	Precambrian	M. Heeremans
78	Holtbråten 1	59.7196	10.6662	Gneiss	Precambrian	A. Saintot
79	Holtbråten 2	59.719	10.6627	Syenites	Permian	A. Saintot
80	Hallangshagen	59.716	10.645	Granitic to Tonalitic gneiss	Precambrian	A. Saintot
81	Hyggen	59.7156	10.3704	Granite (Drammen)	Permian	M. Heeremans
82	Hallangen	59.6991	10.6134	Gneiss	Precambrian	M. Heeremans
83	Selvik	59.6403	10.4491	Granite (Drammen)	Permian	M. Heeremans
84	Heistadmoen	59.6004	9.66287	Amphibolite, Gneiss	Precambrian	M. Heeremans
85	Tofte Tronstad	59.5508	10.4971	Granite (Drammen)	Permian	M. Heeremans
86	Jeløya 2	59.4886	10.6417	Sandstone (Ringerike Group)	Cambro-Silurian	A. Saintot
87	Jeløya 3	59.4872	10.6564	Basalt (Basalt 1and 2)	Permian	A. Saintot
88	Jeløya 1	59.4831	10.6367	Sandstone (Ringerike Group)	Cambro-Silurian	A. Saintot
89	Jeløya 4	59.4475	10.6225	Basalt (Basalt 1and 2)	Permian	M. Heeremans
90	Horten	59.4328	10.4535	Basalt (Basalt 1and 2)	Permian	M. Heeremans
91	Steinholt	59.4091	10.4075	Larvikite	Permian	M. Heeremans
92	Himberg	59.3254	10.296	Larvikite	Permian	M. Heeremans
93	Lakstjen	59.3252	10.0675	Porphyritic lava	Permian	M. Heeremans
94	Skoppum	59.2381	9.65564	Rhomb porphyry lava	Permian	M. Heeremans
95	Eidanger	59.118	9.70649	Limestone	Ordovician-Silurian	M. Heeremans
96	North of Brevik	59.0557	9.70287	Slates and Limestone	Ordovician	A. Saintot
97	Tveidalen	59.0309	9.84897	Larvikite	Permian	A. Saintot
98	NW-Nevlunghavn	58.996	9.85471	Larvikite	Permian	A. Saintot
99	Nevlunghavn 1	58.9677	9.8693	Larvikite	Permian	A. Saintot
100	Nevlunghavn 2	58.9668	9.86734	Larvikite	Permian	A. Saintot
101	Nevlunghavn 3	58.9657	9.86893	Larvikite	Permian	A. Saintot

2 Fault-slip analysis and paleostress reconstruction

The present study on the evolution of paleostress fields in the Central European Basin System is primarily based on signs of brittle deformation observable in the field. The basic assumption of fault-slip analysis is that the pattern of striated faults in a portion of rock can be correlated with a state of stress responsible for the observed faulting (Carey & Brunier, 1974; Angelier, 1979). In the following, a summary is given on the basics of fault-slip analysis before a new strategy is introduced for estimating stress states even from heterogeneous data. Finally, some concepts are demonstrated regarding a correlation of locally estimated paleostress states to deduce the evolution of regional stress fields in an area.

2.1 Basics

According to Wallace (1951) and Bott (1959), it is possible to predict the slip direction along a plane of known orientation (with unit normal $\vec{n}$) under a given stress tensor σ, assuming that slip takes place parallel to the direction of maximum resolved shear stress $\vec{\tau}_{max}$ (Fig. 8a):

$$\vec{\tau}_{max} = \sigma \cdot \vec{n} - \left[\vec{n}^{T} \cdot \sigma \cdot \vec{n}\right] \cdot \vec{n} \qquad \text{(Eq. 1)}$$

where the superscript T means the transpose of the matrix. On the other hand, a fracture plane will be created with a stress state dependent orientation that allows the relative magnitudes of the shear stress τ and the normal stress σ_n in this plane to meet with the Mohr-Coulomb yield criterion,

$$\tau = C + \mu\sigma_n \qquad \text{(Eq. 2)}$$

where C and μ are the material-specific cohesion and coefficient of friction, respectively (Fig. 8b; Coulomb, 1776; Mohr, 1900).

Whereas Equation 1 considers any (re)activation of a fault plane, Equation 2 is valid only for newly-formed faults, i.e. fractures which are opened and sheared under the same stress state. These two principles allow predictions about fault kinematics given a known stress field that acts on an elastic material of known properties. To solve the inverse problem, which is to derive a stress state from observed fault kinematics, two types of techniques have been established through the last decades, some based on slip criteria, others on frictional criteria (Angelier, 1994; Ramsay & Lisle, 2000). To allow for solutions as realistic as possible, some techniques even combine both concepts (Reches, 1987; Célérier, 1988; Angelier, 1990; Žalohar & Vrabec, 2007).

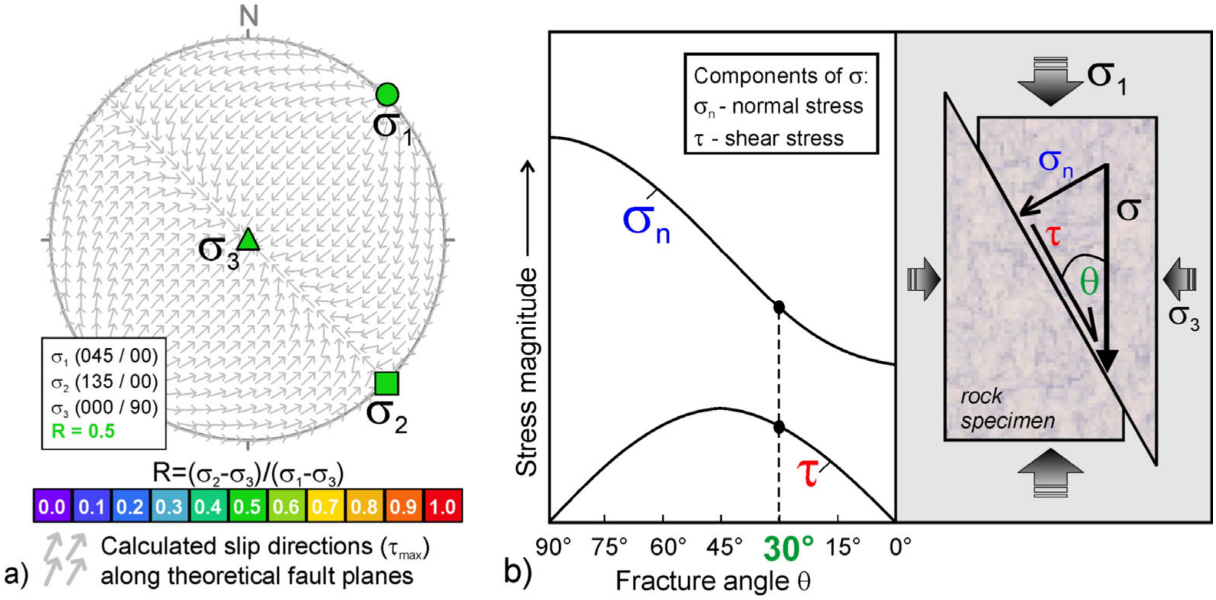

Figure 8: Fault kinematics. a) For a known reduced stress tensor, the directions of the maximum shear stress, τ_{max}, along fault planes of known orientation can be calculated (Wallace-Bott hypothesis). Theoretical fault-slip data are presented in a *tangent-lineation plot* (Hoeppener, 1955; Twiss & Gefell, 1990): each arrow in this lower-hemisphere, equal-area projection represents one fault-slip datum; the centre of each arrow indicates the pole to the respective fault plane while the arrowhead indicates the slip direction of the footwall block. Hence, the plot displays the directions in which material would move past the outside of a fixed lower hemisphere under the given stress. b) *Left*: Relative magnitudes of the shear stress, τ, and the normal stress, σ_n, on a plane as a function of the fracture angle θ (modified after van der Pluijm & Marshak, 2004). At θ=30°, the ratio of shear stress to normal stress σ_n/τ is at a maximum (Mohr-Coulomb fracture criterion), so that shear fracturing is facilitated. *Right*: A rock sample cracked in laboratory (biaxial conditions; σ_2 equals σ_3): the angle between σ_1 and the fracture plane is measured as θ=30°.

Striae on a fault plane, such as slickenside lineations, may unambiguously document the sense of relative movement between the footwall block and the hanging-wall block of a fault (Fig. 9; Fleuty, 1974; Doblas, 1998), thus providing the essential part for stress tensor calculations based on the "Wallace-Bott hypothesis" (Fig. 8a). Beside the sense of slip (reverse, normal, dextral, or sinistral), a complete fault-slip datum comprises the orientation of the fault plane (dip direction and dip) and the orientation of the striae (azimuth and plunge). Knowing the fault-slip attitudes of at least four independent faults, it is possible to directly calculate the corresponding 'reduced stress tensor' which comprises (i) the orientations of the three mutually perpendicular principal stress axes σ_1, σ_2, and σ_3 with $\sigma_1 \geq \sigma_2 \geq \sigma_3$ and (ii) the ratio of principal stress differences, shortly "stress ratio", $R=(\sigma_2-\sigma_3)/(\sigma_1-\sigma_3)$ (Fig. 3; Carey & Brunier, 1974; Angelier, 1979). The procedure for estimating the best-fitting reduced stress tensor for a group of faults varies among different researchers (Angelier, 1994, Michael, 1984, Gephart & Forsyth, 1984, Gephart, 1990, Yin & Ranalli, 1992). One potential measure for the fit between a certain stress state and observed fault kinematics is provided by the misfit angle, β, which is defined as the angular difference between the calculated maximum shear stress, τ_{max}, and the observed slip direction along a fault plane (Fig. 10a). The reduced stress tensor may then be estimated as the one that is associated with the least sum of all misfit angles (Angelier, 1979).
In the following, a new computer-aided strategy towards stress inversion of heterogeneous fault populations is presented (Chapter 2.2). Since this new approach combines the concepts of the "Multiple Inverse Method" (Yamaji, 2000) and the "PBT-axes-method" (Turner, 1953; Sperner et al., 1993), both methods are shortly introduced.

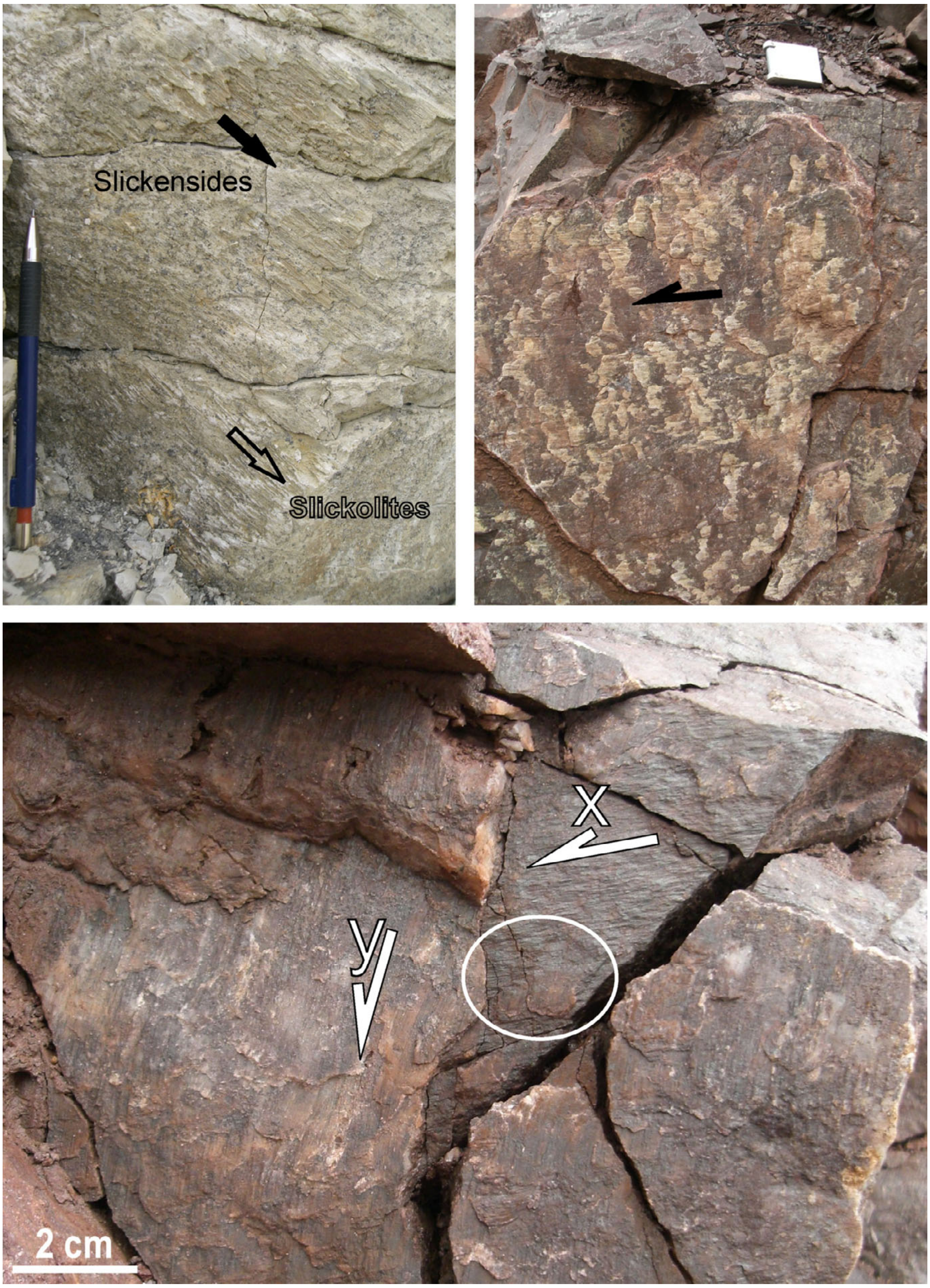

Figure 9: Slickensides and striae. a) Calcite fibres and slickolites indicate the same oblique-normal sense of movement (*Langelsheim* quarry, #29). The fibres result from precipitation of calcite which was formerly dissolved by pressure solution of the host rock (limestone). Pressure solution, in turn, created the slickolites. b) Slickenside with calcite fibres indicating dextral slip (andesites, *Mammendorf* quarry, #36); c) Steeply SSW-dipping fault surface (198/77) covered by two superimposed sets of striae (*Bodendorf* quarry, #32). Note the configuration of striae framed by the circle: assuming that late-stage coatings usually conceal earlier striae, i.e. that younger slickensides lie above older slickensides (Meschede, 1994; Doblas, 1998), it can be concluded that sinistral displacement (x: subhorizontal frictional grooves covered with hematite) took place before the fault plane was reactivated with a normal sense (y: subvertical calcite fibres). The difference in type of mineralisation confirms that the two fault/striae pairs belong to different subsets (*bod1* and *bod3*, below), each related to a specific paleostress state.

2.1.1 Multiple Inverse Method (MIM; Yamaji, 2000)

MIM is a modification of the Direct Inverse Method (Angelier, 1984). The latter assumes slip to be parallel to the maximum resolved shear stress and calculates iteratively the best-fitting stress tensor for a group of faults by minimizing the sum of associated misfit angles (Fig. 10a). Being developed particularly for the separation of heterogeneous data sets, MIM comprises the following steps which are implemented in the respective software package (Yamaji et al., 2005; Yamaji & Sato, 2005): Firstly, all possible subsets of *k*-elements are created from a complete data set (Fig. 10b). For *k*=4, any possible group of 4 faults is created so that each fault is related to any possible combination of three other faults. Secondly, Angelier's (1984) inverse technique is applied to each of these artificial *k*-fault-subsets to estimate the respective best-fitting stress tensors. Finally, all calculated reduced stress tensors (i.e. one for each artificial subset) are plotted in a pair of lower-hemisphere plots (Fig. 11c). With this technique, all significant stress states inherent in a heterogeneous data set can be detected as they are indicated by clusters of symbols that agree in terms of the directions of principal axes as well as the stress ratio, R.

For the calculation of best-fitting stress tensors, MIM uses a computational grid of 60,000 points evenly distributed in the parameter space of σ_1, σ_2, σ_3, and R. The ideal stress for a single *k*-fault-subset is approximated by the nearest grid point. Thus, the stress states derived from several *k*-fault-subsets may be tied to the same grid point. Grid points with a large number of stress states automatically correspond to solutions that are more significant for the entire fault population. The enhance factor *e* (freely selectable by the user with $0 \leq e \leq 99$) controls the minimum number of solutions at a grid point which is required for this stress state to appear in the MIM stereograms. By selecting *e*=0, all solutions for a data set are plotted. Larger values of *e*, on the other hand, correspond to a reduced number of plotted solutions and are chosen to thin out less significant stress states. In this way, the most relevant clusters indicating the best-fitting solutions can be detected. To further test the significance of a single stress state, the MIM software provides a tool for a simulation of stresses (Chapter 2.2.1).

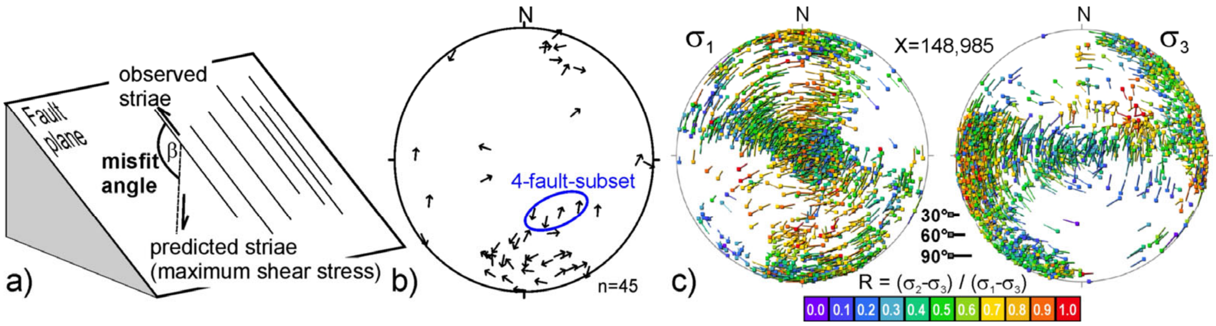

Figure 10: The Multiple Inverse Method (MIM) exemplarily introduced using faults-slip data from *Bodendorf* (#32). a) A misfit angle is defined as the angular difference between the observed striae and the direction of maximum shear stress, τ_{max}, calculated for a given stress state; b) All fault-slip data from *Bodendorf* plotted in a tangent-lineation plot: each arrow in the lower-hemisphere, equal-area projection represents one fault-slip datum; the centre of an arrow indicates the pole to the respective fault plane while the arrowhead indicates the slip direction of the footwall block. One potential 4-fault-subset is exemplarily accentuated; c) Stress states calculated by MIM for the number of n=45 striated faults presented in (b). A number of n fault-slip data produces a number of $X=n!/(k!\cdot(n-k)!)$ *k*-fault-subsets. Thus, for n=45 and *k*=4, a number of 148,985 solutions is obtained. Each stress state is plotted with its σ_1-axis in the left stereonet and the associated σ_3-axis in the right stereonet (enhance factor *e*=0; lower hemisphere, equal-area projections). The diamonds represent the directions (azimuth and plunge) of stress axes. The tail of a σ_1 (σ_3) symbol indicates the direction and plunge angle of the corresponding σ_3- (σ_1-) axis. The stress ratio, R, is colour-coded.

2.1.2 PBT-axes Method (PBT; Sperner et al., 1993)

PBT is a kinematic approach that graphically constructs a triple of theoretical strain axes for a single fault-slip datum (Turner, 1953, after a solution of Sperner et al., 1993): a P-axis in the direction of contraction, a neutral B-axis lying in the fault plane, and a T-axis in the direction of extension (Fig. 11). By assuming a coincidence of σ_1 with P and of σ_3 with T as well as an arbitrary shear stress magnitude of $\tau=1$ on each fault plane, the Numeric Dynamic Analysis (NDA) calculates a reduced stress tensor for a set of fault-slip data (Spang 1972, after a solution of Sperner et al., 1993). By regarding all faults as neoformed, i.e. as fractured *and* moved by the same stress state, the concepts of PBT and NDA assume the orientation of a fault plane to depend on the acting stress field. For this reason, P is constructed with a defined angular distance from the respective fault plane: the fracture angle θ (measured in the plane containing the fault plane normal and the slip line). A fracture angle of $\theta=30°$ is adequate for many data sets, as this value (i) corresponds to laboratory studies on brittle deformation (Hubbert, 1951; Byerlee, 1968; Jaeger & Cook, 1979), (ii) is associated with high shear-to-normal stress ratios on the fault planes (Mohr-Coulomb fracture criterion; Fig. 8b) and (iii) already has proved to be appropriate for natural fault-slip data (Sperner, 1996; Reicherter & Peters, 2005).
TectonicsFP 1.6.5 by Reiter & Acs (1996-2008) is the software package which is used throughout this study for the realisation and further interpretation of PBT results. Despite potentially heterogeneous material properties, PBT applies a uniform angle θ to a group of fault-slip data (30° throughout the present study). The coeval consideration of various fault-slip data results in a comprehensive pattern of kinematic axes (Fig. 11b) which facilitates kinematic consistencies to be detected as clusters of P-, B-, and T-axes. In this way, kinematically consistent subsets of faults can be separated from a heterogeneous fault population (Chapter 2.2.1). Another tool incorporated in *TectonicsFP 1.6.5* calculates the mean vector for any type of directional data sets as well as the associated cone of confidence (a small circle within which the true mean of the sampled population of structures is expected to lie; “R% and Centre Method”, Wallbrecher, 1986). Thus, a further analysis of the P-, B-, and T-clusters is possible.

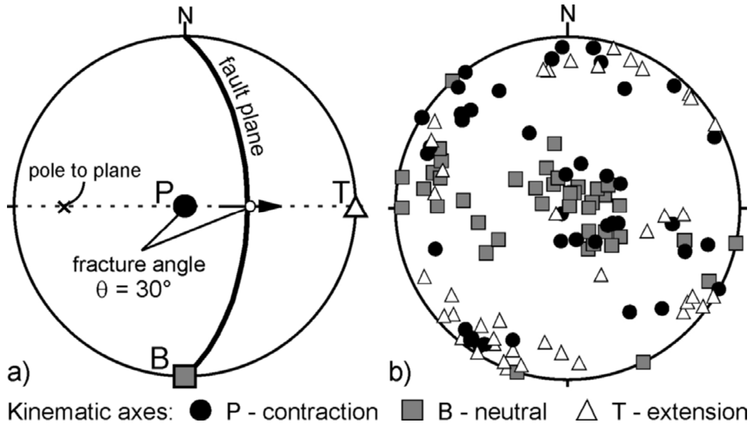

Figure 11: PBT-axes Method (PBT). a) Construction of the kinematic axes P, B, and T for a normal fault by applying a fracture angle of $\theta=30°$ (lower-hemisphere, equal-area projection). The neutral axis B lies in the fault plane (090/60=dip direction/dip). The contraction axis P and the extension axis T lie in a plane constituted by the shear plane normal and the slip line. The centre of the slip line arrow indicates the attitudes of the striae (090/60=azimuth/plunge) and the arrow points the slip direction of the hanging wall block (normal sense of movement). P is constructed with an angular distance of $\theta=30°$ from the slip line in a direction opposite to the one indicated by the slip line arrow. P, B, and T are mutually perpendicular. b) Results of PBT for the entire population of fault-slip data from *Bodendorf* quarry (Fig. 10b). A fracture angle of $\theta=30°$ is used for each fault-slip datum. The wide scattering of P-, B-, and T-axes, respectively, reflects heterogeneity of the data set.

2.2 A new strategy for stress inversion from (heterogeneous) fault-slip data

To demonstrate the strategy developed in this study, the data set from *Bodendorf* quarry is exemplarily used. These fault-slip data are heterogeneous as indicated by both clusters of differently oriented stress axes (Fig. 10c) and a wide scattering of kinematic axes (Fig. 11b). To find the most relevant stress states that explain the kinematics of this fault population as complete as possible, a stepwise procedure is used (Sippel et al., in press).

2.2.1 Stress Inversion Via Simulation (SVS)

Step 1: Preliminary separation by clusters of P-, B-, and T-axes.

The clusters of kinematic axes in the PBT plot (Fig. 11b) indicate groups of faults with the same kinematic trend. Based on such consistencies, three kinematically homogeneous subsets can be separated for the *Bodendorf* data: *bod1*, *bod2*, and *bod3* (Fig. 12a). For each of the obtained subsets, the mean vectors of P-, B-, and T-axes, respectively, are calculated and the clusters of stress axes accentuated by plotting the associated cones of confidence (with a significance of 99%). Part of the data cannot be assigned to any consistent subset ("remnants" in Fig. 12a). Moreover, the kinematic axes associated to these remaining faults are non-horizontal and/or non-vertical, a configuration which identifies them as non-Andersonian (Anderson, 1942) or oblique-slip faults.

Since PBT processes each fault-slip datum separately, the separation is very rapid and straightforward. We conclude that the subsets *bod1* and *bod2* represent strike-slip regimes with a vertical B-axis each and horizontal contraction and extension axes. In the case of subset *bod1*, the sub-horizontal contraction axes strike approximately NE-SW and the extension axes NW-SE, whereas for *bod2* it is vice versa. Subset *bod3*, on the other hand, corresponds to an extensional regime with a vertical contraction axis and an extension axis striking horizontally NNE-SSW.

Step 2: Application of MIM to the PBT-derived subsets.

Since PBT regards all faults as neoformed and uncertainties concerning the value of θ are accepted by the method, we complementary apply MIM which considers also slip along pre-existing planes. MIM yields the complete number of stress states for a data set, i.e. all solutions that fulfil the low-misfit-angle criterion for at least part of the data. This approach results in a large number of diffuse clusters of corresponding σ_1- and σ_3-axes in the MIM plot, including but also concealing the best-fitting stress states for a fault population (Fig. 10c).

When applying MIM to each of the separated homogeneous subsets *bod1*, *bod2*, and *bod3*, respectively, the patterns of solutions are much clearer. By transferring the mean vectors and cones of confidence from the PBT plots (Fig. 12a) to the MIM plots (Fig. 12b), considerable consistencies between the results of PBT and MIM become obvious. The cones of confidence enclose clusters of stress axes in the MIM plots, thus obviously exposing these clusters as significant solutions. Even when adopting slightly different fracture angles for PBT, such as θ=20° or θ=40° as exemplarily shown for the subset *bod1*, the same trends of stress axes are indicated as significant (Fig. 12b, left plot).

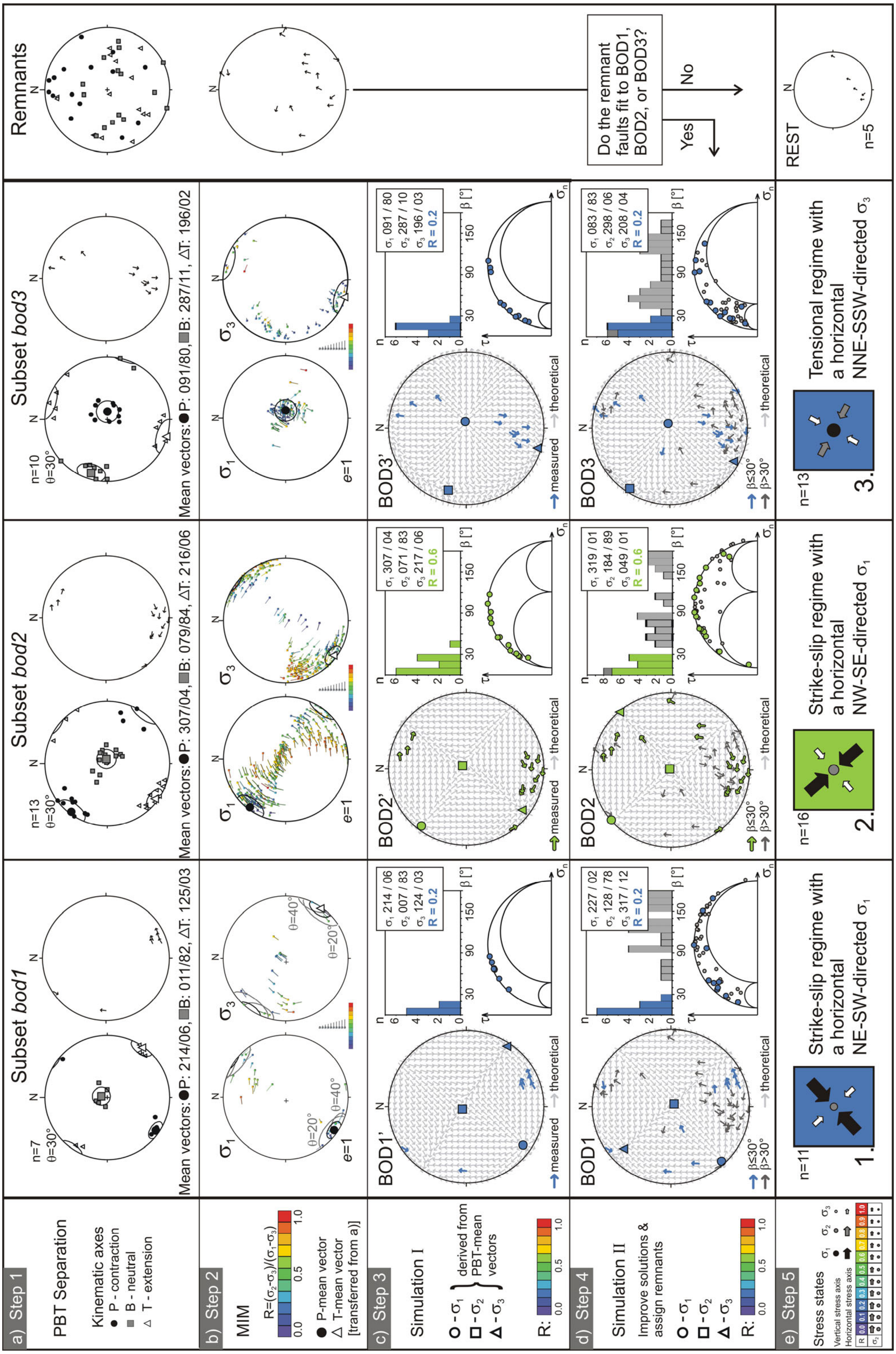

a) Step 1
PBT Separation
Kinematic axes
P - contraction
B - neutral
T - extension
b) Step 2
MIM
R=(σ2-σ3)/(σ1-σ3)
P-mean vector
T-mean vector [transferred from a)]
c) Step 3
Simulation I
O - σ1
□ - σ2
Δ - σ3
derived from PBT-mean vectors
d) Step 4
Simulation II
Improve solutions & assign remnants
e) Step 5
Stress states
Vertical stress axis
Horizontal stress axis
Subset bod1
Mean vectors: ●P: 214/06, ■B: 011/82, ΔT: 125/03
Subset bod2
Mean vectors: ●P: 307/04, ■B: 079/84, ΔT: 216/06
Subset bod3
Mean vectors: ●P: 091/80, ■B: 287/11, ΔT: 196/02
Remnants
BOD1'
BOD2'
BOD3'
BOD1
BOD2
BOD3
measured
theoretical
σ1 214 / 06
σ2 007 / 83
σ3 124 / 03
R = 0.2
σ1 307 / 04
σ2 071 / 83
σ3 217 / 06
R = 0.6
σ1 091 / 80
σ2 287 / 10
σ3 196 / 03
R = 0.2
σ1 227 / 02
σ2 128 / 78
σ3 317 / 12
R = 0.2
σ1 319 / 01
σ2 184 / 89
σ3 049 / 01
R = 0.6
σ1 083 / 83
σ2 298 / 06
σ3 208 / 04
R = 0.2
Do the remnant faults fit to BOD1, BOD2, or BOD3?
Yes
No
REST
n=5
1. Strike-slip regime with a horizontal NE-SW-directed σ1
n=11
2. Strike-slip regime with a horizontal NW-SE-directed σ1
n=16
3. Tensional regime with a horizontal NNE-SSW-directed σ3
n=13

Figure 12: Stress inversion for the fault-slip data from *Bodendorf* (#32): a) PBT separation. The separation by clusters of P-, B-, and T-axes yields three homogeneous subsets (*bod1*, *bod2*, and *bod3*) of kinematically consistent faults. The PBT plots (*left*) are complemented by the mean vectors calculated for P-, B-, and T-clusters (larger PBT symbols) and their associated cones of confidence for 99% significance (Wallbrecher, 1986). A fault-slip datum is regarded as belonging to a cluster if none of its three axes deviates by more than 40° from the respective mean vectors. Subsets are additionally shown by tangent-lineation plots (*right*) presenting each striated fault as an arrow that points the slip direction of the footwall-block. Data with non-uniform kinematics ('Remnants', *rightmost column*) mainly comprise oblique-slip faults.
b) Complete number of reduced stress tensors calculated by MIM for *bod1*, *bod2*, and *bod3* (plot properties as in Fig. 10c with *e*=1). σ_1- and σ_3-plots are complemented by the mean vectors and the cones of confidence derived from the respective P- and T-clusters in (a). For subset *bod1*, also the cones of confidence and mean vectors for P- and T-clusters constructed with θ=20° and θ=40° are plotted.
c) Results of the first stress simulation: Stress axes are derived from corresponding PBT axes. As the mean vectors for P-, B-, and T-axes are calculated separately, they are not necessarily mutually perpendicular. Thus, the directions selected for σ_1, σ_2 and σ_3 are slightly deviating from those of P, B, and T to achieve the required perpendicularity. Stress states BOD1', BOD2', and BOD3' are 'preliminary' solutions for the subsets *bod1*, *bod2*, and *bod3*, respectively. *Tangent-lineation plots, left*: The theoretical slip patterns (light grey arrows) of the stress states BOD1-3' coincide very well with the measured slip patterns of *bod1*, *bod2*, *bod3* (coloured arrows). *Fluctuation histograms, right*: The low degree of misfits of BOD1', BOD2', and BOD3' are expressed by a large number of faults with low misfit angles (mainly $\beta \leq 30°$). *Mohr-circles diagrams*: Each striated fault is indicated by its shear-to-normal-stress ratio (τ/σ_n) calculated for the associated stress state. The values of τ/σ_n are remarkably high.
d) Results of the second stress simulation: Each of the stress states BOD1, BOD2, and BOD3, is set in relation to the complete fault population from *Bodendorf*. *Tangent-lineation plots*: Given the theoretical slip pattern of BOD1, BOD2, and BOD3 (thin grey arrows), faults with misfit angles $\beta \leq 30°$ (coloured arrows) can be separated from faults of low slip potentials indicated by $\beta > 30°$ (dark grey arrows). *Mohr-circles diagrams*: Black dots indicate faults with misfit angles $\beta \leq 30°$, grey dots represent faults with $\beta > 30°$. Most faults with a low misfit angle show a high τ/σ_n, thus reflecting a high slip tendency.
e) Symbols for the reduced stress tensors: Sub-horizontal principal stress axes are projected to the horizontal and plotted as arrows (in black, grey, and white for σ_1, σ_2, and σ_3, respectively). Sub-vertical principal stress axes are projected to the vertical and plotted as solid circles (also black, grey, and white for σ_1, σ_2, and σ_3). To illustrate the value of R, the σ_2-symbol is plotted by variable sizes (e.g. equally sized to σ_1, if $\sigma_1=\sigma_2$, and equally sized to σ_3, if $\sigma_2=\sigma_3$). Furthermore, the background colour is plotted according to the value of R.

Step 3: Find preliminary stress states (first simulation)

To find the best-fitting stress state for a kinematically homogeneous subset, different stress states are simulated and compared (*step 3* and *step 4*). In this context, a simulation run implies, first, to define directions for the principal stress axes and a value for R, and second, to check the associated misfit angle distribution. To obtain the latter, the programme *MI Viewer 4.10* calculates the direction of maximum shear stress, τ_{max}, for each fault plane (Yamaji & Sato, 2005). At the same time, the angular distance between the theoretical and the observed slip is estimated. The resulting misfit angles (β) are visualized collectively by a lower-hemisphere, equal-area projection (*tangent-lineation plot* as in Fig. 8a) and by a fluctuation histogram (Fig. 12c). The β-distribution finally serves as a measure for the consistency between a stress state and a set of fault-slip data, thus providing the base for a comparison of the fit of different stress states.

In a first series of simulations, stress states are tested only against the particular fault-slip data of a separated PBT-subset (Fig. 12c). The first stress state tested is characterised by (i) directions of σ_1, σ_2 and σ_3 derived from the mean vectors of the associated P-, B-, and T-axes, respectively, and (ii) an R value derived from the corresponding MIM clusters. Interestingly, the misfit angles calculated for *bod1*, *bod2*, and *bod3*, respectively, already tend to low values (mostly $\beta<30°$). By testing different R values indicated by the different colours of the respective MIM clusters, the solutions can be improved. Finally, the stress states BOD1', BOD2', and BOD3' correspond to low degrees of misfit, which is indicated by the fluctuation histograms as well as the tangent-lineation plots where the measured data are subparallel to the theoretical slip directions (Fig. 12c). Furthermore, these stress configurations would induce relatively high shear-to-normal-stress ratios (τ/σ_n) on the respective faults as indicated by the presence of many τ/σ_n-values near the external envelopes of the Mohr-circles diagrams (τ/σ_n calculated by the software *FLUMO*, Sperner, 1993). Such values of τ/σ_n plotting close to the Mohr-Coulomb fracture criterion (tangential to the σ_1-σ_3 circle) confirm a high potential of slip along the faults. Hence, both criteria for faulting are fulfilled and the stress states BOD1', BOD2', and BOD3' can be regarded as realistic solutions for the subsets *bod1*, *bod2*, and *bod3*, respectively.

For estimating the slip potential of a single fault-slip datum under a certain stress field, the upper limit for misfit angles has been proposed to be either $\beta=20°$ (Etchecopar et al., 1981, Sperner et al., 1993) or $\beta=30°$ (Nemcok & Lisle, 1995). In the case of the preliminary stress states BOD1', BOD2', and BOD3', the majority of respective fault-slip data are related to misfit angles of $\beta\leq20°$. As none of the few faults with $20°<\beta\leq30°$ would fit better to any alternative solution (neither in terms of misfit angles, nor of shear-to-normal-stress ratios), the PBT separation can be regarded as reasonable. However, the solutions BOD2' and BOD3' are not ideal, since the peaks of the respective cumulative curves are shifted away from the origin. Such distributions indicate potentials for better solutions.

Step 4: Complete separation and improve solutions (second simulation)

By performing a second simulation series, the relevancies of BOD1', BOD2', and BOD3' are assessed and the solutions further improved. Each preliminary stress state is tested against the entire fault population to estimate its potential to be responsible also for the activation of other fault-slip data from the outcrop, in particular, those of the group of 'Remnants' (*Step 1*). A single fault-slip datum is regarded as fitting to a certain stress state if the associated misfit angle is less than 30°.

After having identified all fault-slip data that are consistent with a stress state, the degree of misfit can further be minimised. The minimisation is done by interactively following any changes of misfit angles when slightly changing the parameters of stress. For our example, this means, we start with BOD1', BOD2', and BOD3', modify successively their parameters by selecting alternative values for σ_1, σ_3, and R, to finally find the most appropriate solution for *bod1*, *bod2*, and *bod3*. The analysis of numerous data sets has shown that this interactive search can be restricted to a space which is indicated by consistent solutions of MIM and PBT, i.e. MIM-clusters which overlap with PBT-derived cones of confidence. Thus, within only a few simulation runs, the stress states BOD1, BOD2, and BOD3 are determined as optimal solutions for the subsets *bod1*, *bod2*, and *bod3*, respectively (Fig. 12d).

As expected from the PBT results, the stress states BOD1 and BOD2 correspond to strike-slip regimes with a sub-vertical σ_2-axis each. For stress state BOD1, the maximum principal stress axis strikes sub-horizontally NE-SW, whereas for BOD2 it strikes NW-SE. These stress states differ also in the derived stress ratios: in the case of BOD1 the ratio tends towards an axially compressive state of stress (R=0.2) and for BOD2 it represents a plane deviatoric stress state (R=0.6). Finally, stress state BOD3 corresponds to an extensional regime (sub-vertical σ_1) with a sub-horizontal, NE-SW-directed σ_3-axis. The various dip and slip directions of the associated normal faults in subset *bod3* require a relatively low R value for BOD3 (R=0.2).

Step 5: Presentation of stress states

With the four steps of separation and stress inversion introduced above, it is possible to estimate the reduced stress tensor for a group of striated faults. Given large data sets from a large number of closely-spaced sites, it is necessary to find a simple way of presenting numerous stress states in maps. The stress symbols used in this study have been conceived to integrate all parameters of the reduced stress tensor (Fig. 12e). Typically, most of the estimated stress states reveal sub-vertical and sub-horizontal principal stress axes. Thus, the axes can be projected to the vertical and horizontal, respectively. Accordingly, vertical axes are plotted as dots and horizontal axes as arrows. The stress ratio R is expressed by the relative size of the σ_2-symbol and, for the sake of a faster recognition, also by a specific colour code for the background of the stress symbol. If none of the principal stress axes is sub-vertical, i.e. plunging by more than 70°, the stress state is regarded as "oblique" and presented by a lower hemisphere, equal-area projection revealing the precise orientations of stress axes and a colour-coded background for R.

2.2.2 Stress inversion by MIM and simulation - a comparative test

MIM has been invented as an independent approach (Yamaji, 2000). According to its original concept, significant stress state(s) inherent in a fault population are indicated by clusters in the associated σ_1-/σ_3-pair of stereograms. Consequently, the most significant stress state should be indicated by the grid point that combines the largest number of solutions. This implies, in turn, that isolating the most relevant stress state should be possible by enlarging the enhance factor *e* of the corresponding MIM plot. In the following, the validity of thusly identified solutions shall be checked: First, the results of MIM for *bod1*, *bod2*, and *bod3* are plotted (Fig. 13b). In contrast to Figure 12b, however, solutions are plotted with an enhance factor that large that only one stress state is shown while all other solutions are filtered out. It is obvious that the remaining stress states BODx, BODy, and BODz are different from the solutions BOD1, BOD2, and BOD3 (Fig. 12d): For subset *bod1*, the grid point with the maximum number of solutions indicates a compressional regime (BODx) instead of a strike-slip system (BOD1). BODy corresponds to a tensional regime, whereas BOD2 is strike-slip in character. For *bod3*, finally, the solutions BODz and BOD3 differ in terms of directions of minimum horizontal stress (σ_3).

Considering only the misfit angle distributions, BODx, BODy, and BODz correspond well with most of the observed fault-slip data of *bod1*, *bod2*, and *bod3*, respectively. However, as the data mainly plot to the lower right in the corresponding Mohr-circles diagrams, they are associated with very low shear-to-normal-stress ratios (Fig. 13c). Since the slip tendency of a fault plane is larger for high values of τ/σ_n, this comparative test suggests BODx, BODy, and BODz not to be as relevant for the *Bodendorf* fault population as the stress states BOD1, BOD2, and BOD3.

Since it is one of the most frequently used methods, also the results of the Direct Inverse Method (DIM; Angelier and Goguel, 1979, after a solution of Sperner et al., 1993) shall be considered here. Alike MIM, the Direct Inverse Method is based on the 'low misfit-angle criterion': it calculates the best-fitting stress tensor for fault-slip data directly by minimising the sum of all misfit angles. Unlike MIM, this calculation is performed only once, i.e. for a whole set of fault-slip data. Considering the orientations and misfit angle distributions, the solutions produced by DIM and MIM are similar. Accordingly, the solutions generated by DIM for the subsets *bod1* and *bod2* are also related to very low shear-to-normal-stress ratios which implies that these stress states similarly must be challenged (Fig. 13d).

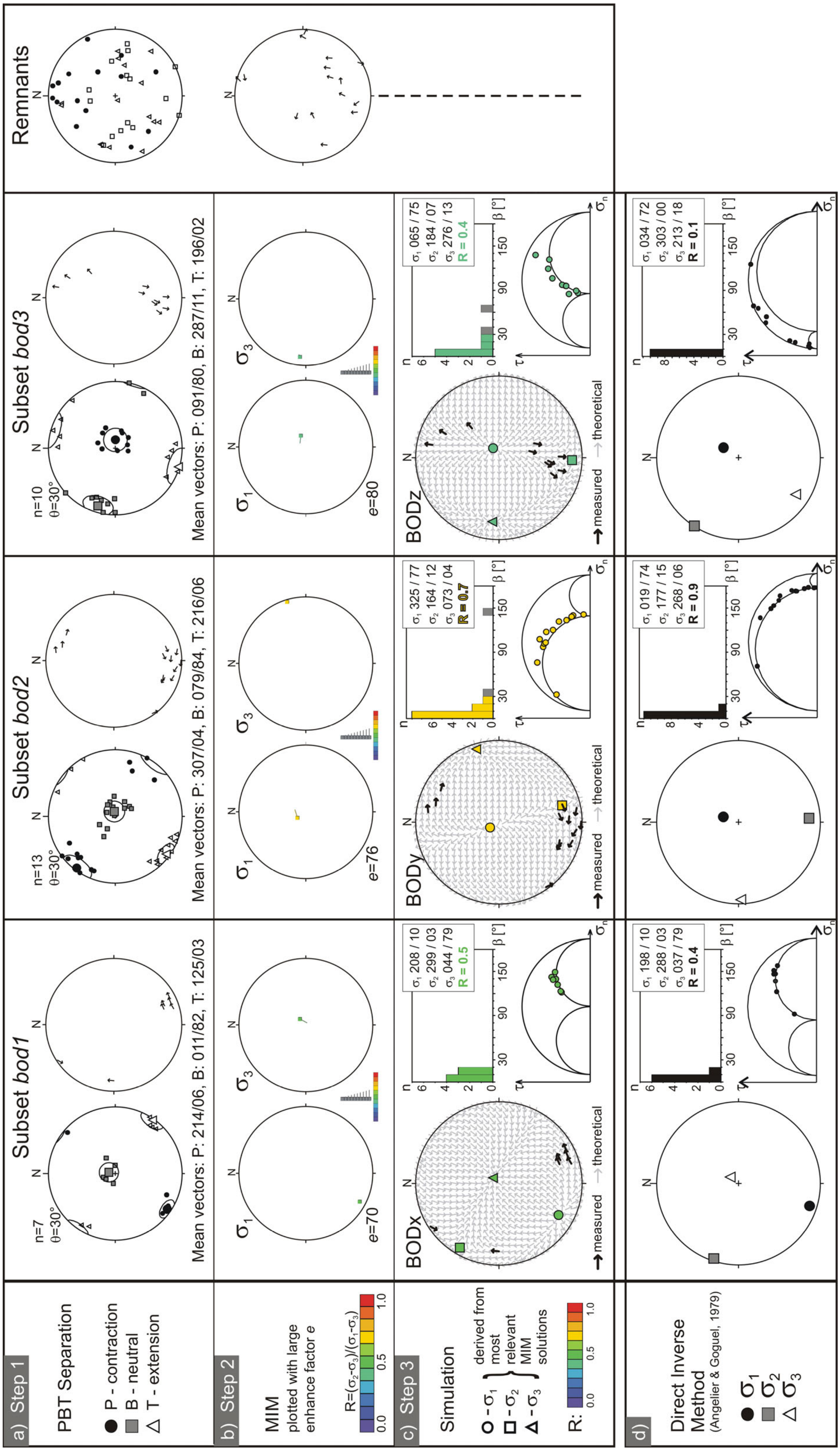
a) Step 1
PBT Separation
P - contraction
B - neutral
T - extension
b) Step 2
MIM
plotted with large enhance factor e
R=(σ2-σ3)/(σ1-σ3)
c) Step 3
Simulation
O - σ1
□ - σ2
Δ - σ3
derived from most relevant MIM solutions
R:
d) Direct Inverse Method (Angelier & Goguel, 1979)
Subset bod1
n=7
θ=30°
Mean vectors: P: 214/06, B: 011/82, T: 125/03
e=70
BODx
σ1 208 / 10
σ2 299 / 03
σ3 044 / 79
R = 0.5
σ1 198 / 10
σ2 288 / 03
σ3 037 / 79
R = 0.4
Subset bod2
n=13
θ=30°
Mean vectors: P: 307/04, B: 079/84, T: 216/06
e=76
BODy
σ1 325 / 77
σ2 164 / 12
σ3 073 / 04
R = 0.7
σ1 019 / 74
σ2 177 / 15
σ3 268 / 06
R = 0.9
Subset bod3
n=10
θ=30°
Mean vectors: P: 091/80, B: 287/11, T: 196/02
e=80
BODz
σ1 065 / 75
σ2 184 / 07
σ3 276 / 13
R = 0.4
σ1 034 / 72
σ2 303 / 00
σ3 213 / 18
R = 0.1
Remnants
measured
theoretical
β [°]

Figure 13: Comparative test. The stress states BODx, BODy, and BODz are tested against the fault-slip data from *Bodendorf* as they are the most relevant solutions according to MIM. a) PBT separation (as in Fig. 12a). b) Stress tensors calculated by MIM for the subsets *bod1*, *bod2*, and *bod3*. Note the large enhance factors which were selected to filter out all stress states but the ones with the largest number of solutions. c) The stress states BODx, BODy, and BODz which are indicated by the MIM solutions in (b), are set in relation to the subsets *bod1*, *bod2*, and *bod3*, respectively. Note the difference of these stress states compared to BOD1, BOD2, and BOD3, respectively (Fig. 12d). *Tangent-lineation plots*: The measured fault-slip data (black arrows) fit well with the theoretical slip patterns of BODx, BODy, and BODz (grey arrows). *Fluctuation histograms*: A maximum number of fault-slip data is related to the simulated stress states by misfit angles of $\beta \leq 30°$. *Mohr-circles diagrams*: The fault-slip data reveal relatively low shear-to-normal-stress ratios reflecting minor slip tendencies of the faults under the given stress states. d) Results of the Direct Inverse Method applied to the subsets *bod1*, *bod2*, and *bod3*, respectively (*TectonicsFP* by Reiter & Acs, 1996-2008). Note the large number of faults with low shear-to-normal-stress ratios in the Mohr-circles diagrams.

2.2.3 Discussion

For the exemplarily selected fault population from *Bodendorf*, the Stress Inversion Via Simulation (SVS) integrating the concepts of PBT and MIM yields three stress states which together almost completely explain the observed fault-slip pattern. Each solution is related to the associated fault-slip data by a maximum number of misfit angles of $\beta \leq 20°$ which in general is regarded as the primary criterion for a reasonable solution. The main aspects of the introduced stepwise procedure are the following:

(1) *PBT allows a fast and straightforward separation of heterogeneous fault-slip data.* Unlike other separation methods which merge fault-slip data, then calculate a stress state with associated misfit angles in order to finally separate data again (e.g. Etchecopar et al., 1981), PBT processes each fault-slip datum separately.

(2) *The results of PBT are used to identify the most relevant stress states for a set of fault-slip data among the numerous solutions provided by MIM.* As PBT is only used for a pre-separation of data sets (later verified by various simulation runs), the selected value of the fracture angle of $\theta=30°$ does not directly influence the results of the subsequent stress inversion. By separating heterogeneous data sets before applying MIM, a major problem of MIM is solved, which concerns minor subsets that may not be indicated adequately when appearing together with much larger subsets (Liesa & Lisle, 2004). Moreover, in the case of girdle distributions of σ_1- and σ_3-axes, PBT results help designating the most realistic direction of the unknown σ_2-axis in terms of shear-to-normal-stress ratios. As demonstrated (Fig. 13), the most relevant solutions produced by MIM might represent stress states associated with unrealistically low shear stresses on the respective faults. Though pre-existing discontinuities may require relatively low shear-to-normal-stress ratios for slip to occur (Twiss & Moores, 1992), solutions with higher ratios are regarded as more realistic.

(3) *The interactive stress simulation provides direct control on the relation of a single fault-slip datum to a given stress state.* Thus, all data from an outcrop can either be assigned to a specific stress state or isolated as outliers – which thus do not further influence the stress inversion. With this simulation procedure, also the data that formerly had to be separated as 'Remnants' due to their PBT-axes can be set in relation to potential stress states. To consider these data is essential because (i) as mostly being oblique and generally not containing a principal stress axis, they more closely constrain the stress ratio, R (Angelier, 1989) and (ii) as mainly being reactivated, they may document age relations to other fault-slip data, thus

providing constraints on the chronology of stress states. Furthermore, the simulation allows checking the separation of fault-slip data in terms of potential relationships to the qualities of kinematic indicators. Finally, since the simulation tool interactively provides a tangent-lineation plot showing the theoretical slip patterns for a stress state (Fig. 12c,d), also incomplete data with unknown senses of slip might be correlated with any of the estimated stress configurations.

(4) *The estimated stress states fulfil both the criterion of low misfit-angles and that of high shear-to-normal-stress ratios.* The distribution of misfit angles correlating a set of fault-slip data with a specific reduced stress tensor as illustrated by a histogram serves as the primary measure for the quality of a stress state. An ideal solution for a homogeneous data set is characterised by a unimodal distribution of misfit angles with a maximum close to the axis of frequency. By performing the fourth step of the introduced inversion procedure, i.e. the second simulation, such an ideal solution can be found.
The distribution of shear-to-normal-stress ratios of a data set illustrated by a dimensionless Mohr-circles diagram serves as the second, even though more qualitative, measure for the fit of a stress state. For each fault-slip datum, PBT constructs a triple of kinematic axes. If these kinematic axes are interpreted as stress axes – with a parallelism between σ_1 and P, between σ_2 and B, and between σ_3 and T – the respective stress state would induce the largest possible shear stress (a maximum of τ/σ_n) on the respective fault given that θ=30°. By restricting the search of a best-fitting stress state to the space indicated by consistent results of PBT and MIM, the solution found to be best for a group of fault-slip data in terms of misfit angles is guaranteed to be related also to relatively high shear-to-normal-stress ratios. If there are no consistencies observable between PBT and MIM (in the case of a pure set of reactivated faults, for instance), the simulation runs still should aim at improving the fit of stress states in terms of both misfit angles and shear-to-normal-stress ratios.

2.2.4 Summary

The Stress Inversion Via Simulation (SVS) is a stepwise technique combining a graphical method which is based on the Mohr-Coulomb fracture criterion (PBT-Method) with a numerical method based on the Wallace-Bott criterion (Multiple Inverse Method, MIM). The final steps of SVS correspond to a simulation of different stress states – a forward modelling that provides direct control on the relationships of a set of fault-slip data to any potential reduced stress tensor. In this way, SVS allows detecting the stress tensor(s) that best fit(s) a fault population in terms of slip and frictional criteria.
SVS integrates two techniques (PBT, MIM) each of which has been developed as a self-contained approach on fault-slip analysis. However, there are some critical aspects related to both these methods which are overcome by a combination as involved in SVS. The main differences between SVS on the one side and PBT, MIM, the Numeric Dynamic Analysis (NDA; Sperner et al., 1993), and the Direct Inverse Method (DIM; Angelier & Goguel, 1979) on the other, are compiled by Figure 15.
The main critical aspect of both PBT and NDA originates from the basic assumption that the orientation of a fault plane (expressed by the fracture angle θ) depends on the state of stress that causes faulting which is, however, only valid for neoformed faults. The uncertainty inherent in the choice of a uniform fracture angle, in turn, directly involves an ambiguity in the resulting orientations of kinematic axes. In averaging across all PBT-axes of a set of fault-slip data, NDA interprets these axes as stress axes while, however, not considering any potential heterogeneity among them. For the latter reason, performing a separation according to clusters of PBT-axes before applying NDA is reasonable. In the case of the presence of

reactivated faults, this might result in rejecting a number of inconsistent data (remnants). Neoformed faults alone, however, would not perfectly constrain the stress ratio R (Angelier, 1989). Likewise problematic is the NDA approach of calculating the stress ratio: NDA derives the value of R from the eigenvectors and eigenvalues of the cumulative pattern of PBT-axes instead of deriving R directly from the fault-slip pattern. Finally, the reduced stress tensor as deduced from the orientations of PBT-axes might not be perfectly consistent with a set of fault-slip data in terms of misfit angles.

Alike NDA, DIM calculates a reduced stress tensor for a set of fault-slip data directly. Potential heterogeneities of a data set thus are not considered and each datum deviating from the general trend may significantly falsify the solution of the iterative search. This problem is overcome by MIM by calculating reduced stress tensors for any possible subsets of a fault population. Since DIM and MIM are based on the Wallace-Bott hypothesis, the solutions are generally related to misfit angles that tend towards low values. Due to a consideration of oblique-slip (reactivated) faults, the stress ratio may also be well constrained (provided, of course, that the data show a sufficiently great diversity of orientations). However, the stress tensors found by DIM and MIM might still be far from being the best-fitting ones as indicated by unrealistically low shear-to-normal-stress ratios.

The intention of SVS is to explain a measured population of (heterogeneous) fault-slip data as complete as possible in terms of causative stress states. Each of the estimated stress states is guaranteed to fulfil the criterion of low misfit angles and that of high shear-to-normal-stress ratios (first simulation). Furthermore, each of the tensors is representative for as many fault-slip data as possible (second simulation).

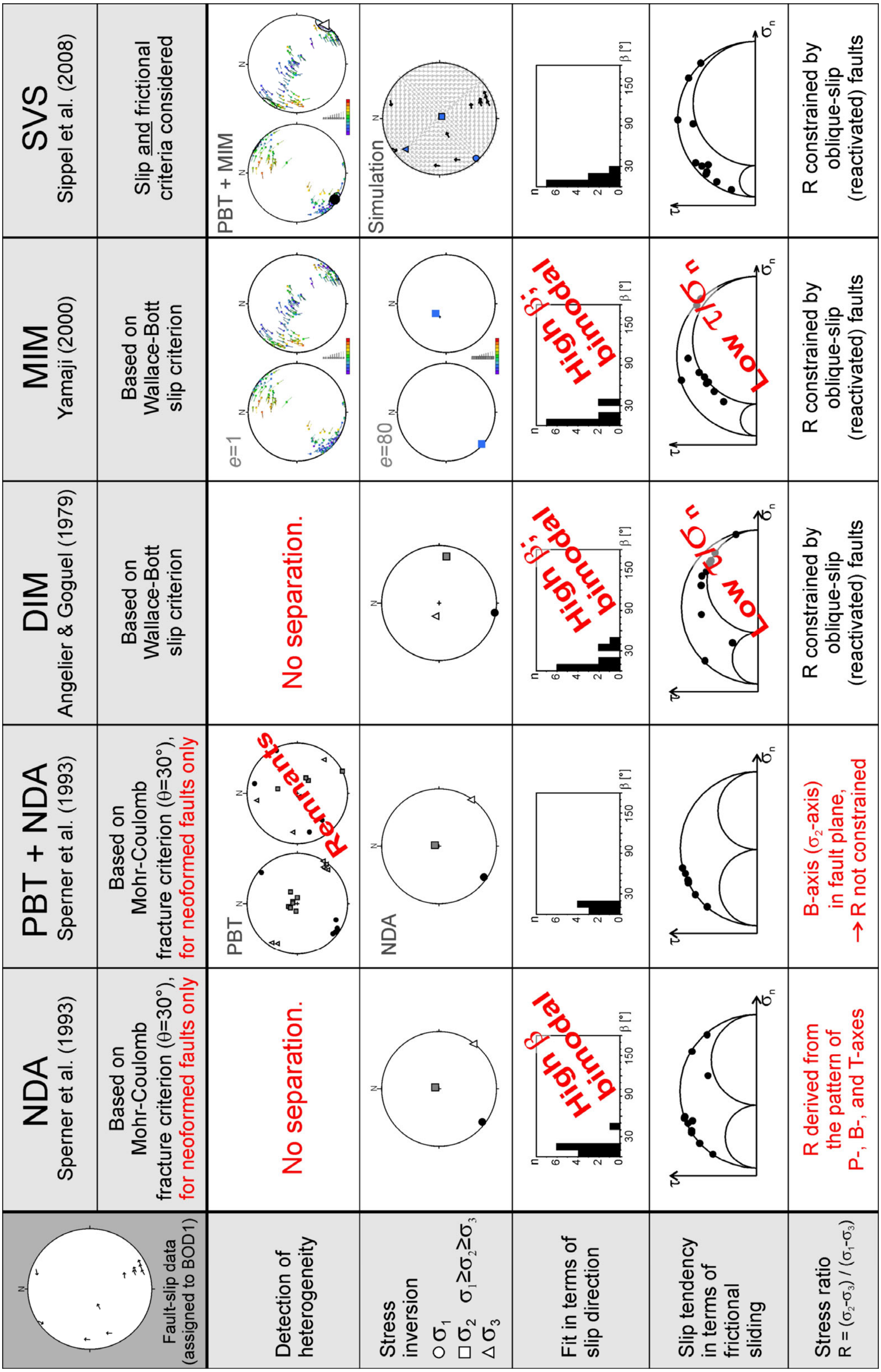
Fault-slip data (assigned to BOD1)
NDA
Sperner et al. (1993)
Based on Mohr-Coulomb fracture criterion (θ=30°), for neoformed faults only
PBT + NDA
Sperner et al. (1993)
Based on Mohr-Coulomb fracture criterion (θ=30°), for neoformed faults only
DIM
Angelier & Goguel (1979)
Based on Wallace-Bott slip criterion
MIM
Yamaji (2000)
Based on Wallace-Bott slip criterion
SVS
Sippel et al. (2008)
Slip and frictional criteria considered
Detection of heterogeneity
No separation.
PBT
Remnants
No separation.
e=1
PBT + MIM
Stress inversion
σ1 σ2 σ3 σ1≥σ2≥σ3
NDA
e=80
Simulation
Fit in terms of slip direction
High β, bimodal
High β, bimodal
High β, bimodal
Slip tendency in terms of frictional sliding
Low τ/σn
Low τ/σn
Stress ratio R = (σ2-σ3) / (σ1-σ3)
R derived from the pattern of P-, B-, and T-axes
B-axis (σ2-axis) in fault plane, → R not constrained
R constrained by oblique-slip (reactivated) faults
R constrained by oblique-slip (reactivated) faults
R constrained by oblique-slip (reactivated) faults

Figure 14: Different techniques of fault-slip analysis. The different approaches are exemplarily applied to the subset of fault-slip data that formerly has been related to the stress state BOD1 (Fig. 12). Critical aspects related to the different techniques are highlighted in red.
DIM – Direct Inverse Method, MIM – Multiple Inverse Method, NDA – Numeric Dynamic Analysis, PBT – PBT-axes Method, SVS – Stress Inversion Via Simulation

2.3 From local fault-slip data to regional stress fields

SVS provides a strategy for estimating a stress state from a number of striated faults. However, SVS is only one step on the way from sampling fault-slip data in an outcrop of limited extension to correlating reconstructed regional stress fields with the geodynamic history of an entire sedimentary basin.

2.3.1 Data acquisition

A complete fault-slip datum integrates the orientation of a fault plane, the orientation of the shear-related striations, the sense of shear movement along the plane (sense of slip) and the quality and type of shear sense indicators (Fig. 15). The most widespread type of indicators found in the study area is provided by *accretionary mineral steps* or *crystal fibres* mostly made of calcite (e.g. ~65% of indicators at the southern margin of the CEBS; Fig. 9). Such fibres develop due to directed growth of minerals in shadow zones of a sheared fault plane while the direction of growth is parallel to the movement direction of the opposite block (congruous growth; Petit et al., 1983). Another type of kinematic indicators in the study area is provided by slickolites which are oblique stylolized peaks resulting from pressure solution (Hancock, 1985). Slickolites form incongruous steps, in other words, they point in opposite direction of movement of the missing fault block and they are very frequently found in limestones (Fig. 9a). Crystal fibres and slickolites are among the most reliable indicators for the sense of slip along fault planes (Doblas, 1998) which is expressed accordingly by mostly ‘excellent’ or ‘good’ qualities in the data records for the study area. Where bedding planes, veins or other structural elements are offset along a fault plane, the sense of movement is similarly well constrained. Other types of indicators are less frequent and summarized as ‘non-specified’ steps respectively ‘non-specified’ striations.

Site	Site #	Data #	DipDir	Dip	Azimuth	Plunge	Sense	Quality	Indicators + mineral coatings
Wettringen	1	1	170	57	122	50	2	3	3, 4
Wettringen	1	2	206	89	116	5	3	2	1(cc)
Wettringen	1	3	210	65	210	65	2	3	5
Höste	6	1	333	89	244	23	4	1	2
Bodendorf	32	6	358	80	270	5	3	1	1(cc), hem

Figure 15: Raw data as sampled for a fault-slip analysis (total data sets are presented in Appendices A and B). The orientation of a fault plane is indicated by its dip direction (DipDir; 0-360° in the horizontal) and its dip (Dip; 0-90° in the vertical). The orientation of striations is indicated by their azimuth (0-360°) and their plunge (0-90°). The sense of shear along a fault is reverse (1), normal (2), dextral (3), or sinistral (4). The quality of the interpreted shear sense indicators is excellent (1), good (2), or poor (3; after a classification of Sperner et al., 1993). The type of kinematic indicators corresponds to crystal fibres (1), slickolites (2), non-specified steps (3), non-specified striations (4), or offsets of structures (5). Mineral coatings which occasionally form crystal fibres include calcite (cc), chlorite (chl), hematite (hem), and quartz (qz) in the here studied areas.

2.3.2 Data presentation

Throughout the present study, fault-slip data are presented by arrows in *tangent-lineation plots* (Fig. 8a; Hoeppener, 1955; Twiss & Gefell, 1990): Each arrow in such a lower-hemisphere, equal-area projection represents one fault-slip datum. The centre of an arrow indicates the pole to the fault plane while the arrowhead indicates the slip direction of the footwall block. Hence, this type of plot displays the directions in which material would move past the outside of a fixed lower hemisphere.

2.3.3 Data correction

One factor determining data quality is related to measurement inaccuracies: Due to, for instance, the unevenness or the bad accessibility of a fault plane, the associated striae may not be precisely parallel to the plane – at least according to the measured orientations. For this reason, fault-slip data are checked and if necessary corrected before applying SVS ('Correct Fault Data'-tool; Reiter & Acs, 1996-2008). This correction corresponds to rotating the striae along a great circle (defined by the pole to the plane and the striae) to finally align on the fault plane. Usually, these corrections are minor: For example, less than 4% of the data from the southern margin of the CEBS are corrected by more than 10°.

2.3.4 Stress inversion

SVS is performed for each investigated outcrop separately. For a whole fault population, this procedure potentially results in a number of reduced stress tensors as well as some "outliers" that cannot be explained by a common stress state. All fault-slip data are treated equally in the present study which means independently of the size of the faults and the quality of kinematic indicators. Firstly, data are not weighted because the sizes of measured faults in the study area are relatively uniform (mainly between several and several tens of metres) while fault mechanisms can be assumed to be consistent on various scales (Angelier, 1994). Secondly, the classification according to qualities of indicators has turned out not to correlate with the separation of stress states: Fault-slip data of different qualities are rather uniformly distributed among the differentiated stress states and the groups of outliers.

According to the Direct Inverse Method (Angelier & Goguel, 1979) which requires at least four fault-slip data for constraining the reduced stress tensor, also the stress states estimated by simulation are based on at least four different fault-slip data. Of course, the quality of a stress tensor increases as the number of related fault-slip data increases. According to statistical studies, stress estimates based on eight or less faults should even be treated with great suspicion (Orife & Lisle, 2006). For this reason, stress symbols used in the present study are marked if the respective stress tensor is based on less than nine fault-slip data.

Since faults can be classified according to their kinematics as reverse, normal, dextral, and sinistral, stress states can be classified according to the relative magnitude of the vertical principal axis: stress states with a vertical σ_1 are referred to as tensional, stress states with a vertical σ_2 as strike-slip or wrench, and stress states with a vertical σ_3 are called compressional (Marrett & Peacock, 1999).

Finally, the comparison of stress states estimated at different sites provides perceptions on regionally acting paleostress fields. Such a correlation takes into account consistencies in the parameters of reduced stress tensors and consistencies in the ages of stress states. Though fault-slip data are difficult to date absolutely, field observations may provide constraints on the relative timing of stress states – relative to the age of the rock that has preserved the associated fault-slip data or relative to other deformation structures.

2.3.5 Constraints on the chronology of stress states

SVS provides an effective way for separating heterogeneous fault-slip data and for deriving the full variety of causative paleostress states. The computer-aided separation of data, of course, should not conflict with, but confirm any previously gathered field observations. Exposed kinematic inconsistencies, such as superimposed striae on a single fault plane or cross-cutting relations between different fault planes, render it possible to separate data and also to determine their chronological order. A relative timing of stress states can also be derived from the relationships of fault-slip data to other deformed structures such as tilted bedding planes.

Superimposed striae

For the fault population from *Bodendorf* quarry (#32), it is shown how most of the fault-slip data have been assigned to one of three specific stress states (Fig. 12). According to overprinting relationships between individual striae on the same fault plane (such as in Fig. 9c), it can be concluded that both the stress states BOD1 and BOD2 have been active before BOD3 (Fig. 12e). According to such overprinting criteria, the two differently oriented strike-slip stress states were postdated by a tensional stress state with a NNE-SSW-directed σ_3. The interpretation of superimposed striae is based on the assumption that late-stage coatings usually develop above initial striae which, in turn, are (partly) concealed (Meschede, 1994; Doblas, 1998). This wide-spread concept becomes doubtful when considering that the question which fibres are placed on top and which there under is dependent on the fault block which was accidentally removed by erosion (Sperner and Zweigel, unpublished manuscript). For this reason, superimposed striae are critical where used as chronological indicators. However, different types of mineralisation may confirm that two fault/striae pairs belong to different subsets related to different paleostress states (Fig. 10c).

Cross-cutting relationships - Case study 1: Barntrup quarry (#14)

At *Barntrup* located in the Lower Saxony Basin, Mid Triassic (*Muschelkalk*) limestones are exposed. The sampled fault-slip data comprise two kinematically homogeneous subsets, *bar1* and *bar2* (Fig. 16a), which document the activity of the two strike-slip stress states, BAR1 and BAR2, respectively. According to field observations, a WNW-dipping dextral fault belonging to subset *bar1* (Fig. 16c) is offset by a SSW-dipping oblique-reverse fault which has been assigned to *bar2* (Fig. 16b). This situation indicates that the strike-slip stress state with NE-SW-directed maximum compression (BAR1) has been active prior to the strike-slip stress state with NW-SE-directed σ_1 (BAR2).

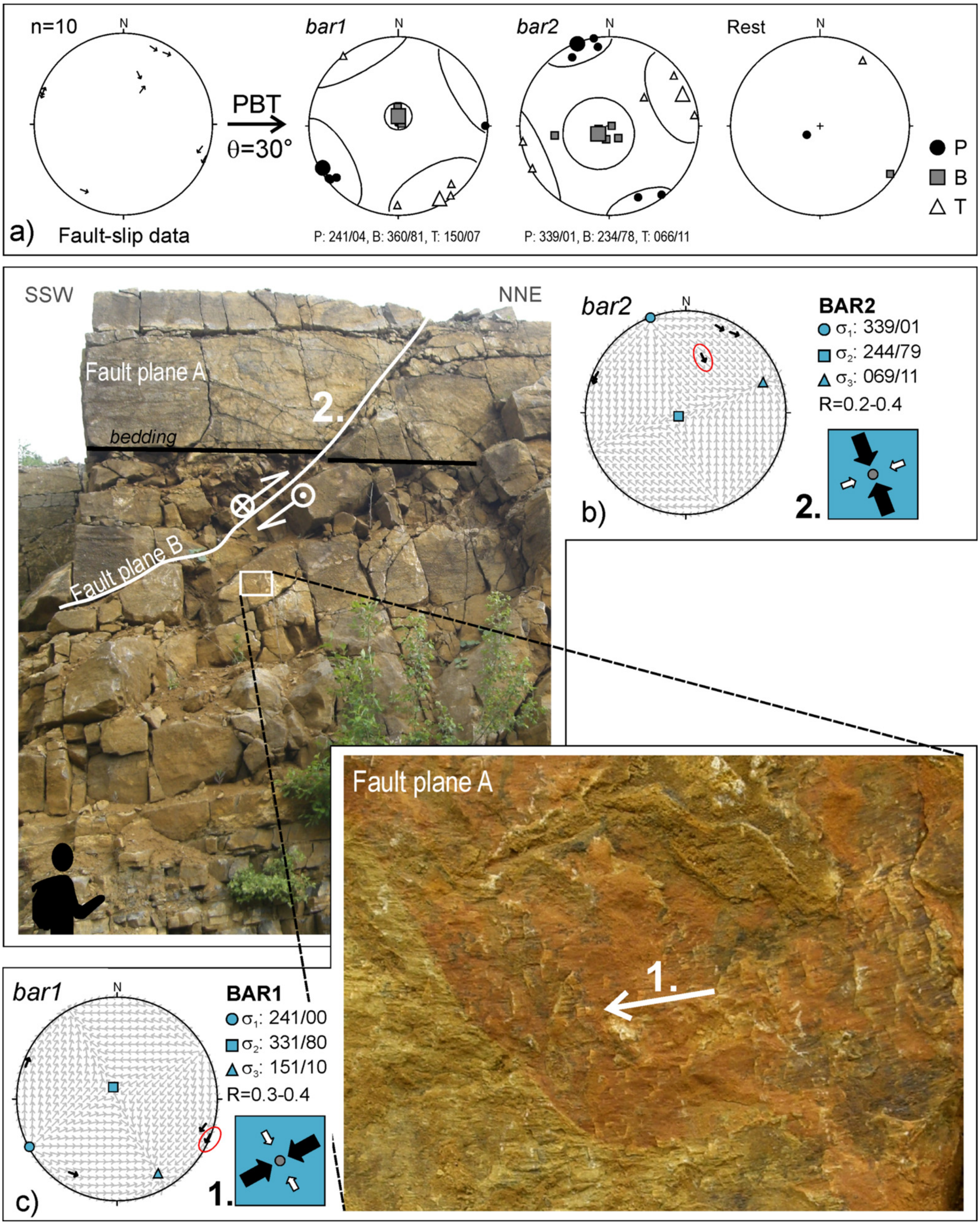

Figure 16: Cross-cutting relationships and stress states at *Barntrup* quarry (#14). The arrangement of fault-slip data constrains the chronology of related stress states. a) Fault-slip data in a tangent-lineation plot (*left*) and results of PBT after separation according to kinematic axes (*right*). b) An older WNW-dipping dextral fault (fault plane A) is offset by a younger SSW-dipping oblique-reverse fault (fault plane B). Note the dextral component offsetting fault plane A. Fault plane B belongs to the homogeneous subset *bar2* which documents the stress state BAR2. c) Fault plane A is part of the subset *bar1* which corresponds to the stress state BAR1. Both faults illustrated are marked by red circles in the respective tangent-lineation plots.

Relations to other structures - Case study 2: Halle quarry (#11)

A frequently encountered situation concerns the chronological relationship between faulting on the one side and folding/tilting on the other (Lamarche et al., 1999, 2002; Homberg et al., 2002; Lacombe et al., 2006). To diagnose if a volume of rock is presently in a tilted position, a reference frame is required. In the case of sedimentary rocks, such a frame is often provided by the attitudes of bedding planes which generally are assumed to form in a horizontal position. To determine if a set of fault-slip data within a tilted volume of rock once has been affected by the process of tilting or if faulting postdated tilting, mostly is a more delicate issue. The following example shall illustrate the integrated use of sedimentary structures and fault-slip data to unravel a local deformation history.

At *Halle* (#11) an overturned sequence of Cenomanian to Turonian limestones reveals a heterogeneous fault population (Fig. 17). A preliminary separation of the data results in three homogeneous subsets (*hal1*, *hal2*, *hal3*) and a group of inconsistent fault-slip data (Fig. 17e). Assuming the clusters of kinematic axes to indicate potential directions of stress axes, it is obvious that two of the homogeneous subsets, *hal1* and *hal2*, respectively, would reflect “non-Andersonian” stress states (as none of the respective stress axes would be vertical; Anderson, 1942). These subsets reveal oblique P- and T-axes of which the orientations provide strong evidence for a tilting of the whole strata that postdated the respective phases of faulting. Thus, before any stress inversion can be performed, a back-tilting of part of the fault-slip data is required to estimate the original stress configurations that caused faulting (Fig. 17f).

An adequate rotation axis for the back-tilting procedure is inferred from the mean strike of bedding planes (111/00) which is sub-parallel to the mean strike of B-axes associated to *hal1* and *hal2*. Considering the overturned bearing of rocks (Fiedler, 1984), the sense of rotation must be carried out anticlockwise looking down-plunge the rotation axis. By coevally tilting back fault-slip data and bedding planes until the latter achieve their original horizontal position (i.e. through 138°), the P- and T-clusters of subset *hal1* are transferred to subhorizontal and subvertical positions, respectively. For subset *hal2*, on the other hand, such an “Andersonian” orientation of kinematic axes is achieved by applying a rotation angle which is derived from the mean plunge of P-axes (i.e. 64°). Subsequent to the back-tilting process, each subset is subjected to the stress inversion procedure described above (SVS). This analysis results in three stress states which resemble remarkably in terms of both the directions of maximum compression (σ_1) and the stress ratios (Fig. 17g). However, whereas the subsets *hal1* and *hal2* correspond to compressional stress states, subset *hal3* reflects a strike-slip system.

The illustrated relation between bedding planes and fault-slip data in conjunction with the “Andersonian” concept of stress states, argues for the following deformation model (Fig. 17h): The Cenomanian and Turonian limestones at *Halle* quarry firstly were disrupted by reverse faults (subset *hal1*), when a stress state with a NNE-SSW-directed maximum compression and a vertical σ_3-axis was active (HAL1). This stress configuration probably kept constant for a certain time during which the strata successively were (i) tilted around an ESE-WNW-directed rotation axis, (ii) disrupted by another set of reverse faults (subset *hal2*; stress state HAL2) and (iii) tilted again. After the pile of rocks had achieved its recent orientation (taking the orientation of bedding planes as a reference frame), a permutation of the minimum and intermediate stress axes resulted in a vertical σ_2 (HAL3) and the activation of strike-slip faults (subset *hal3*).

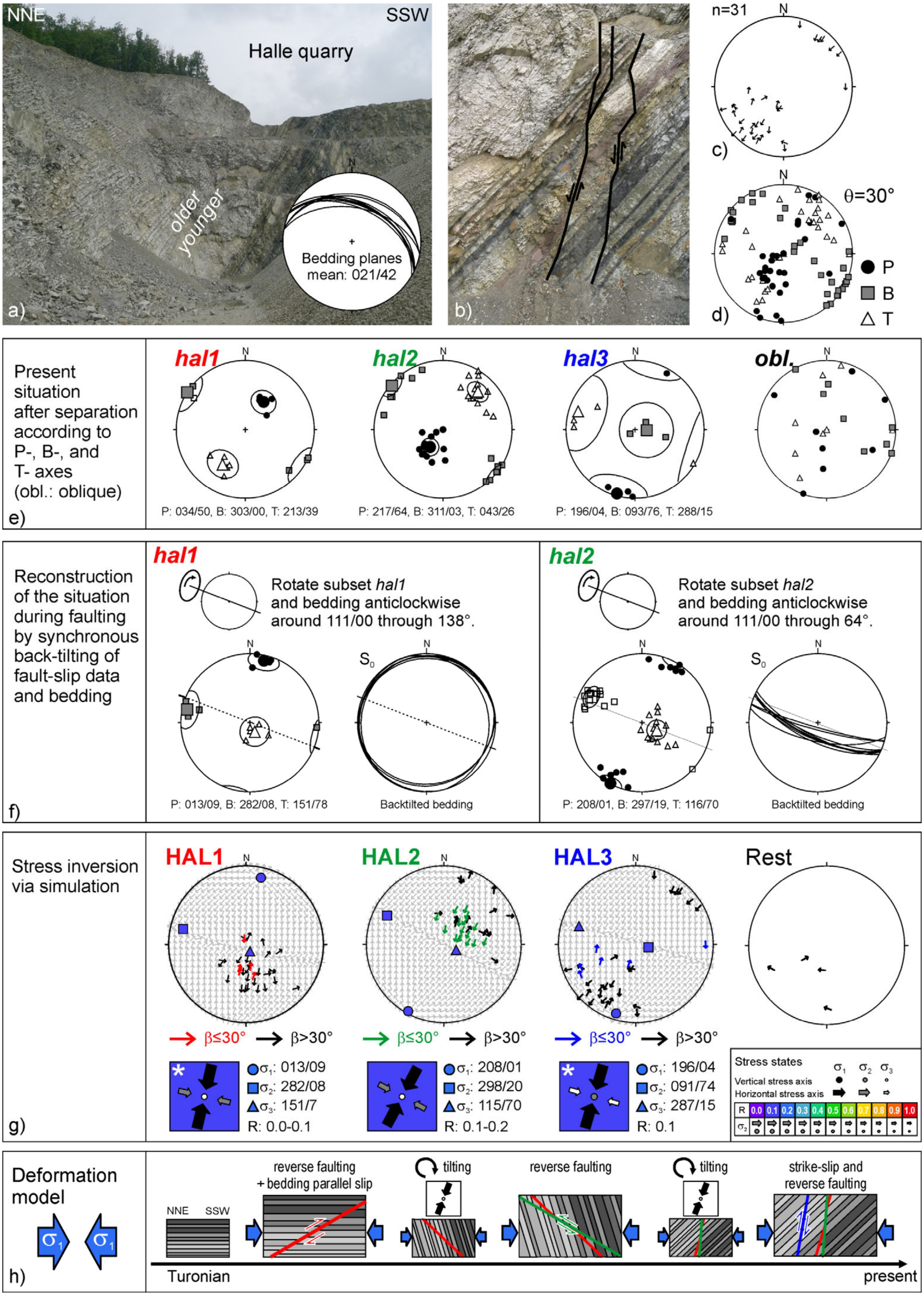

NNE
SSW
Halle quarry
older
younger
Bedding planes
mean: 021/42
a)
b)
n=31
c)
θ=30°
P
B
T
d)
Present situation after separation according to P-, B-, and T- axes (obl.: oblique)
e)
hal1
hal2
hal3
obl.
P: 034/50, B: 303/00, T: 213/39
P: 217/64, B: 311/03, T: 043/26
P: 196/04, B: 093/76, T: 288/15
Reconstruction of the situation during faulting by synchronous back-tilting of fault-slip data and bedding
f)
Rotate subset hal1 and bedding anticlockwise around 111/00 through 138°.
Rotate subset hal2 and bedding anticlockwise around 111/00 through 64°.
P: 013/09, B: 282/08, T: 151/78
Backtilted bedding
P: 208/01, B: 297/19, T: 116/70
Backtilted bedding
Stress inversion via simulation
g)
HAL1
HAL2
HAL3
Rest
β≤30° β>30°
σ1: 013/09
σ2: 282/08
σ3: 151/7
R: 0.0-0.1
σ1: 208/01
σ2: 298/20
σ3: 115/70
R: 0.1-0.2
σ1: 196/04
σ2: 091/74
σ3: 287/15
R: 0.1
Stress states
Vertical stress axis
Horizontal stress axis
R 0.0 0.1 0.2 0.3 0.4 0.5 0.6 0.7 0.8 0.9 1.0
Deformation model
h)
NNE SSW
reverse faulting + bedding parallel slip
tilting
reverse faulting
tilting
strike-slip and reverse faulting
Turonian
present

Figure 17: Separation and stress inversion for the fault-slip data from *Halle* quarry (#11). a) The Upper Cretaceous strata is overturned presently dipping towards NNE; b) Pseudo-normal faults which show reverse senses of movement when tilted back to their original position; c) Tangent-lineation plot of the heterogeneous fault-slip data; d) Result of PBT: cumulative plot of P-, B-, and T-axes for the whole data set; e) Results of separation according to clusters of P-, B-, and T-axes; f) Back-tilting procedure for the subsets *hal1* and *hal2* (see text for details); g) Results of the stress inversion via simulation. The stress states HAL1, HAL2, and HAL3 have been found to excellently fit with the previously separated subsets *hal1*, *hal2*, and *hal3*, respectively. Fault-slip data that fit a respective stress state (misfit $\beta \leq 30°$) are distinguished from data that do not fit ($\beta > 30°$). Moreover, half of the previously out-sorted data (oblique) can be explained by these stress states, so that finally only 4 faults remain as a “rest”. Stress states based on less than 9 fault-slip data are marked by an asterisk. h) Derived chronology of deformation phases after consolidation of rocks in the Turonian (time is not to scale). Symbols for phases of tilting indicate the directions of maximum horizontal compression (black arrows) inferred from the present orientation of tilted bedding planes.

3 Structural evolution of the CEBS – state of the art

As a result of its post-Variscan tectonic evolution, the CEBS contains the thickest Permian-Cenozoic sedimentary succession in Central Europe (>10 km; Scheck-Wenderoth & Lamarche, 2005). The present geometries and thickness distributions of preserved sedimentary layers in the CEBS are the expression of a succession of different phases of localized sedimentation, erosion and inversion (Fig. 18). They provide first perceptions on the deformation of the basin system and qualitative ideas about the stress fields that controlled the different stages. Since the geological record of the CEBS is the base for any reconstruction of its tectonic history, the main stages of basin evolution are described in the following together with the main rock units produced by each stage.

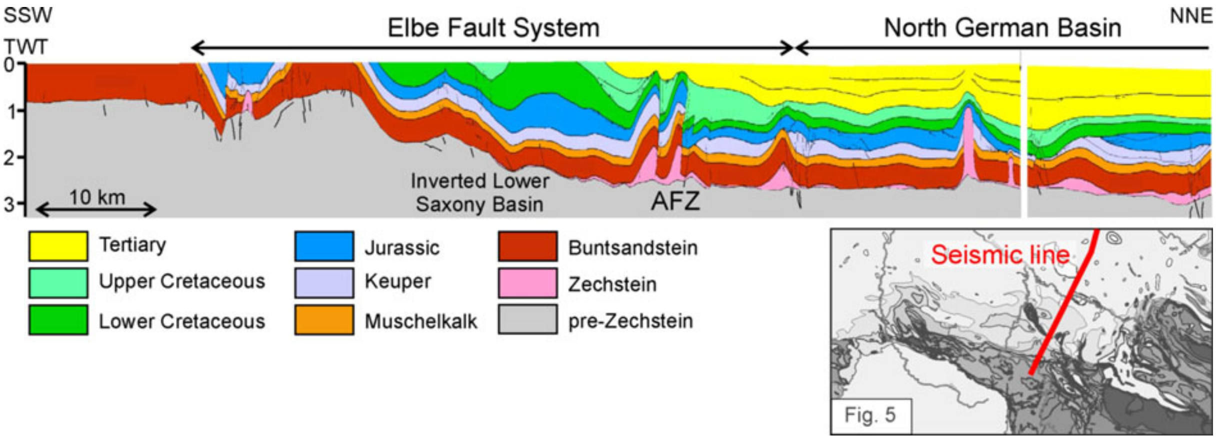

Figure 18: Regional geological profile across southwestern parts of the North German Basin (modified after Mazur et al., 2005). Note the uplifted position of the southern basin margin including the Lower Saxony Basin with respect to the North German Basin. The fault-slip data for the present study are derived from rocks cropping out along such uplifted parts of the south-western inverted margin of the CEBS. Vertical scale (seconds, two-way travel time) is twofold depth exaggerated. AFZ – Aller Fault Zone.

3.1 Initial rift phase

The Latest Carboniferous / Early Permian *initial rift phase* is supposed to be a late pulse of the Variscan Orogeny: The northern foreland of the collapsing Variscan mountain chain, including the area of the future CEBS, shows signs of deformation under roughly N-S-oriented compression and E-W-oriented extension (Heeremans et al., 1996; Lamarche et al., 1999, 2002; Vandycke, 2002). The extensional component is supposed to be responsible for the development of the intracontinental Oslo Rift system (Ziegler, 1990; Olaussen et al., 1994). Furthermore, the generation of a large variety of igneous products has been related to the development of several magmatic provinces within the collage of basement terranes in North Central Europe (Neumann et al., 2004). Accordingly, the dominant products of the Permo-Carboniferous *initial rift phase* comprise large amounts of igneous rocks. The most intensive magmatism took place in the Oslo Graben (c. 120000 km^3; Neumann et al., 1992). The preserved thicknesses of volcanic rocks in the CEBS (Fig. 19) indicate further centres of volcanism to have developed in the Skagerrak Graben (with c. 1000 m-thick lavas; Heeremans et al., 2004) and in the Northeast German Basin (more than 2500 m-thick volcanics; Benek et al., 1996).
Geochemical and geophysical data from different places of eruption argue for the Permo-Carboniferous volcanics in northern Europe to represent a common tectono-magmatic event

(Neumann et al., 2004). Today, remnants of this early period in the history of the CEBS are exposed at the surface in the areas of the Flechtingen High (Fig. 5) and of the Oslo Graben (Fig. 7). The period of magmatic activity in the Oslo Graben was estimated to have lasted between 308 Ma (syenitic sill intrusions, Sundvoll et al., 1992; Sundvoll & Larsen, 1994) and 245 Ma (granitic intrusions, Sundvoll et al., 1990). The main stage of magmatism started with the eruption of basaltic lavas (B_1 basalts, <300 Ma; Corfu & Dahlgren, 2007) which are followed by numerous lava flows of intermediate composition termed rhomb-porphyry (RP) lavas (Sundvoll et al., 1990). The youngest products of the volcanic phase are ring dykes and explosion breccias which are related to a stage of caldera formation (Ramberg & Larsen, 1978). In the Northeast German Basin, the main period of volcanic activity was estimated to be shorter and to have occurred between 307-294 Ma (±3 Ma, respectively; Breitkreuz & Kennedy, 1999). The volcanics exposed in the Flechtingen High area are regarded as part of the calc-alkaline, SiO_2-rich Altmark-Flechtingen-Block-Subhercyn volcanic suite which consists mainly of rhyolites and andesites (Benek et al., 1996).

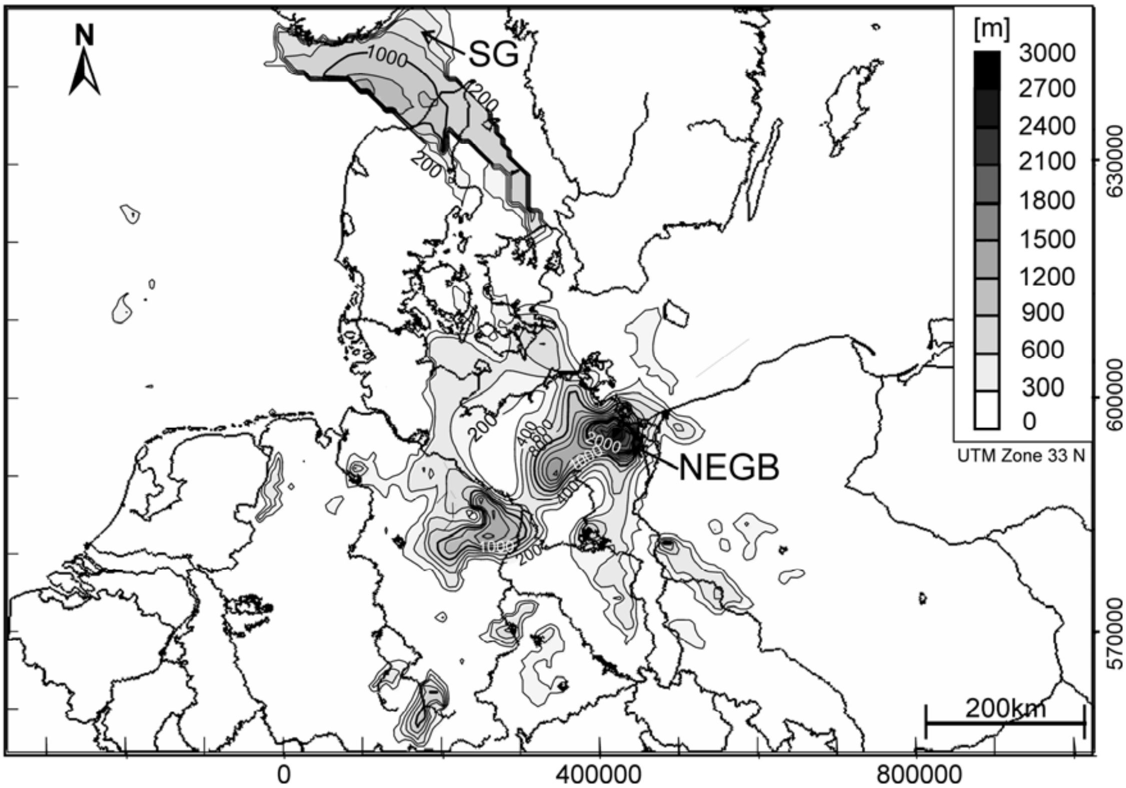

Figure 19: Preserved thickness of Permo-Carboniferous volcanics in the CEBS (isolines in 200m steps; modified after Scheck-Wenderoth et al., 2008a). Main centres of volcanism were located in the Skagerrak Graben (SG) and its northern prolongation, the Oslo Graben, as well as in the Northeast German Basin (NEGB). Reduced thicknesses of volcanics can be found from the southern North Sea through northern Germany into central Poland.

3.2 Post-rift phase of thermal subsidence

From latest Early Permian until Mid-Triassic, north Central Europe was mainly affected by a phase of thermal subsidence in the course of which former N-S trending graben-like depocentres joined to form the large NW-SE- to WNW-ESE-trending Northern and Southern Permian basins (Ziegler, 1990). Whereas the Norwegian-Danish Basin and the North German

Basin experienced later structural differentiation, the dominant NW-SE-direction of structures in the Polish Basin persisted throughout the entire basin history, which is supposed to be a result of its position above the Tornquist Zone which thenceforward controlled its development (Scheck-Wenderoth et al., 2008a).

In the Southern Permian Basin, an at least 2300 m-thick succession of continental *Rotliegend* clastics was deposited comprising sandstones and siltstones with intercalated evaporites (Fig. 20; Dadlez et al., 1995, 1998; Kiersnowski et al., 1995; Plein, 1995; Benek et al., 1996; Bachmann & Hoffmann, 1997; Lokhorst, 1998; Baldschuhn et al., 2001). Paleostress studies in the Lower Saxony Basin and its northwestern prolongation (Groningen Block) have shown that these clastics have been affected by ENE-WSW-directed extension still during the Permian (Lohr, 2007; van Gent et al., in press).

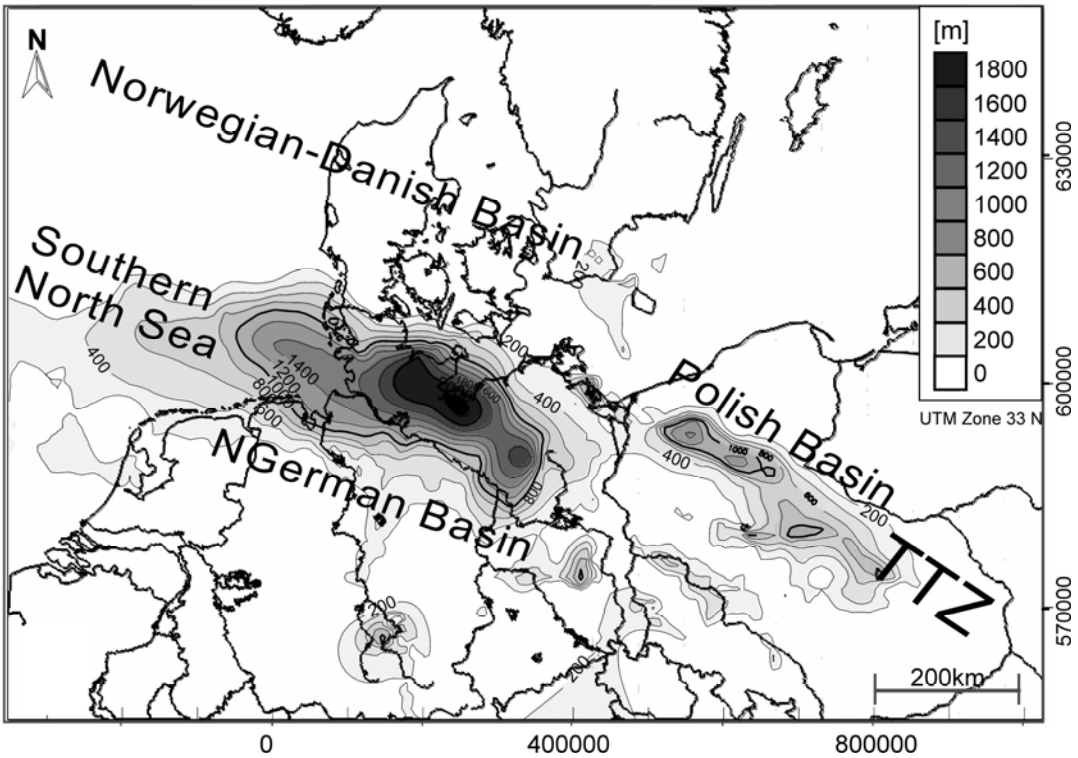

Figure 20: Preserved thickness of Lower Permian *Rotliegend* sediments (isolines in 200 m steps; modified after Scheck-Wenderoth et al., 2008a). TTZ – Teisseyre-Tornquist Zone.

During the Late Permian, a paleo-surface lowering was accompanied by a global glacio-eustatic sea-level rise, enabling a marine transgression from the Arctic Ocean into the southern North Sea and across much of Central Europe (Ziegler, 1988, 1990; Coward et al., 2003). The respective Upper Permian sedimentary formations are known as the *Zechstein* (Fig. 21). The formations of the *Zechstein* Sea comprise the products of several evaporation cycles ranging from limestones and dolomites to the economically important units of rock salt in northern Germany. Within the investigated areas, rocks of the *Zechstein* period (mainly carbonates) are exposed where the inversion-related uplift of the Paleozoic block of the Harz Mountains involved the ascent of adjacent sediments along the Northern-Harz-Boundary Fault and along fault arrays structuring the western and southern borders of the Harz block (Fig. 5). The recurrent post-depositional mobilisation of *Zechstein* evaporites played a decisive role for the later structural evolution of much of the CEBS.

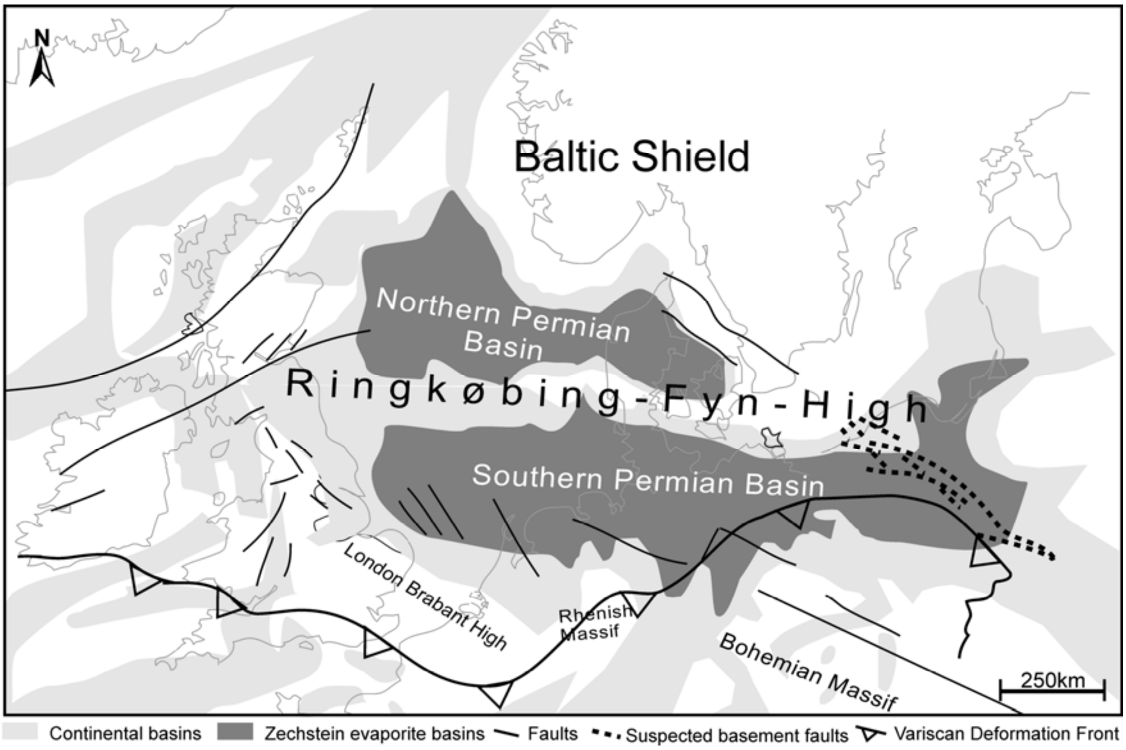

Figure 21: Areas of Late Permian deposition of Zechstein salt (modified after Scheck-Wenderoth et al., 2008a). The outlines of evaporite deposition indicate that two individual sub-basins, the so-called Northern and Southern Permian Basins (Ziegler, 1990), were separated by the Mid-North Sea–Ringkøbing –Fyn chain of structural highs.

Until the Mid-Triassic, ongoing thermal subsidence with minor tectonic activity led to a continuous broadening of the depositional area of Central Europe where – after the ultimate evaporation of the *Zechstein* Sea – the continental red-bed clastics of the *Buntsandstein* were deposited. In the central parts of the North German Basin, the average thickness of the *Buntsandstein* sediments attains a few thousand metres. Maximum thicknesses, however, are located where the earliest influence of E-W-directed extension has been recorded, such as in the N-S-trending Glückstadt Graben which shows up to 5000 m of *Buntsandstein* (Baldschuhn et al., 2001; Maystrenko et al., 2005). As a result of two main phases of eustatic sea-level rise between 248 Ma and 221 Ma, much of Central Europe developed towards a marine depositional environment with mainly carbonate deposition, the *Muschelkalk* sequences (Rüffer & Zühlke, 1995). Aside from the large N-S-oriented grabens, the CEBS reveals a rather uniform thickness distribution varying in the range of hundreds of metres of *Muschelkalk* (Scheck-Wenderoth et al., 2008a). At present, *Muschelkalk* limestones are among the most prevalent rocks outcropping along the southern inverted margin of the CEBS. They are exposed in southwestern Poland (Fig. 6), as well as in the Subhercynian Basin, in the Lower Saxony Basin, and in the northern parts of the N-S trending Hessian Depression between the Egge Lineament and the Leine Graben (Fig. 5).

3.3 Mid-Triassic – Jurassic phase of E-W extension

A period of roughly E-W-oriented extension commencing in the Mid Triassic is indicated by mainly N-S-trending axes of depocentres that partly dissect the Mid-North Sea-Ringkøbing-Fyn High (Fig. 22; Scheck-Wenderoth & Lamarche, 2005). The E-W-directed extension induced accelerated tectonic subsidence of N-S-trending basins like the Central Graben, the Horn Graben, and the Glücksstadt Graben. In general, the depositional area of the CEBS became shallower from Mid to Late-Triassic while the depositional setting changed from marine to continental again (fluvial to lacustrine *Keuper* sediments). Considering the locally increased thickness of *Keuper* sediments within the Glücksstadt Graben where it attains up to 5800 m, maximum extension can be dated back to Mid-Late Triassic times (Maystrenko et al., 2005). Localized subsidence in the N-S grabens was strongly enhanced by salt tectonics, as the salt withdraw from the axial parts of the grabens to rise along graben-parallel faults (Scheck et al., 2003a,b; Maystrenko et al., 2006).

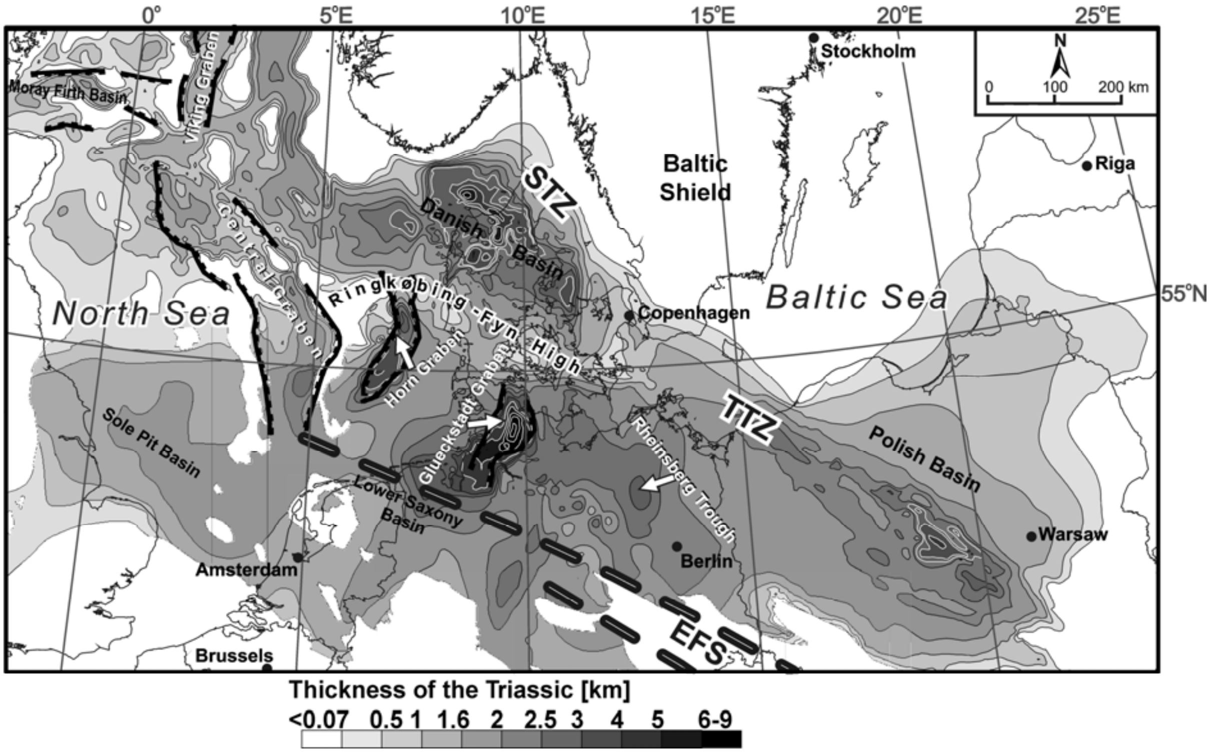

Figure 22: Thickness distribution of preserved Triassic deposits (modified after Maystrenko et al., 2006). N-S-oriented grabens and troughs show increased thicknesses. A further main depocentre is provided by the Polish Basin which strikes NW-SE. EFS – Elbe Fault System, STZ – Sorgenfrei-Tornquist Zone; TTZ – Teisseyre-Tornquist Zone.

3.4 Mid-Jurassic phase of uplift

The Mid-Jurassic period is mainly controlled by uplift of the central North Sea in the course of which large parts of North Central Europe successively have been elevated (Fig. 23; Scheck-Wenderoth et al., 2008). Accordingly, the northern parts of the CEBS around the Mid-North Sea-Ringkøbing Fyn chain of highs became the main erosional area and the Jurassic formations in the CEBS widely reflect a transition from deep to shallower water conditions. While this successively southward moving uplift affected the northern parts of the North German Basin (Pompeckj Block) – thus restricting Jurassic strata mainly to salt-rim synclines in the area (Maystrenko et al., 2005) – the southern parts of the North German Basin provided the frontal space for an accommodation of locally up to 1000 m of mainly clastic sediments (Walter et al., 1995).

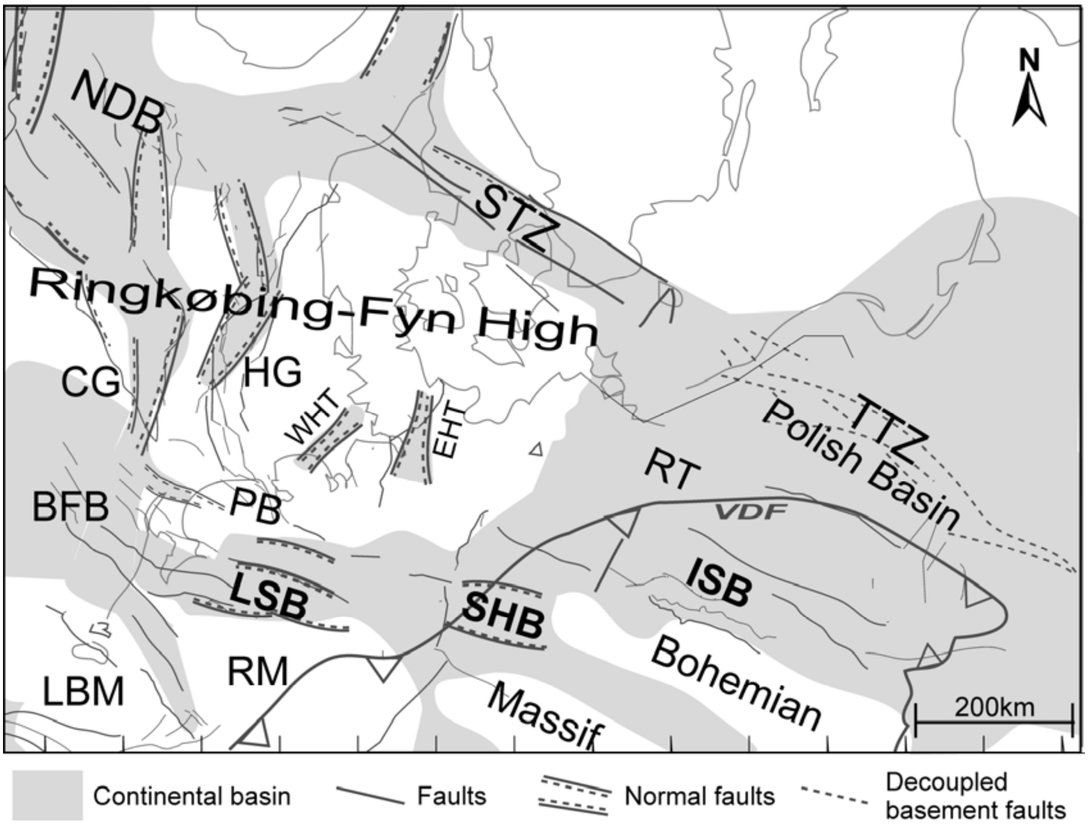

Figure 23: The CEBS in Mid Jurassic times (modified after Scheck-Wenderoth et al., 2008a). Large parts of the CEBS represent structural highs.
BFB – Broad Fourteens Basin; CG – Central Graben; EHT – East-Holstein Trough; HG – Horn Graben; ISB – Intra-Sudetic Basin; LBM – London Brabant Massif; LSB – Lower Saxony Basin; NDB – Norwegian-Danish Basin; PB – Pompeckj Block; RM – Rhenish Massif; RT – Rheinsberg Trough; SHB – Subhercynian Basin; STZ – Sorgenfrei Tornquist Zone; TTZ – Teisseyre Tornquist Zone; WHT – West-Holstein Trough.

3.5 Late Jurassic – Early Cretaceous phase of localized subsidence

Until the beginning of the Late Jurassic, regional uplift had turned much of the CEBS into an erosional area while deposition was restricted to WNW- to NW-trending subsidence centres located at the margins of the CEBS. While the central parts of the CEBS experienced uplift affecting the Ringkøbing-Fyn High as well as Pompeckj Block, localized subsidence was found, for instance, along the Sorgenfrei-Tornquist Zone (Surlyk, 2003), along the Teisseyre-Tornquist Zone (i.e. in the Polish Basin; Dadlez et al., 1995, 1998), and in numerous basins along the southern margin, such as the Lower Saxony Basin (Betz et al., 1987). In the western parts of the Elbe Fault System, localized subsidence was accompanied by another phase of mobilisation of *Zechstein* salt (Scheck et al., 2002a; Scheck-Wenderoth & Lamarche, 2005). This generated space for the accumulation of shallow marine and lacustrine sediments, such as marine sandstones, clay stones, marls, and limestones including calcareous ooliths (Walter et al., 1995; Kossow & Krawczyk, 2002). Due to their weathering resistance, these limestones presently constitute the stabilising elements of some mountain ridges in the German parts of the Elbe Fault System where they widely are economically produced.
At the beginning of the Early Cretaceous (Berriasian), the connection of the Lower Saxony Basin to open marine water was interrupted (Fig. 24) leading to desalinisation, deposition of the limnic-brackish *Wealden* facies, and locally to an erosional hiatus (the base Lower Cretaceous unconformity; Kossow et al., 2000; Kossow & Krawczyk, 2002). During the

following transgressive phase (Valanginian to Aptian), the marine flooding gradually transcended beyond the boundaries of the localised Upper Jurassic depocentres so that much of the North German Basin (including the Pompeckj Block) and the Polish Basin were included in a common marine depositional environment. While tectonic activity was strongly reduced during this phase, some 800-1000 m of *Wealden* sequences and 1500-1650 m of post-Berriassian sediments have been deposited in the Lower Saxony Basin (Klassen, 1984; Betz et al., 1987; Mutterlose & Böckel, 1998).

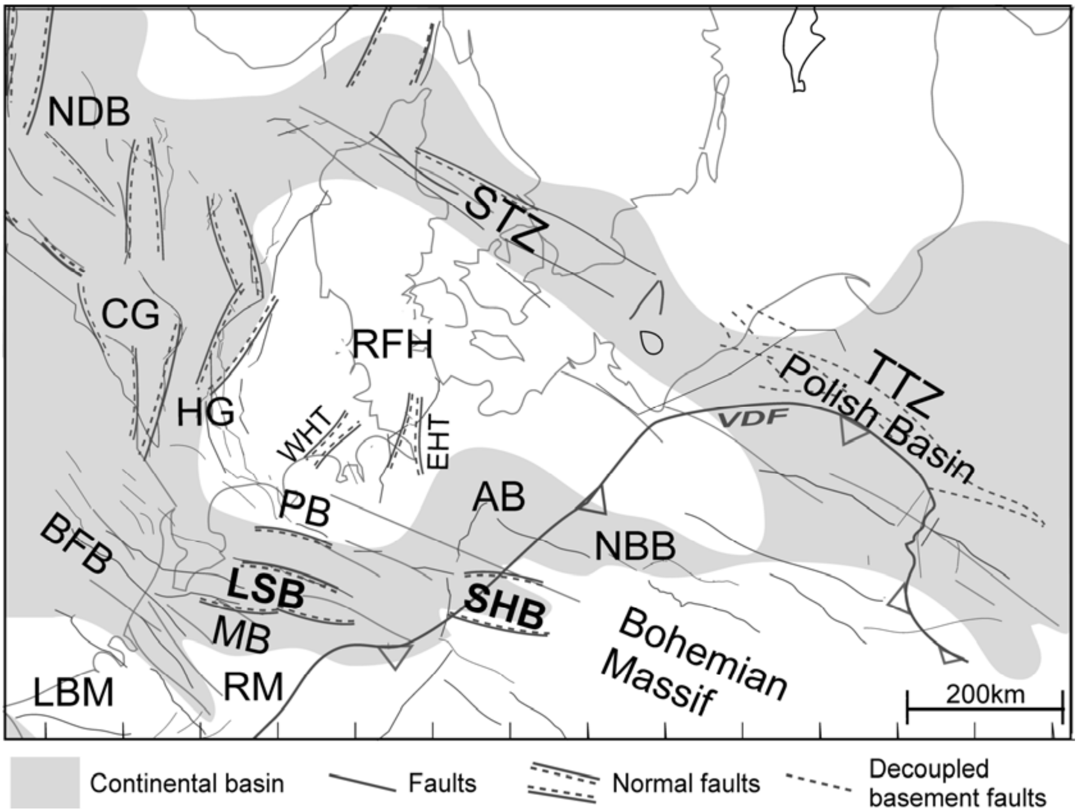

Figure 24: The CEBS in Early Cretaceous times (modified after Scheck-Wenderoth et al., 2008a). Subsidence was restricted to NW-SE trending depocentres as the Polish Basin and the northern Norwegian-Danish Basin, and to basins along the southern margin of the North German Basin.
AB – Altmark Basin; BFB – Broad Fourteens Basin; CG – Central Graben; EHT – East-Holstein Trough; HG – Horn Graben; LBM – London Brabant Massif; LSB – Lower Saxony Basin; NBB – North Bohemian Basin; NDB – Norwegian-Danish Basin; PB – Pompeckj Block; RFH – Ringkøbing-Fyn High; RM – Rhenish Massif; SHB – Subhercynian Basin; STZ – Sorgenfrei Tornquist Zone; TTZ – Teisseyre Tornquist Zone; WHT – West-Holstein Trough.

3.6 Late Cretaceous – Early Tertiary phase of inversion

At the beginning of the Late Cretaceous, a globally elevated sea level (Torsvik et al., 2002) and probably minor extensional stresses induced by divergent plate movements in the North Atlantic (Stampfli & Borel, 2002; Torsvik et al., 2002) resulted in flooding of much of Central Europe. The sediments related to this marine transgression are predominantly carbonates which are developed as chalk in the northern parts of the CEBS and as limestones with clastic intercalations along the southern margin of the basin system (Scheck-Wenderoth et al., 2008a).

Subsequently, the style of intra-plate deformation changed drastically from an extensional (and transtensional) to a compressional (and transpressional) mode. As a result, WNW- and NW-striking blocks that previously had experienced subsidence were inverted and exposed to erosion whereas adjacent blocks were taking up large amounts of Upper Cretaceous sediments (Fig. 25; Scheck-Wenderoth & Lamarche, 2005). Stratigraphic and thermochronologic data indicate that one main phase of shortening covers the Latest Turonian and Campanian time (Ziegler et al., 1995; Hejl et al., 1997; Thomson & Zeh, 2000; Vejbaek & Andersen, 2002; Kockel, 2003; Voigt et al., 2004, 2006; Senglaub et al., 2006).

The Lower Saxony Basin, for instance, experienced strong uplift which culminated in the Coniacian and Santonian. The amount of related erosion is debated but proposed values range up to several thousand metres of sediments (Senglaub et al., 2006). At the same time, areas to the north (Pompeckj Block) and to the south (Münsterland Basin) experienced subsidence, thus providing space for the deposition of up to 2000 m of Upper Cretaceous sediments (Walter et al., 1995). Along the southern flank of the Lower Saxony Basin, uplift-related movements were strongly localized along the Osning Lineament. This structure roots in the pre-Permian basement of the Lower Saxony Basin separating the Rhenish Massif below the Münsterland Basin in the south from the Lower Saxony block in the north (Fiedler, 1984; Drozdzewski, 1988). The outcropping prolongation of this lineament is a zone of inversion-related thrust faults along which Mesozoic to Lower Cretaceous sediments of the Lower Saxony Basin have been thrust southwards over the stable Münsterland platform and its thick cover of Upper Cretaceous rocks.

Similar inversion-related phenomena as described for the Lower Saxony Basin have also been reported for other sub-basins of the Elbe Fault System: the Sole Pit Basin (Badley et al., 1993; Nalpas et al., 1995; Buchanan et al., 1996), the Broad Fourteens Basin (De Lugt et al., 2003; Nalpas et al., 1995), and the Subhercynian Basin (Kossow et al., 2001; Otto, 2003; Franzke et al., 2004; Voigt et al., 2004). The uplift of these basins was accompanied by a new phase of salt movement during which salt diapirs with NW-SE-trending axes formed parallel to the uplifted blocks (Scheck-Wenderoth et al., 2008a). The western parts of the Allertal Fault Zone (Fig. 5), for instance, show locally increased thicknesses of Upper Cretaceous in salt rim synclines and reduced thicknesses where diapirs have developed (Lohr et al., 2007). The Northern Harz Boundary Fault which is another major fault zone exposed in the study area separates the Hartz block in the south – comprising Variscan-deformed Devonian to Lower Carboniferous sediments – from the Mesozoic sediments of the Subhercynian Basin in the north. During the phase of inversion, the basin fill of the Subhercynian Basin was tilted and partly overthrust by the Variscan basement due to the relative uplift of the Harz block along the Northern Harz Boundary Fault (Thomson et al., 1997; Voigt et al., 2004). Thereby, the Subhercynian Basin was progressively filled with locally more than 1500 m of Upper Cretaceous rocks consisting of marginal sandstones of the Upper Cretaceous chalk sea. At the same time (mainly during the Coniacian and Santonian), also the block of the Flechtingen High experienced uplift, its transition to the north, however, evolving as a flexure rather than a fault (Scheck et al., 2002a).

Alike the Elbe Fault System, also the Sorgenfrei-Tornquist Zone acquired its principal inversion structures with an uplifted central zone limited by reverse faults during Late Cretaceous and Early Tertiary phases of inversion (Berthelsen, 1992). The related uplift of the Norwegian-Danish Basin occurred synchronous with the inversion of the NW-trending branch of the Danish Central Graben (Vejbaek & Andersen, 2002). Finally, a Late Cretaceous reverse reactivation of basement-cutting normal faults has also been observed along the Teisseyre-Tornquist Zone in the axial part of the Polish Basin (Erlström et al., 1997; Krzywiec, 2002; Krzywiec et al., 2003). In all of these sub-basins, the location of inversion is spatially linked to NW-SE-trending Upper Jurassic-Lower Cretaceous depocentres. This preferred orientation of inverted basins, the weak intensity of observed contraction within N-S-trending basins (Maystrenko et al., 2005), and the results of fault-slip analysis performed in some parts of Central Europe (Lamarche et al., 2002; Vandycke et al., 2002; Franzke et al., 2007; Bergerat

et al., 2007) consistently argue for a NNE-SSW- to NE-SW-direction of maximum compression that was responsible for the basin-wide inversion.
In many sub-basins, signs of inversion have not only been recorded for the Late Cretaceous but also for the Cenozoic, while the structural style was established to have changed between the Late Cretaceous and the Early Tertiary phase (Nielsen et al., 2005). Existing models characterising the phase of inversion (e.g. Ziegler et al., 1995) have recently been put up for a new discussion (Nielsen et al., 2005; Scheck-Wenderoth et al., 2008a; Kley & Voigt, 2008). These new perceptions have been developed especially in the light of the latest results concerning the causal interrelations between intraplate compressional stresses in Central Europe and Late Cretaceous orogenic processes in southern Europe where the early orogeny of the Alps coincided with the onset of Africa-Iberia-Europe convergence.

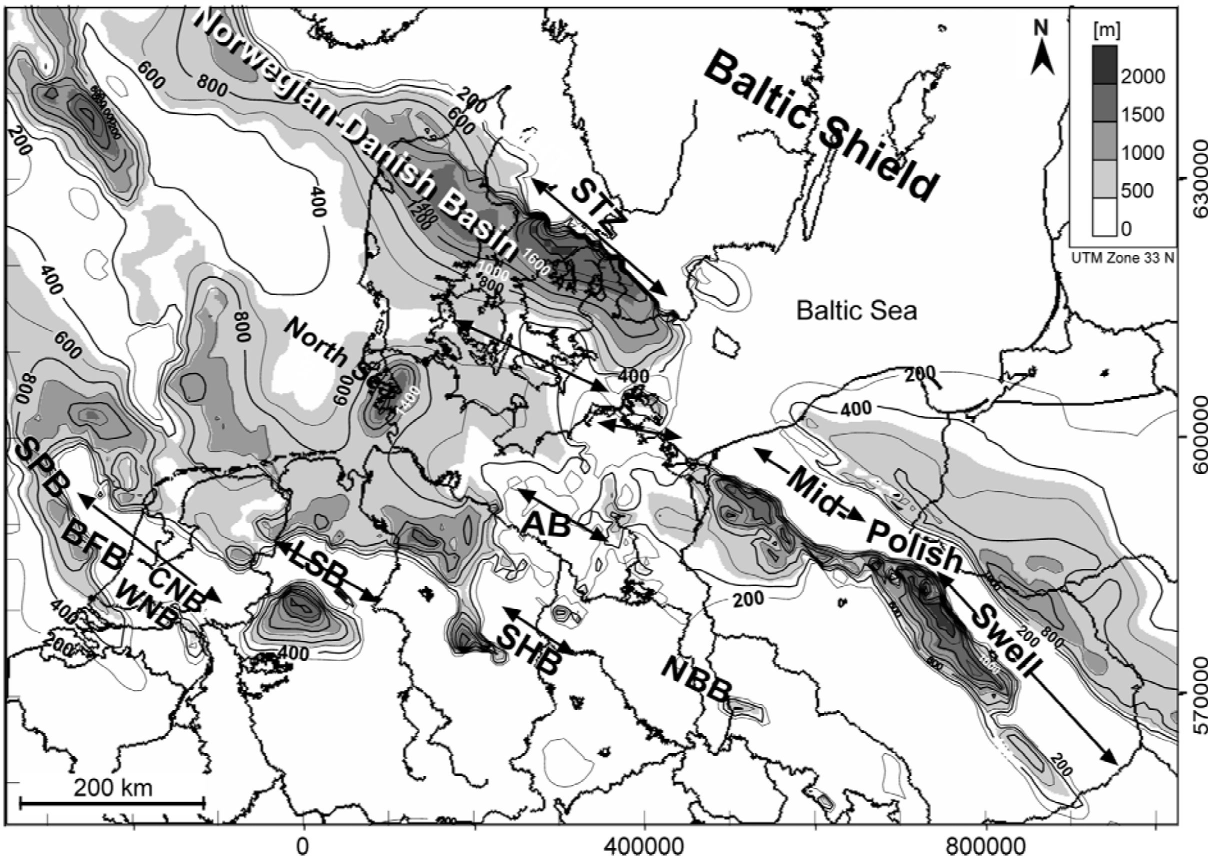

Figure 25: Distribution of preserved thickness of Upper Cretaceous rocks (isolines in 200 m steps; modified after Scheck-Wenderoth et al., 2008a). The axes of inverted blocks strike around WNW (double arrows) indicating a roughly NNE-directed maximum compression that induced inversion of Upper Jurassic to Lower Cretaceous basins.
AB – Altmark Basin; BFB – Broad Fourteens Basin; CNB – Central Netherlands Basin; LSB – Lower Saxony Basin; NBB – North Bohemian Basin; SHB – Subhercynian Basin; SPB – Sole Pit Basin; STZ – Sorgenfrei Tornquist Zone; WNB – West Netherlands Basin

3.7 Cenozoic subsidence and transition to present-day stress conditions

The Cenozoic represents a period when Africa and Europe were converging, when a major hotspot developed in the Faeroe-Greenland area, when seafloor spreading commenced in the North Atlantic between Greenland and Europe, and when NW Europe became part of a thermally subsiding passive continental margin from Eocene times onwards (Rasser et al., 2008). During this phase of thermal subsidence, the CEBS experienced little faulting but renewed salt mobilisation while mainly N-S- and NW-SE-trending subsidence axes have been created (Scheck-Wenderoth & Lamarche, 2005). The major depocentre of this period with up to 3500 m of Cenozoic sediments is located in the Central North Sea.

Much of the Cenozoic evolution of North Central Europe was and still is controlled by far-field stresses resulting from continent collision farther to the south such as in the Pyrenees or the Alps (Reicherter et al., 2008). The earliest pulses of collision resulted in the formerly addressed phase of Late Cretaceous – Early Palaeogene inversion. During the Eocene to Miocene, in contrast, Central Europe has been governed by extensional tectonics that created the European Cenozoic Rift System including, for instance, the Upper Rhine Graben. Finally, there are indications that between the Eocene and the Miocene the direction of maximum horizontal stress (S_{Hmax}) rotated from a NE-SW- to a NW-SE-direction (Bergerat, 1987; Schreiber & Rotsch, 1998; Hinzen, 2003). The 'neotectonic period' of Central Europe thus began in the Late Miocene with the initiation of the present-day stress field which is predominantly characterised by NW-SE compression and NE-SW extension (Heidbach et al., 2008).

The super-regional present-day stress field in Central Europe is generated by Atlantic ridge push forces and forces related to collision/convergence of the Eurasian and African plates (Gölke & Coblentz, 1996; Goes et al., 2000). The general trend of NW-SE-directed maximum horizontal compression (S_{Hmax}) is complicated by varying plate boundary conditions, salt movements, and the coexistence of rheologically different domains (Grünthal & Stromeyer, 1992; Cacace et al., 2008). Such local disturbances of stresses are reported, for instance, for the North German Basin where S_{Hmax} swings from a NW direction in the west to a NNE direction in the east (Roth & Fleckenstein, 2001; Heidbach et al., 2008). Further local perturbations of the present (and Pleistocene) stress field are related to the post-glacial isostatic rebound of the Baltic Shield (Scherneck et al., 1998; Kaiser et al., 2005; Reicherter et al., 2005).

3.8 Salt tectonics

From the Mid Triassic onward, the tectonic activity of the CEBS was recurrently accompanied by a mobilisation of *Zechstein* salt layers (Scheck et al., 2003a; Scheck-Wenderoth et al., 2008b) which formerly had been deposited in the areas of the Northern and Southern Permian Basins during the Late Permian (Fig. 21). The present distribution and geometries of salt structures in the CEBS reflect different phases of salt (re)mobilisation resulting in diverse maturities of the structures in terms of pillow stage versus diapiric stage.

The first major phase of salt movement was related to the *Mid-Triassic – Jurassic phase of E-W extension* which initiated N-S striking salt walls and diapirs mainly in the large N-S trending grabens of the Southern North Sea and in parts of the North German Basin. The *Late Jurassic – Early Cretaceous phase of basin differentiation* affected mainly the northern and southern marginal parts of the CEBS where local subsidence was accompanied by normal faulting and the formation of NW-SE oriented salt structures and pillows. The *Late Cretaceous – Early Tertiary phase of inversion* which mainly affected WNW- and NW-striking blocks enhanced the growth of NW-SE salt structures, whereas N-S-oriented salt structures experienced a phase of stability during this phase. This configuration changed again, when during the phase of *Cenozoic subsidence* N-S-oriented salt walls experienced a new phase of growth parallel to the mainly N-S-trending depositional axes of this time.

As described, the post-depositional mobilisation of salt temporally correlates well with the main regional tectonic phases in the CEBS. There are, however, differences between the central and the marginal parts of the basin system concerning their evolution and resulting salt structures (Scheck-Wenderoth et al., 2008b). According to the outlines of the Northern and

Southern Permian Basins, the reconstructed initial thicknesses of *Zechstein* salt layers generally increases from the marginal to the central parts of the basin system. As a result of its mechanical properties (Hudec & Jackson, 2007; Kukla et al., 2008), the salt locally acted as a decoupling horizon during post-depositional deformation phases. This applies mainly to the central parts of the CEBS, where the salt cover was mechanically decoupled from the deformation of the salt basement (thin-skinned deformation; Hecht et al., 2003; Scheck et al., 2003b). Accordingly, the patterns of the present-day direction of maximum horizontal stress, S_{Hmax}, in subsaline and in suprasaline formations of the North German Basin show differences that argue for a decoupling also of the regional stress field due to *Zechstein* salt layers (Roth & Fleckenstein, 2001). On the contrary, along the marginal parts of the Norwegian-Danish Basin, the North German Basin, and the Polish Basin, deformation of the salt cover and diapir location are directly linked to basement faults (thick-skinned deformation) and the recorded intensity of deformation is generally higher. As a result of the lateral variations in deformation history – controlled to a large extent by pre-existing of zones of crustal weakness as the Sorgenfrei-Tornquist Zone, the Teisseyre-Tornquist Zone, and the Elbe Fault System – salt structures at the margins of the CEBS predominantly strike NW-SE, whereas in the central parts they trend N-S (Fig. 26).

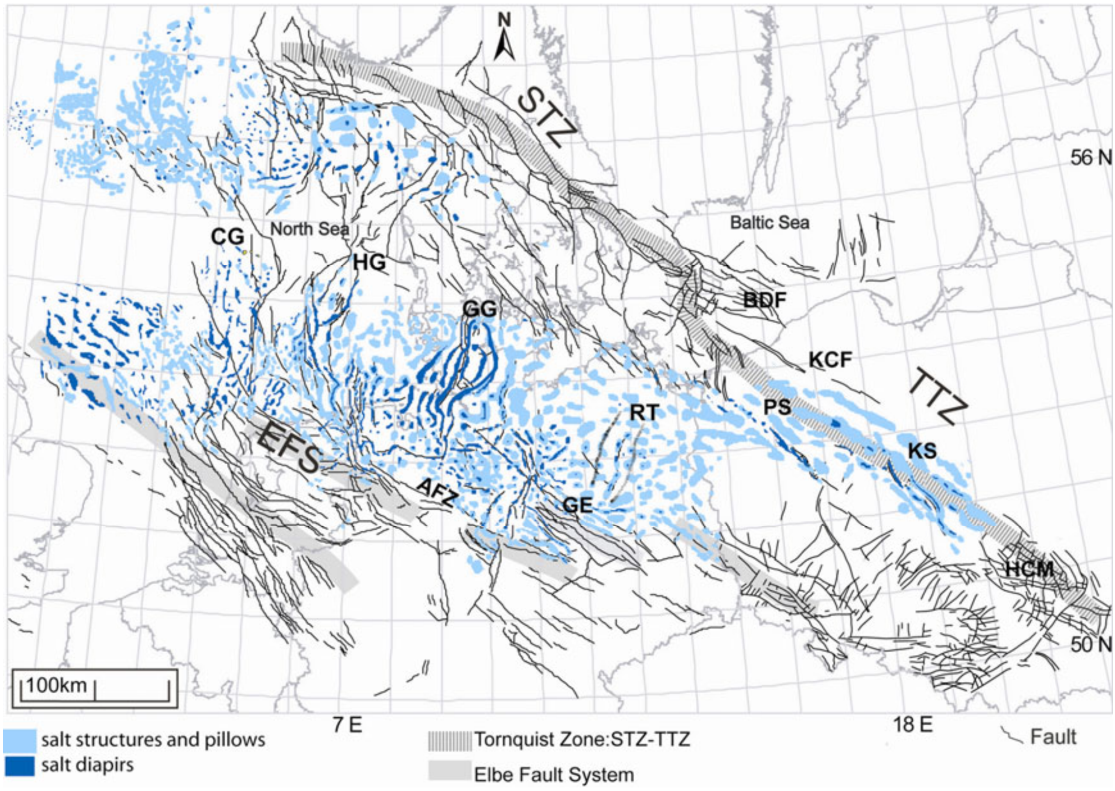

Figure 26: Present distribution of salt structures in the CEBS (Maystrenko et al., 2006; Baldschuhn et al., 2001; Dadlez et al., 1998; Evans et al., 2003; Jaritz, 1987; Lockhorst et al., 1998; Nalpas and Brun, 1993; Remmelts, 1995; Scheck et al., 2003b).

In the Southern North Sea and the North German Basin, the mobilisation of the Zechstein salt resulted in two main types of structures: (1) in the northern half of this province, NNW- to NNE-striking salt walls were initiated during the Mid-Triassic phase of E-W extension and (2) in the southern half, NW-SE-striking salt structures developed in the Cretaceous coevally with the subsidence and inversion of NW-SE-trending sub-basins. In the Polish Basin, the salt structures follow the trend of the Teisseyre-Tornquist-Zone while documenting different mobilisation ages.

AFZ - Allertal Fault Zone, BDF - Bornholm-Darlowo Fault Zone, CG - Central Graben, EFS - Elbe Fault System, GE - Gardelegen Escarpment, GG - Glückstadt Graben, HCM - Holy Cross Mountains, HG – Horn Graben, KCF - Koszalin-Chojnice Fault Zone, KS - Kuiavian Segment, PS - Pomeranian Segment of Mid-Polish Trough, RT - Rheinsberg Trough, STZ - Sorgenfrei-Tornquist Zone, TTZ - Teisseyre-Tornquist Zone.

4 The southern margin of the CEBS

The presented thickness distributions of specific sedimentary layers in the CEBS reflect shifts in the depositional and erosional areas over time and thus provide first perceptions on the structural evolution of the basin system. This evolution is strongly controlled by major WNW-ESE- and N-S-trending structures, respectively, which document remarkably consistent developments and recurrent activation since Permian times. However, such interpretations are based on seismic-scale present-day geometries of the basin fill. To constrain more closely the modes and causes of deformation in the CEBS, an outcrop-scale study focusing on the kinematic interpretation of brittle faults has been performed. Such a fault-slip analysis yields states of paleostress which can be discussed in the framework of the evolution of the CEBS known so far.

To potentially distinguish between different phases of faulting, a broad range of differently-aged rocks has been investigated. However, the CEBS is widely covered by unconsolidated Cenozoic units so that field-based studies on the pre-Cenozoic evolution are limited to areas where increased uplift and erosion (especially during the *Late Cretaceous-Early Tertiary phase of inversion*) have exposed pre-Cenozoic rocks.

Along the Elbe Fault System, Upper Carboniferous to Upper Cretaceous rocks are exposed, thus potentially attesting to the tectonic evolution of the southern margin of the CEBS from the time of rock formation until present (Fig. 5, 6). A total number of 906 fault-slip data have been sampled from 40 sites revealing Upper Carboniferous, Upper Permian, Mid Triassic, Upper Jurassic, and Upper Cretaceous rocks (Tab. 1). Sampling of the data was restricted to limestones and volcanics because these lithologies offer the most favourable conservation conditions for kinematic indicators on fault planes in the area. Where possible, the fault-slip data are complemented by information on their spatial and chronological relationships to other structures, such as faults, bedding planes, folds, or veins.

After data acquisition, the stepwise fault-slip analysis introduced in Chapter 2 ("Stress Inversion via Simulation", SVS) has been performed separately for each investigated site. For every site, the complete population of fault-striae pairs is subjected to this procedure. Where possible, the chronology of paleostress states has been estimated directly based on relationships of different fault-slip data observable in the field.

4.1 Estimated paleostress tensors

A number of 77 reduced stress tensors have been determined for the area of the Elbe Fault System (EFS; Fig. 27). Many of the investigated sites show heterogeneous fault populations indicated by several different paleostress tensors. According to the principles of SVS, each separated homogeneous subset is related to the associated reduced stress tensor by relatively low misfit angles and high shear-to-normal-stress ratios. In some cases, the stress ratio R covers a certain range instead of being a discrete number which is due to a limited number or restricted orientations of the fault-slip data that thus imprecisely constrain the value of R. Most of the investigated outcrops reveal fault-slip data that correspond to "Andersonian" stress states, i.e. stress states with sub-vertical and sub-horizontal principal axes. In some cases, such a typical orientation of stress axes is already the result of a back-tilting of the associated fault-slip data performed before the inversion of the related stress state.

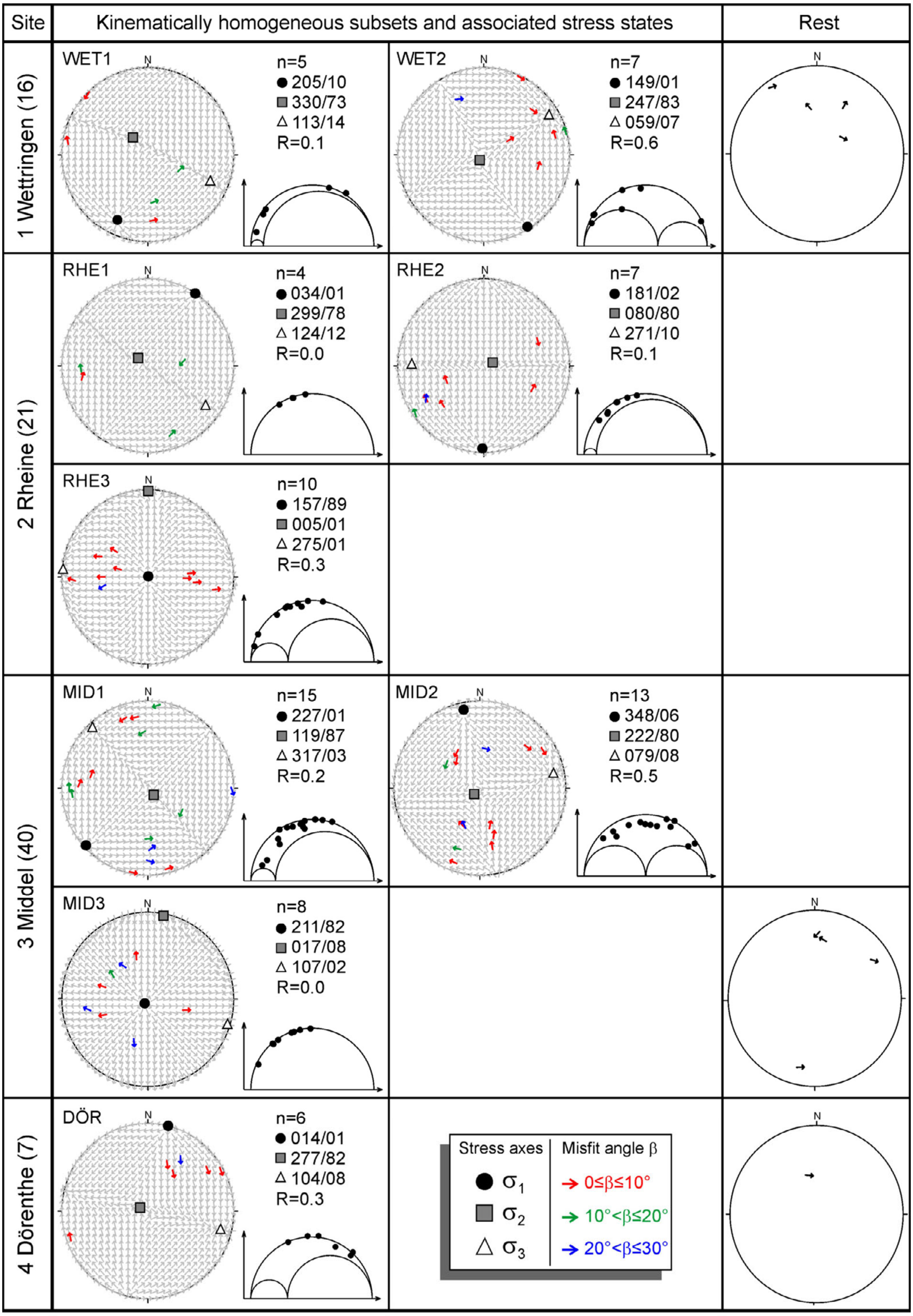

Figure 27: (continued next page)

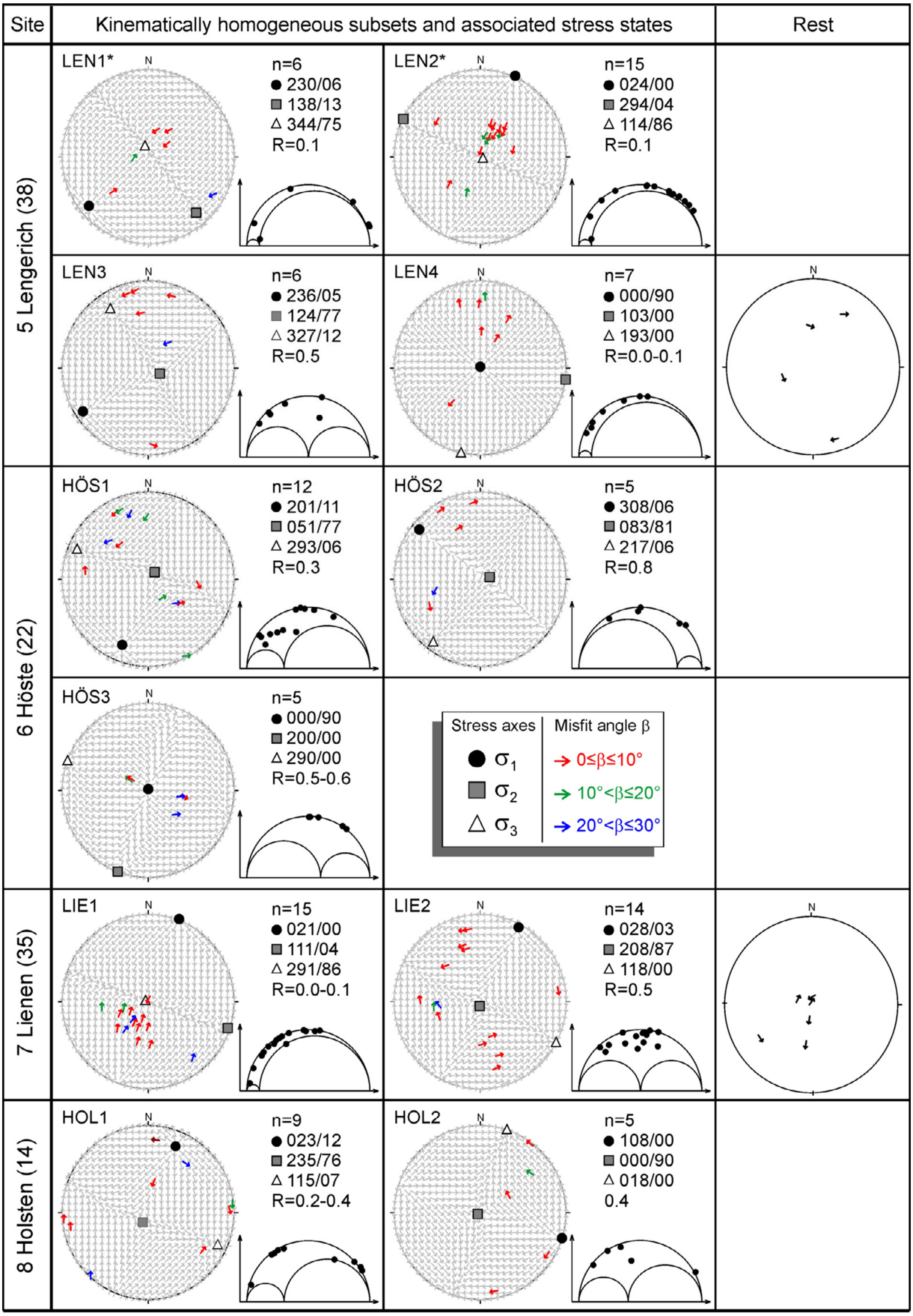

Figure 27: (continued next page)

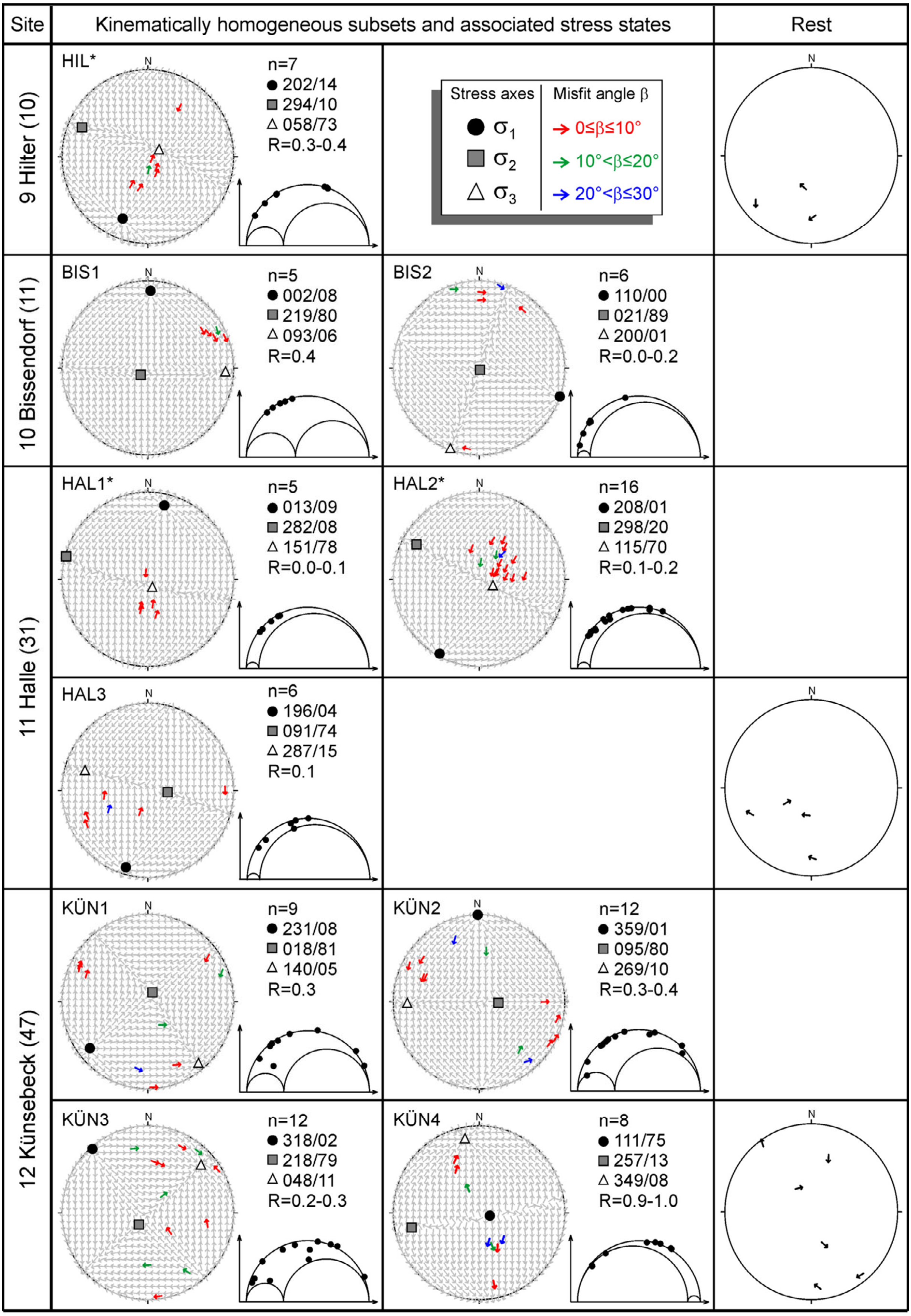

Figure 27: (continued next page)

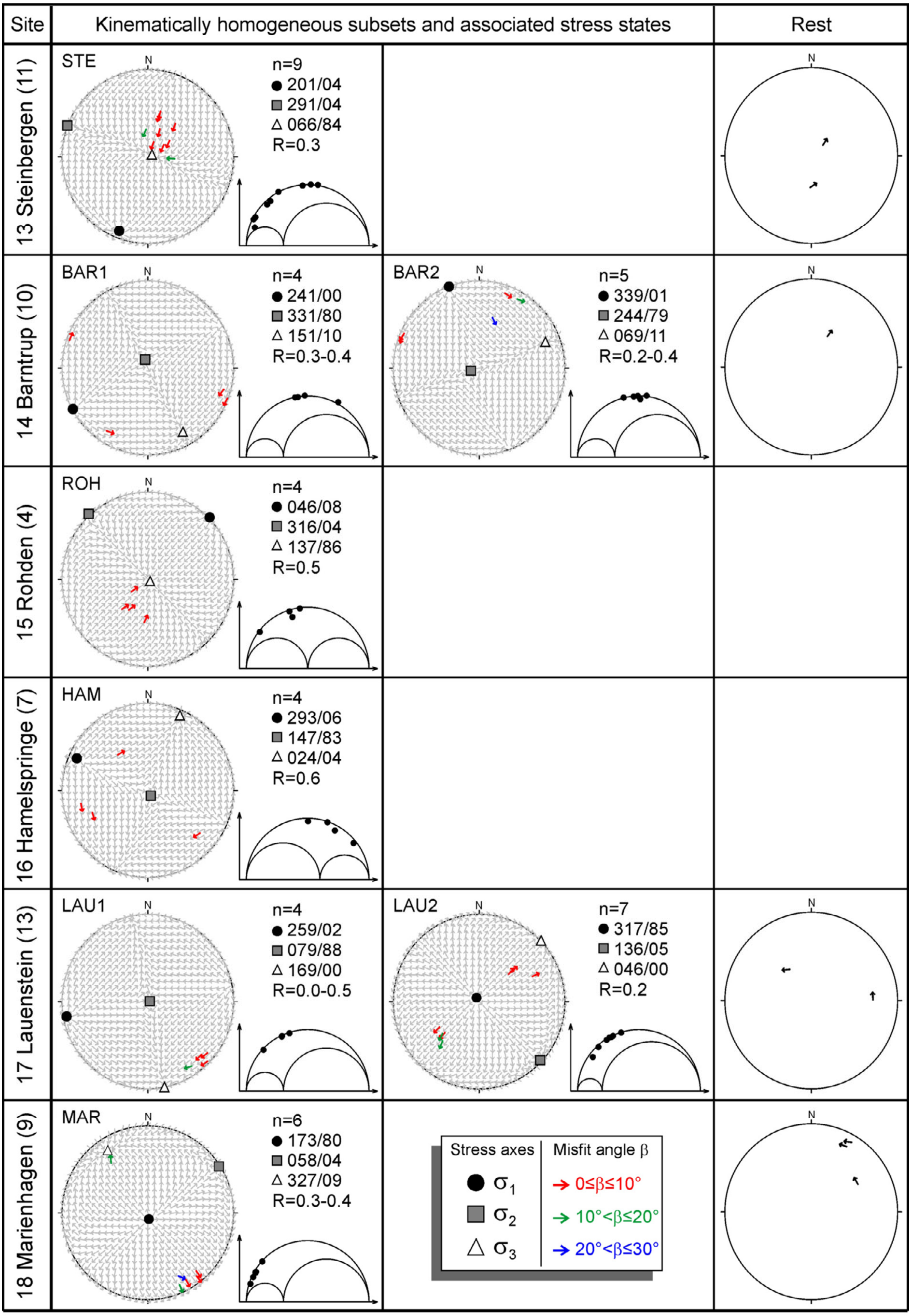

Figure 27: (continued next page)

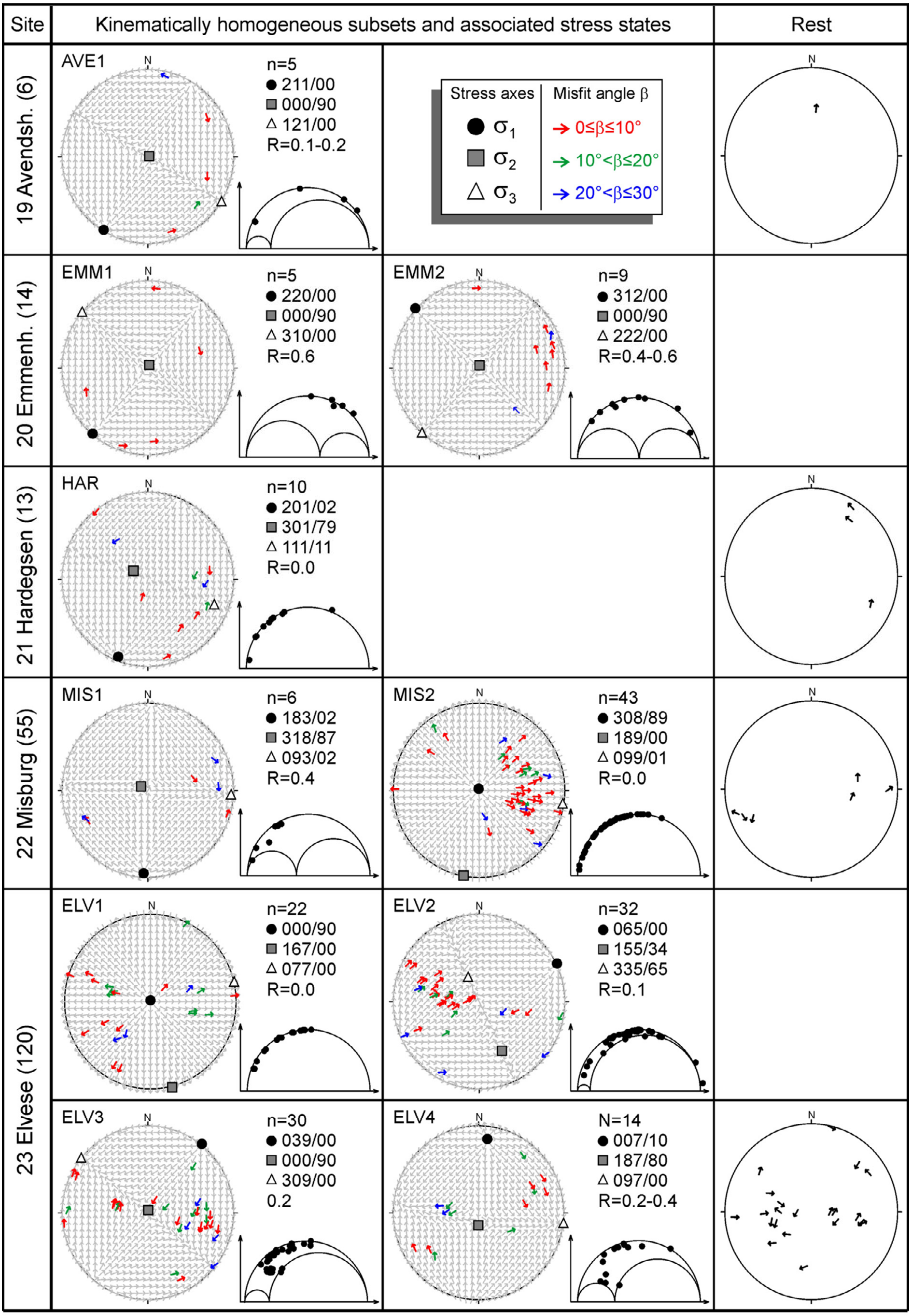

Figure 27: (continued next page)

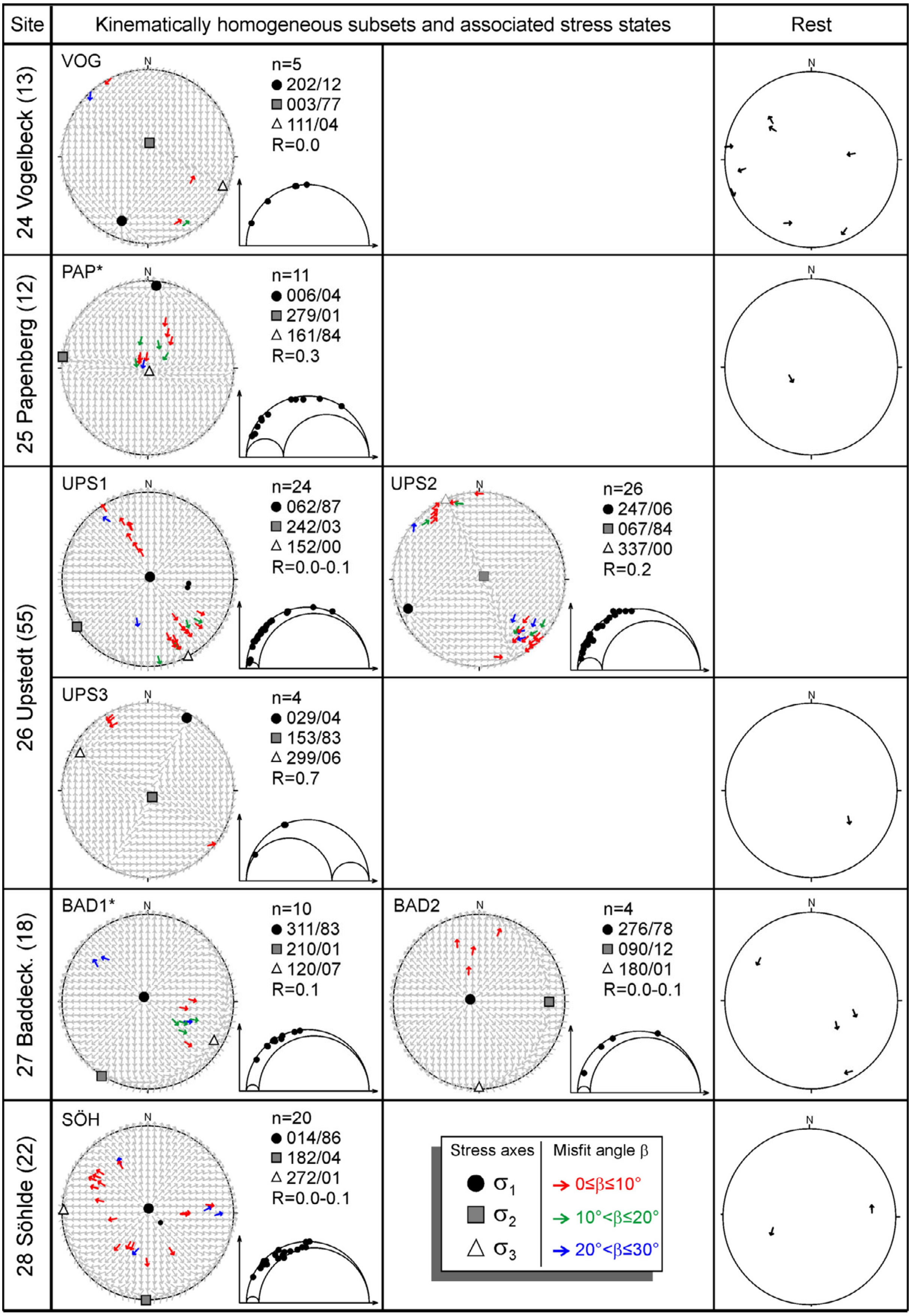

Figure 27: (continued next page)

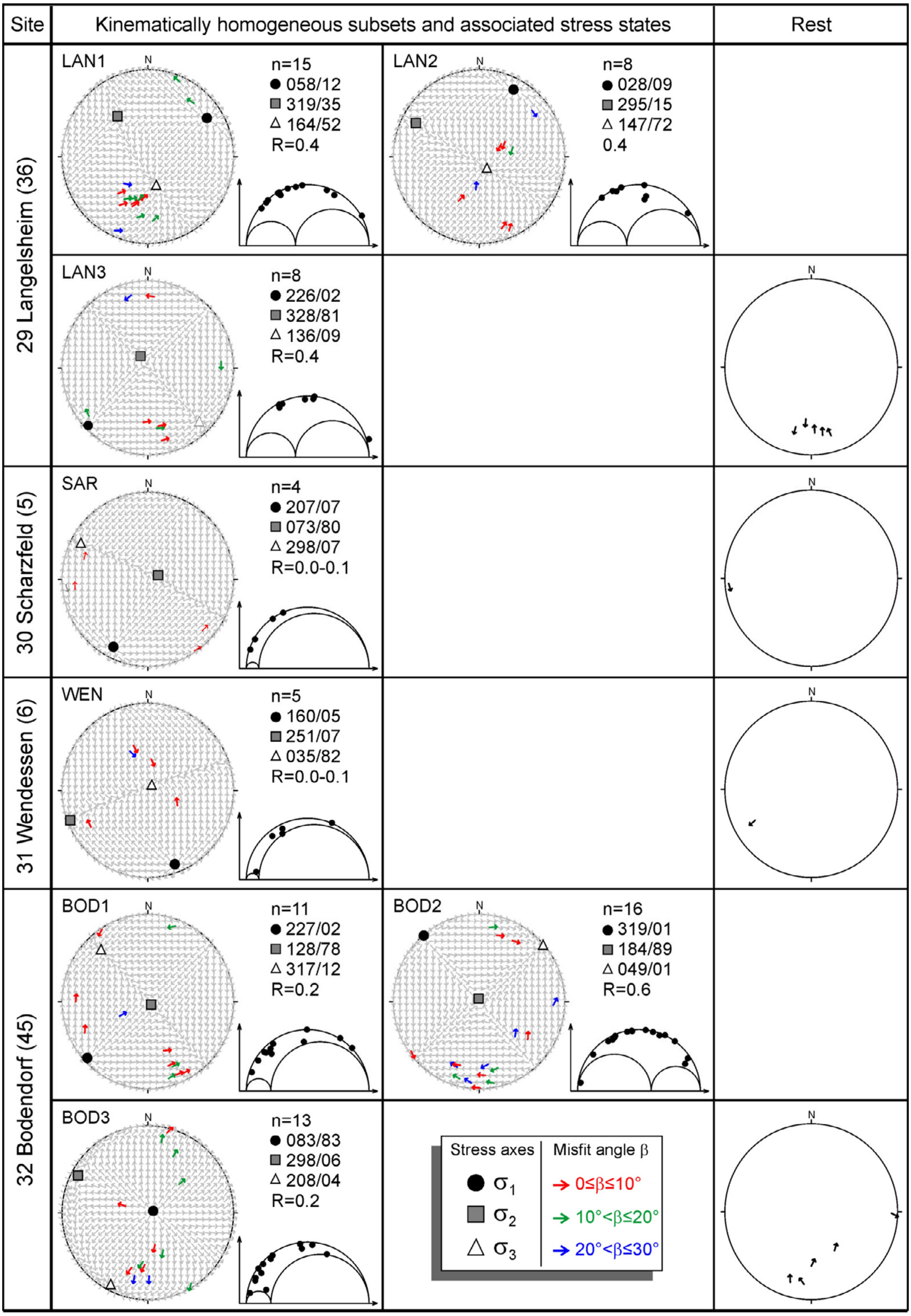

Figure 27: (continued next page)

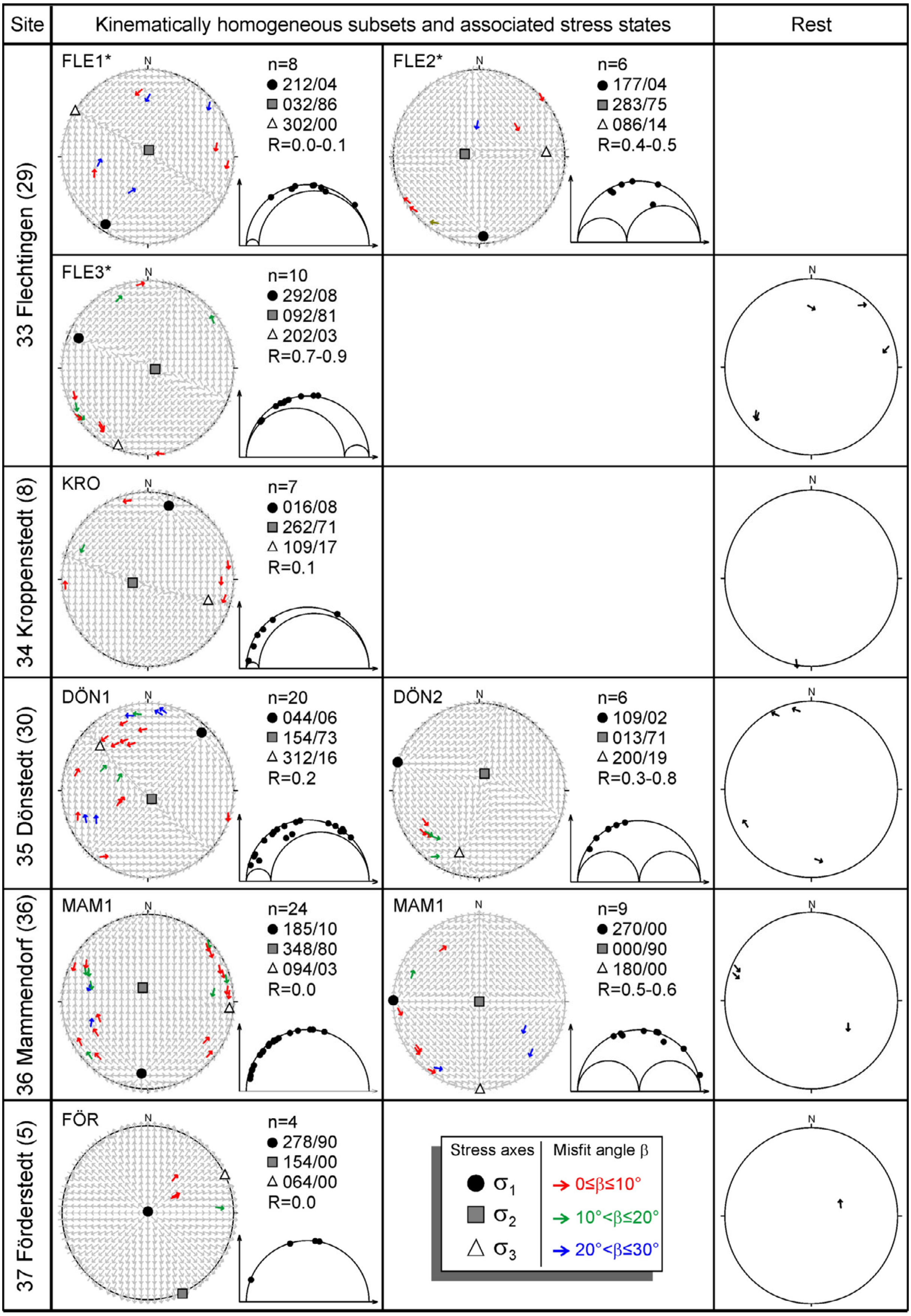

Figure 27: (continued next page)

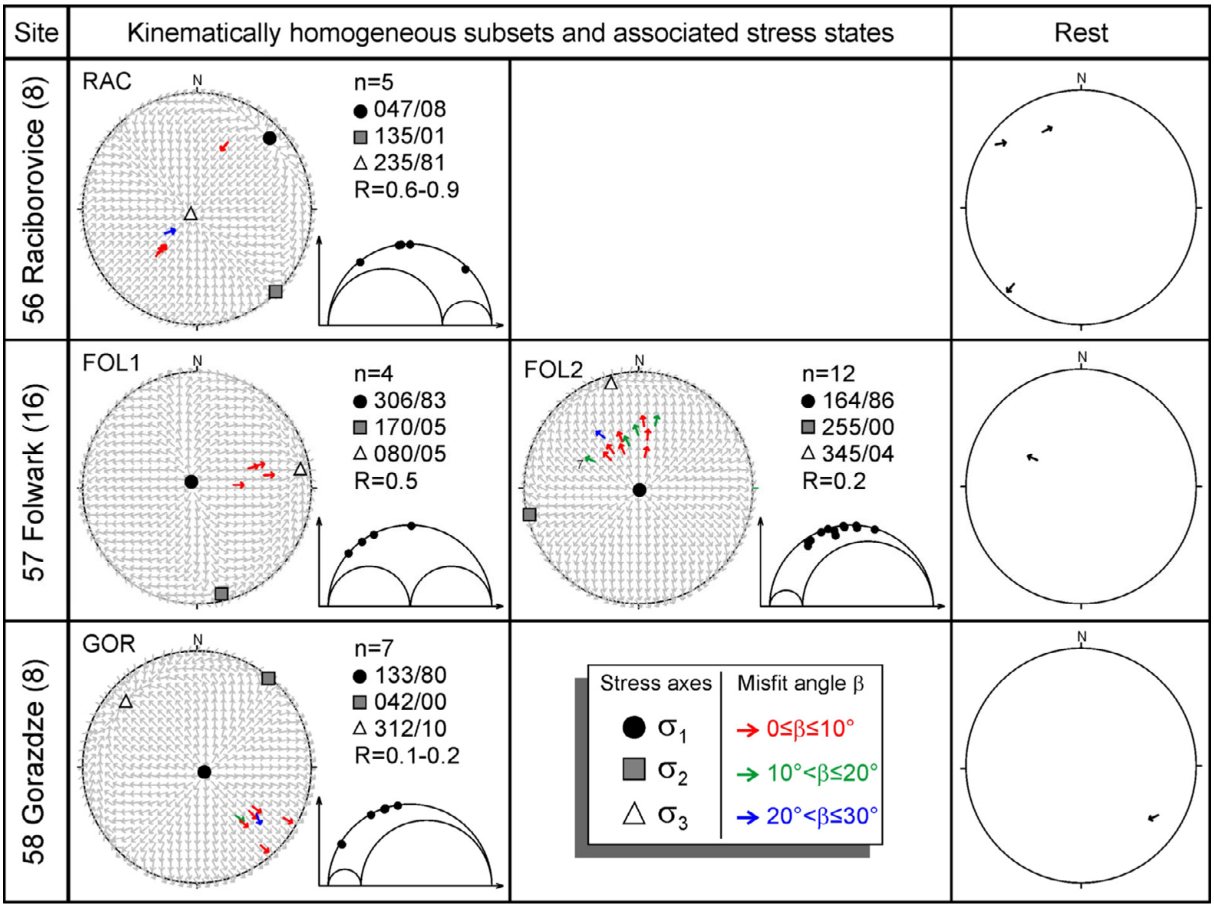

Figure 27: Reduced stress tensors estimated for fault-slip data from the EFS area. Sites are indicated by number, name, and total number of fault-slip data (in brackets). Each row shows the complete number of sampled fault-slip data from a specific site. The data are plotted as assigned to a specific reduced stress tensor or rejected as outliers ("Rest"). Each reduced stress tensor is presented by a lower-hemisphere equal-area projection which includes the corresponding measured fault-slip data (thick arrows) and the calculated theoretical slip directions (thin grey arrows). The measured fault-slip data are colour-coded according to the associated misfit angles (β) which are the primary criterion for the fit between a group of faults and a stress tensor. The respective Mohr-circles diagram illustrates the shear-to-normal-stress ratios for a group of fault-slip data under the specific stress tensor. Datasets marked by an asterisk indicate that the fault-slip data have been tilted back prior to the stress inversion.

4.2 Analysis of chronological indicators

Before the reconstructed stress states can be correlated with any temporal stages in the evolution of the CEBS, some case studies are presented documenting phenomena that appear locally but help deciphering the regional chronology of stress states. These examples illustrate, for instance, relations between folding and faulting, relations of stress states to large-scale deformation structures or the occurrence of oblique stress states.
In the following, estimated paleostress states are presented according to *Step 5* in chapter 2.2.1: For Andersonian stress states, sub-vertical principal stress axes are projected to the vertical and sub-horizontal axes to the horizontal (Fig. 12e). Oblique stress states with none of the principal axes being sub-vertical, on the other hand, are presented by lower hemisphere, equal-area projections.

4.2.1 Faulting vs. folding

At many sites, the signs of brittle deformation do not only include striated faults but also indications for a folding or tilting of the rock mass. For the sedimentary rocks of the Lower Saxony Basin, the Hessian Depression and the Subhercynian Basin, a general trend is observable from gentle and open folds below outcrop scale in the central parts of the basins to a large-scale tilting of the strata close to the Osning Lineament and the Northern-Harz-Boundary Fault (bedding planes listed in Appendix A).
As illustrated for *Halle* quarry (#11), the geometrical relations between bedding planes and fault-slip data may help unravelling a local deformation history (*Case study 2*; Fig. 17). In the following, several other case studies are presented: A direct constraint on the timing of folding is provided at *Künsebeck* quarry (#12), where synsedimentary structures document a Cenomanian to Turonian age of the monoclinal tilting (*Case study 3*, below). For this site, the direction of maximum compression inferred from the tilted bedding planes is shown to correlate with the direction of σ_1 derived from a subset of fault-slip data. At *Lengerich* quarry (#5), two stress states are shown to predate a final phase of tilting, while two other stress states demonstrably postdate the tilting (*Case study 4*). The bedding planes measured at Papenberg (#25) indicate two phases of folding and tilting with different rotation axes, respectively (*Case study 5*). Finally, *Case study 6* shall document that in the case of the volcanic rocks from *Flechtingen* (#33), the lack of bedding planes is compensated by mineral veins that alternatively serve as a suitable indicator and reference for the rotation of the rock mass.

Case study 3: Künsebeck quarry (#12)
At *Künsebeck* quarry, which is located close to the Osning Lineament, an angular unconformity cuts the Cenomanian to Turonian limestones and separates them into a lower, more steeply inclined part from an upper, almost flat-lying part (Fig. 28). The shape of this unconformity, in turn, can be interpreted as a result of gravitational slumping which has been induced by tilting during times when the strata had been incompletely consolidated. Both facts argue for a tilting of the strata that had already begun during deposition of the sedimentary sequence. On the contrary, the faults observed at this place clearly have formed as discrete planes within an already consolidated pile of rocks (Fig. 28c). Obviously, faulting postdated folding at *Künsebeck* quarry.
From the attitudes of bedding planes, it is possible to infer an approximate direction of maximum horizontal compression that potentially caused the observed tilting of strata (Fig. 28b). The inferred NE–SW-directed compression corresponds well with the NE–SW-directed σ_1-axis derived from the strike-slip faults that have been separated as *kün1* and related to the paleostress state KÜN1 (Fig. 28e). This correlation in terms of directions of maximum horizontal compression argues for a close relationship between the phase of tilting and the derived stress state KÜN1. Assuming a reverse stress state with a NE–SW-directed σ_1-axis to be responsible for the tilting, the transition towards KÜN1 would only require a permutation between the σ_2- and the σ_3-axis. Consequently, it is probable that the time of activity of KÜN1 directly followed the process of folding while the other stress states estimated at *Künsebeck* (KÜN2, KÜN3, KÜN4) postdated KÜN1.

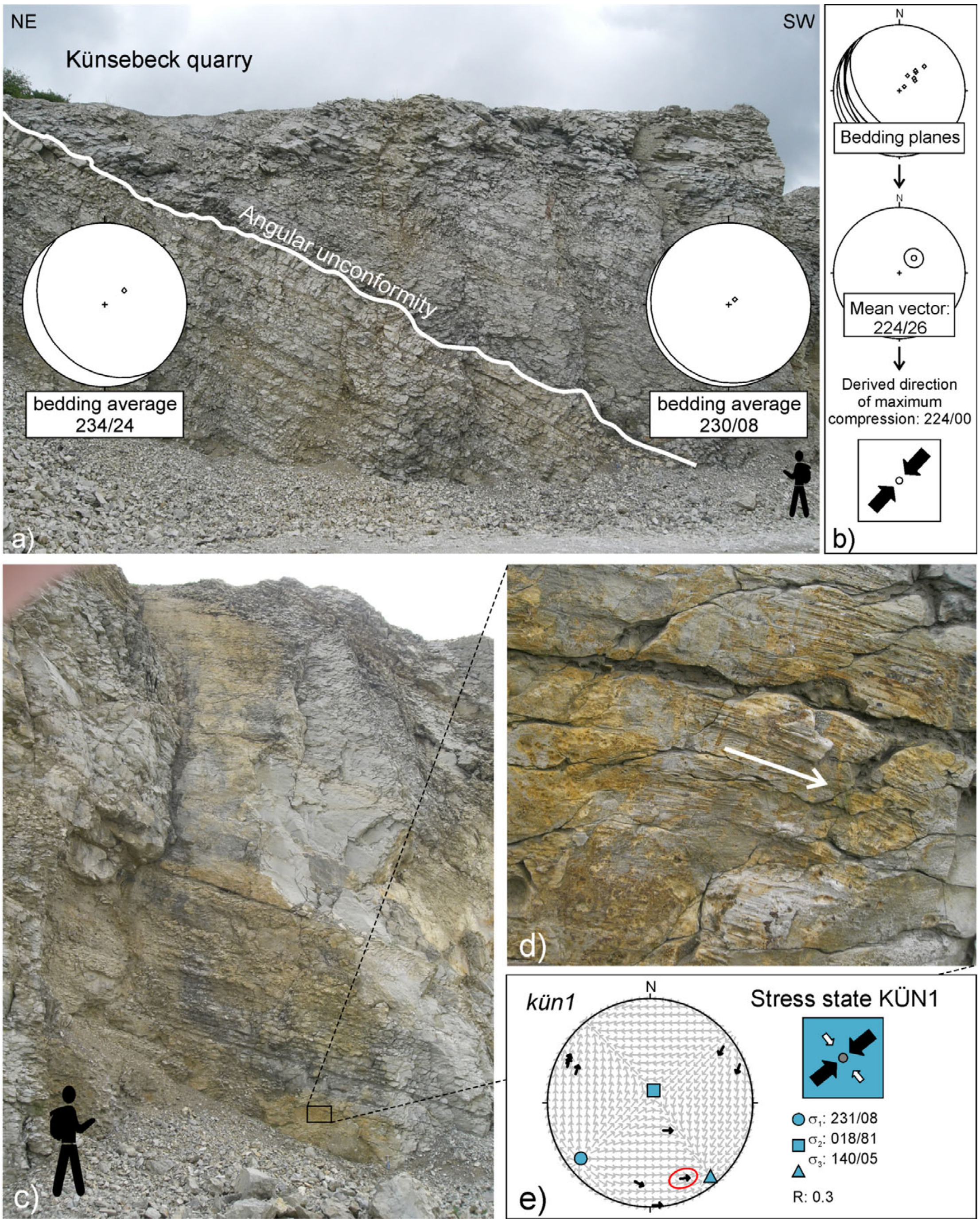

Figure 28: Analysis of structures within Cenomanian limestones exposed at *Künsebeck* (#12). a) Angular unconformity. The mean attitudes of bedding planes are plotted as great circles and poles to planes separately for parts above and parts below the unconformity, respectively. The difference in the mean dip angles and the shape of the unconformity, both indicate synsedimentary tilting of the strata; b) The variously dipping bedding planes show a common trend of dips which is represented by the azimuth of their calculated mean vector. The mean dip direction, in turn, is interpreted as the tilting-related direction of maximum horizontal compression; c) Large strike-slip fault that cuts the strata; d) Grooves and calcite fibres indicate a sinistral sense of movement along the fault plane; e) Strike-slip stress state KÜN1 with a NE-SW-directed σ_1 is derived from the subset of fault-slip data *kün1*. The fault-slip datum presented in (c) and (d) is indicated by the red circle. The direction of maximum compression corresponds with the one derived from the tilted bedding planes in (b) implying a close relationship between tilting and this particular phase of strike-slip faulting.

Case study 4: Lengerich quarry (#5)

Lengerich is located close to the Osning Lineament. Like at *Halle* quarry (Chapter 2.3.3), the Cenomanian-Turonian strata show strong deviations from their original horizontal bearings (Fig. 29). The mean strike of bedding planes is estimated as 114/00 (dip direction/dip) indicating a direction of maximum compression trending around 024/00 (assuming a horizontal maximum compression). The plunges of bedding planes, however, vary remarkably (between 35° and 81°) which reflects the presence of folds with amplitudes of several metres superimposing the large-scale tilting of the whole exposed sequence (Fig. 29).

Given the present orientation of fault-slip data, the kinematic PBT-axes of the separated subsets *len1* and *len2* suggest non-Andersonian stress states as indicated by P- and T- axes, respectively, that deviate far from a vertical or horizontal orientation (Fig. 30c). By rotating these subsets (i) around an axis inferred from the mean strike of bedding planes (114/00) and (ii) through 46° respectively 37° as indicated by the plunges of P-axes of *len1* and *len2*, respectively, Andersonian configurations are realised (Fig. 30d). This proceeding demonstrates that the orientation of PBT-axes can complement bedding planes in serving as a reference frame for the back-tilting of fault-slip data.

By performing a stress inversion via simulation for the back-tilted and non-rotated subsets, the stress states LEN1, LEN2, LEN3, and LEN4 are estimated (Fig. 30e). The different angles used for the back-tilting of *len1* respectively *len2* suggest that LEN1 has been active before LEN2. As the subsets *len3* and *len4* do not show evidence for having been affected by tilting after faulting (due to sub-vertical and sub-horizontal P-, B-, and T-axes; Fig. 30c), the associated stress states LEN3 and LEN4 are assumed to postdate the phase of tilting of the strata (Fig. 30f). Furthermore, two superimposed generations of striae on the same fault plane document that LEN3 predated LEN4 (Fig. 30a).

Figure 29: Upper Cretaceous limestones exposed in the Osning Lineament area (*Lengerich*, #5). As indicated by the great circles and poles to planes in the stereographic projection, the bedding planes show different dip angles varying between 35° and 81° while the very consistent strike directions indicate a common direction for tilting and folding.

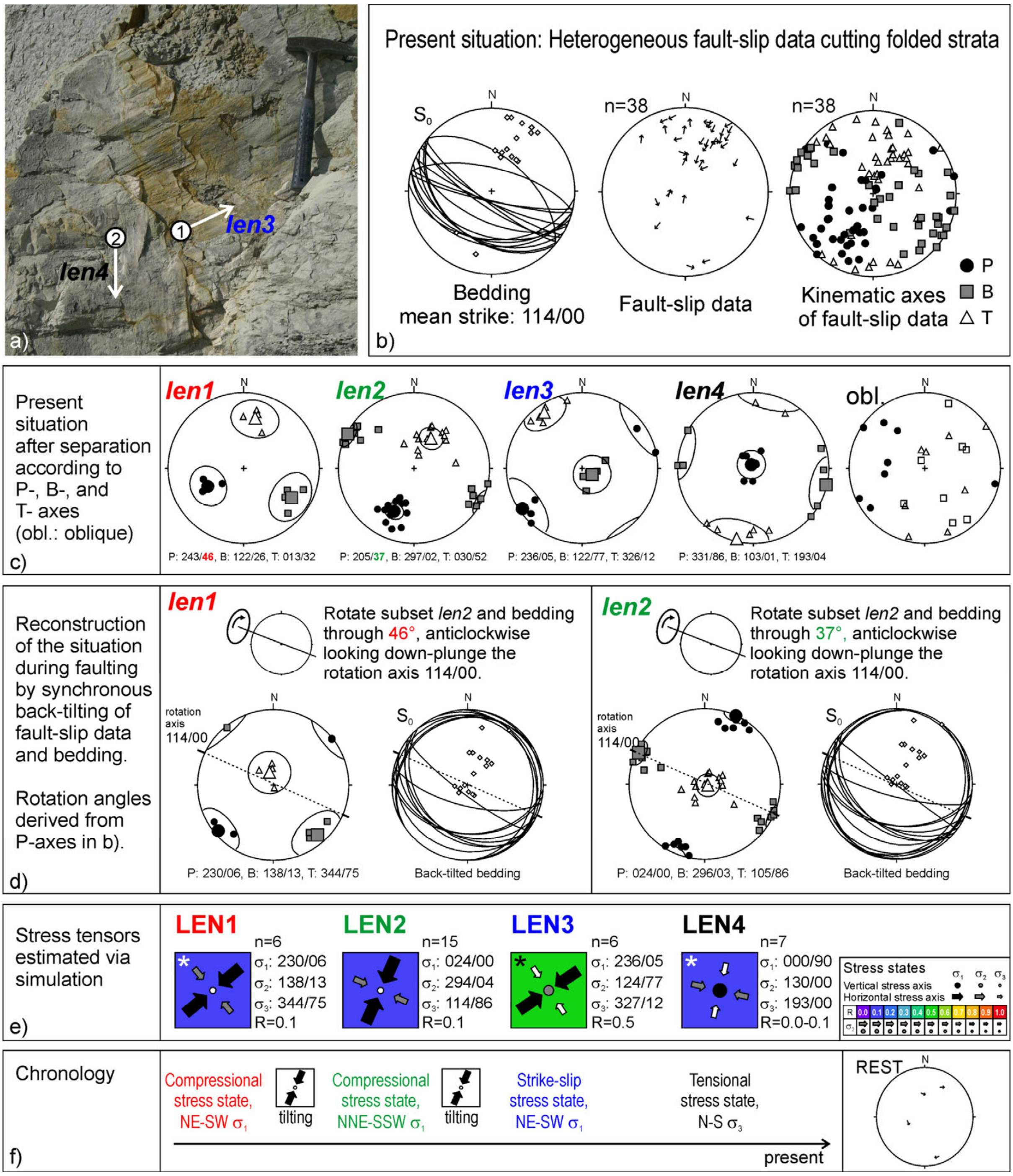

Figure 30: Separation and stress inversion for the fault-slip data from *Lengerich* (#5; Upper Cretaceous limestone). a) Slickenside with an older generation of calcite fibres indicating dextral slip (1) and a younger generation of calcite fibres documenting normal slip (2); b) Various attitudes of bedding planes and the heterogeneity of fault-slip data reflect a complex deformation history; applied fracture angle for PBT: θ=30°; c) Results of separation according to clusters of P-, B-, and T-axes; d) Back-tilting procedure for the subsets *len1* and *len2*; e) The stress states LEN1, LEN2, LEN3, and LEN4 excellently fit the previously separated subsets *len1*, *len2 len3*, and *len4*, respectively. Stress states that are based on less than 9 fault-slip data are marked by an asterisk. f) Derived chronology of stress states and tilting events.

Case study 5: Papenberg quarry (#25)

Papenberg (#25) is located at the eastern flank of the Leine Graben where rocks of the Mid Triassic *Muschelkalk* sequence crop out (Fig. 5). According to dip directions, two subsets of bedding planes can be distinguished. On the outcrop scale, the exposed strata dip uniformly towards the east indicating a N-S-trending axis of tilting (Subset A; Fig. 31a). On the other hand, parts of the outcrop reveal folds with amplitudes of only a few metres and a common strike of bedding which indicates a fold axis striking around east (Subset B; Fig. 31b).

A fault-slip analysis is enabled by the presence of reverse faults with calcite slickenfibres in all parts of the quarry. Most of the fault-slip data constitute a kinematically homogeneous set with N-trending P-axes and sub-vertical T-axes (Fig. 31c). However, considering the precise plunges of B- and T-axes, it is obvious that they deviate from the horizontal and vertical, respectively, by about 20°. This fits well with the general dip of bedding planes which are inclined to the east by about 20° (Fig. 31a). In addition, both measured and constructed fold axes associated to subset B of bedding planes show similarly directed inclinations of c. 20°. These observations argue for a late tilting process that obviously had affected all the described structural elements.

According to the described findings, all elements are back-tilted using a rotation axis and a respective rotation angle both derived from subset A of bedding planes (i.e. a rotation axis oriented 185/00 and an angle of 20°; Fig. 31d). After the back-tilting procedure, the average dip of bedding planes of subset A as well as the fold axes associated to subset B are horizontal. Furthermore, the B- and T-axes of subset *pap* are sub-horizontal and sub-vertical, respectively, thus reflecting a typical Andersonian configuration.

These findings support the following succession of events: After sedimentation and consolidation of the *Muschelkalk* sequence in Mid Triassic times, the strata have been folded under a N-S directed compressional stress regime as indicated by the roughly E-W-trending fold axes. At probably the same time, reverse faults were activated which document the presence of a compressional stress state (vertical σ_3) characterised by a NNE-SSW-directed maximum compression (σ_1) and a low stress ratio (R=0.3). The youngest signs of deformation documented by the structural inventory at *Papenberg* correspond to a tilting of the strata around a N-S-trending axis.

Some rather speculative considerations regard the large N-S trending discontinuities found at Papenberg ('fractures'; Fig. 31a). Since these fractures are offset along bedding-parallel slip surfaces probably activated by the proposed tilting, it can be assumed that they had been included in the tilting process. There are no direct kinematic indicators that would identify these surfaces as faults. However, contrary to their present, strongly inclined bearings, their back-tilted sub-vertical orientations may indicate that these planes originally had been formed as strike-slip faults. This interpretation is remarkable, as these faults strike N-S which is parallel to the presumed master faults flanking the Leine Graben – a "graben" system of which the main kinematics is not well constrained up to date.

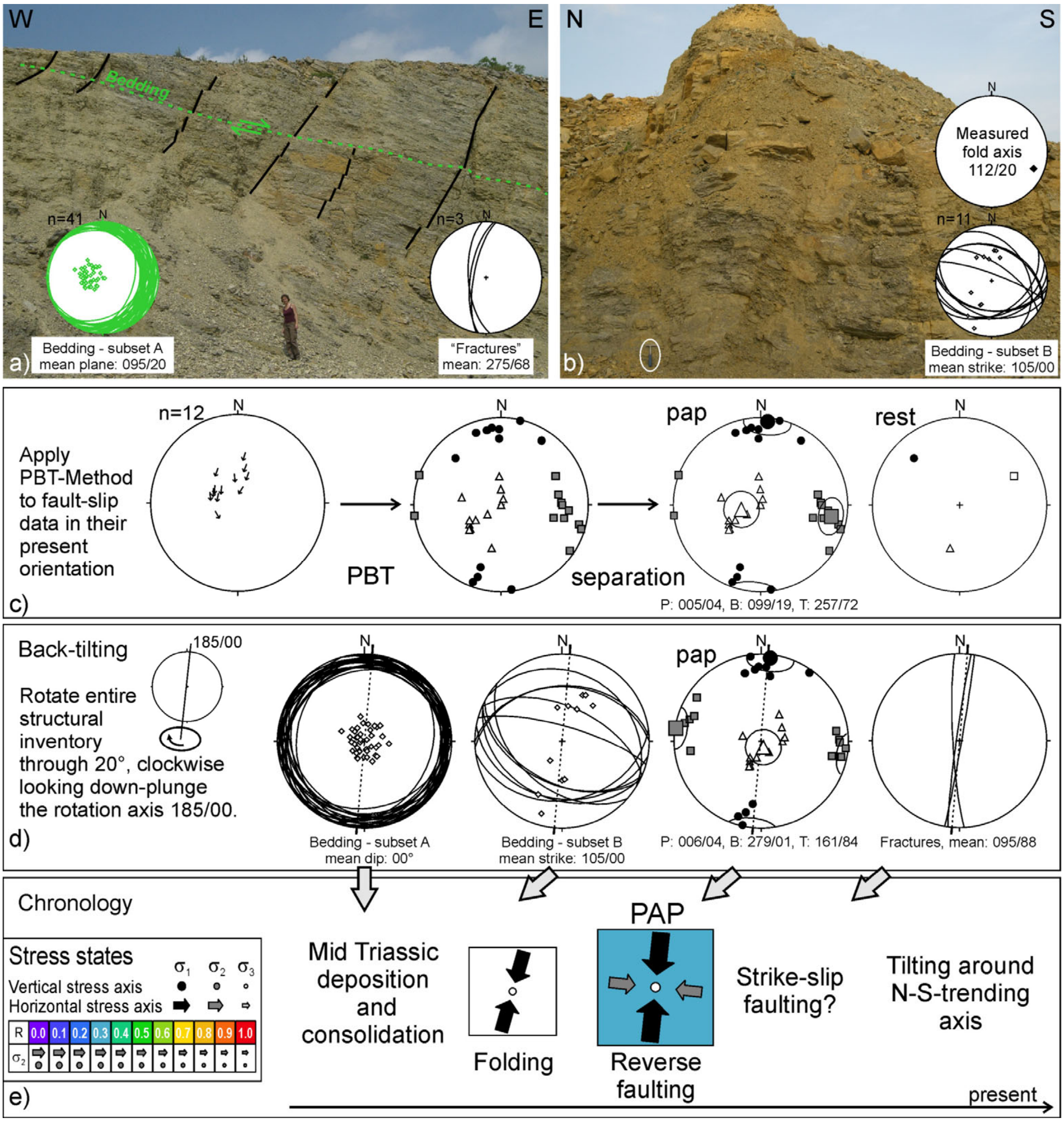

Figure 31: Analysis of structural data from *Papenberg* (#25; Mid Triassic limestone). a) The *Muschelkalk* strata show a general dip towards the east (subset A of bedding planes). Large fractures with unknown mode of deformation are offset by bedding-parallel slips. b) In parts of the outcrop, the strata are more closely folded around ESE-trending fold axes (subset B of bedding planes; hammer for scale). c) *Left*: Tangent-lineation plot of the sampled fault-slip data; *middle*: cumulative plot of P-, B-, and T-axes for the whole data set (applied fracture angle θ=30°); *right*: Results of separation according to clusters of P-, B-, and T-axes. d) Results of the back-tilting procedure applied to the subsets A and B of bedding planes, to the subset *pap* of fault-slip data, and to the large fractures. f) Deformation model including the compressional paleostress state PAP derived from the subset *pap*.

Case study 6: Flechtingen quarry (#33)

At *Flechtingen* (#33), the kinematic (PBT-) axes of the separated subsets *fle1* and *fle3* deviate from Andersonian configurations which typically would comprise horizontal and vertical clusters of axes (Fig. 32d). The given configurations argue for a tilting of the structural inventory which occurred subsequent to faulting. However, an unambiguous indicator for tilting such as elsewhere provided by tilted bedding planes is missing in the volcanics at *Flechtingen*.

According to *Case study 4* which has demonstrated that PBT-axes may provide suitable parameters for a back-tilting of fault-slip data, the subsets from *Flechtingen* are analysed regarding orientations of PBT-axes. *fle1* shows a sub-horizontal mean P-axis, while B and T seem to be affected by rotation. *fle2* shows a sub-horizontal mean T-axis, while B and P seem to be rotated. Comparing *fle1* and *fle3*, it becomes obvious that the mean vectors of sub-horizontal axes are almost parallel, thus indicating a uniform rotation axis oriented 208/00 (Fig. 32e). The angular range for the supposed back-tilting (29°), in turn, can be derived from the plunge of the mean P-axis of the larger subset which is *fle3*. A back-tilting performed with these parameters (around 208/00, through 29°) results in sub-horizontal respective sub-vertical mean vectors for the kinematic axes of *fle3*. Interestingly, the same procedure applied to *fle1* and *fle2* also produces sub-horizontal respectively sub-vertical kinematic axes, thus confirming the parameters of the supposed rotation. Another positive argument for the selected procedure is provided by the bearings of calcite-filled veins sampled in the outcrop (Fig. 32c): Assuming the veins to have formed in a vertical position (as pure tensile structures), the back-tilting of the presently inclined veins reproduces their presumed original orientations.

After having reconstructed the original settings, the analysis of each subset of fault-slip data results in the stress states FLE1, FLE2, and FLE3, respectively (Fig. 32f). As there are no further chronological indicators observed in the outcrop, the relative timing of these stress states is derived from the findings at other locations (see below). The present orientations of fault-slip data and veins must be regarded as the result of a phase of block rotation around a NNE-striking axis that postdated the activity of the three estimated strike-slip stress states (Fig. 32g).

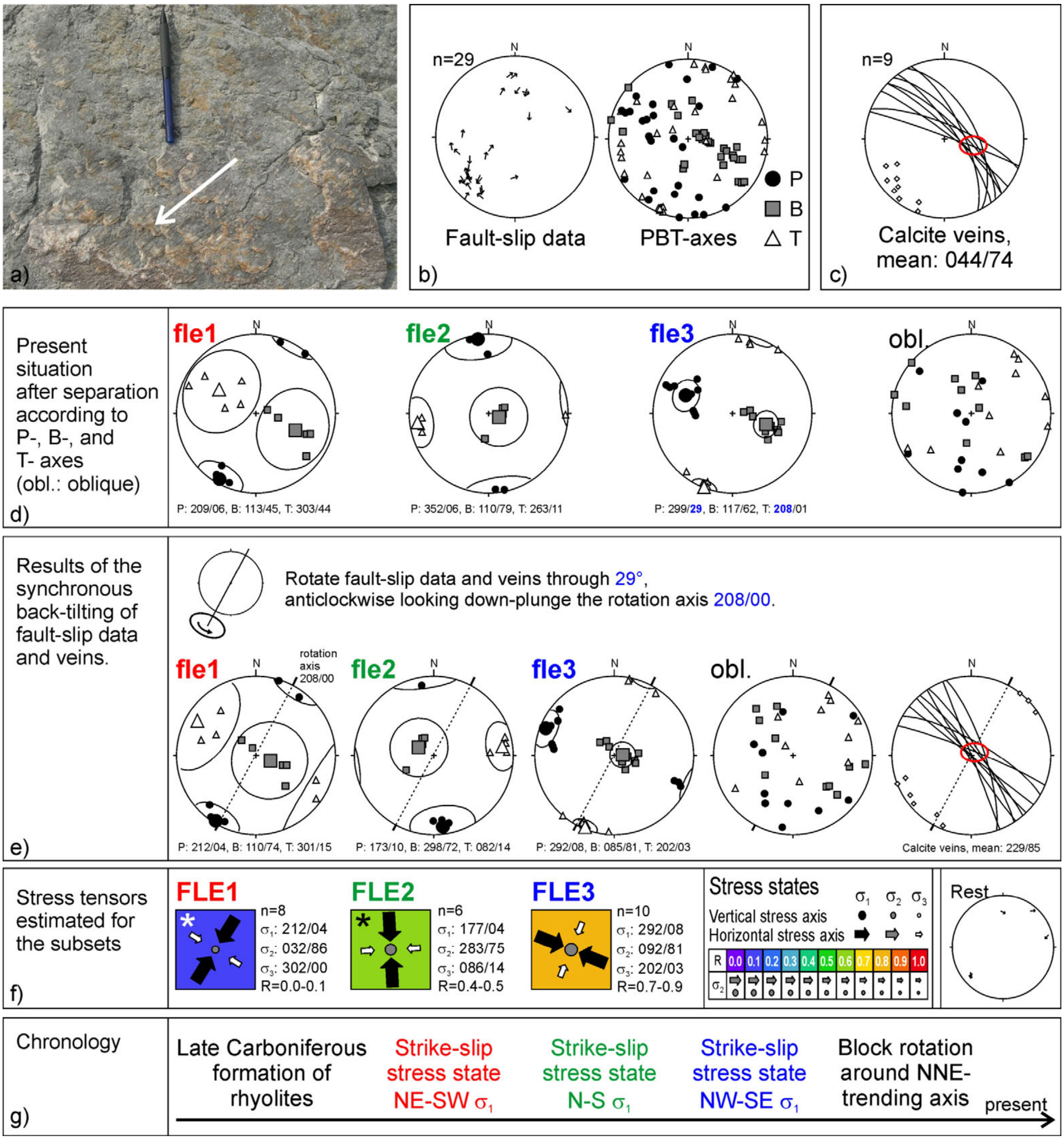

Figure 32: Interpretation of brittle structures from *Flechtingen* (#33; Upper Carboniferous rhyolite); a) Slickenside with calcite fibres indicating oblique-normal slip (arrow points the slip direction of the missing hanging-wall block). b) Sampled fault-slip data in a tangent-lineation plot (*left*) and results of PBT (*right*; applied fracture angle θ=30°). c) Orientations of calcite-filled veins plotted as great circles and corresponding poles in the lower hemisphere. d) Result of separation according to clusters of P-, B-, and T-axes. e) Back-tilting of the whole structural inventory according to rotation parameters derived from the present-day orientation of PBT-axes of subset *fle3*. f) Best-fitting stress states estimated for the back-tilted subsets in (e) and remnant fault-slip data (Rest). Stress states based on less than 9 fault-slip data are marked by an asterisk. g) Derived chronology of stress states and deformation.

4.2.2 Stress states vs. large-scale structures - the Osning Lineament area

Nine of the investigated outcrops are scattered around the Osning Lineament for which an array of WNW-ESE-striking, Upper Cretaceous thrust faults has been mapped mainly based on seismic data (Baldschuhn et al., 1996; Fig. 33). At each of these sites, at least one compressional or strike-slip stress state shows a roughly NNE-SSW-striking σ_1-axis which is almost perpendicular to the large-scale thrust faults of the area. However, at some of the sites, normal faults document extensional tectonics to have also affected the area. The extension-related directions of minimum compression show two opposing horizontal trends: N-S- and WNW-ESE-oriented σ_3-axes, respectively. As inferred from chronological indicators observed in the field, the tensional stress state with a N-S-directed σ_3-axis found at *Lengerich* quarry (#5) has postdated the compressional and strike-slip stress states with a NE-SW-directed σ_1 (Fig. 30).

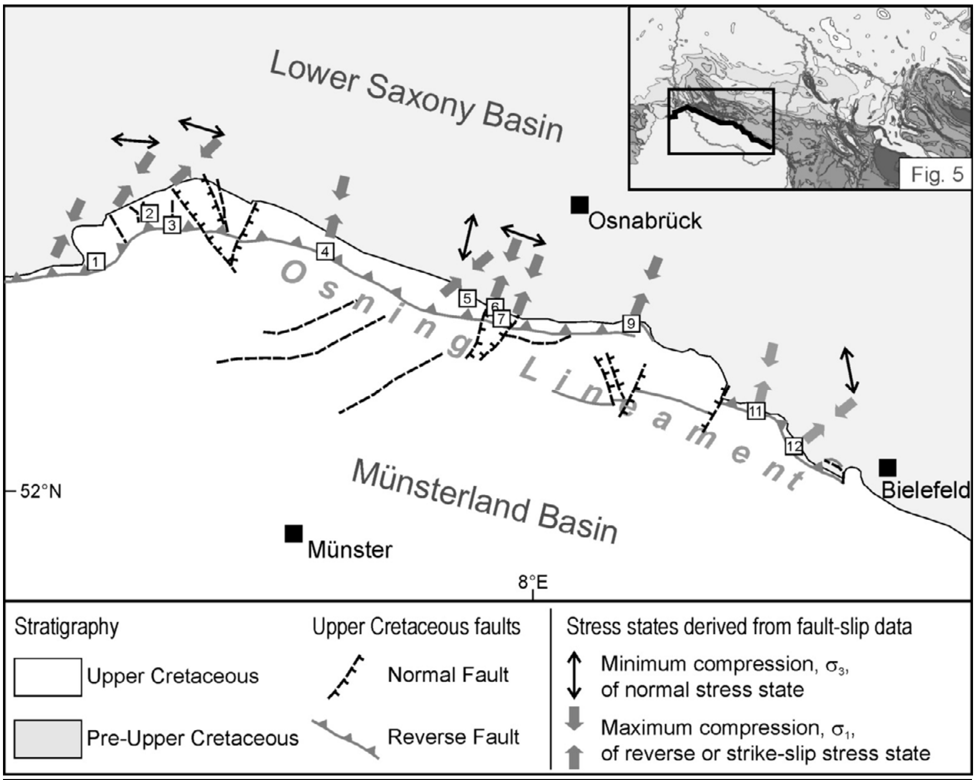

Figure 33: Correlation of large-scale structures and stress states inferred from fault-slip data. The simplified geological subcrop map of the base of Cenozoic units reveals the largest recorded reverse and normal faults of Late Cretaceous ages (modified after Baldschuhn & Kockel, 1996). Normal faults locally offset reverse faults, thus documenting that normal faulting postdated reverse faulting. Nine outcrops are located close to the Osning Lineament. Estimated compressional and strike-slip stress states are simplified to the directions of maximum compression (σ_1; grey arrows), whereas tensional stress states are shown by the directions of minimum compression (σ_3; black arrows). σ_1-directions related to compressional and strike-slip stress states strike almost perpendicular to the large reverse faults that mark the Osning Lineament. Some of the normal stress states show σ_3-directions which are perpendicular to large normal faults that locally offset large reverse faults.

Unfortunately, at other sites considered here, information on the relative timing of tensional stress states is not available. However, the strike directions of several large-scale normal faults (NNE to NNW; Fig. 33) locally correlate with the roughly WNW-ESE-directed σ_3 indicated by some tensional stress states obtained from measured fault-slip data. Since it is known that the normal faults based on seismic data locally offset WNW-striking reverse faults, it can be concluded that the normal faulting observed in outcrops also postdated reverse and strike-slip faulting. Hence, the tensional stress states estimated for *Rheine* (#2), *Middel* (#3), and *Höste* (#6), are supposed to be younger than the compressional and strike-slip stress states found at these sites.

4.2.3 Oblique stress states

At two sites along the southern margin of the CEBS, the measured fault-slip data document the activity of oblique paleostress states (#23, #29). These stress states are unique in the sense that they do not show a vertical stress axis as would typically be expected for the shallowest parts of the Earth's crust (Anderson, 1942).

Case study 8: Elvese quarry (#23)

The Mid Triassic (*Muschelkalk*) sequence exposed at *Elvese* (#23) is intensively deformed as indicated by both folds and a number of 120 sampled fault-slip data (Fig. 34).

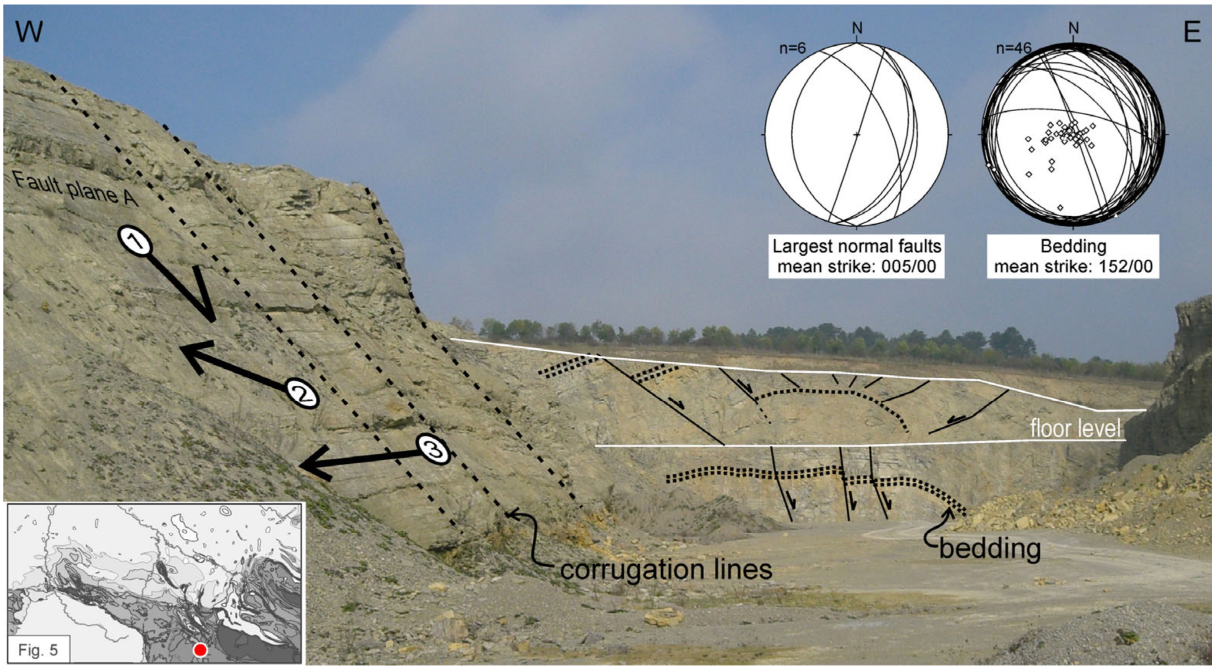

Figure 34: Mid Triassic (*Muschelkalk*) sequence of limestones exposed at *Elvese* (#23). The largest normal faults strike roughly N-S (*left stereogram*). The eastward dipping fault plane A documents various signs of (re)activation (numbered arrows, left). Corrugation lines on this plane (dashed) indicate that the plane has been formed as a dip-slip fault. The strata are folded as shown by the great circles and poles to planes (*right stereogram*). Given the geometry of faults and folds, the profile in the background might be interpreted as a "flower structure". Despite the apparently prevailing normal offsets within this structure ("phaeno-normal faults"), the sampled fault-slip data argue for a phase of transpression which postdated normal faulting.

Based on the results of PBT, four kinematically homogeneous subsets have been separated from the heterogeneous fault population (Fig. 35c). Accordingly, the Stress Inversion Via Simulation (Fig. 35d) yields four stress states the modes of which are tensional (ELV1), oblique (ELV2), and strike-slip (ELV3, ELV4), respectively (Fig. 35e). The tensional stress state ELV1 corresponds to radial extension as the stress ratio is R=0.0. The oblique stress state ELV2 is characterised by a horizontal, ENE-WSW-striking σ_1-axis, whereas ELV3 and ELV4 show σ_1-directions striking NE-SW and NNE-SSW, respectively. The directions of σ_2 and σ_3 of the oblique stress state ELV2 deviate by c. 35° from a vertical respectively a horizontal orientation. In this case, the obliquity of stress axes does not correspond with the attitudes of measured bedding planes since any back-tilting of the respective fault-slip data (*elv2*) around the mean strike of bedding planes would not transfer this subset into an Andersonian one. Thus, in this case, the obliquity of principal axes actually seems to attest to the action of an untypical stress state.

One key for understanding the role of different stress states at *Elvese* is provided by an array of large N-S-striking fault planes (mean strike: 005/00; Fig. 34). Normal movements along these faults are documented by offset and dragged bedding planes, calcite-filled pinnate fractures and calcite fibres on slickensides. Together with a number of smaller variably striking normal faults, these large faults correspond to the normal stress state ELV1. This stress state fits also with the mean NW-SE-directed strike of extensional veins which indicate a NE-SW-directed σ_3. One of the large N-S-striking faults is exposed over a distance of more than 250 m revealing generations of kinematically different superimposed striations that document a multiple reactivation of this surface ('Fault plane A'; Fig. 35a,b; Fig. 34). The morphology of this fault plane argues for the plane to have newly formed under extension (Fig. 34): Assuming the dip slip-oriented corrugations along its surface (i) to result from the linkage of smaller fault segments (Walsh et al., 1999; McLeod et al., 2000; Mansfield & Cartwright, 2001; Marchal et al., 2003) and (ii) to indicate a respective dip slip movement (Hancock & Barka, 1987; Needham et al., 1996; Lohr, 2007), this plane has originally been formed as a normal fault, whereas other shear movements have obviously occurred later. This observation is verified by superimposed striations along several other faults which indicate that oblique and strike-slip faulting postdated normal faulting at *Elvese*.

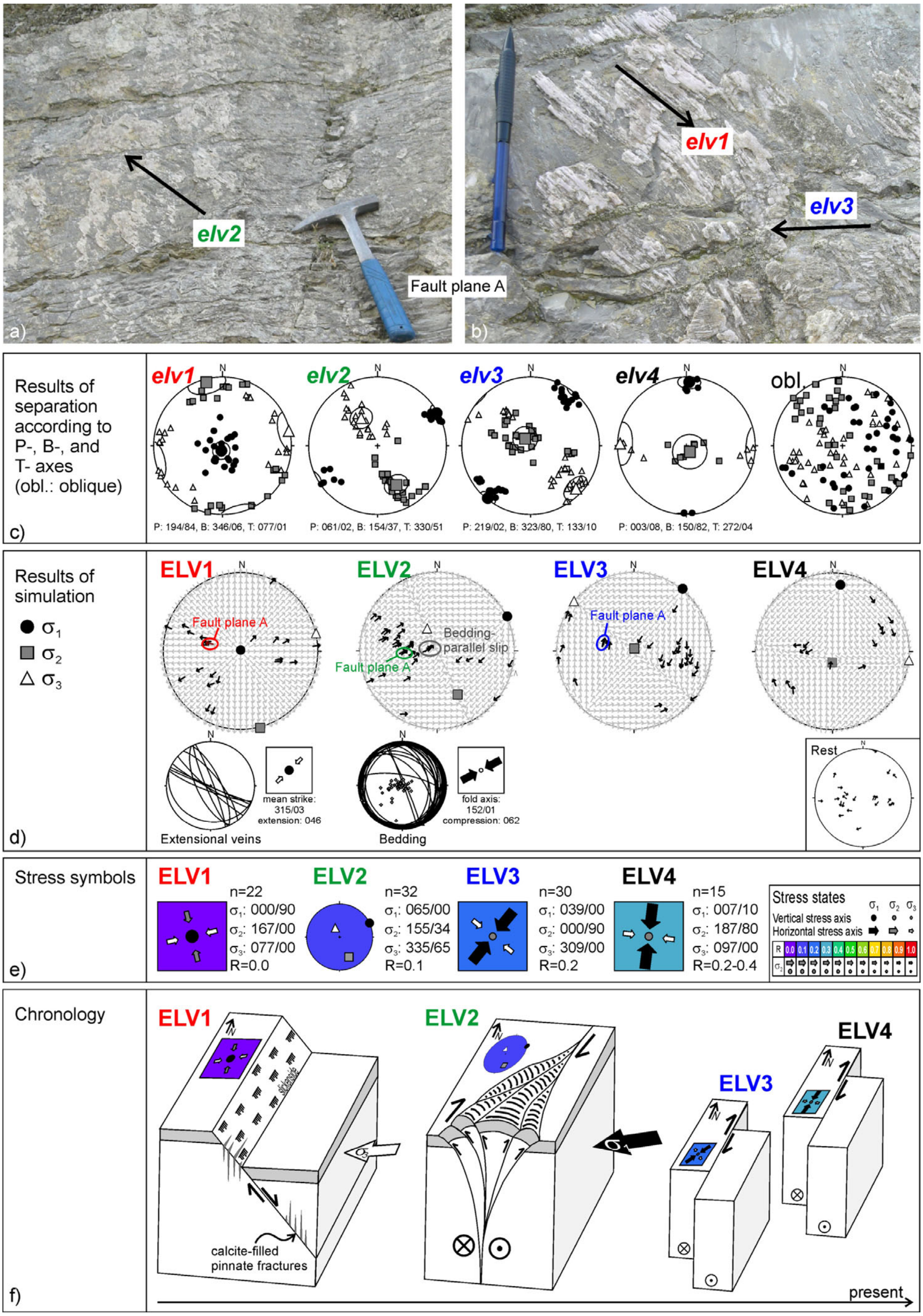

Figure 35: Stress inversion for fault-slip data from *Elvese* (#23, Mid Triassic limestone). a) Slickenside with calcite fibres indicating oblique-reverse slip. The fault-slip datum is part of subset *elv2*. b) Calcite fibres document that normal slip (*elv1*) predated sinistral slip (*elv3*) along fault plane A. c) The separation according to PBT axes results in four homogeneous subsets and a group of inconsistent fault-slip data (applied fracture angle θ=30°). d) Results of Stress Inversion Via Simulation for each PBT subset. e) Estimated stress tensors. f) Chronology of deformation phases with conceptual block models illustrating the kinematic style of each phase.

The abundance of N-S-striking fault planes recorded at *Elvese* quarry provides a possible explanation for the obliquity of ELV2. This stress state is related to oblique-reverse movements along many faults that have previously been formed as N-S-striking normal faults (Fig. 35d). According to the prevailing reverse components relative to strike-slip components of slip along these faults, the σ_3-axis of ELV2 plunges more steeply (65°) than the σ_2-axis (34°). The low stress ratio of R=0.1 indicates that σ_2 and σ_3 are almost equal in magnitude. Given, in addition, the direction of maximum compression indicated by ELV2 (σ_1=065/00) in relation to the preferred orientation of planes of weakness, the whole configuration associated to the oblique stress state can best be described as transpression along a N-S-striking array of pre-existing faults (Fig. 35f). Slip along such pre-existing discontinuities requires less energy than stresses released exclusively by the formation of new faults. Since in the case of ELV2, stresses are released predominantly by oblique slip, the estimated stress state is accordingly oblique. A transpressional regime is also indicated by the structural relations between faults and folds in the outcrop ("flower structure"; Fig. 34). In fact, some of the fault-slip data assigned to ELV2 correspond to bedding-parallel movements which, in general, are often observed in connection with a folding of strata. These observations fit well with the fact that the direction of maximum compression derived from folded bedding planes (062/00) is parallel to the σ_1-axis of ELV2. Hence, folding occurred coevally with transpression at *Elvese* quarry.

The deformation model developed for *Elvese* includes four main stages that postdated the Mid Triassic formation of limestones: Signs of extension reflect the early activity of a tensional stress state, ELV1, which corresponds to a regime of vertical flattening. Despite the various dip directions of normal faults, the largest faults among them strike roughly N-S, thus further constraining the derived E-W-direction of σ_3. The N-S-striking normal faults have widely been reactivated during a phase of transpression related to stress state ELV2 which coevally led to a folding of the strata. The obliquity of ELV2 probably corresponds to a local expression of a regional compressional stress state with an ENE-WSW-directed σ_1 that induced transpression and associated oblique slip along a N-S-oriented array of pre-existing faults. For many planes, the reverse component of movement did not induce a displacement as large as to compensate fully the previously obtained normal offset (Fig. 34). The strike-slip stress states ELV3 and ELV4 differ slightly in terms of σ_1 of which the directions are NE-SW and NNE-SSW, respectively. These stress states are supposed to be younger than ELV2, as this chronology would conform to the transition from reverse to strike-slip stress states observed at other locations where the directions of maximum compression also range between N-S and NE-SW (below).

Case study 9: Langelsheim quarry (#29)

Langelsheim is located close to the northwestern parts of the Northern-Harz-Boundary Fault along which the sedimentary fill of the Subhercynian Basin is widely tilted due to the inversion-related uplift of the structural block of the Harz Mountains (Fig. 36a). The pre-separation of the sampled fault population results in three homogeneous subsets (*lan1*, *lan2*, *lan3*; Fig. 36d).

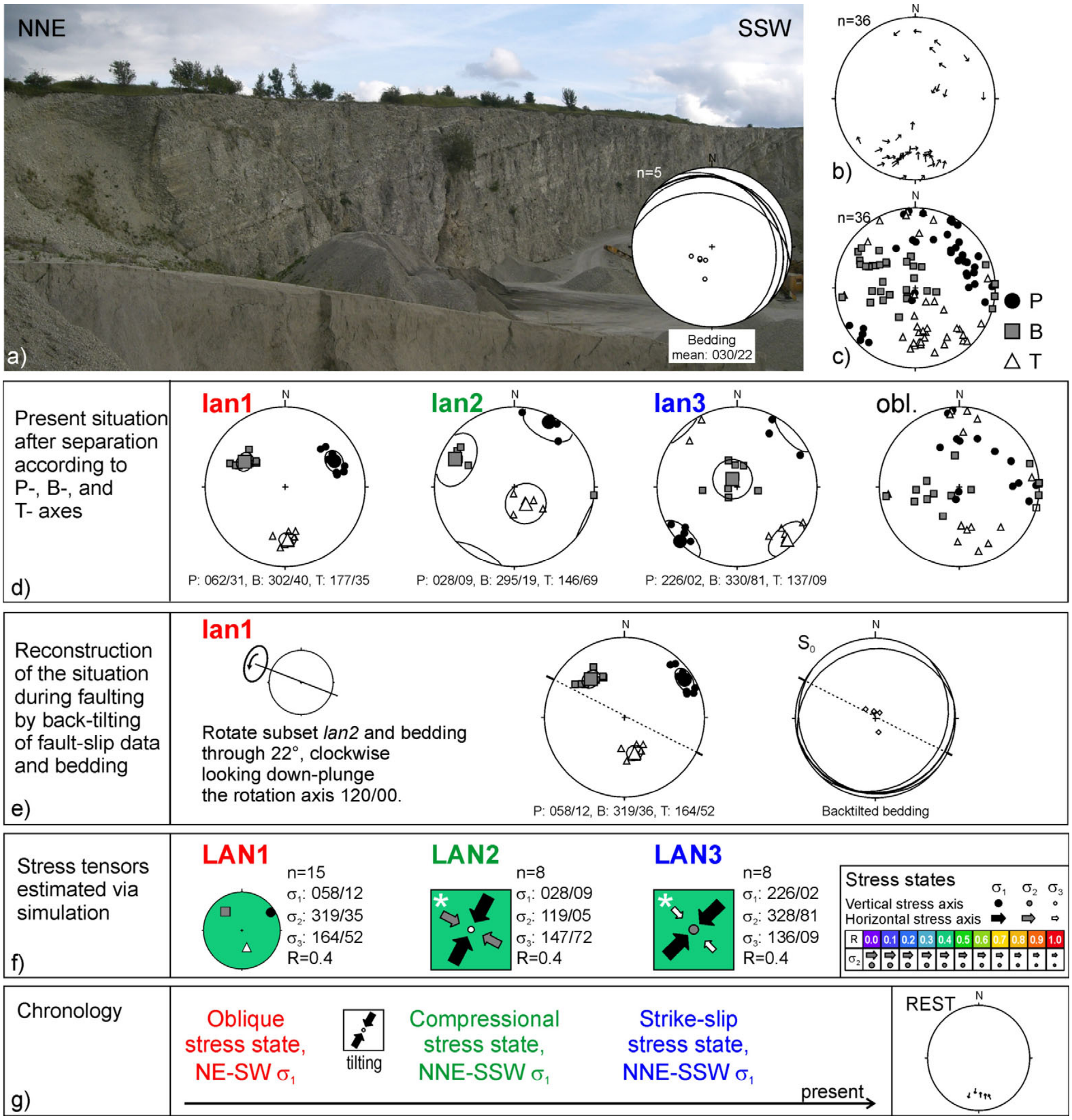

Figure 36: Separation and stress inversion for fault-slip data from *Langelsheim* (#29, Upper Cretaceous limestone). a) The Cenomanian-Turonian strata are dipping towards NNE; b) Tangent-lineation plot of the heterogeneous set of fault-slip data; c) Result of PBT: cumulative plot of P-, B-, and T-axes for the whole data set (applied fracture angle θ=30°); d) Results of separation according to clusters of P-, B-, and T-axes; e) Back-tilting procedure for the subset *lan1*; f) Results of the Stress Inversion Via Simulation. The stress states LAN1, LAN2, and LAN3 have been found to excellently fit the previously separated subsets *lan1*, *lan2*, and *lan3*, respectively. Stress state LAN1 is oblique as none of the principal stress axes dips by more than 70°. For this reason, LAN1 is plotted as a stereographic projection with the background colour representing the stress ratio, R. Stress states based on less than 9 fault-slip data are marked by an asterisk. g) Derived chronology of deformation stress states.

Subset *lan1* reveals kinematic axes that deviate far from vertical respectively horizontal orientations indicating that the fault-slip data have been rotated after faulting. To check the supposed rotation of *lan1*, this subset and the strata have been back-tilted adopting a rotation axis derived from the mean strike of bedding planes (120/00). After tilting back the strata into

their original horizontal position (through 22°), the P-axes of *lan1* are sub-horizontal which confirms this subset to have been involved in the tilting process (Fig. 36e). However, the B- and T-axes still do not show typical vertical or horizontal orientations after back-tilting. Accordingly, none of the inferred principal stress axes is vertical (i.e. plunging by >70°; Fig. 17f). A potential explanation for this obliquity of stress axes might be provided by the position of the related fault-slip data relative to large-scale structures in close vicinity of *Langelsheim* quarry (chapter 4.4.5).
Subsequent to the activity of LAN1, the whole rock mass has been tilted under a presumably NE-SW-directed maximum horizontal compression (Fig. 36g). The stress states LAN2 and LAN3 which have been derived from the subsets *lan2* and *lan3*, respectively, document processes of faulting that occurred subsequent to the tilting of strata. Finally, LAN2 is interpreted as having predated LAN3 since such a succession would reflect a development from folding and reverse faulting to a later strike-slip stress regime as observed in other parts of the study area (below).

4.3 Cross-outcrop correlation of paleostress states

After having estimated paleostress states and their relative timing separately for all investigated sites, cross-outcrop correlations of results shall provide the next step towards a comprehensive model for the evolution of regional paleostress fields that affected the entire southern margin of the CEBS. Such correlations of local stress states in the Elbe Fault System area are based on the widespread relation between folding and faulting, the locally derived chronologies of stress states and on consistencies in the directions of principal stress axes.

4.3.1 Consistencies between folding and faulting

A widespread phenomenon observed regards corresponding kinematics of folds and fault patterns. At many sites, the direction of maximum compression inferred from folded or tilted bedding planes corresponds with the direction of σ_1 derived from fault-slip data (Fig. 37). Comparing the results from different locations, the respective axes consistently strike around NNE-SSW. This phenomenon is observed in Mid Triassic, Upper Jurassic (Fig. 38), as well as Upper Cretaceous rocks. In some cases, the fold-related direction of maximum compression is consistent with a compressional stress state, in others it corresponds with a strike-slip stress state. At any of these sites, however, the twofold obtained direction of maximum compression argues for a close mechanical and temporal relationship between folding of the rocks and faulting under a N-S- to NE-SW-directed σ_1.

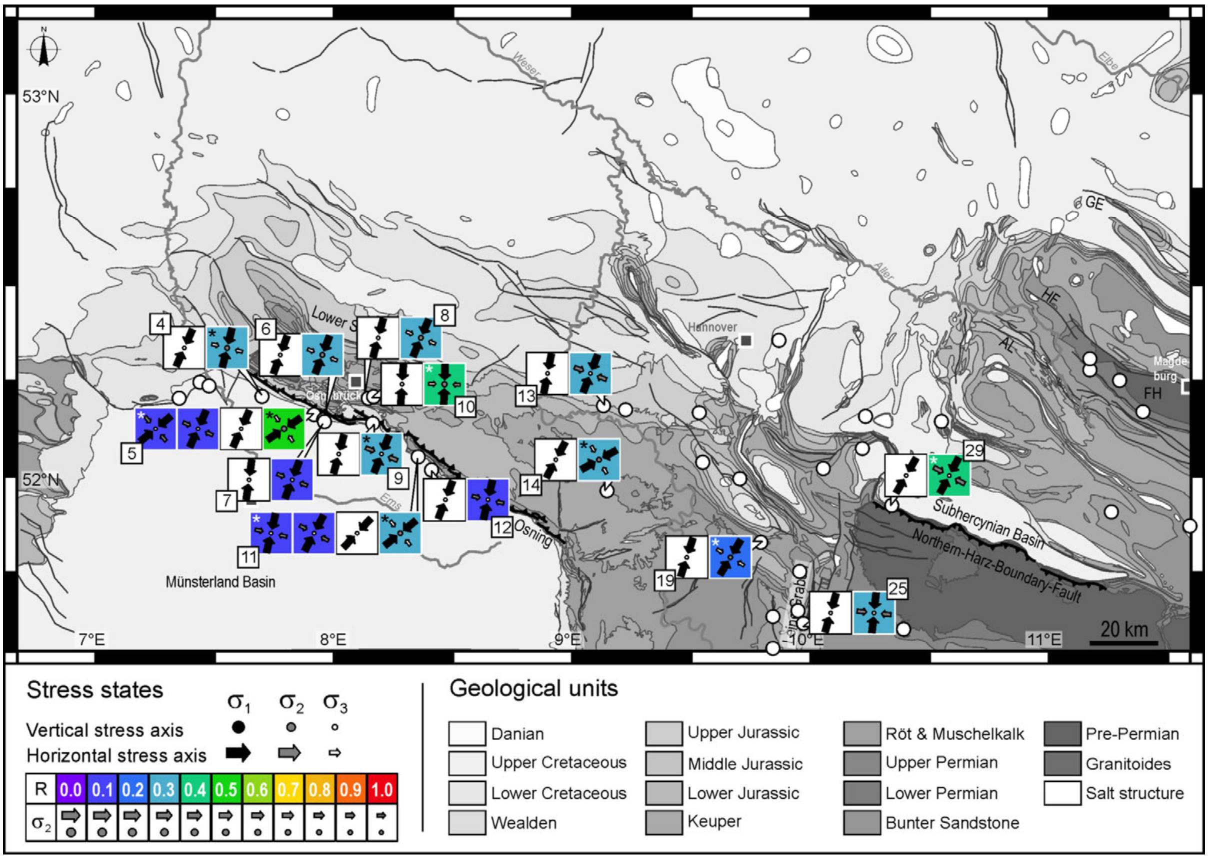

Figure 37: Folding and faulting in the German parts of the Elbe Fault System. A remarkable sub-parallelism between directions of maximum horizontal compression derived from folded bedding planes (black arrows on white grounds) and σ_1-directions inferred from fault-slip data (coloured stress symbols) can widely be observed. At each site, the relative ages of stress states and stages of folding decrease from left to right. Stress states based on less than 9 fault-slip data are marked by an asterisk.

Figure 38: Gently folded Upper Jurassic limestones exposed in the Lower Saxony Basin (*Steinbergen*, #13). The bedding planes are offset by thrust faults which are related to a compressional stress state (NNE-SSW-directed σ_1).

4.3.2 Locally estimated chronologies of paleostress states

As illustrated by the previously presented case studies, the chronology of stress states is locally constrained by indicators such as superimposed striations or the relation of fault-slip data and bedding planes. The total number of chronological indicators observed in the study area and their implications on the relative timing of associated stress states are summarized in Figure 39. For most of these indicators, detailed descriptions are provided by the paragraphs on single case studies. Other observations on the relative timing of structures include, for instance, a north dipping reverse fault exposed at *Lienen* (#7) which shows indications for a later reactivation as a dextral fault. Thus, the two generations of striations reveal that the compressional stress state LIE1 has been active before the strike-slip stress state LIE2. At Upstedt (#26), a NW-dipping fault plane shows an older generation of slickolites that indicate normal faulting, while a younger generation of striations indicates strike-slip movements. This argues for the normal stress state UPS1 to have been active before the strike-slip stress state UPS2. At Baddeckenstedt (#27), an older generation of normal faults has been affected by tilting of the whole rock mass, while a younger generation of normal faults is interpreted to have postdated the tilting event. Consequently, a normal stress state related to N-S directed extension (BAD1) has obviously predated a normal stress state related to WNW-ESE-directed extension (BAD2). A corresponding development of normal stress states has been developed for the fault pattern exposed at Folwark (#57): a south dipping normal fault crosscuts a west dipping normal fault indicating that N-S-directed extension (FOL1) had taken place after E-W-directed extension (FOL2).

Considering the locally derived chronologies of stress states and consistencies in the orientations of principal stress axes, a cross-outcrop correlation of paleostress states can be performed (Fig. 39). A classification according to directions and modes (i.e. compressional, strike-slip, tensional, or oblique) of stress states is based on two assumptions: first, regional stress regimes of different modes and directions are unlikely to control the same area at the same time and, secondly, stress states of consistent modes and directions derived from different sites potentially have been active coevally, thus representing a common regional stress field.
Interestingly, the chronological constraints derived from single outcrops are very consistent in the sense that they would not much complicate a classification of stress states which is merely based on the directions of principal axes (Fig. 39). Compressional stress states, for example, are older than strike-slip stress states regardless of the site at which the relationship between compression and strike-slip stress has been recorded. Furthermore, two groups of strike-slip stress states with different directions of maximum horizontal compression (σ_1) can be classified following the observation that at site #14 a stress state with NE-SW-directed σ_1 had been active before a stress state with NNW-SSE-directed σ_1. The role of tensional stress states, in turn, is twofold: Tensional states derived from Upper Cretaceous and Upper Carboniferous rocks are younger, whereas tensional states from two sites of Mid Triassic rocks are older than the respective compressional or strike-slip stress states. Finally, the oblique stress state found at site #29 is correlated with compressional stress states since they reveal agreeing directions of maximum compression and agreeing relations to folding.
Altogether, consistent stress states can be combined to five categories each representing a separate temporal status: a group of “older” tensional stress states, a group of compressional stress states, a group of strike-slip stress states with N-S- to NE-SW-directed σ_1, a group of strike-slip stress states with E-W- to NW-SE-directed σ_1, and a group of “younger” tensional stress states. Interestingly, these groups partly integrate stress states derived from different rock ages. Strike-slip stress states with a N-S- to NE-SW-directed σ_1, for instance, have been documented by fault-slip data preserved within Upper Carboniferous, Mid Triassic, as well as Upper Cretaceous rocks.

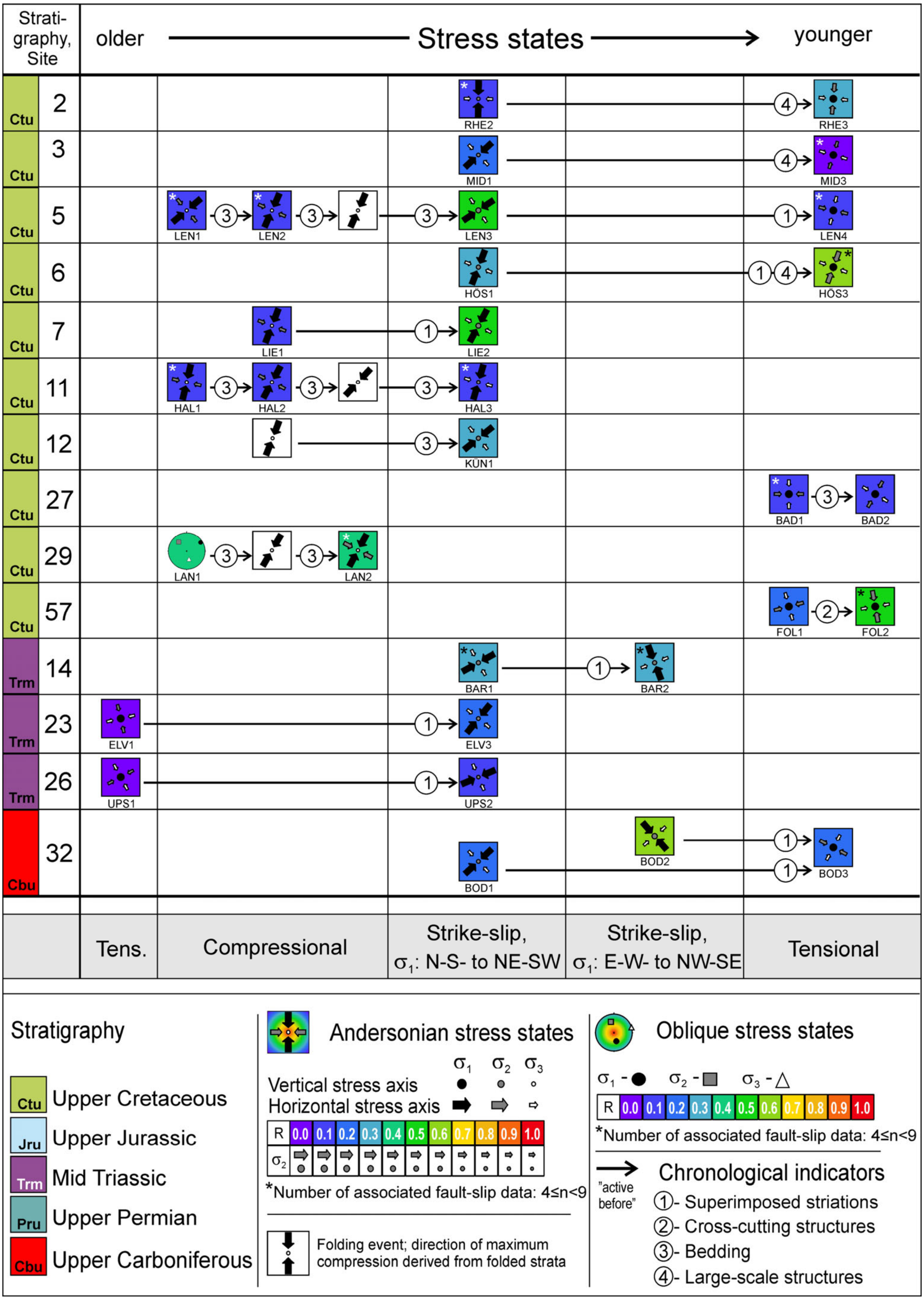

Figure 39: Correlation of stress states with known relative chronologies. Sites are stratigraphically ordered. Relative timing of stress states is constrained by locally observed relationships between different fault-slip data or between fault-slip data and other structural elements (indicated by numbers). Stress states with consistent directions of principal axes and a consistent temporal rank are assumed to represent a common stress regime (same column). Stress states based on less than 9 fault-slip data are marked by an asterisk.

4.3.3 Consistencies in the directions of principal axes

The previously described correlation only integrates those paleostress states that show detected temporal relations to other stress states. These stress states, however, correspond to less than half of the total number of 77 paleostress states found at the southern margin of the CEBS. To reconstruct regional stress fields that affected the whole study area, it is indispensable to consider as many estimated stress states as possible. However, for a large number of stress states, information is restricted to the determined parameters of the reduced stress tensor and the ages of host rocks providing a maximum age for the associated faulting. For this reason, the previous correlation (Fig. 39) is taken as a base for a synthesis of all estimated stress states (Fig. 40).
It is obvious that stress states found in older rocks generally do not differ much from stress states detected in younger rocks. As a consequence, the complete number of paleostress states can be correlated according to the same five categories of stress states distinguished before (Fig. 39). This consistency of results derived from rocks of different ages widely excludes the possibility of applying the principles of paleostress stratigraphy. The agreeing stress states derived from differently aged rocks rather indicate that the respective stratigraphic units have been affected by stress states of the same ages and causal mechanisms. The maximum age of consistent stress states would then be constrained by the youngest rocks documenting associated fault-slip data. Following this line of argument, the groups of compressional, strike-slip, and “younger” tensional stress states are related to (post-) Late Cretaceous deformation events since the youngest rocks affected by these stress states are of Late Cretaceous ages. On the contrary, the two tensional stress states that have been shown to be older than strike-slip stress states (sites #23 and #26) must be assigned to earlier stages of deformation with a maximum age of Mid Triassic.

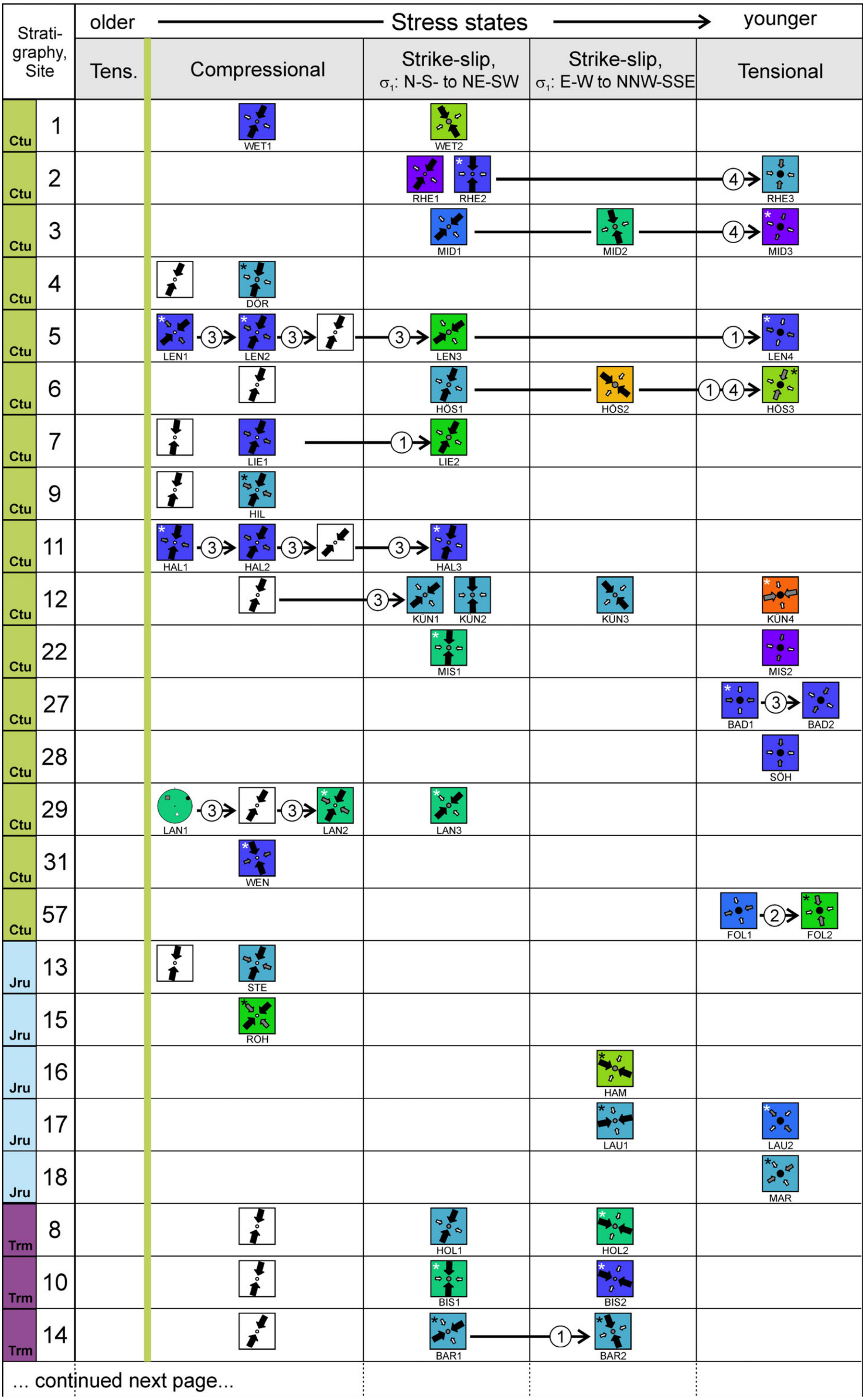

Strati-graphy, Site
older
Stress states
younger
Tens.
Compressional
Strike-slip, σ1: N-S- to NE-SW
Strike-slip, σ1: E-W to NNW-SSE
Tensional
Ctu 1
WET1
WET2
Ctu 2
RHE1
RHE2
4
RHE3
Ctu 3
MID1
MID2
4
MID3
Ctu 4
DÖR
Ctu 5
LEN1
3
LEN2
3
3
LEN3
1
LEN4
Ctu 6
HÖS1
HÖS2
1
4
HÖS3
Ctu 7
LIE1
1
LIE2
Ctu 9
HIL
Ctu 11
HAL1
3
HAL2
3
3
HAL3
Ctu 12
3
KUN1
KUN2
KUN3
KUN4
Ctu 22
MIS1
MIS2
Ctu 27
BAD1
3
BAD2
Ctu 28
SÖH
Ctu 29
LAN1
3
3
LAN2
LAN3
Ctu 31
WEN
Ctu 57
FOL1
2
FOL2
Jru 13
STE
Jru 15
ROH
Jru 16
HAM
Jru 17
LAU1
LAU2
Jru 18
MAR
Trm 8
HOL1
HOL2
Trm 10
BIS1
BIS2
Trm 14
BAR1
1
BAR2
... continued next page...

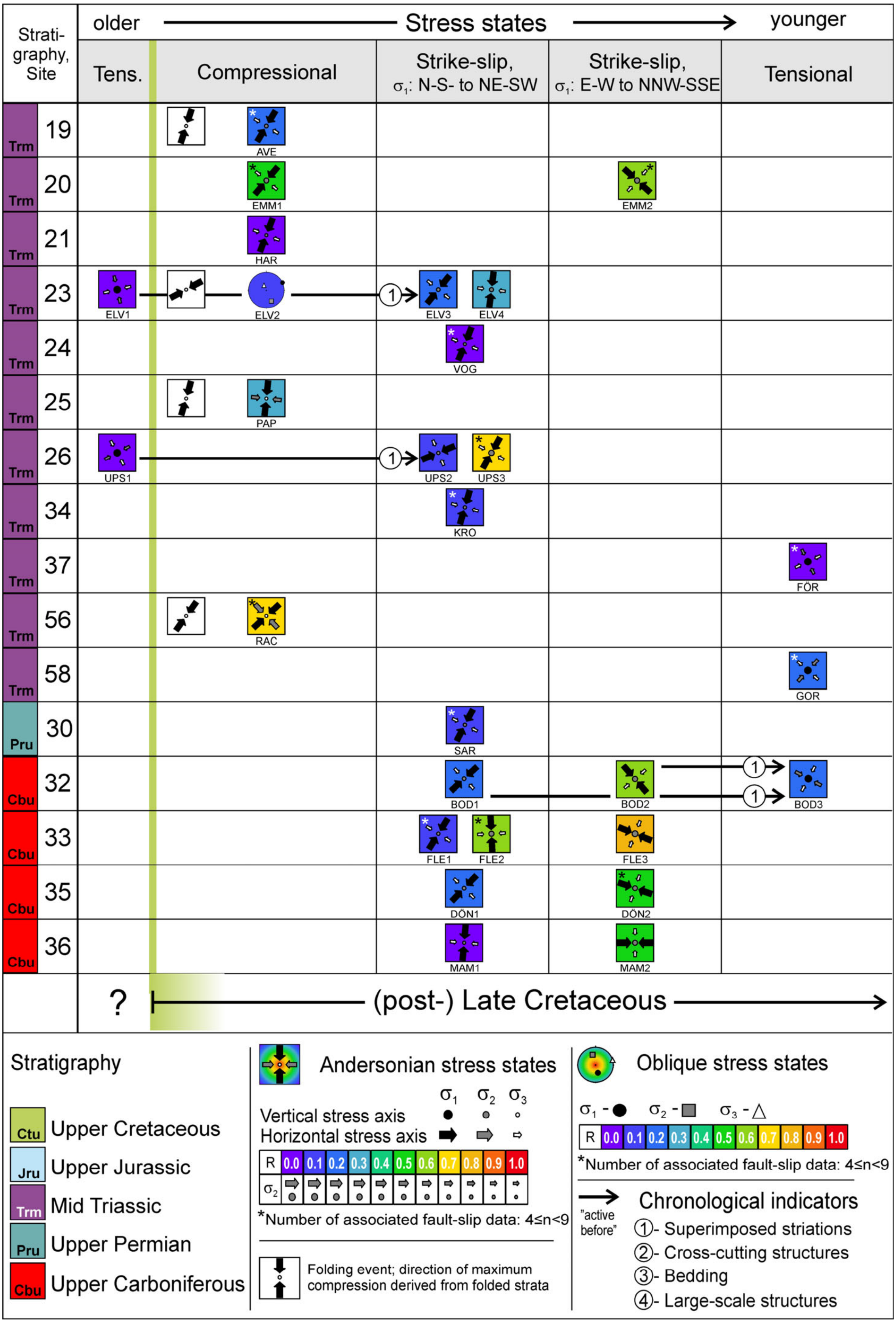

Figure 40: Cross-outcrop correlation of stress states derived from the Elbe Fault System area. Sites are stratigraphically ordered to control the variation of stress states in different rock ages. The stress states, in turn, are horizontally arranged according to consistent directions of principal stress axes and locally derived chronologies. According to this synthesis of results, most stress states must be assigned to (post-) Late Cretaceous times. Stress states based on less than 9 fault-slip data are marked by an asterisk.

4.4 Regional vs. local phenomena

Considering the range of investigated rock ages, the estimated paleostress states show remarkable consistencies (Fig. 40): Most of the compressional stress states are characterised by a N-S- to NE-SW-directed maximum compression (σ_1). The estimated strike-slip stress states have been demonstrated to consistently be younger than compressional stress states and/or the locally observed folding of rocks. The directions of σ_1 are various among the strike-slip stress states but two directions prevail: strikes around NE-SW and around NW-SE, respectively. At many sites, the youngest signs of deformation are related to tensional stress states, even in Upper Carboniferous rocks. The various directions of extension (σ_3) revealed by the different tensional stress states, in turn, are relativised by the fact that most of the associated stress ratios are low indicating almost equal magnitudes of σ_2 and σ_3.
The degree of consistency of locally estimated paleostress states is of relevance for distinguishing regional from local phenomena in the study area. Another aspect, of course, is the spatial distribution of consistent stress states.

4.4.1 Compressional stress states

Stress states with a vertical σ_3 have been derived from sites in the Lower Saxony Basin, the Hessian Depression, and the Subhercynian Basin (Fig. 41) as well as in the Sudetic Mountains (#56; Fig. 42). These stress states mainly show consistent directions of maximum compression (σ_1) trending around NNE and consistently low to intermediate stress ratios ($0.0 \leq R \leq 0.5$) that indicate regimes between uniaxial deviatoric compression and triaxial stress. Only at *Wendessen* quarry (#31), σ_1 is striking NNW, thus showing a slight deviation from the general trend, while at *Raciborovice* (#56) the stress ratio is much larger than the average. The youngest rocks which have preserved corresponding reverse faults are the Turonian-Coniacian limestones exposed at *Halle* quarry (#11). However, also Upper Jurassic and Mid Triassic rocks show signs of a N-S to NE-SW-directed compression.

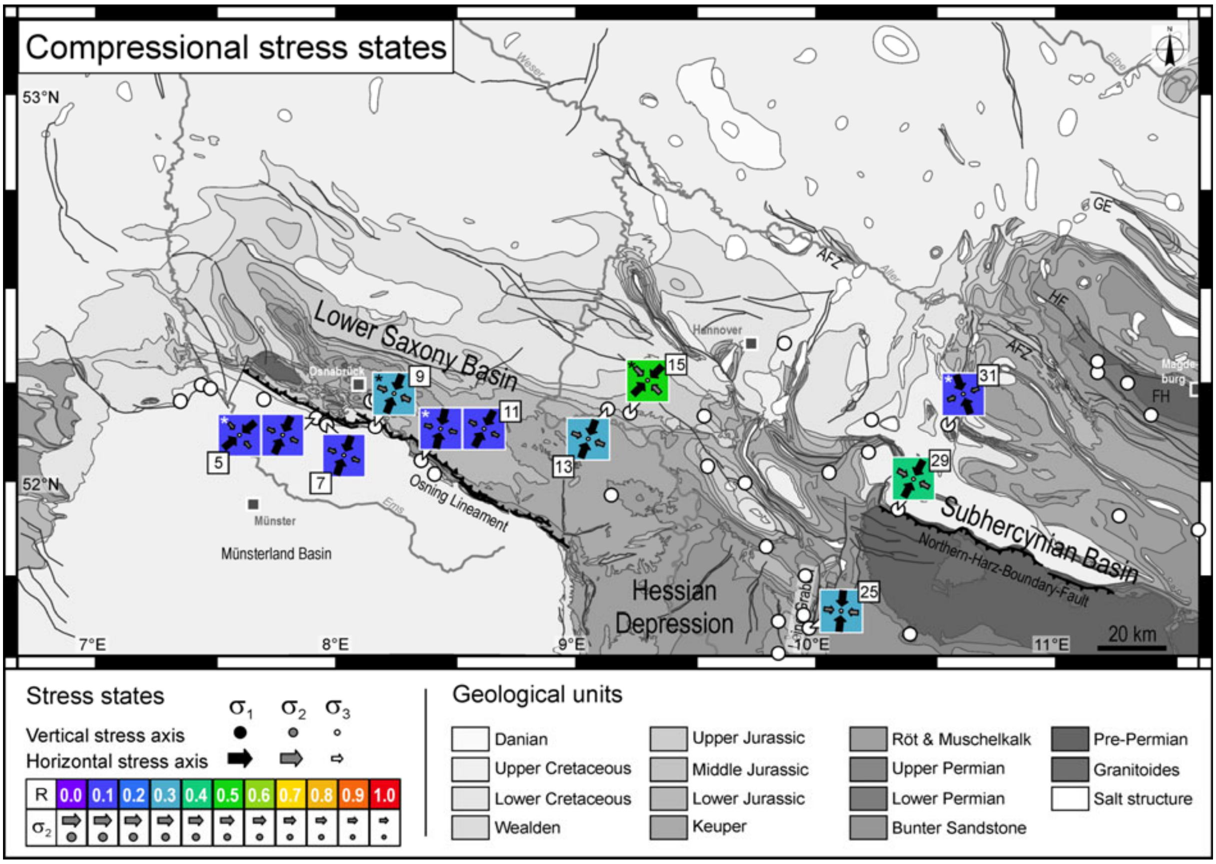

Figure 41: Compressional stress states estimated for the German parts of the Elbe Fault System. Beside a sub-vertical σ_3, these stress states are consistent in terms of a N-S- to NE-SW-directed maximum compression (σ_1) and low to intermediate stress ratios ($0.0 \leq R \leq 0.5$). At sites with several inferred stress states, older ones are shown to the left and younger ones to the right. Stress states that are based on less than 9 fault-slip data are marked by an asterisk.

Main structures: AFZ – Allertal Fault Zone, FH – Flechtingen High, GE – Gardelegen Escarpment, HF – Haldensleben Fault, WHBF – Western Harz Boundary Fault.

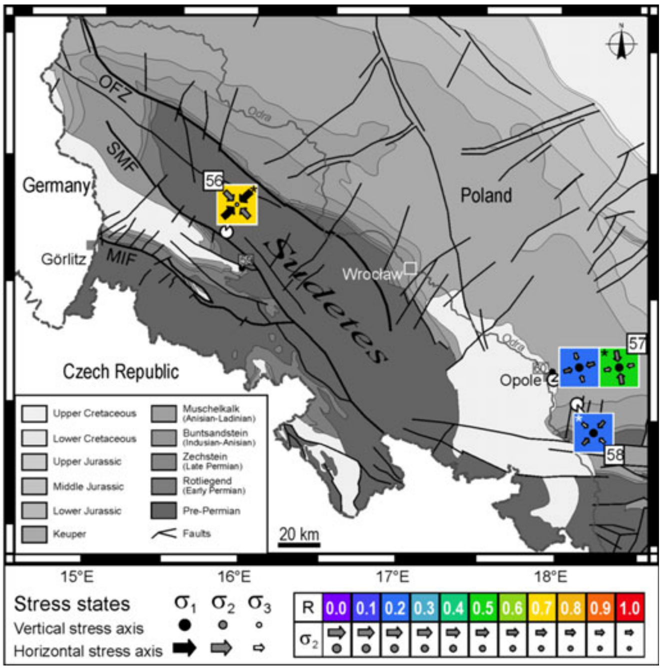

Figure 42: Paleostress states reconstructed for three sites in southwestern Poland. Geological subcrop map of the base of Cenozoic units modified after Dadlez et al. (2000). Stress states that are based on less than 9 fault-slip data are marked by an asterisk.

The high consistency and the wide distribution of compressional stress states indicate that these local stress configurations are related to a common regional stress field. To characterise this potential stress regime, the parameters of the 12 compressional stress states have been analysed comprehensively (Fig. 43a). The mean vector of σ_1-axes has been calculated to be oriented 204/00 and the mean stress ratio has been estimated as R=0.26. In the following, this deduced regional stress field is referred to as "Stress field A", while illustrating it by a comprehensive stress symbol (Fig. 43b). According to the youngest rocks that have been affected, Stress field A must be assigned to post-Coniacian times.

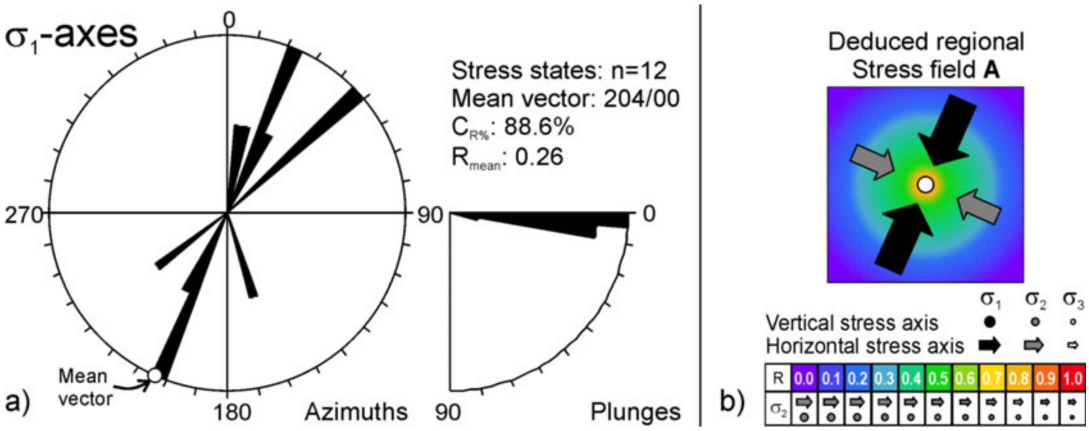

Figure 43: Potential regional "Stress field A" inferred from compressional stress states. a) Rose diagram with σ_1-azimuths of all compressional stress tensors. The σ_1-axes strike consistently around NNE. None of the σ_1-plunges deviates by more than 14° from the horizontal. To infer an overall stress field for these local stress states, the mean vector of σ_1-axes is calculated after Wallbrecher (1986; "$R_{\%}$-and-center-method"). The concentration parameter, $C_{R\%}$, is a measure for the alignment of stress axes with $C_{R\%}$=100% indicating parallel fabrics and $C_{R\%}$=0% indicating a uniform distribution. Here, $C_{R\%}$=88.6% designates a pronounced maximum for the σ_1-axes with a mean oriented 204/00. b) Comprehensive symbol for the deduced regional Stress field A. It integrates the mean directions of principal stress axes projected to the vertical respectively horizontal. The range of background colours reflects the low to intermediate stress ratios of the associated compressional stress states ($0.0 \leq R \leq 0.7$).

4.4.2 Strike-slip stress states with a N- to NE-directed maximum compression

The largest number of paleostress states detected along the southern margin of the CEBS corresponds to strike-slip stress states with a N-S- to NE-SW-directed maximum compression (σ_1) which are distributed all across the German parts of the Elbe Fault System (Fig. 44). The respective stress ratios cover a wide range between R=0.0 and R=0.7. The rocks documenting associated signs of faulting range in age from the Upper Carboniferous volcanics of the Flechtingen High area (Fig. 45) to the Turonian-Coniacian limestones at *Halle* quarry (#11).
This group of stress states provides good arguments for being related to a common regional stress field: a high consistency and a wide spatial distribution. The deduced regional "Stress field B" is characterised by a σ_1-axis which is oriented 209/01 and a mean stress ratio of R=0.25 (Fig. 46). From the local constraints on the chronology of single stress states (Fig. 39) it can be concluded that Stress field B is younger than the previously introduced Stress field A.

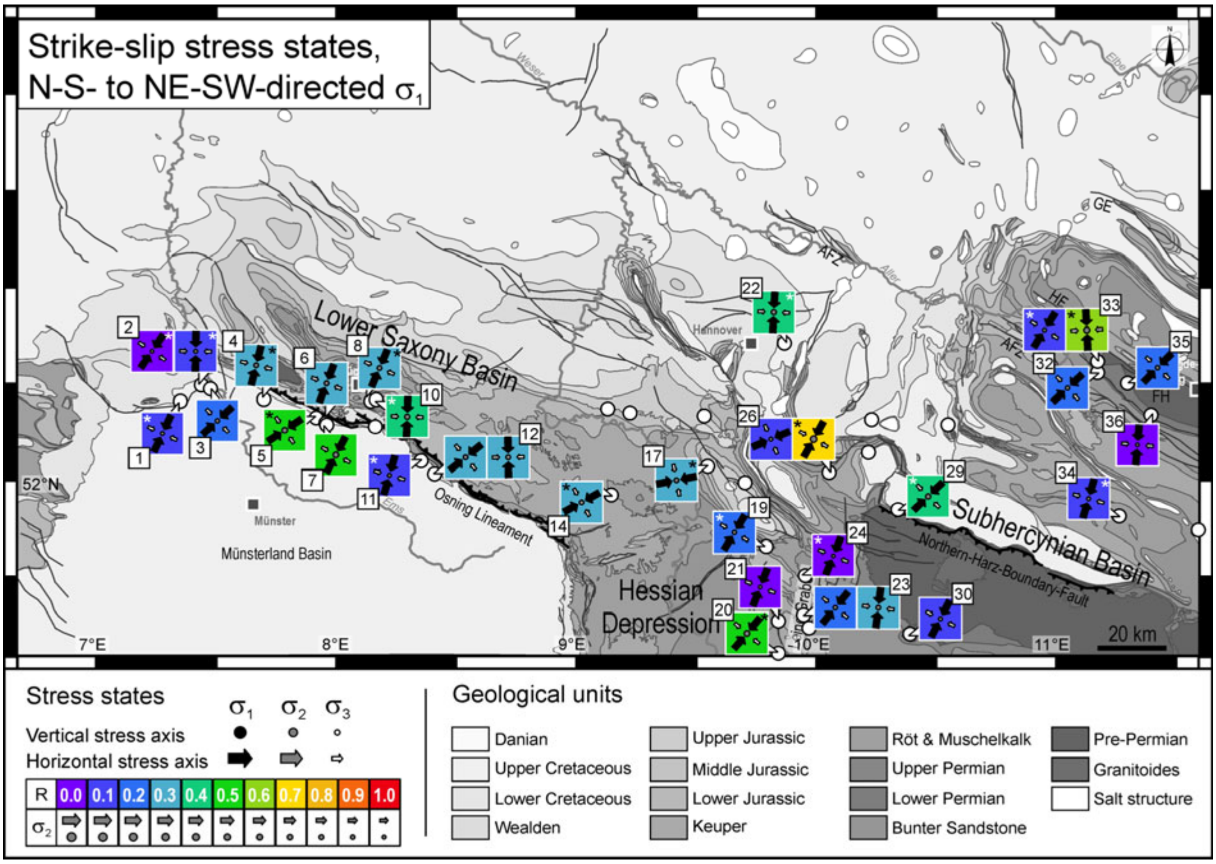

Figure 44: Strike-slip paleostress states with a N-S- to NE-SW-directed σ_1 (German parts of the Elbe Fault System). The stress ratios range between R=0.0 and R=0.7. At sites where several stress states are inferred, ages of stress states decrease from left to right. Stress states that are based on less than 9 fault-slip data are marked by an asterisk. Abbreviations as in Fig. 41.

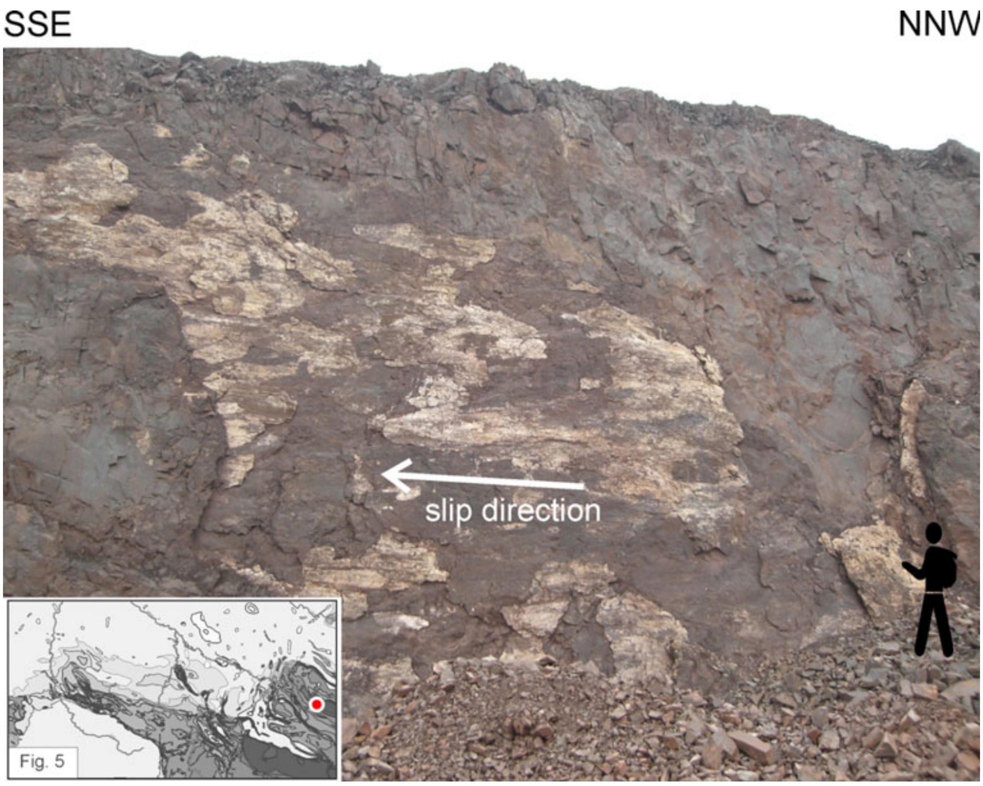

Figure 45: Strike-slip fault within Upper Carboniferous andesites. At *Dönstedt* quarry (#35) in the Flechtingen High area, calcite fibres (white coating) indicate a dextral sense of movement along the fault.

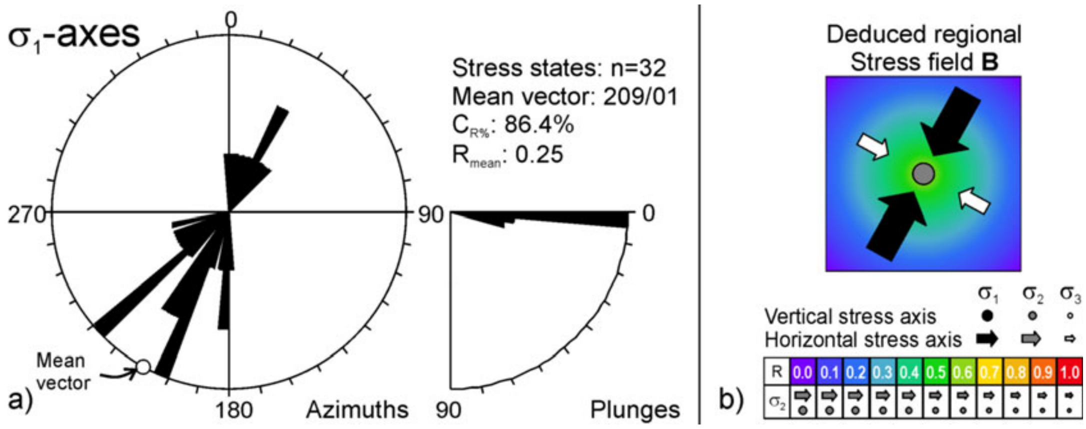

Figure 46: Potential regional "Stress field B" inferred from strike-slip stress states with N-S- to NE-SW-directed σ_1-axes. a) Rose diagram with σ_1-axes that strike consistently around NNE. None of the σ_1-plunges deviates by more than 12° from the horizontal. To infer an overall stress field for these stress states, the mean vector of σ_1-axes is calculated after Wallbrecher (1986; "$R_{\%}$-and-center-method"). The concentration parameter, $C_{R\%}$, is a measure for the alignment of stress axes ($C_{R\%}$=100%: parallel fabrics; $C_{R\%}$=0%: uniform distribution). Here, $C_{R\%}$=86.4% designates a pronounced maximum for σ_1-axes with a mean oriented 209/01. b) Comprehensive symbol for the deduced regional Stress field B. It integrates the mean directions of principal stress axes projected to the vertical respectively horizontal. The predominance of blue background colours reflects a predominance of low stress ratios of the associated strike-slip stress states. In total, the stress ratios vary between R=0.0 and R=0.7.

4.4.3 Strike-slip stress states with a W- to NNW-directed maximum compression

Another group of strike-slip stress states is shown in a separate paleostress map due to a common E-W- to NW-SE-direction of maximum compression (σ_1; Fig. 47). These stress states are obtained from sites scattered all across the German parts of the Elbe Fault System. Most of the respective stress ratios are medium scale, though in total the values range between R=0.1 and R=0.8. The youngest rocks that have preserved respective fault-slip data are the Cenomanian-Turonian limestones exposed at *Künsebeck* (#12). However, such stress states are also documented by fault-slip data sampled from the Upper Carboniferous volcanics of the Flechtingen High area.

Though this group is restricted to 14 local strike-slip stress states, their consistency and regional distribution indicate that they represent local expressions of a common regional stress field. The deduced regional "Stress field C" reveals a σ_1-axis which is oriented NW-SE (127/02) and a mean stress ratio of R=0.51 (Fig. 48). According to local chronological indicators, Stress field C is younger than Stress field B.

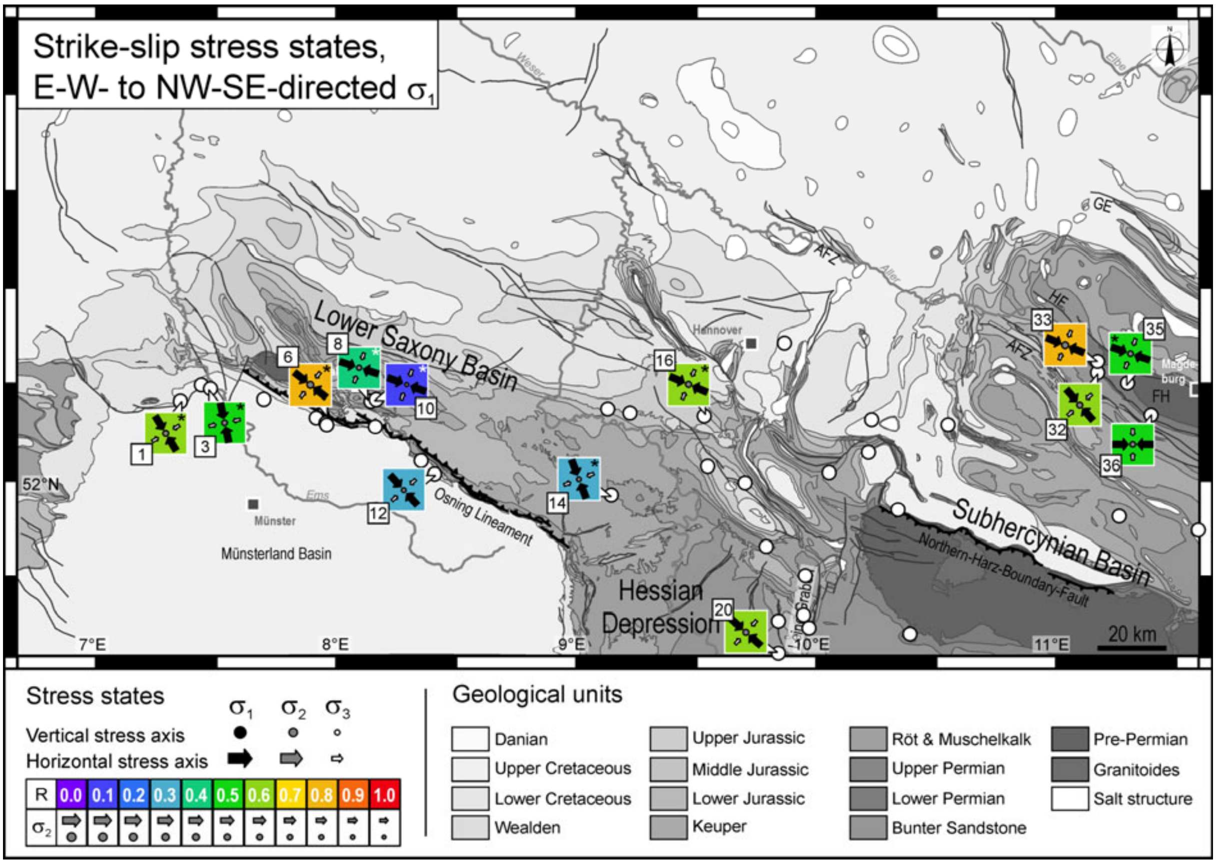

Figure 47: Strike-slip stress states with an E-W- to NNW-SSE-directed σ_1 in the German parts of the Elbe Fault System. The stress states are mainly characterised by intermediate stress ratios ($0.2 \leq R \leq 0.8$). Stress states that are based on less than 9 fault-slip data are marked by an asterisk. Abbreviations as in Fig. 41.

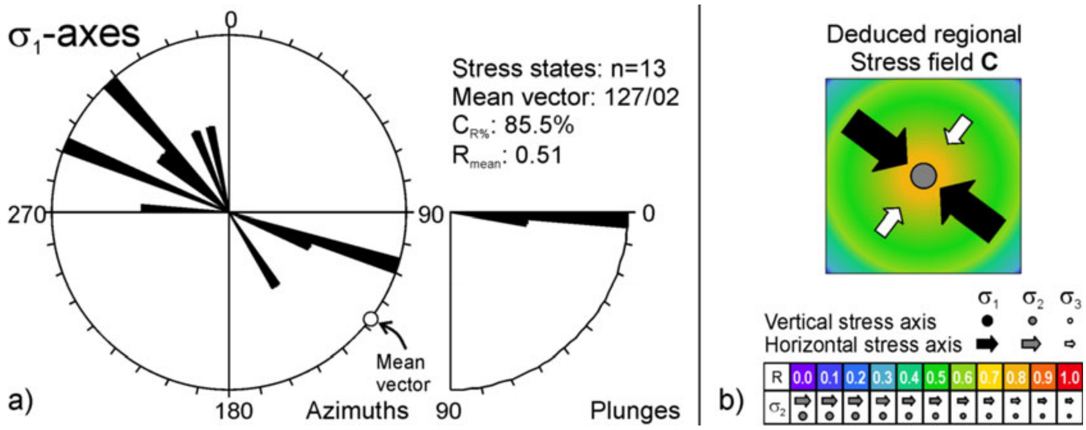

Figure 48: Potential regional "Stress field C" inferred from strike-slip stress states with E-W- to NNW-SSE-directed σ_1-axes. a) Rose diagram of strike-slip stress states with σ_1-directions striking around NW. None of the σ_1-plunges deviates by more than 8° from the horizontal. To infer an overall stress field, the mean vector of σ_1-axes is calculated after Wallbrecher (1986; "$R_{\%}$-and-center-method"). The concentration parameter, $C_{R\%}$, is a measure for the alignment of stress axes ($C_{R\%}$=100%: parallel fabrics; $C_{R\%}$=0%: uniform distribution). Here, $C_{R\%}$=85.5% designates a pronounced maximum for σ_1-axes with a mean oriented 127/02. b) Comprehensive symbol for the deduced regional Stress field C. It integrates the mean directions of principal stress axes projected to the vertical respectively horizontal. The background colours reflect predominantly intermediate stress ratios of the associated strike-slip stress states ($0.1 \leq R \leq 0.8$).

4.4.4 Tensional stress states postdating compressional or strike-slip stress states

The group of "younger" tensional stress states covers sites that are spread from the western parts of the Lower Saxony Basin to the eastern parts of the Subhercynian Basin (Fig. 49) and farther to the study area east of the Sudetic Mountains (Fig. 42). These stress states show a great diversity in the directions of minimum compression (σ_3) and are mostly associated with low stress ratios. Considering the presence of *Zechstein* salt structures in the subsurface, these tensional stress states can be separated into two groups: In subareas presently containing salt structures like the Hessian Depression and the Subhercynian Basin, the stress ratios are remarkably low ($0.0 \leq R \leq 0.3$). The tensional stress states in areas without salt in the subsurface, on the contrary, are characterised by a much greater range of stress ratios. Concerning the horizontal orientations of σ_3, however, both domains show a similarly large diversity.

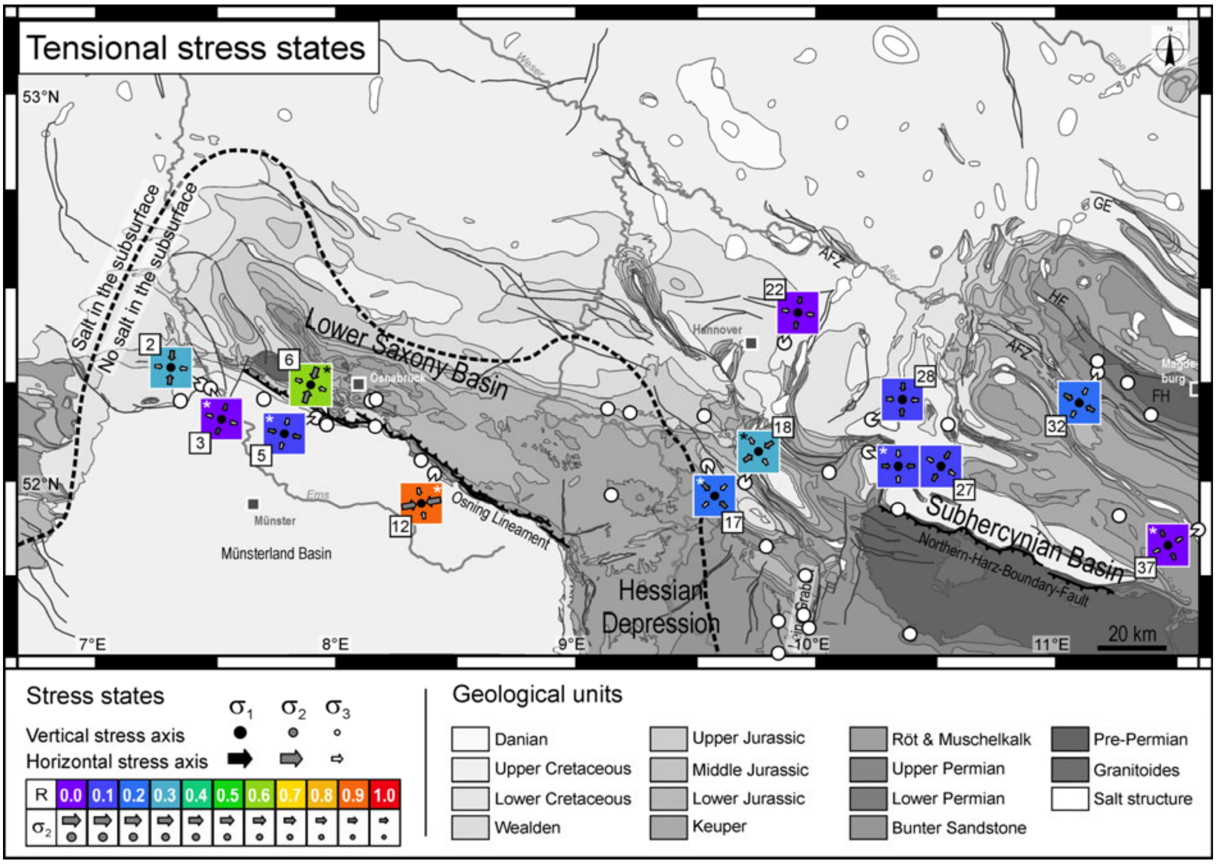

Figure 49: Group of "younger" tensional stress states derived from the German parts of the Elbe Fault System. At sites where several stress states are inferred, ages of stress states decrease from left to right. Stress states that are based on less than 9 fault-slip data are marked by an asterisk. The stress ratios are low in the subarea with Zechstein salt in the subsurface, whereas stress ratios in the area without subsurface salt structures are diverse. For the detailed distribution of Zechstein salt see Fig. 26. Abbreviations as in Fig. 41.

The inconsistency of tensional stress states in terms of directions of extension (σ_3) and the variation of stress ratios with respect to the presence of salt structures argue against a common regional stress field that might be representative for the local tensional stress states. However, the underlying extensional strain has consistently been identified as the youngest imprint of deformation at several sites. Consequently, there is evidence for a vertical σ_1 that controlled deformation along the whole southern margin of the CEBS subsequent to the regional Stress fields A, B, and C. Accordingly, “Stress field D” is introduced which is characterised by a vertical σ_1 and a low average of stress ratios (Fig. 50). To allow for the diversity in σ_3-directions, Stress field D does not include any information about the directions of horizontal principal axes.

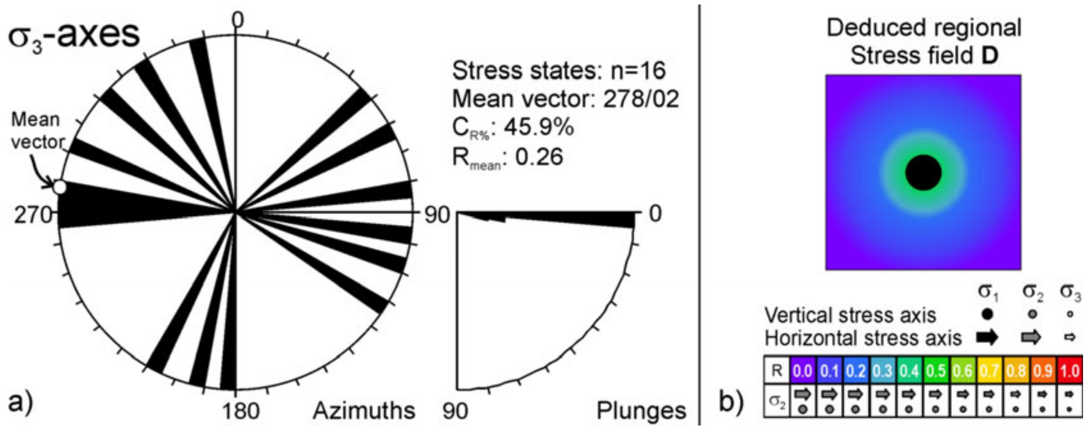

Figure 50: Potential regional “Stress field D” inferred from tensional stress states. a) Rose diagram with σ_3-axes of tensional stress states that are interpreted to be younger than compressional and strike-slip stress states. None of the σ_1-plunges deviates by more than 8° from the horizontal. The azimuths of σ_3-axes show a great diversity. The mean vector of σ_3-axes is calculated after Wallbrecher (1986; “$R_{\%}$-and-center-method”). The concentration parameter, $C_{R\%}$, is a measure for the alignment of stress axes ($C_{R\%}$=100%: parallel fabrics; $C_{R\%}$=0%: uniform distribution). Here, $C_{R\%}$=45.9% designates an insignificant maximum for σ_3-axes. b) Comprehensive symbol for the deduced regional Stress field D. It shows a vertical σ_1-axis. The directions of σ_2 and σ_3 are insufficiently constrained. The background colours reflect predominantly low stress ratios. In total the stress ratios vary between R=0.0 and R=0.9.

4.4.5 Local phenomena

Tensional stress states that are older than compressional or strike-slip stress states

Two tensional stress states are regarded as a local phenomenon as they are unique in predating strike-slip respectively compressional stress states at the specific sites and as they are restricted to the area of the Hessian Depression and its northern prolongation (#23, #26; Fig. 51). For both these tensional stress states (ELV1, UPS1), the directions of extension are not well constrained, as the respective stress ratios are R=0.0 reflecting a deformation mode of vertical flattening.

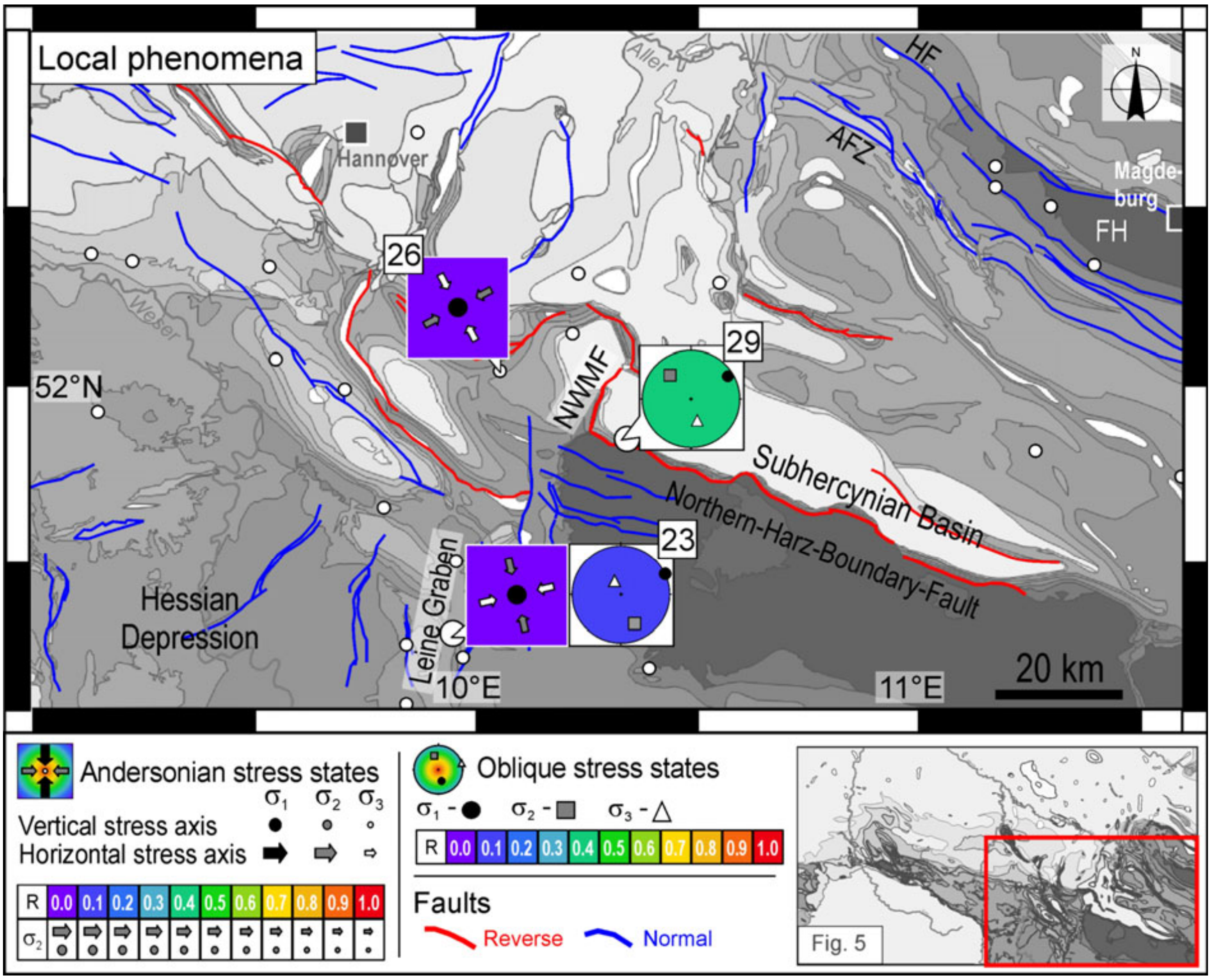

Figure 51: Stress states that are inconsistent with other stress states from the area in terms of directions of principal stress axes or temporal status. The symbolism distinguishes Andersonian stress states with a vertical principal axis from oblique stress states with none of the axes plunging by >70°. NWMF – Neuwallmoden Fault; further abbreviations as in Fig. 41.

Oblique stress states

Most of the stress states derived from sites across the Elbe Fault System are characterised by vertical respectively horizontal principal stress axes indicating typical stress conditions for the shallowest parts of the Earth's crust according to Anderson (1942). However, two of the estimated stress states are oblique in the sense that none of the associated stress axes plunges vertically (i.e. by >70°). These special stress configurations are derived from fault-slip data sampled at *Elvese* (#23; ELV2) which is located within the N-S-trending Leine Graben area and at *Langelsheim* (#29; LAN1) which is situated close to the Northern-Harz-Boundary Fault and the Neuwallmoden Fault (Fig. 51).

The obliquity of stress state ELV2 has been causally related to transpression and associated oblique movements along a pre-existing array of preferentially oriented faults (*Case study 8*). The almost vertical σ_3-axis and the NE-SW-directed σ_1 of ELV2 give reasons for a correlation with the group of compressional stress states (Fig. 40). Consequently, the oblique stress state ELV2 is supposed to correspond to a local expression of the regional Stress field A.

An explanation for the obliquity of LAN1, on the other hand, might be provided by the position of the related fault-slip data relative to large-scale structures in close vicinity of *Langelsheim* quarry. The NE-SW-directed maximum compression (σ_1) of LAN1 is consistent with the directions of σ_1 indicated by the regional Stress fields A and B as well as by other sites along the Northern Harz Boundary Fault (Franzke et al., 2007). The oblique bearings of σ_2 and σ_3, on the other hand, might be related to the position of *Langelsheim* between the WNW-ESE-striking Northern Harz Boundary Fault and the N-S-striking Neuwallmoden Fault (Fig. 51). Both faults are assumed to have been activated as reverse faults during a Late Cretaceous phase of inversion when the Lutter Anticline extending to the west of the Neuwallmoden Fault and the Harz Mountains both experienced uplift relative to the Subhercynian Basin (Mohr, 1982). The formation of the Lutter Anticline is supposed to have been strongly controlled by salt movements (Carlé, 1938). Assuming the reverse movements along the Northern Harz Boundary Fault and the Neuwallmoden Fault to have taken place coevally and considering the perpendicularity of their strike directions, stress states between these closely located faults would have had to balance divergent kinematics. At *Langelsheim*, the regional Stress field A might have been superposed by a more local stress state related to the movements along the Neuwallmoden Fault, thereby leading to a deviation of σ_2 and σ_3 as indicated by LAN1. A superposition of differently-directed stress states east of the Neuwallmoden Fault is also postulated as an explanation for differently-oriented horizontal stylolites (Hosseinidust, 1980).

4.5 Discussion

By applying the Stress Inversion Via Simulation, fault-slip patterns recorded along the Elbe Fault System have reliably been related to specific paleostress states. The correlation of these local stress states and the integration of chronological constraints have allowed a differentiation of four regional paleostress fields and the reconstruction of their relative timing. Finally, focus shall be laid on the role of these regional stress fields with respect to the history of the entire CEBS and concerning the mechanisms that characterise the interim rearrangements of stress configurations.

4.5.1 Chronology

Given the well-established evolution of the CEBS which implies several stages of intense tectonic activity – especially related to the *Initial rift phase*, the *Mid Triassic-Jurassic phase of E-W extension*, and the *Late Cretaceous-Early Tertiary phase of inversion* – it should be expected that the pattern of deformation structures presently observable within the basin reflects a wide variety of deformation events. The analysed fault-slip data, however, provide a less complex picture. Though the investigated units cover a wide stratigraphic scope from Upper Carboniferous to Upper Cretaceous rocks, the diversity of stress states indicated by the youngest rocks is not much expanded when considering also the results from stratigraphically older units. Accordingly, each of the deduced regional stress fields A, B, C, and D is documented by fault-slip data preserved within Upper Cretaceous rocks. Thus, these regional stress fields have verifiably been active during and/or after Late Cretaceous times which is during or after the basin-wide *Late Cretaceous – Early Tertiary phase of inversion*. Any pre-Late Cretaceous signs of deformation, on the other hand, are scarce.

Pre-Late Cretaceous signs of deformation

At two sites across the Hessian Depression, tensional stress states are interpreted to have predated stress states that are (post-) Late Cretaceous in age. The two tensional stress states show remarkably low stress ratios indicating regimes of vertical flattening. According to the stratigraphic position of the faulted rocks (*Muschelkalk*), the maximum age of these stress states dates back to Mid Triassic. According to their E-W- respectively NE-SW-directed σ_3-axes, the stress states might be related to the *Mid Triassic – Jurassic phase of E-W extension* which initiated the large N-S-striking grabens in the CEBS (e.g. Central Graben, Horn Graben, Glückstadt Graben). However, since the directions of extension are poorly constrained (due to low stress ratios), they might reflect any phase of extension between the Triassic and the Late Cretaceous.

Stress fields A and B: the phase of basin inversion

Stress field A corresponds to a (post-) Late Cretaceous compressional stress regime with a roughly NNE-SSW-directed σ_1 and a low stress ratio. This configuration complies with compressional strain indicated by folded or tilted structures across the whole study area. Furthermore, Stress field A has been identified as the oldest regionally detectable imprint which corresponds with the fact that the mentioned folding or tilting locally affected Upper Cretaceous strata already during sedimentation (during the Cenomanian). Stress field B, on the other hand, is strike-slip in character and corresponds to the most prominent imprint in the study area as indicated by the largest number of related local stress states. Stress fields A and B agree well in terms of a NNE-SSW-trending maximum compression and a low stress ratio, while there is clear evidence that B postdated A.

Considering the large-scale deformation pattern proposed for the *Late Cretaceous - Early Tertiary phase of inversion* in the CEBS – for example, the roughly WNW-ESE-trending inversion axes reconstructed from the distribution of preserved thicknesses of Upper Cretaceous rocks (Scheck-Wenderoth & Lamarche, 2005; Fig. 25) – the movements of individual blocks indicate a roughly NNE-SSW-directed contraction. This direction corresponds with the NNE-SSW-directed maximum compression indicated by the reconstructed stress fields A and B. Hence, during times of ongoing closure of the Tethys and rifting in the North Atlantic, the southern margin of the CEBS first experienced folding and reverse faulting under stress field A before the mode changed to strike-slip faulting controlled by stress field B.

A number of paleostress studies using fault-slip data from different areas across North Central Europe confirm the occurrence of Late Cretaceous - Early Tertiary stress states with a N-S- to NE-SW-directed σ_1. The respective compressional and strike-slip stress fields are consistently related to the phase of CEBS-wide inversion, irrespective if the fault-slip data have been sampled in southern Wales (Lisle & Vandycke, 1996), England, Northern France and Belgium (Vandycke, 2002), Germany (Franzke et al., 2007), or southern Poland (Lamarche et al., 1999, 2002).

The well-established NNE-SSW-direction of intraplate shortening can be correlated with geodynamic processes that originated far to the south of the CEBS: From ~85 Ma on, Africa was converging against Europe in a NE direction (Rosenbaum et al., 2002) while respective compression was controlling deformation in the Pyrenees (Capote et al., 2002). Based on fission track data, a similar timing has been determined for the initiation of inversion-related uplift in parts of the CEBS such as the Lower Saxony Basin (c. 89-72 Ma; Senglaub et al. 2005, 2006) and the Subhercynian Basin (85 Ma; Thomson et al.; 1997).

A correlation of Late Cretaceous intraplate stresses in the CEBS with the Africa-Iberia-Europe convergence agrees with a recently published concept on causal mechanisms for the CEBS-wide inversion (Kley & Voigt, 2008). On the other hand, N- to NNE-directed contraction is also supposed to have been induced by early (e.g. Eocene) stages in the evolution of Alpine convergence indicated, for instance, by movements of the Austroalpine and Penninic thrust complex over the Helvetic units of the European shelf (Schmid et al., 1996; Pfiffner et al., 2002). Accordingly, an Eocene N-S-directed compression has been

derived from fault-slip data in southern Germany and eastern France (Bergerat, 1987; Homberg et al., 2002).
In the studied area of the Elbe Fault System, any closer constraints on the timing of the regional Stress fields A and B are missing due to mainly unconsolidated Cenozoic rocks that do not provide adequate data for a fault-slip analysis. For this reason, both stress fields might be causally related to the Late Cretaceous Africa-Iberia-Europe convergence and/or a Tertiary phase of Alpine orogeny. Despite of some sites in the study area that indicate a shift from a NE-directed σ_1 to a NNE- or N-directed σ_1, it has been desisted from a more detailed temporal differentiation of stress states, since the spatial variations of σ_1 are as large as any temporal ones would be (Fig. 44).
Better conditions for a fault-slip analysis on the post-Late Cretaceous evolution of stress states are given in parts of southern Poland where a Maastrichtian–Paleocene strike-slip regime with NE-SW-oriented σ_1 has been distinguished from a late Mid Miocene N-S-directed compression (Lamarche et al., 2002). The reconstructed Maastrichtian–Paleocene regime caused tectonic inversion of the Mid-Polish Trough accompanied by strike-slip faulting as well as localized folding. The respective deformation patterns observable in the Holy Cross Mountains are interpreted as being related to a shallow reactivation of the pre-existing Teisseyre-Tornquist Zone. After a Mid Miocene interim phase of N-S-directed extension, a phase of late Mid Miocene N-S-directed compression has been induced by the Carpathian orogeny and affected predominantly the Carpathian Front while the Holy Cross Mountains remained mainly unaffected.

Stress fields C and D: the transition to present-day stress conditions
Stress field C integrates strike-slip stress states with a horizontal, roughly NW-SE-directed maximum compression and mainly intermediate stress ratios. Though a number of 12 outcrops reveal fault-slip data attesting to both B-related and C-related stress states, the posteriority of Stress field C relative to B is only poorly constrained by field observations. However, palinspastic reconstructions implementing paleomagnetic measurements and Cenozoic kinematics of major structures in Central Europe argue for an Eocene to Miocene aged rotation of the direction of maximum horizontal stress (S_{Hmax}) from a NNE- to a NW-direction (Schreiber & Rotsch, 1998). This rearrangement of stress states would confirm Stress field C to have postdated Stress field B. Furthermore, the direction of maximum compression indicated by Stress field C coincides with the NW–SE-directed S_{Hmax} of the present-day stress field within the subsalt layers of large parts of the study area (Roth & Fleckenstein, 2001; Heidbach et al., 2008). Since the present-day stress conditions in the study area are supposed to have been initiated in the Miocene, Stress field C would be related to post-Miocene times.
According to the present paleostress analysis, the latest signs of preserved faulting correspond to the tensional stress field D which widely corresponds to radial extension as indicated by a low mean of stress ratios and a large diversity of locally estimated σ_3-axes. Extensional tectonics are supposed to have governed areas north of the Alps during most of the Palaeogene (Reicherter et al., 2008), but also recent stresses are partly released by normal kinematics in the study area (Heidbach et al., 2008). Moreover, wide parts of North Central Europe provide evidence for extensional regimes of Neogene ages such as a N–S-directed extension detected in SE Poland (Lamarche et al., 2002), a NE–SW-directed extension in prominent N–S-striking structures of Central Europe (Reicherter et al., 2008) or differently oriented extensional regimes found in southern Wales and NE-Belgium (Vandycke, 2002). A succession of differently oriented tensional stress states is also indicated by subsurface fault-slip patterns in the Groningen Block northwest of the Lower Saxony Basin: a first E-W-directed extension is dated to the latest Cretaceous, a later E-W-directed extension is dated to 52-19 Ma, and a phase of NE-SW-directed extension is supposed to have started after 19 Ma

and to have persisted until the present (van Gent et al., in press). Hence, also stress field D might potentially have led over to present-day stress configurations. A more precise dating of this stress field would require a correlation with fault-slip data and stresses derived from differently aged Cenozoic rocks which, however, are not available in the study area.

4.5.2 Mechanisms

The described evolution of regional stress fields has been developed based on the assumption that any fundamental difference in the directions of principal stress axes corresponds to a change of the overall tectonic stress field. However, observations on present-day stress states inferred from earthquake focal mechanisms, for instance, show that the mode of a local stress state might change during a single earthquake while the deformation-controlling plate tectonic setting remains the same (Giner-Robles et al., 2003). A very frequent type of stress change recorded during a seismic cycle corresponds to a permutation of principal stress (or strain) axes while the relative orientation of the stress ellipsoid remains constant. Most permutations concern σ_2 and σ_3, or σ_1 and σ_2, but switches between σ_1 and σ_3 have also been described (Angelier et al., 2008). The authors relate the widespread phenomenon of permutations to an elastic response of the shallow crust to deformation, including elastic rebound and stress drop. Furthermore, Hu & Angelier (2004) showed on the base of numerical modelling that major causes for stress permutations include the heterogeneity of brittle deformation and the resulting anisotropy of rock mechanical properties due to fracturing and faulting.
Considering the reconstructed regional stress fields, it is obvious that the difference between A and B corresponds to a permutation of σ_2 and σ_3, whereas the difference between B and C roughly matches a permutation of σ_1 and σ_3. In light of this, the mechanical relationships between different stress states are discussed including arguments for posteriority or simultaneity of stress states.

Stress fields A and B

The temporal relation between the compressional Stress field A and the strike-slip Stress field B is unambiguously constrained at sites along the Osning Lineament where phases of reverse faulting and folding clearly have predated strike-slip faulting (*Case studies 2, 3, 4*). A general simultaneity of A and B thus can be excluded. The observation that folding in the Lower Saxony Basin already began during deposition of Upper Cretaceous rocks, on the other hand, corresponds with a synsedimentary tilting of Upper Cretaceous strata in the Subhercynian Basin as indicated by several angular unconformities which are regarded as being partly related to the activation of the Northern Harz Boundary Fault (Voigt et al., 2004). In general, the effects of Stress field A are more restricted to areas close to large fault zones (such as the Osning Lineament), whereas the effects of Stress field B can be traced also farther to the north, i.e. into the Flechtingen High area (Fig. 41, 44). The large number and the wide distribution of local stress states related to Stress fields A and B document a strong intensity of deformation during the *Late Cretaceous - Early Tertiary phase of inversion*. This effectiveness might explain why the traces of older phases of brittle deformation are scarcely observable: Signs of the inversion phase are preserved by the whole range of differently-aged rocks arguing for a high degree of reactivation of potentially pre-existing faults and fractures. Furthermore, the observed intensity of faulting complies with strong vertical movements documented by individual blocks: According to fission track analysis, the Paleozoic block of the Harz Mountains is supposed to have been uplifted along the Northern Harz Boundary Fault by at least 5 km (at c. 85 Ma; Thomson et al., 1997), while the sediments of the Lower Saxony Basin experienced uplift along the Osning Lineament by at least 4 km (c. 89-72 Ma; Senglaub et al. 2005, 2006).

There is an ongoing discussion on the general mode of deformation along the faults of the Elbe Fault System. For example, Voigt et al. (2004) regard the Northern Harz Boundary Fault as a frontal thrust above a steep basement thrust, while others consider both the Osning Lineament and the Northern Harz Boundary Fault to have been activated as large wrench fault systems during the phase of inversion (Drozdzewski, 1988; Wrede; 1988). The contribution of the present study to this discussion is limited as it is not known at what depth the recorded faults have been activated. If having been activated at greater depth, the reverse faults of Stress field A may identify the basement faults as flat thrusts. Any activation at shallower depth, on the other hand, might reflect either a thrust environment or a deeply-rooted strike-slip fault under transpression. Interestingly, there are no steeply inclined reverse faults observable, neither along the Osning Lineament nor along the Northern Harz Boundary Fault. In any case, the great number of strike-slip stress states which exceeds the number of reverse stress states in the study area, argues for a considerable intensity of wrench tectonics along the Elbe Fault System.

Stress field C

As mentioned, the difference between the strike-slip Stress fields B and C could be explained by a permutation of σ_1 and σ_3 corresponding to a change in the direction of maximum horizontal compression from NE-SW to NW-SE. This regional permutation can also be found on the outcrop scale: At *Mammendorf* (#36), for instance, a B-related stress state shows a N-S-striking σ_1, while a C-related stress state reveals an E-W-striking σ_1. For comparison, at *Bodendorf* (#32), σ_1 “changes” from NE-SW to NW-SE. Thus, at both sites – like at several others – the axial orientation of the respective stress ellipsoid remains constant while its shape changes. The assumption that the regional Stress field C corresponds to a discrete event that has postdated B is rather based on consistencies between C and the present-day stress conditions in the area than on unambiguous chronological indicators derived from the field which are remarkably scarce.

Summarising the facts, for stress field C and its relation to B the concept of axes permutations under a constant overall stress provides a solution at least as reasonable as the concept of superposed tectonic phases. Consequently, the stress states related to C might not be indicative for a separate tectonic phase, but for local variations of stress during the strike-slip phase of inversion.

Stress field D

The posteriority of the tensional stress field D relative to compression and wrench in the study area is well constrained due to related large-scale structures as well as several superimposed striations. This temporal consistency between locally derived tensional stress states is in contrast to the great diversity in related directions of minimum compression that might imply a diversity of related mechanisms.

Along the Osning Lineament, basically two different directions of extension have been observed, one roughly parallel and one perpendicular to the strike of the lineament (Fig. 33). Extension perpendicular to the Osning Lineament corresponds to movements which are parallel to but opposing the former inversion-related direction of maximum compression. Such a σ_1/σ_3-permutation might be related to a drop of the tectonic (inversion-related) stress component and a sudden predominance of the vertical component of stress. Accordingly, Kockel (2003) describes such a relaxation of stresses as a major cause for normal faulting affecting many of the formerly inverted structures in northern Europe.

In principle, the observed extension parallel to the WNW-striking Osning Lineament could likewise be related to stress relaxation and associated permutations. On the other hand, such a roughly E-W-directed extension fits with the predominantly N-S-trending Cenozoic depocentres in the CEBS the formation of which is supposed to have been controlled by thermal relaxation or flexural bending of the North Sea lithosphere (Ziegler, 1990; van Wees & Beekman, 2000; Hansen & Nielsen, 2003; Scheck-Wenderoth & Lamarche, 2005). Furthermore, Central Europe has been governed by extensional tectonics that created the roughly N-S-trending European Cenozoic Rift System during the Eocene to Miocene (Reicherter et al., 2008).

In contrast to the Osning Lineament area, the Hessian Depression and the Subhercynian Basin show tensional stress states with mainly low stress ratios. Such stress conditions correspond to radial extension and might be associated to the rise of salt structures. It is known, that since Mid Triassic times, *Zechstein* salt layers have recurrently been mobilised, in particular during late Tertiary regional extension (Scheck et al. 2002a,b; 2003a,b; Kockel, 2003; Maystrenko et al., 2006). It should be noted, however, that tensional stress states with low stress ratios have also been obtained from rocks without any salt structures underneath, as the Upper Carboniferous volcanics at of the Flechtingen High area (#32). This observation accounts for the fact that salt movements in general do not trigger but result from differential stresses. In the study area, tectonically induced extension might thus have initiated the ascent of salt structures which, in turn, might have altered the local stress states and promoted radial extension. Such a process is comparable to stress modifications in the vicinity of uprising magmatic material (Suppe, 1985): the ascent of material may exert an additional component to the vertical stress axis while indirectly decreasing the relative magnitudes of horizontal axes. Local variations of stress states caused by salt tectonics are also expressed by the recent stress field in northern Germany which shows differences in the orientations of S_{Hmax} between subsaline and suprasaline formations (Roth & Fleckenstein, 2001).

Comprehensive deformation model

The reconstructed succession of a compressional stress field (A) followed by a strike-slip stress field (B) and finally by a tensional stress field (D) is comparable to the Cenozoic evolution of paleostresses in the Alpine foreland as described by Letouzy (1986; Fig. 52). For both areas, the development of stress fields occurred under a constant orientation of the principal axes while implying two stages of stress permutation. The causative mechanisms for such a development as provided by Letouzy's (1996) model comprise (i) gradual decrease of the tectonic components of stress and (ii) uplift to shallower depth where non-isotropic stress conditions are supposed to be related to an increasing relative magnitude of the vertical stress component. Accordingly, this model implements a main phase of intense compression which is followed by weaker phases of strike-slip and normal faulting. This development corresponds with the findings from the Elbe Fault System area where the inversion-related stress fields A and B are the dominant imprints and supposed to have acted coevally with the strongest recorded uplift, whereas the weaker tensional stress field D has postdated A and B.

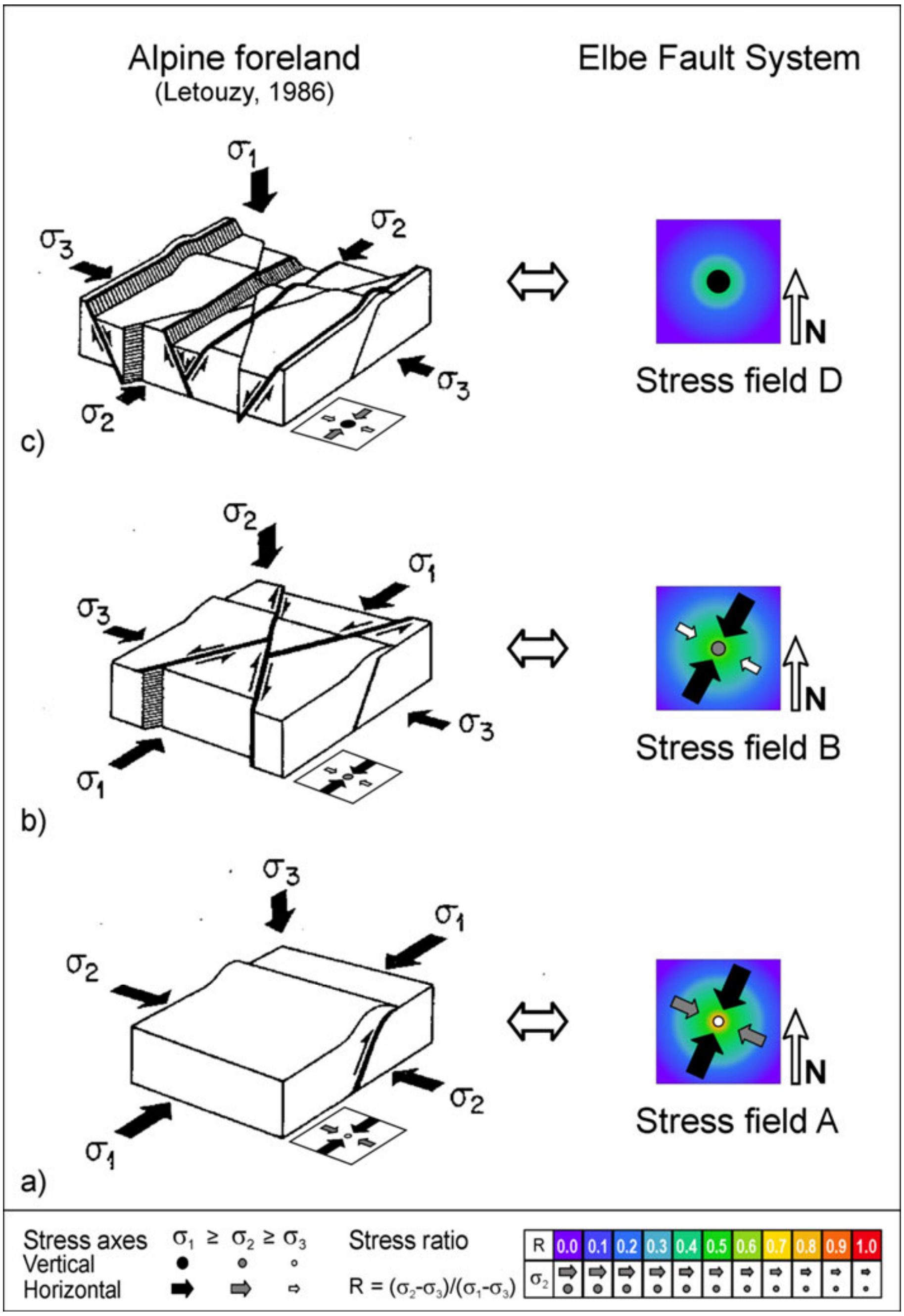

Figure 52: Correlation of the reconstructed regional paleostress fields (A, B, D) with a stress and strain model derived from structural data in the Alpine foreland (Letouzy, 1986). According to Letouzy's model, a gradual decrease of the magnitudes of compressive tectonic stresses and a continuous increase of the relative magnitude of the vertical stress component due to uplift to shallower depths are supposed to result in a regional development from a compressional stress regime (a) to a strike-slip stress regime (b) and finally to a tensional stress regime (c).

4.6 Summary and conclusions

The fault-slip analysis performed for the area of the Elbe Fault System argues for the following evolution of regional paleostress fields:

- A compressional Stress field A with a N-S- to NE-SW-directed maximum compression induced reverse faulting and folding in large parts of the area. This stress field is at most as old as Cenomanian/Turonian and related to the *Late Cretaceous - Early Tertiary phase of inversion* that affected much of the CEBS.
- Postdating Stress field A, a strike-slip Stress field B with a N-S- to NE-SW-directed maximum compression produced the strongest imprint of brittle deformation detectable in the area. Stress field B can likewise be correlated with the *Late Cretaceous - Early Tertiary phase of inversion*.
- A number of local strike-slip stress states with E-W- to NW-SE-directed maximum compression might be interpreted as indicating a regional stress field C that postdated B. This stress field corresponds well with the present-day stress field of the area in terms of the direction of maximum horizontal compression. On the other hand, the local stress states associated to C might be related to permutations of principal axes induced by stress relaxation due to faulting under Stress field B.
- The youngest reconstructed stress regime is tensional in character with no pronounced direction of horizontal extension. It can temporally be correlated with the *Cenozoic phase of subsidence* which induced strongest vertical movements in the North Sea while kinematically it corresponds with Palaeogene to recent extensional tectonics recorded for large parts of Central Europe. The predominantly low stress ratios of tensional stress states (radial extension) might locally have been induced by uprising salt structures.

Despite a wide stratigraphic scope of investigated rocks covering Upper Carboniferous to Upper Cretaceous units, the brittle signs of deformation regionally traceable in the rocks are exclusively (post-) Late Cretaceous in age. The scarcity of pre-Late Cretaceous signs of faulting indicates that inversion-related deformation widely overprinted potential traces of earlier deformation corresponding to an extensive “reprogramming” of the observable signs of deformation. This reprogramming might be related to the role of the Elbe Fault System during the phase of inversion: Being characterised by a weak and stress-sensitive zone in the lower crust, strain localisation may have turned the Elbe Fault System into one of the most intensely deformed areas. This is in contrast to more central parts of the CEBS where fault structures also document stress states of pre-inversion phases (Lohr, 2007; van Gent et al., in press). Finally, the high consistency of local paleostress states characterises the investigated area as a relatively homogeneous unit without any major kinematic differences between single domains.

5 The Oslo Graben area

To shed light on the evolution of paleostress fields in the northern parts of the CEBS, the present study has laid one of its foci on the Oslo Graben area which is located north of the Tornquist Zone (TZ). The on-land Oslo Graben and the offshore Skagerrak Graben constitute together the roughly N-S-trending Oslo Paleorift System which was one of the areas of pronounced magmatic activity during the Permo-Carboniferous *initial rift phase* that affected almost the entire CEBS. During this phase, areas like the Oslo Graben in the north and the North German Basin in the south were belonging to an extensive volcanic province (Neumann et al., 2004). During later times, the Oslo Rift area is supposed to have acted as the prolonged northern arm of the Northern Permian Basin (Larsen et al., 2008). These connections indicate that the developments of the Oslo Rift and the CEBS have been related – at least during early stages in the evolution of the CEBS. Due to the abundance of Permo-Carboniferous magmatic rocks in the Oslo Graben area (Fig. 7), its rift-related history is well known. A reconstruction of the post-rift development, in contrast, is complicated by the lack of any outcropping post-Permian units.

5.1 The Oslo Graben as part of the Oslo Rift System

The Oslo paleorift system terminates to the south in the Sorgenfrei-Tornquist Zone (STZ) which is the northwestern prolongation of the Teisseyre-Tornquist Zone (TTZ; Fig. 1). The TTZ forms the boundary between the Precambrian East European Platform and the accreted parts of Phanerozoic Western Europe. On the contrary, there is still an ongoing discussion on the structural role of the STZ with respect to the Baltic Shield. Some authors regard the STZ to lie within the Precambrian Baltic shield (EUGENO-S Working Group, 1988), whereas more recent studies postulate the STZ to represent the border of Baltica (Lie & Anderson, 1998; Babuska & Plomerova, 2004). Several authors have suggested that the Permo-Carboniferous initiation of the Oslo Rift has been closely tied to concurrent tectonics along the TZ (Glennie, 1984; Sundvoll et al., 1990; Ziegler, 1990; Veevers et al., 1994). During Variscan times, for example, the TZ is supposed to have experienced wrench deformation and dextral movements controlled by collision-related stresses in the south which, in turn, have induced approximately E-W directed extension north of the TZ, i.e. in the Oslo Rift (Sundvoll et al., 1992). Moreover, the main phase of extension affecting the Oslo region went along with a deepening of pull-apart basins within the TZ (Erlström et al., 1997).

5.1.1 Geometry and structure of the Oslo Rift System

The Oslo Rift is constituted by an en-echelon array of graben segments (Ramberg, 1976; Ramberg & Larsen, 1978; Larsen et al., 2008): the Rendalen, Akershus and Vestfold Graben Segments form the northern and central on-land parts, whereas the Skagerrak Graben is the southern off-shore segment of the rift system (Fig. 53). These segments reveal sigmoidal plan view and form an overall rift axis trending roughly NNE-SSW as confirmed by fault patterns and geophysical features. In cross-section, the on-land segments represent asymmetrically shaped half-grabens with different subsidence polarities: The Rendalen Graben segment is bordered to the east by a west-verging master fault system (Skjeseth, 1963; Larsen et al., 2006). The Akershus Graben segment reveals an east-verging master fault to the west, while the Vestfold Graben segment shows a west-verging master fault to the east (Ramberg & Larsen, 1978). The latter two segments are linked by an accommodation zone with a joining fault to the west of the city of Oslo, the Kjaglidalen-Krokkleiva Tranfer Fault (KKTF; Heeremans et al., 1996). Finally, the Skagerrak Graben which abuts against the STZ is composed of several more or less overlapping graben segments (Heeremans et al., 2004).

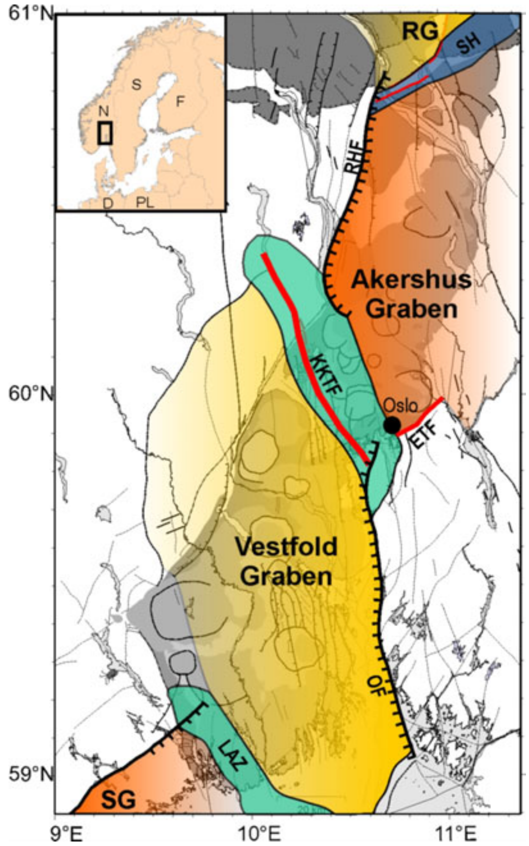

Figure 53: Sketch map of the Oslo Rift System (modified after Larsen et al., 2008 and Ranberg & Larsen, 1978). This paleorift is structured by an array of graben segments with different graben polarities. Master faults (black), accommodation structures (green and blue) and transfer fault zones (red) are labelled by abbreviations: ETF - Ekeberg Transfer Fault, KKTF - Kjaglidalen-Krokkleiva-Transfer Fault, LAZ - Langesund Accommodation Zone, OF - Oslofjord Fault, RG - Rendalen Graben, RHF - Randsfjorden-Hunnselv Fault, SG - Skagerrak Graben, SH – Solberg Horst.

5.1.2 Permo-Carboniferous rift evolution

After a first tectonomagmatic model for the evolution of the Oslo Rift has been provided by Ramberg and Larsen (1978), an ever growing pool of seismic, structural, geochemical, and paleomagnetic data has allowed refining the respective models (Russell, 1983; Sundvoll et al., 1990; Neumann et al., 1992; Neumann, 1994; Ro and Faleide, 1992; Sundvoll et al., 1992; Sundvoll and Larsen, 1994; Olaussen et al., 1994; Heeremans et al., 1996; Torsvik et al., 1998; Larsen et al., 2008). According to Larsen et al. (2008), the evolution of the Oslo Rift can be subdivided into 6 progression phases commencing in Late Carboniferous times and spanning about 65 million years:
During the proto-rift stage (*rift stage 1*), a thin sequence of clastic and evaporitic sediments ("Asker Group") has been deposited into a shallow depression unconformably on top of a deformed Cambro-Silurian sedimentary succession. Coevally, magmatic activity started with the emplacement of sill intrusions (ca. 305-300 Ma old syenites and basic camptonites; Sundvoll et al., 1992; Sundvoll & Larsen, 1994). The initial rifting phase (*rift stage 2*) mainly exhibits basaltic lava flows ("B1"), the oldest of which are found in the southern parts of the Oslo Graben area where they exhibit a radiometric age of 300±1 Ma (Corfu & Dahlgren,

2007). The climax stage of rifting (*rift stage 3*) is marked by intensive eruptions of trachyandesitic rhomb porphyry lavas (Larsen et al., 2008). In the southern parts of the graben, the rhomb porphyry lavas were dated to 294-283 Ma, whereas for the northern parts ages of 290-276 Ma were estimated (Sundvoll et al., 1990). Postdating this main volcanic phase, but still occurring during the main phase of rifting, extensive vertical movements along graben-flanking master faults have been discovered (Heeremans & Faleide, 2004). During *rift stage 4*, central volcanoes first produced mainly alkaline olivine basalts, and then matured petrologically to leave residual felsic melt products that finally erupted explosively by caldera formation. Some of the caldera-related ignimbrites have been dated to 288 Ma and 285 Ma (Sundvoll & Larsen, 1990), thus marking the end of the main extrusive period in the Oslo Graben. The magmatic aftermath stage (*rift stage 5*) is supposed to have lasted from ca. 265 to 255 Ma and has been characterised by the emplacement of mostly alkali syenitic to alkali granitic batholiths (Larsen et al. 2008). Finally, during the last stage of magmatic activity (*rift stage 6*), granitic intrusions with ages between 250 and 245 Ma have been emplaced (Sundvoll et al., 1990).

5.1.3 Post-rift evolution

As a result of 65 Ma of intense tectonomagmatic activity, the present total volume of magmatic rocks in the Oslo Graben amounts to about 28,000 km^3 (Ramberg, 1976). However, the lavas presently exposed in fault-bounded blocks along the graben are only remnants of a formerly much larger lava cover; they are estimated in total to about half the originally generated volume, whereas large amounts already have been eroded. The causes for erosion are provided by two phases of uplift reflected by apatite fission track data (Rohrman et al., 1995): during Triassic-Jurassic times (~220-160Ma) a total of 1.3-3.5 km of overburden is supposed to have been removed as a result of rift margin erosion. On the other hand, a Neogene (~30 Ma) phase of domal uplift caused erosion of 1.5-2.5 km of overburden. This younger phase of denudation is supposed to be related to a combination of mantle convection and the operation of intraplate stresses which are slightly overprinted by Plio-Pleistocene glacial erosion effects. Postglacial unloading is documented to have had its dominant impact right after the end of the latest ice age (ca. 9 ka) as indicated by signs of large earthquakes (Gregersen, 1992). Beside the described mostly vertical movements, no major tectonic or magmatic activity has been denoted for post-rift times (Sundvoll & Larsen, 1994). This long-lasting tectonic quiescence is supported by the outcomes of an earlier paleostress study based on fault-slip data from the Oslo Graben area (Heeremans et al., 1996).
As inferred from earthquake focal mechanisms in the area of the Oslo Graben and surroundings, the present-day regional stress field is characterised by a NW-SE-direction of maximum horizontal compression (S_{Hmax}; Gregersen, 1992; Lindholm et al., 2000) which correlates with large parts of Northern Europe (Heidbach et al., 2008) and is mainly regarded a result of ridge push forces induced by spreading in the Atlantic domains.

5.2 Estimated paleostress states

A total number of 2191 fault-slip data are used for the present paleostress analysis in the Oslo Graben area (Appendix B; Fig. 54). These fault-slip data are complemented by 157 dykes and 232 veins, all having been assembled from 101 locations spread all across the graben area with exposed rocks of Precambrian, Cambro-Silurian and Permian ages (Fig. 7; Tab. 2).
In analogy to the processing of fault-slip data from the southern margin of the CEBS (Chapter 4), the Stress Inversion Via Simulation is applied separately to fault populations

from different sites in the Oslo Graben area. This procedure results in a total number of 194 reduced stress tensors (Fig. 55). At many sites, the preserved fault populations are heterogeneous resulting in several estimated stress tensors. In total, these locally derived stress states comprise 7 compressional stress states (sub-vertical σ_3), 70 tensional stress states (sub-vertical σ_1), 37 strike-slip stress states (sub-vertical σ_2), and 80 oblique stress states (no vertical principal axis). Such a kinematic pre-classification follows the assumption that regional stress regimes of a different mode (i.e. compressional, wrench, tensional, or oblique) are unlikely to control the same area at the same time. Hence, this arrangement is a first step in unravelling the evolution of paleostress fields in the area – a preliminary step that will have to be verified though.

Figure 54: Slickenside with calcite fibres indicating oblique-normal slip along a fault-plane within Upper Silurian limestones exposed at Åsa (site #17; photo by M. Heeremans).

Figure 55: (continued next page)

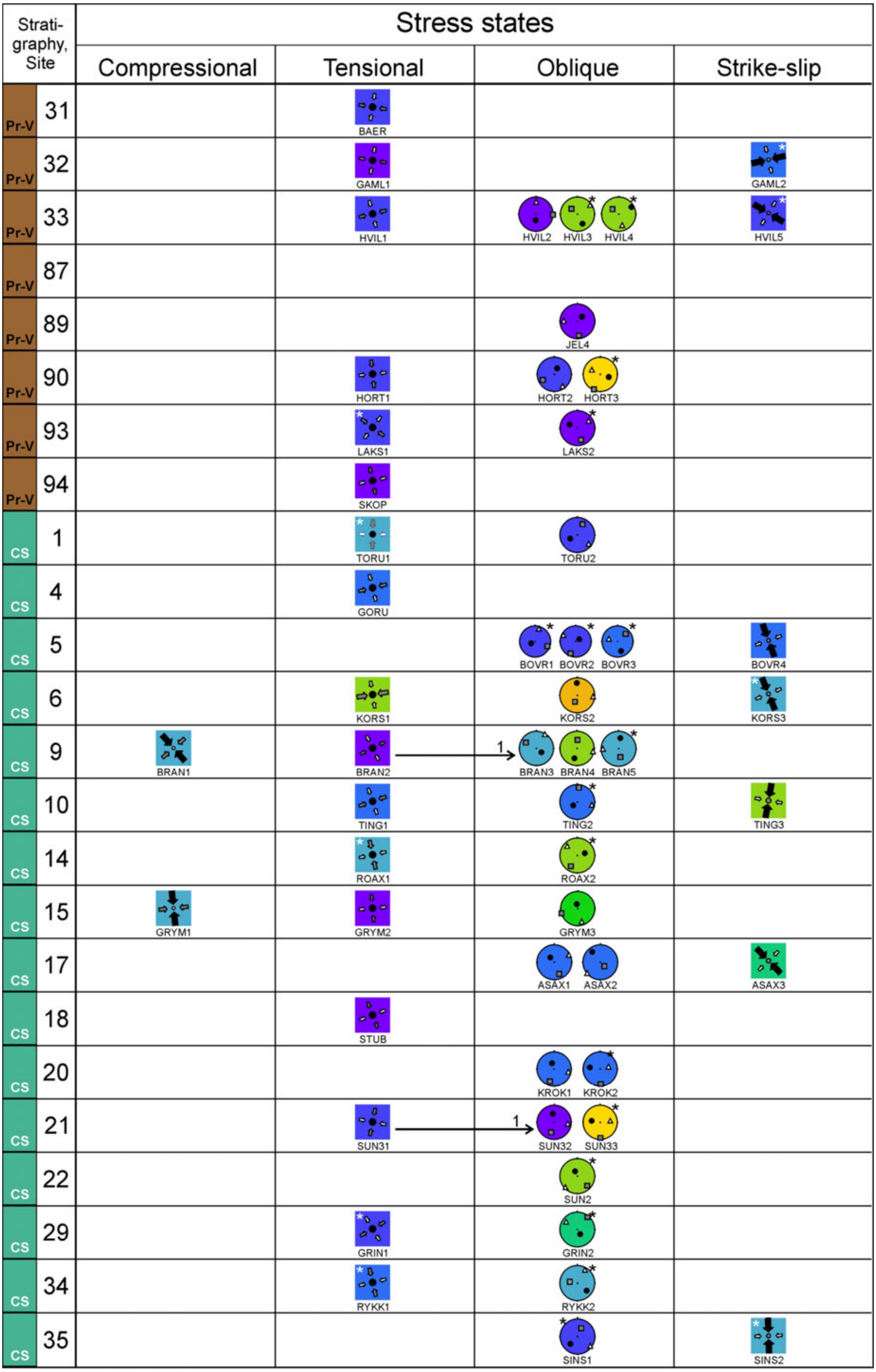

Figure 55: (continued next page)

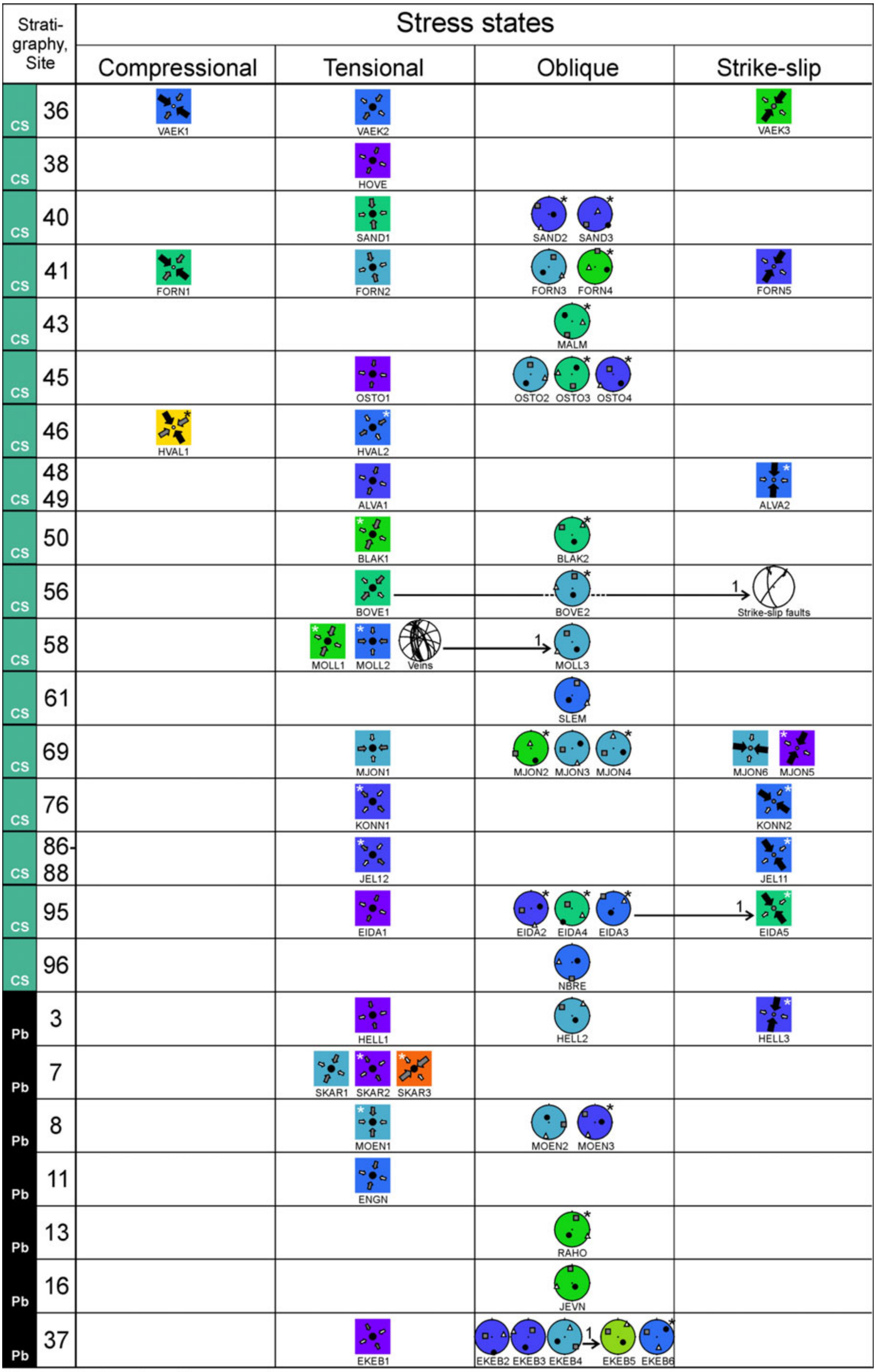

Figure 55: (continued next page)

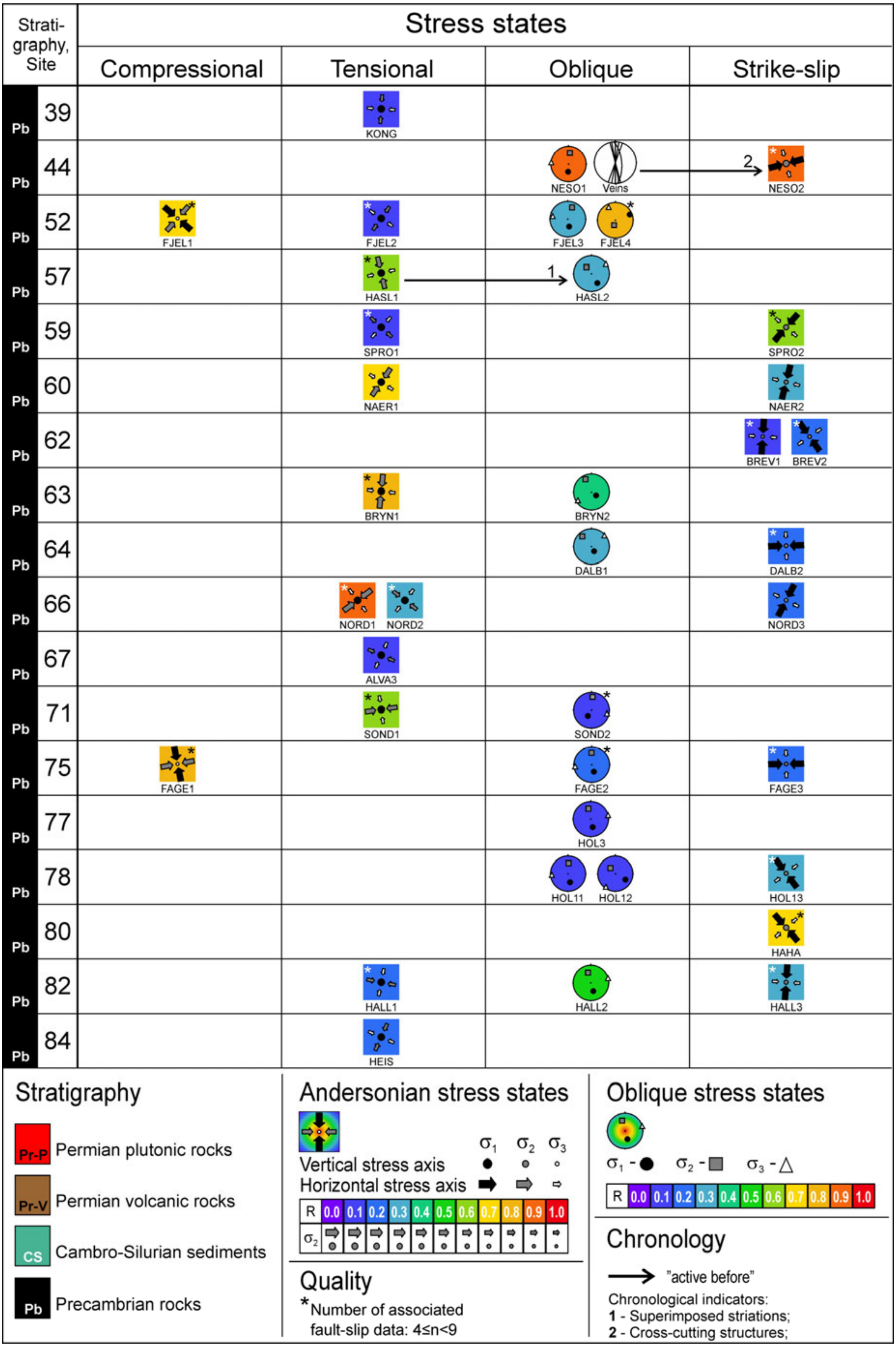

Figure 55: Paleostress tensors estimated for the Oslo Graben area. Sites are stratigraphically ordered. Stress states that are based on less than 9 fault-slip data are marked by an asterisk. Locally observed chronologies are indicated by arrows connecting the respective stress states.

5.2.1 Direct constraints on the relative timing of stress states

The ages of investigated rocks and the relative arrangement of individual fault-slip data observed in the field are the two first-order criteria for the relative timing of stress states. In the Oslo Graben area, the occurrence of compressional stress states is restricted to Precambrian and Cambro-Silurian rocks while tensional, strike-slip, and oblique stress states are documented by fault-slip data preserved by all exposed rock ages (Fig. 55). The lack of any compressional stress states in Permian rocks thus may identify this group of stresses as pre-Permian aged.
Other indicators for a temporal classification of stress states in the Oslo Graben area are provided by superimposed striations and relations of fault-slip data to other preserved structural elements (Fig. 55). At Hasle (#57), for example, several N-S-striking fault planes show two generations of striations: an older group of striae related to the tensional stress state HASL1 (E-W extension) and a younger group of oblique-normal senses related to the oblique stress state HASL2. Superimposed striations that locally prove a tensional stress state to have been active before an oblique stress state are also found at Brandbu (#9), at Jaren (#12) and at Sundvollen3 (#21). An agreeing relative timing of tensional and oblique stress states is found at Mølleveien (#58) where some sub-vertical surfaces striking N-S are interpreted as having initially been formed as calcite-filled veins which were later reactivated as oblique-normal (sinistral) faults. The pure tensile component of these structures (the veins) may correspond to the tensional stress state MOLL1 with an E-W-directed σ_3, whereas the oblique-normal slip direction clearly is related to the oblique stress state MOLL3.
At other places, superimposed striations argue for strike-slip stress states to be younger than tensional stress states (Boveien, #56) or strike-slip stress states to be younger than oblique stress states (Eidanger, #95). A more indirect indication for the relative timing of an oblique stress state and a strike-slip stress state is given at Nesoddtangen (#44): a N-S-striking calcite-filled vein indicates approximately E-W-directed extension corresponding with the σ_3-axis of the oblique stress state NESO1. This calcite vein is offset by a WNW-ESE-striking sinistral fault which is related to the strike-slip stress state NESO2. Assuming the vein to have formed under NESO1, the strike-slip stress state is younger than the oblique stress state.
The local chronologies presented in Figure 55 show consistencies that are a first approval of a cross-outcrop correlation of locally estimated stress states. Considering all available chronological indicators, tensional stress states tend to be older than oblique stress states, while the latter in turn tend to be older than strike-slip stress states. As these tendencies are based on only 8 single observations, a generalisation for the total diversity of inferred stress states in the Oslo graben area must remain tentative. However, the previously proposed separation of a group of oblique stress states from the classical Andersonian stress states is confirmed: though the oblique stress states are non-uniform in terms of directions of principal stress axes, their consistent relative timing clearly distinguishes them as a group of a separate and maybe common temporal status.

5.2.2 Regional implications

Compressional stress states
The occurrence of compressional stress tensors in the Oslo Graben area is not only restricted stratigraphically to pre-Permian rocks but also spatially to only seven locations (Fig. 56). The seven compressional stress tensors are very consistent with regard to the directions of σ_1 which strike roughly NW-SE (Fig. 57a). This kinematic consistency, in turn, argues for a common causal source – a common regional stress field – that these stress states have been related to.

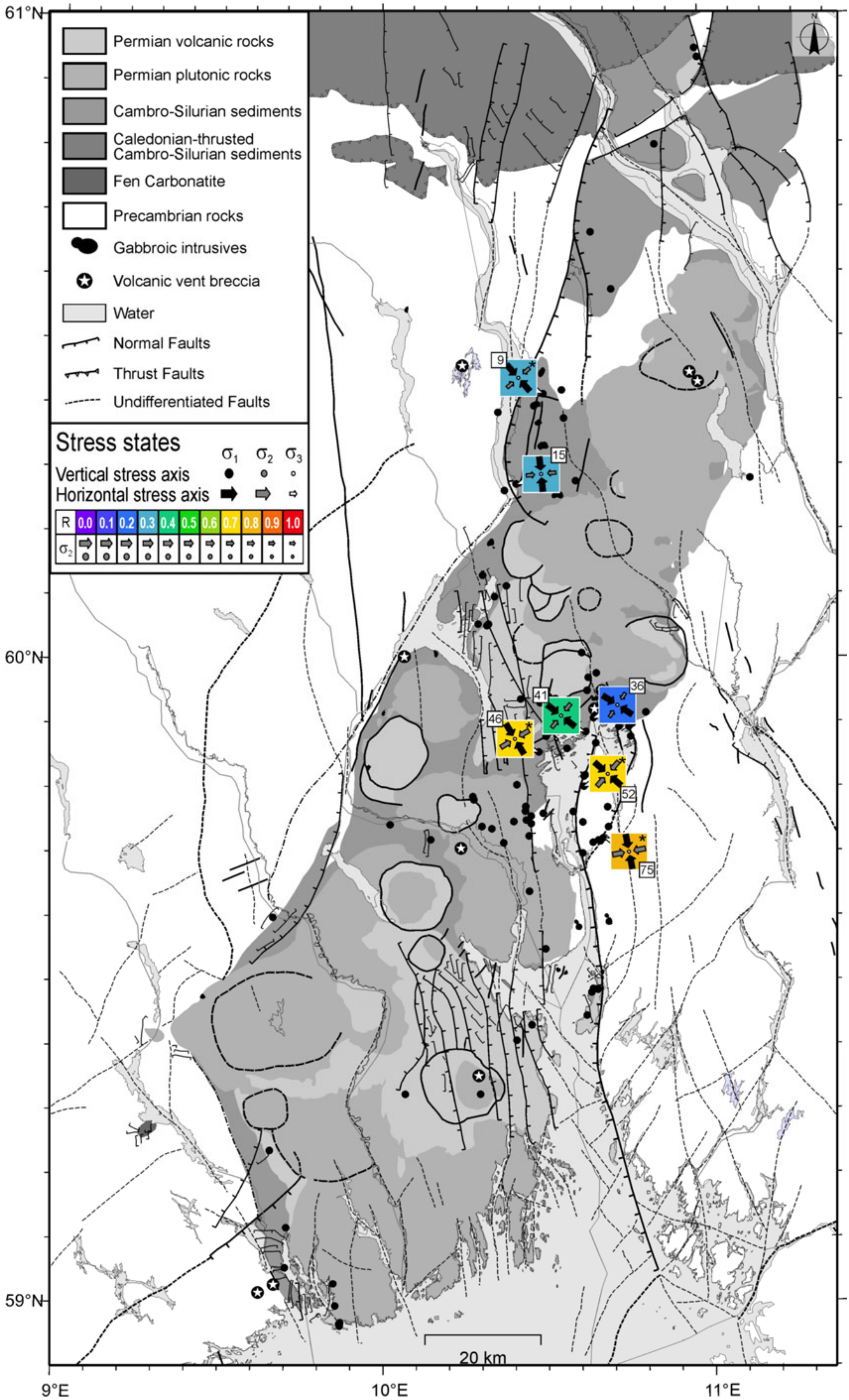

Figure 56: Compressional stress states derived from fault-slip data in the Oslo Graben area. Stress states that are based on less than 9 fault-slip data are marked by an asterisk.

To characterise this particular stress regime ("Stress field X"), the mean vector of σ_1-axes has been calculated to be oriented 324/07. Interestingly, the mean direction of σ_1 corresponds well with the direction of maximum compression derived from folded bedding planes within Cambro-Silurian sediments (324/00; Fig. 58). These rocks are supposed to have been folded in the course of the Caledonian Orogeny (Worsley et al., 1982; Bjørlykke, 1983; Bockelie & Nystuen, 1985). Regarding the compressional stress states and the folding as being related to the same tectonic stage, the deduced regional stress field consequently reflects a Caledonian phase of compression controlled by a NW-SE-directed σ_1 and an intermediate stress ratio (R=0.2 to R=0.8; Fig. 57b).

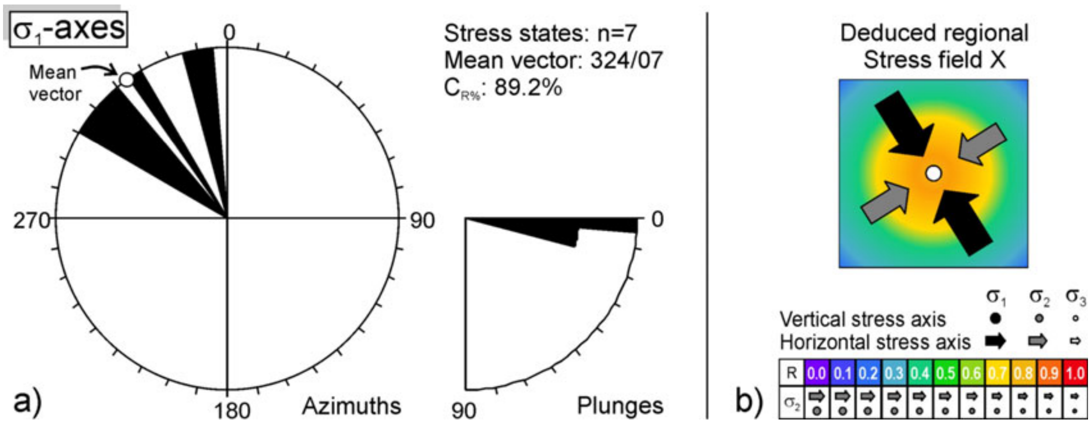

Figure 57: Potential regional Stress field X inferred from compressional stress states. a) Rose diagram with σ_1-directions of all compressional stress tensors. The azimuths of σ_1-axes strike consistently around NW. None of the σ_1-plunges deviates by more than 13° from the horizontal. To infer an overall stress field for these consistent stress states, the mean vector of σ_1-axes is calculated after Wallbrecher (1986; "$R_{\%}$-and-center-method"). The concentration parameter, $C_{R\%}$, is a measure for the alignment of stress axes with $C_{R\%}$=100% indicating parallel fabrics and $C_{R\%}$=0% indicating a uniform distribution. Here, $C_{R\%}$=89.2% designates a pronounced maximum for the σ_1-axes oriented 324/07. b) Comprehensive symbol for the deduced regional Stress field X. It integrates the mean directions of principal stress axes projected to the vertical respectively horizontal. The range of background colours reflects the large variety of stress ratios (0.2≤R≤0.8) indicated by the associated compressional stress states.

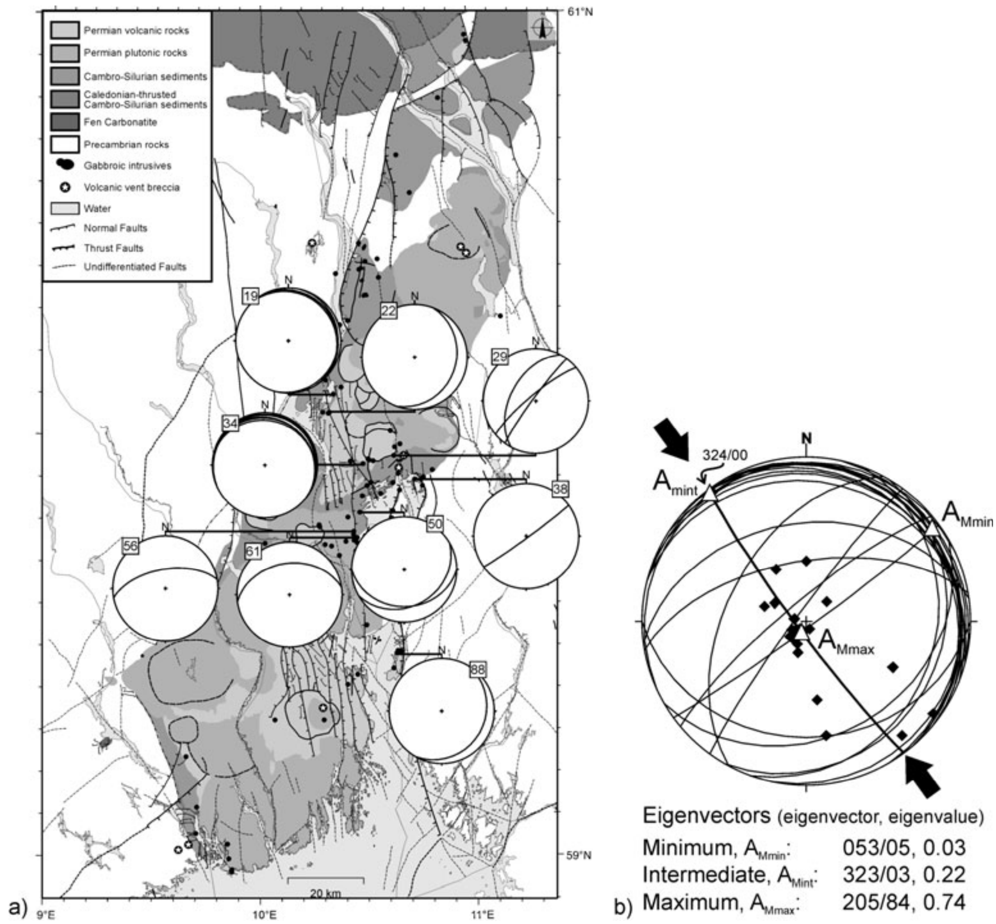

Figure 58: Tilted bedding planes in Cambro-Silurian sediments; a) Tectonomagmatic map of the Oslo Graben area (modified after Ramberg & Larsen, 1978) with measured bedding planes as great circles in lower-hemisphere, equal-area projections; b) Cumulative plot of all bedding planes shown as great circles and poles to planes. The eigenvectors and eigenvalues for the poles to all bedding planes are calculated according to Bingham (1964). The great circle spanned by the eigenvectors of maximum and intermediate eigenvalues (thick line), respectively, cuts the horizontal at 324/00. This direction is interpreted as the direction of maximum compression (black arrows) which caused folding of the initially horizontal bedding planes. Note the similarity to the direction of σ_1 of Stress field X (Fig. 57).

Tensional stress states

Tensional stress states have been derived from sites spread all across the Oslo Graben area (Fig. 59) and from fault-slip data preserved by rocks of all ages including the youngest exposed rocks, i.e. Permian magmatic rocks (Fig. 55). The associated directions of sub-horizontal σ_3-axes vary strongly among all of the estimated stress tensors (Fig. 60a). Even when comparing the distributions of σ_3-directions for stress states derived from differently aged rocks, the variety of horizontal extension directions is similarly large (Fig. 61). Only the stress ratios (R) show a certain rock age dependent trend with values increasing from Precambrian to Cambro-Silurian and to Permian rocks. Altogether, most of the tensional stress tensors are characterised by low stress ratios reflecting configurations of radial extension, or "vertical flattening".

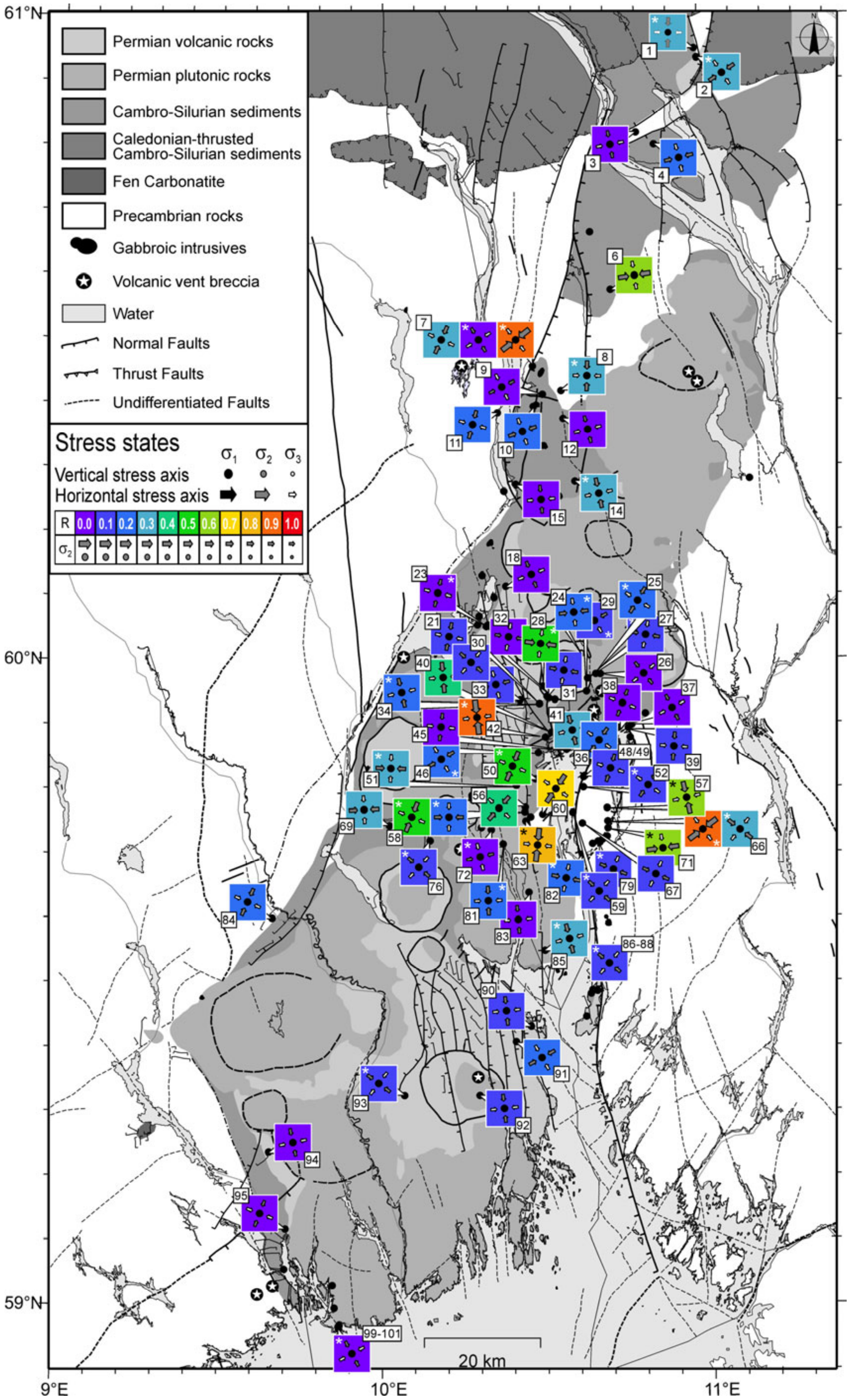

Figure 59: Tensional stress states derived from fault-slip data from the Oslo Graben area. Stress states that are based on less than 9 fault-slip data are marked by an asterisk.

Considering the lack of any field-derived indicators that may argue for a succession of different phases of normal faulting, and given the uniform variation of tensional stress states between different parts of the graben system as well as differently-aged rocks, any separation into different groups of tensional stress states would not be justified. This conclusion includes the possibility that all tensional stress states are related to the same tectonic phase in the evolution of the Oslo Graben. Following this, the mean vector for σ_3-axes of all tensional stress tensors is calculated (Fig. 60a). The potential regional stress field thus deduced ("Stress field Y") shows a maximum of σ_3 that strikes horizontally WNW-ESE (293/00), though this maximum is only weakly pronounced ($C_{R\%}$=38.4%). This weakly constrained σ_3, in turn, corresponds well with the predominance of low stress ratios which indicate σ_2 and σ_3 to be almost equal in magnitude.

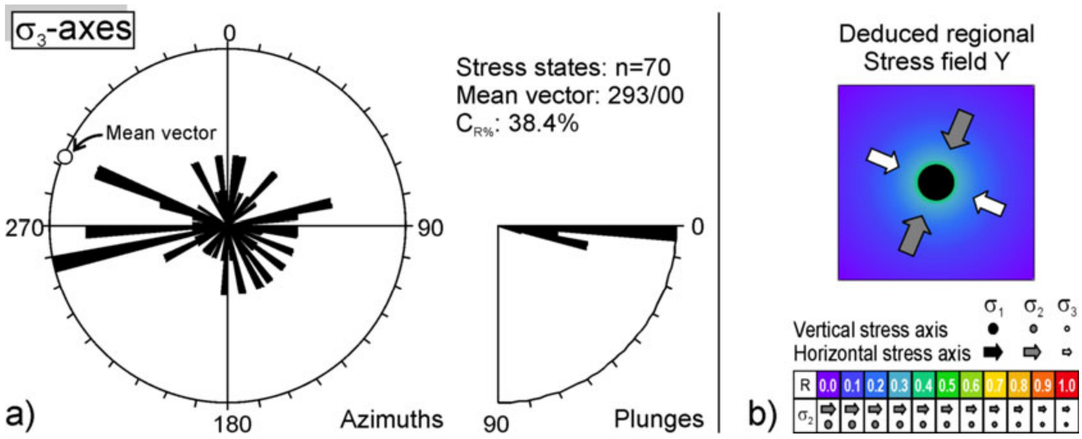

Figure 60: Potential regional Stress field Y deduced from tensional stress states. a) Rose diagram with σ_3-directions of all tensional stress tensors. The azimuths of σ_3-axes show various strike directions. None of the σ_3-plunges deviates by more than 19° from the horizontal. To infer an overall stress field for these stress states, the mean vector of σ_3-axes is calculated after Wallbrecher (1986; "$R_{\%}$-and-center-method"). The concentration parameter, $C_{R\%}$, is a measure for the alignment of stress axes ($C_{R\%}$=100%: parallel fabrics; $C_{R\%}$=0%: uniform distribution). $C_{R\%}$=38.4% designates a weakly pronounced maximum for σ_3. b) Comprehensive symbol for the deduced regional Stress field Y. It integrates the mean directions of principal stress axes projected to the vertical respectively horizontal. The background colours illustrate the predominance of low stress ratios.

Since the youngest rocks documenting tensional stress states are of Permian ages, the supposed tensional stress field must have been active during Permian or post-Permian times. Despite the weak intensity of the calculated mean of σ_3, this direction of extension fits very well with the supposed kinematics of the master faults that flank the different graben segments of the Oslo Rift system (Fig. 53): These major planes are suggested to have been active as normal faults during the Permo-Carboniferous phase of rifting (Swensson, 1990; Olaussen et al, 1994; Heeremans & Faleide, 2004). Striking roughly N-S, these faults indicate a roughly E-W-oriented extension. Likewise, tensile structures such as dykes and veins indicate pronounced directions of extension around WNW-ESE and E-W (Fig. 62). Dyke emplacement is supposed to have taken place over the entire time-span of Permo-Carboniferous rifting (Heeremans, 2005). Consequently, as the regional direction of σ_3 derived from fault-slip data corresponds with the extensional directions deduced from other rift-related structures, the tensional stress field is interpreted to be related to the phase of Permo-Carboniferous rifting.

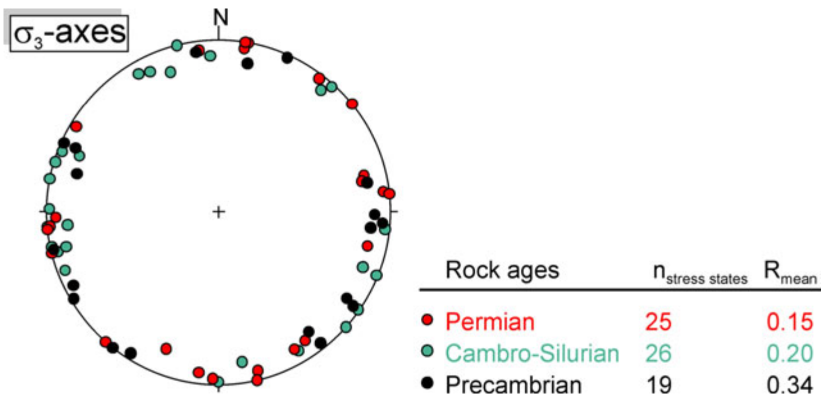

Figure 61: Orientations of σ_3-axes for the 70 tensional stress states plotted in a stereographic projection (lower hemisphere, equal area). The stress states have been derived from fault-slip data preserved by rocks of Precambrian, Cambro-Silurian, and Permian ages. Irrespective of the age of the rocks, the σ_3-axes show a great variation of sub-horizontal directions. However, the younger the rocks are, the smaller is the mean of stress ratios, R_{mean}. $n_{stress\ states}$ – number of locally derived stress states; $R=(\sigma_2-\sigma_3)/(\sigma_1-\sigma_3)$.

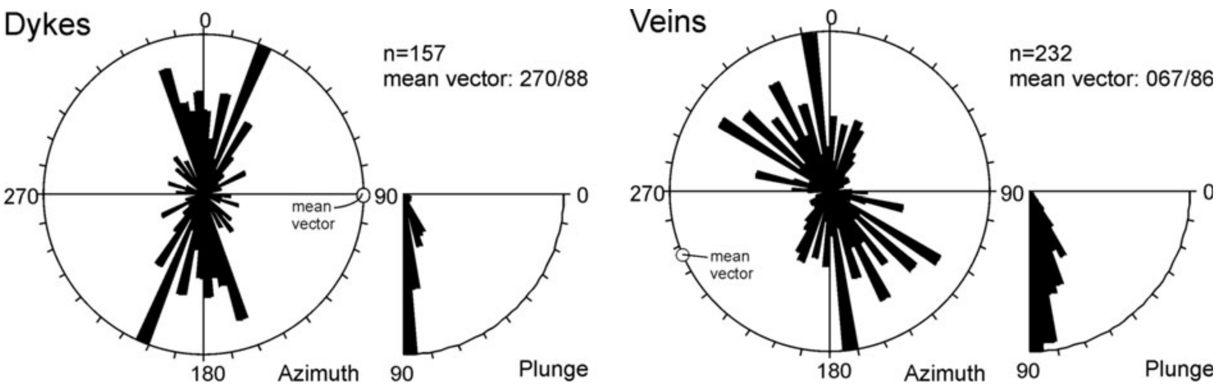

Figure 62: Orientations of dykes and veins. According to Anderson's (1942) principles, the direction of extension during the formation of pure tensile structures is perpendicular to these planes. Thus, the mean vectors calculated for the poles to dykes respectively veins (Wallbrecher, 1986) are interpreted to indicate the most probable directions of extension, being E-W for the dykes and ENE-WSW for the veins.

Oblique stress states

The greatest number of stress tensors derived from fault-slip data preserved in the Oslo Graben area corresponds to oblique stress states that are characterised by a lack of any sub-vertical principal stress axis, since neither σ_1 nor σ_2 or σ_3 plunges by more than 70° (Fig. 63). These non-Andersonian stress states have been derived from fault-slip data spread all across the Oslo Graben area and preserved by units of all investigated rock ages (Fig. 55). As obvious from this paleostress map, these stress states do not show any prominent consistencies in terms of directions of principal axes. Similarly, the stress ratios vary almost over the complete possible range ($0.0 \leq R \leq 0.9$).

Following the principles of paleostress stratigraphy, the directions of principal stress axes are plotted according to the different investigated rock ages (Fig. 64). It is obvious that the principal axes show a similarly wide variety of directions whatever the age of the host rock. Likewise, the mean value of R is independent of rock ages. Moreover, a spatial correlation of consistent stress states is impossible: firstly, as agreeing directions of principal stress axes can be found all across the graben area and, secondly, as various oblique stress states locally occur at the same place.

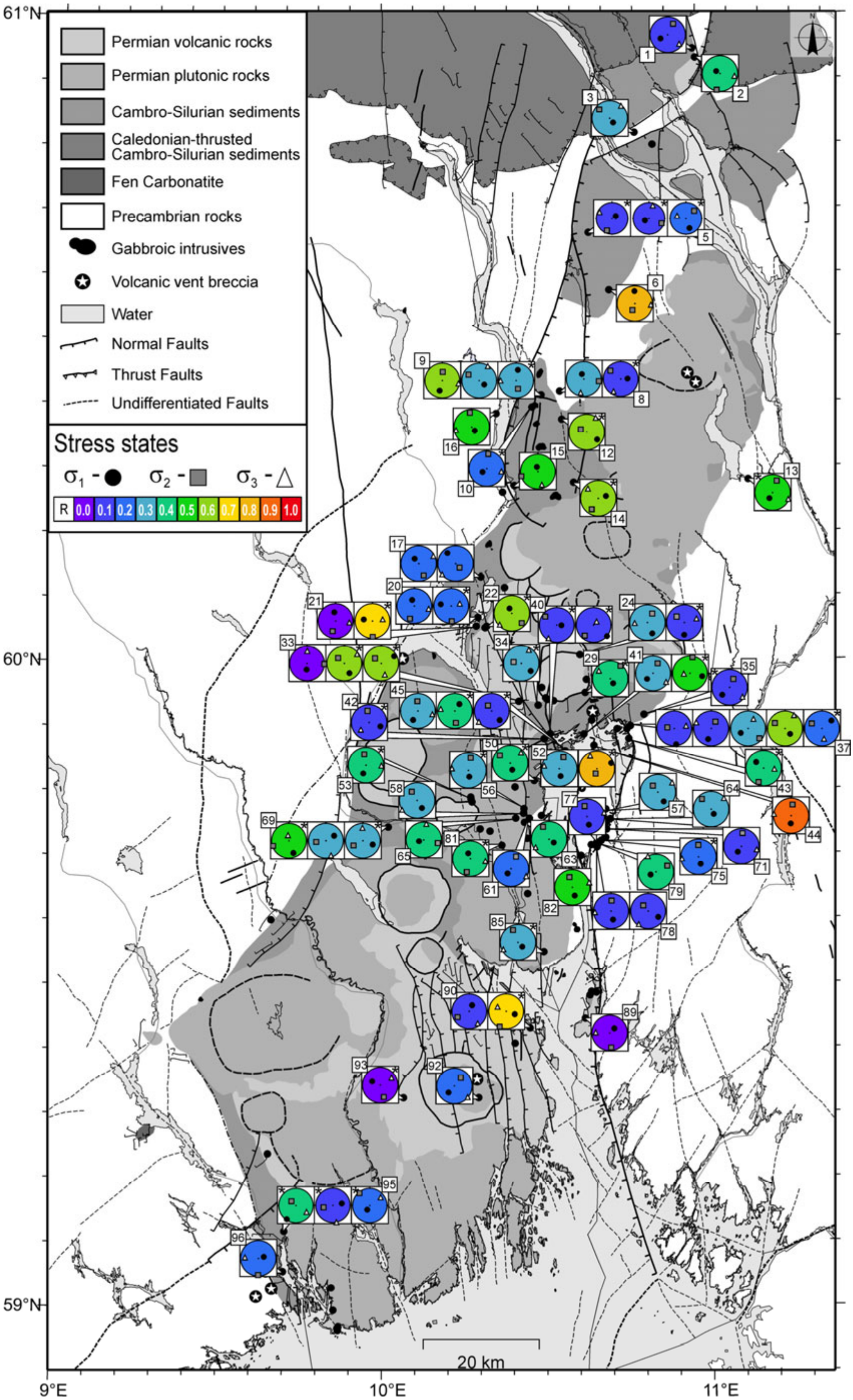

Figure 63: Oblique stress states in the Oslo Graben area. None of these stress tensors comprises a sub-vertical principal stress axis, i.e. a stress axis that plunges by ≥70°. Stress states that are based on less than 9 fault-slip data are marked by an asterisk.

Given the described variation of local stress states as well as the scarcity of evidence concerning the relative timing of different oblique stress states (Fig. 55), the group of non-Andersonian stress states is further analysed as a whole. When plotting the different types of principal stress axes separately, they reveal some remarkable trends (Fig. 64): the plunges of σ_1-axes tend to be steeper than those of σ_2-axes, while the majority of σ_3-axes are almost horizontal. Despite the low consistency of oblique stress states arguing against a common regional stress field, the mean vectors have been calculated for all three types of principal stress axes. According to these mean directions, a respective overall stress field would be characterised by a sub-vertical σ_1, a sub-horizontal N-S-striking σ_2, and a sub-horizontal E-W-striking σ_3. Interestingly, this configuration resembles the deduced Permo-Carboniferous tensional Stress field Y.

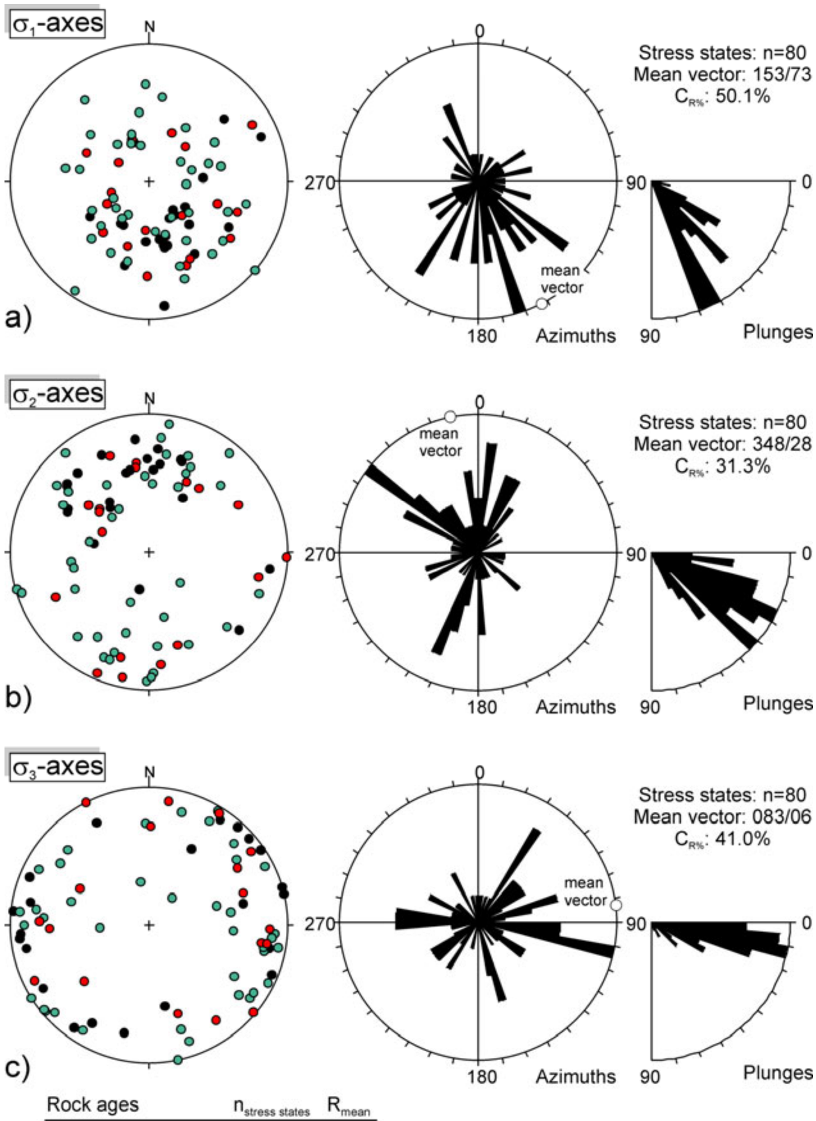

Rock ages	$n_{stress\ states}$	R_{mean}
Permian	18	0.30
Cambro-Silurian	40	0.30
Precambrian	22	0.33

d)

Figure 64: Variations of orientations of σ_1-axes (a), σ_2-axes (b), and σ_3-axes (c) for all oblique stress states shown by stereographic projections (lower hemisphere, equal area; *left*), by rose diagrams (*centre*), and by plunge scaling (*right*). The mean vectors are calculated after Wallbrecher (1986; "*R%*-and-center-method"). d) Number of stress states ($n_{stress\ states}$) and mean values of the stress ratio (R_{mean}) derived from the different investigated rock ages [with $R=(\sigma_2-\sigma_3)/(\sigma_1-\sigma_3)$].

The supposed relationship between oblique and tensional stress states is more clearly illustrated by a triangle diagram (Fig. 65). This type of diagrams has originally been developed for the presentation of earthquake focal mechanisms according to the associated P-, B-, and T-axes (Apperson & Frohlich, 1988; Frohlich, 1992). In the same way, stress states can be plotted in triangle diagrams according to the plunges of principal stress axes based on the following relationship:

$$\sin^2\delta_{\sigma1} + \sin^2\delta_{\sigma2} + \sin^2\delta_{\sigma3} = 1 \qquad \text{(Eq. 3)}$$

where $\delta_{\sigma1}$, $\delta_{\sigma2}$, and $\delta_{\sigma3}$ are the plunges of σ_1, σ_2, and σ_3, respectively. The upper vertex of the triangle diagram represents a stress state for which σ_2 is vertical, while σ_1 and σ_3 are horizontal. Accordingly, the lower left vertex represents a stress state with a vertical σ_3 and the lower right vertex corresponds to a vertical σ_1. The exact centre of the diagram, on the other hand, represents a stress state for which σ_1, σ_2, and σ_3 show the same plunge of 35.26°. By using the triangle diagram, stress states can be characterised as compressional (sub-vertical σ_3), strike-slip (sub-vertical σ_2), and tensional (sub-vertical σ_1). For the Oslo Graben area, compressional and strike-slip stress states can straightforwardly be distinguished as they form relatively isolated clusters located close to the vertices of vertical σ_3 and σ_2, respectively (Fig. 65). The areas of tensional and oblique stress states, on the other hand, are not clearly outlined against each other. This smooth transition argues for a potential causal relationship between tensional and oblique stress states. Furthermore, it reveals that the threshold between Andersonian and oblique stress states designated in the present study to be 70° is not indisputable.

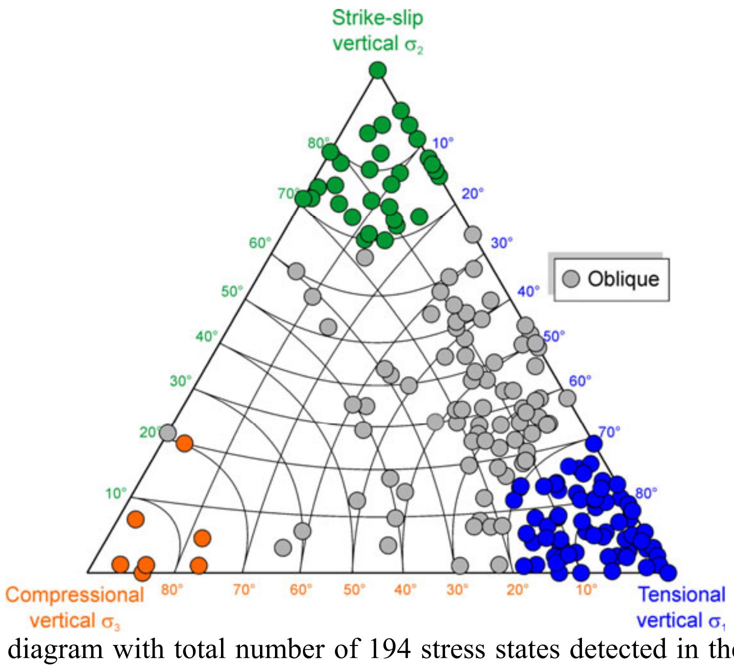

Figure 65: Triangle diagram with total number of 194 stress states detected in the Oslo Graben area. The different types of stress states are colour-coded: Compressional stress states are characterised by a sub-vertical σ_3, strike-slip stress states by a sub-vertical σ_2, and tensional stress states by a sub-vertical σ_1. In this regard, "sub-vertical" is assumed to mean plunging by ≥70°. Thus, oblique stress states are located in the central parts of the diagram (grey dots). However, the densest clusters of oblique stress states plot very close to the area of tensional stress state. This might imply a causal relationship between oblique and tensional stress states.

The great number of oblique stress states poses the problem why the principles of Andersonian faulting should have been invalid at least temporarily for large parts of the Oslo Graben area. As presented by selected examples from the southern margin of the basin system (Chapters 2 and 4), the formation of striated fault planes may be postdated by folding or

tilting of the corresponding rock mass resulting in distorted orientations of fault-slip data and associated paleostress axes.
Since six of the oblique stress states found in the Oslo Graben area have been derived from folded Cambro-Silurian rocks with known bedding attitudes, a test has been performed regarding a potential relationship between folding of these rocks and the obliquity of fault-related stress axes (Fig. 66). Assuming bedding planes to generally form horizontally, their present attitudes serve as a reference frame for each back-tilting test. If the present orientations of fault-slip data and associated stress axes are a secondary result of folding, the tests should restore the original horizontal respectively vertical orientations of principal stress axes. Thus, the back-tilting should reproduce Andersonian stress states. However, in the case of the six examples from the Oslo Graben, only the oblique stress state at site #22 (SUN2) shows Andersonian principal axes after the back-tilting procedure (Fig. 66). For this stress state, the σ_1-axis plunges by 72° after back-tilting. Thus, apart from this particular example, the whole series of back-tilting tests argues against any causal relationship between the folding of Cambro-Silurian sediments and the occurrence of oblique stress states.

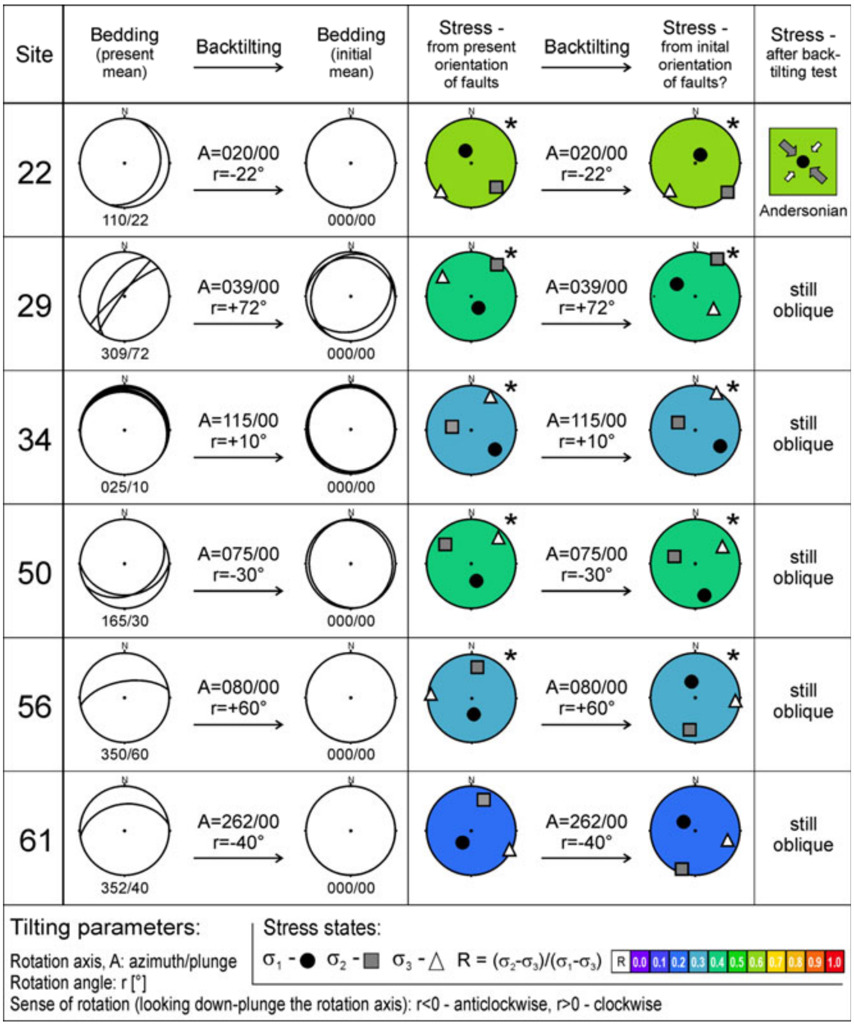

Figure 66: Back-tilting tests for oblique stress states that have been derived from fault-slip data exposed within folded Cambro-Silurian rocks. The parameters used for the back-tilting of principal stress axes (rotation axis, angle and sense of rotation) are derived from the present-day attitudes of folded bedding planes at the respective sites. It is assumed that bedding planes initially formed horizontally. After back-tilting, most of the stress axes are still oblique, thus excluding the folding of rocks as a cause for the obliquity of stress axes. Bedding planes are shown as great circles in stereographic projections (lower hemisphere, equal area). Stress states marked by an asterisk are based on less than 9 fault-slip data.

Strike-slip stress states

All across the Oslo Graben area, in rocks of all exposed ages, fault-slip data are preserved that are indicative for strike-slip paleostress states (Fig. 67). The estimated stress ratios are predominantly low to intermediate with a total range between R=0.0 and R=0.8. Considering the complete number of strike-slip stress states, a great variety of associated directions of maximum compression (σ_1) becomes evident (Fig. 68). However, the largest number of strike-slip stress states is characterised by a σ_1-axis that strikes around NNW-SSE. This predominant direction of maximum compression is consistently indicated by stress states derived from rocks of Precambrian, Cambro-Silurian, and Permian ages (Fig. 68b).

Interestingly, any stress states that deviate extremely from this predominant trend are spatially restricted to the central parts of the area, i.e. mainly to the accommodation zone that links the Akershus and the Vestfold graben segments. Furthermore, most of these extraordinary stress states are not perfectly constrained as they are based on a number of less than nine fault-slip data (Fig. 67). This restricted spatial occurrence of strike-slip stress states with a roughly E-W-directed σ_1 shows that these stresses correspond to a local phenomenon rather than properly indicating any graben-wide stress field.

Consequently, for the estimation of a regional strike-slip stress field only stress states which consistently show the graben-wide trend of a N-S- to NW-SE-directed maximum compression are considered (Fig. 69). The deduced regional “Stress field Z” thus is characterised by a NNW-SSE-striking σ_1-axis (173/01) and a low stress ratio (R_{mean}≈0.3). The youngest units that document fault-slip data related to this strike-slip regime are the Permian volcanic and plutonic rocks which thus provide a maximum age for Stress field Z. Furthermore, there are agreeing indications that strike-slip faulting at least locally postdated tensional stress states that are supposed to be related to the Permo-Carboniferous phase of rifting (Fig. 55). However, a more precise temporal assignment of the strike-slip stress field is complicated by the lack of any rocks being younger than Permian.

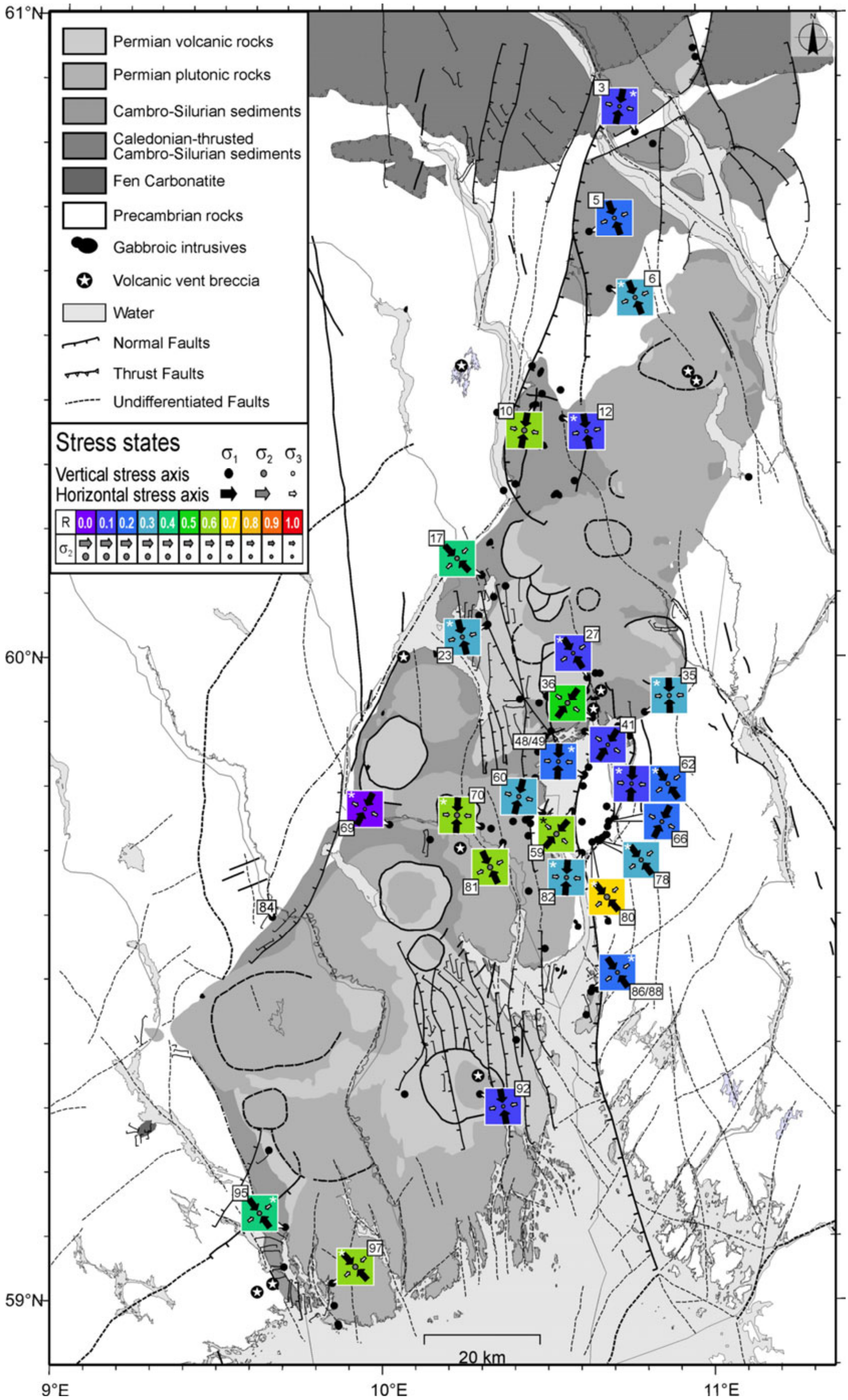

Figure 67: Strike-slip stress states in the Oslo Graben area. Stress states based on less than 9 fault-slip data are marked by an asterisk. The shaded area indicates roughly the extension of the accomodation zone between the Akerhus and the Vestfold graben segments.

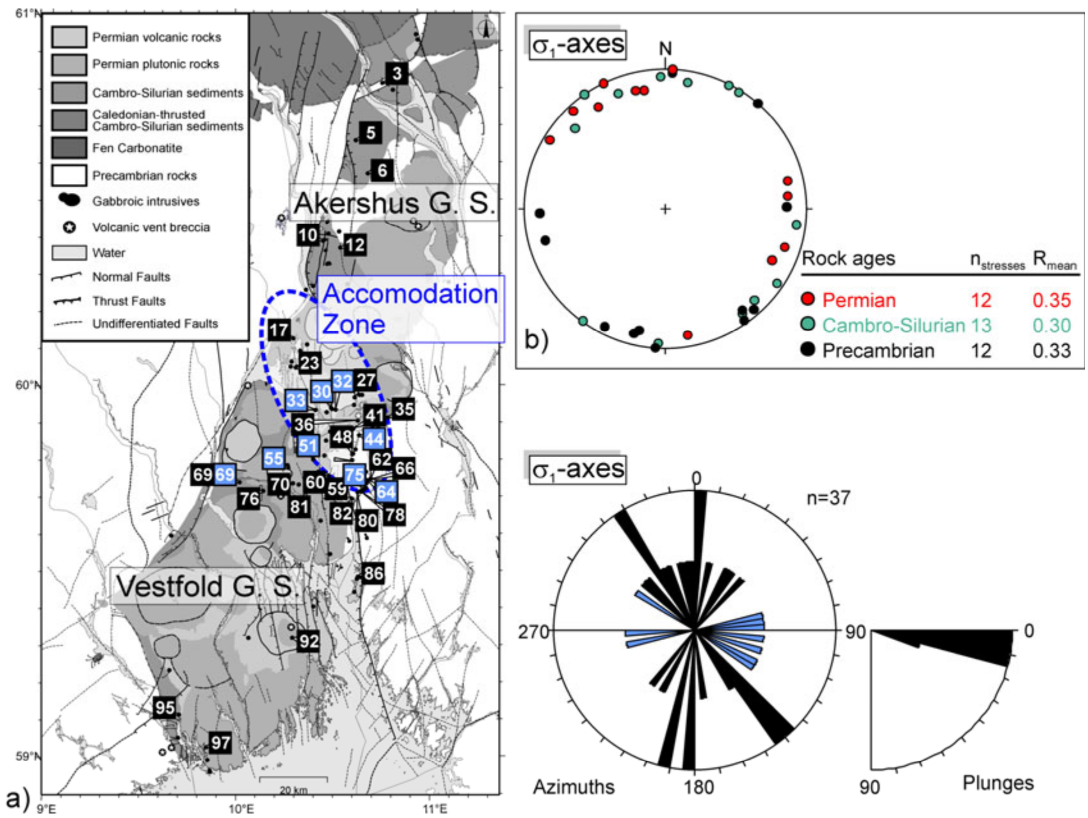

Figure 68: Directions of σ_1-axes for all strike-slip paleostress states. a) Most strike-slip stress states reveal a σ_1 with azimuths striking N-S to NW-SE. Sites with σ_1 striking around NNW-SSE (black) are differentiated from sites with σ_1 striking around E-W (blue). The latter are mainly restricted to the central parts of the Oslo Graben where an accommodation zone links the segments of the Akershus and the Vestfold half grabens. None of the σ_1-plunges deviates by more than 19° from the horizontal. b) σ_1-orientations coloured according the different ages of investigated rocks (lower hemisphere, equal area projection). σ_1-axes derived from rocks of different ages show similarly wide ranges of preferred orientation. $n_{stresses}$ – Number of locally derived stress states; $R=(\sigma_2-\sigma_3)/(\sigma_1-\sigma_3)$.

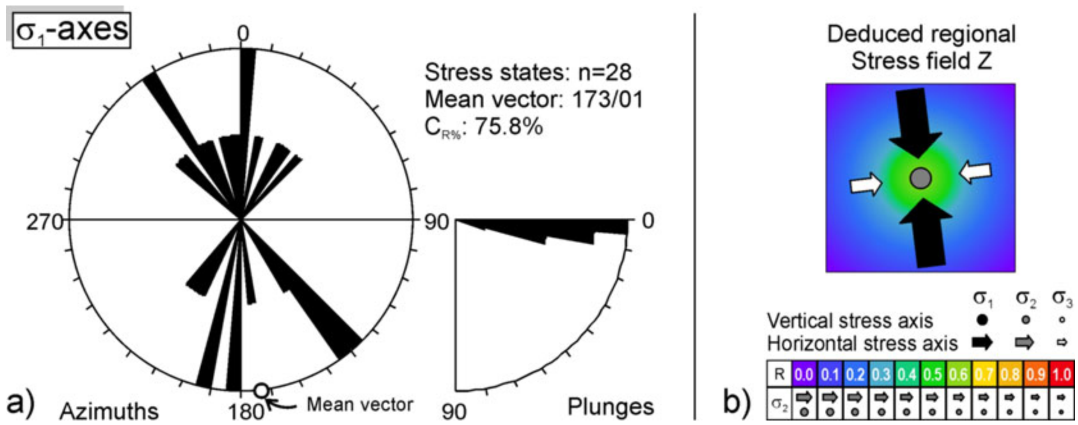

Figure 69: Potential regional Stress field Z inferred from strike-slip stress states with σ_1 striking around NNW-SSE (Fig. 68). a) The rose diagram shows the preferred NNW-SSE-orientation of σ_1-axes. None of the σ_1-plunges deviates by more than 19° from the horizontal. To infer an overall stress field from these stress states, the mean vector of σ_1-axes is calculated after Wallbrecher (1986; "$R_{\%}$-and-center-method"). The concentration parameter, $C_{R\%}$, is a measure for the alignment of stress axes ($C_{R\%}$=100%: parallel fabrics; $C_{R\%}$=0%: uniform distribution). $C_{R\%}$=75.8% designates a clear maximum for σ_1-axes oriented 173/01. b) Comprehensive symbol for the deduced regional Stress field Z. It integrates the mean directions of principal stress axes projected to the vertical respectively horizontal. The background colours reflect the predominance of stress ratios between R=0.2 and R=0.6.

5.3 Discussion

The large number and wide distribution of fault-slip data available for the area of the Oslo Graben provides an excellent base for a graben-wide study of the associated evolution of paleostress fields. A great portion of the locally derived stress states is remarkably consistent across the entire study area. These consistencies between individual stress states give notice of three regionally acting stress fields: a compressional, a tensional, and a strike-slip stress field. These stress configurations differ remarkably from the paleostress fields reconstructed for the southern margin of the CEBS (Chapter 4), concerning both associated kinematics and supposed timing. The use of the principles of paleostress stratigraphy to constrain the timing of stress fields is largely inhibited in the Oslo Graben area by the occurrence of consistent stress states in rocks of different ages and by the lack of any rocks younger than Permian. The few chronological indicators preserved in the field argue for tensional stress states to be older than oblique stress states which, in turn, seem to be older than strike-slip stress states. Another extraordinary aspect characterising the Oslo Graben area is the abundance of oblique paleostress states.

5.3.1 Chronology

Caledonian compressional stress field

The signs of the compressional regional Stress field X with a NW-SE-directed maximum compression are rare and restricted to rocks of Pre-Permian ages. As illustrated, the related kinematics complies with the folding of Cambro-Silurian sediments possibly identifying the respective regional strain as a Caledonian imprint. This correlation corresponds well with the results of Heeremans et al. (1996) who interpret a compressional stress field to have governed the respective Ordovician-Late Silurian phase of deformation. In any case, a minimum age for this stress field seems to be provided by the lack of associated fault-slip data within the Permo-Carboniferous volcanic and plutonic rocks (≥300±1 Ma).

Permo-Carboniferous stress fields

The tensional Stress field Y deduced from the numerous tensional stress states is characterised by a weakly pronounced horizontal WNW-ESE-directed minimum compression (σ_3) and a low stress ratio. A correlation with the supposed kinematics of the rift-flanking master faults of the Oslo Graben facilitates assigning this regional stress field to the Permo-Carboniferous phase of rifting. The estimated direction of σ_3 fits also with other rift-related NNW-SSE- to N-S-trending tensile structures such as open fractures and dykes (Ramberg et al., 1977). Normal movements along roughly N-S-trending faults are supposed to have started in the area during the initial phase of rifting (*rift stage 2*; ~300Ma; Neumann et al., 1992). The associated stress conditions are likely to have prevailed throughout the climax stage of rifting (*rift stage 3*) as indicated by the timing of the most extensive vertical movements along the graben-flanking master faults (Heeremans & Faleide, 2004) as well as by rhomb porphyry lavas and alkaline basalts that are described to have erupted mainly along NNW-SSE-trending fissures (Ramberg & Larsen, 1978).

The tensional character of paleostress fields that controlled the CEBS during Permo-Carboniferous times is confirmed by other paleostress studies: two different Permo-Carboniferous tensional stress fields with a NW-SE-directed σ_3 and a NE-SW-directed σ_3, respectively, are deduced from fault-slip data exposed in Scania (southern Sweden) which is part of the Sorgenfrei-Tornquist Zone (Bergerat et al., 2007). Furthermore, a group of normal faults offsetting Permian *Rotliegend* sediments in the Northwest German Basin have been reconstructed from seismic data and related to a Permian tensional stress state with an ENE-WSW-directed σ_3 (Lohr, 2007).

More than one third of the fault-slip data from the Oslo Graben area documents the occurrence of oblique paleostress states which tend to be younger than tensional stress states. It has successfully been proved for specific sites that there is no relationship between the obliquity of principal axes and the Caledonian folding of Cambro-Silurian sediments. The occurrence of oblique stress related fault-slip data in Permian rocks provides a maximum age for at least part of these atypical stress configurations. Moreover, the mean directions of principal axes with σ_1 being sub-vertical, σ_2 striking N-S, and σ_3 striking E-W resemble those of the tensional stress field. This opens the possibility that the oblique stress states have also been related to the Permo-Carboniferous phase of rifting.

Post-rift stress fields
The regional strike-slip Stress field Z detected in the Oslo Graben area is characterised by a horizontal NNW-SSE-trending maximum compression (σ_1) and a low mean of stress ratios. The maximum age for this regional stress field is provided by the youngest Permian magmatites that have preserved respective fault-slip data, such as the Drammen granite (267±4; Sundvoll & Larsen, 1990). The sparse direct information on the relative timing of strike-slip stress states indicates that strike-slip faulting has taken place after the tensional and oblique stress states had been active. Consequently, the strike-slip stress field might be representative for a late stage of rifting or a post-rift phase. Interestingly, the present-day stress pattern in the Oslo Graben area is characterised by similar directions of maximum compression ranging between NNW-SSE and WNW-ESE while the associated modes of deformation are various (reverse, strike-slip, and normal; Heidbach et al., 2008).
The occurrence of strike-slip stress states in Permian rocks, however, does not exclude the possibility that earlier strike-slip faulting had taken place, for instance, in Late Variscan times as proposed by Heeremans et al. (1996). Indeed, other paleostress studies based on fault-slip data have provided agreeing directions of roughly NNW-directed maximum compression for Variscan times, such as reported for areas in southern England, northern France and Belgium (Vandycke, 1997) or southeastern Poland (Lamarche et al., 2002). The ages of investigated rocks in the Oslo Graben area, however, only support the interpretation that at least the latest phase of strike-slip faulting has taken place after the emplacement of rocks like the Drammen granite which has been dated to the climax stage of rifting.

5.3.2 Mechanisms

Permo-Carboniferous phase of (active?) rifting
The estimated Permo-Carboniferous tensional Stress field Y is based on tensional stress states that show a large variety of horizontal σ_3-directions and predominantly low stress ratios. Interestingly, the mean stress ratios are R=0.34 for Precambrian rocks, R=0.20 for Cambro-Silurian rocks and R=0.15 for Permian rocks. These differences might reflect a development from a pure tensional type of stress before the emplacement of the Permian magmatites to radial extension thereafter as proposed by Heeremans et al. (1996). However, it is not evident from field observations that the diversity of extensional directions or the slight differences in stress ratios reflect a succession of different tensional stress fields. Moreover, the preponderance of low stress ratios indicates that the magnitudes of σ_2 and σ_3 are almost equal and perhaps mutually exchangeable from site to site. For these reasons, only one regional stress field has been inferred from the total number of locally derived tensional stress states. The estimated direction of extension (σ_3) is confirmed by the proposed graben-wide

kinematics during the phase of rifting. The associated low stress ratio might, in turn, be related to the intensive magmatic activity during the Permo-Carboniferous phase of rifting. The emplacement and eruption of large volumes of magmatic material is suggested to have been accompanied by regional uplift (Heeremans et al., 1996). Such a thermally driven doming could have added a significant component of differential stress to the regional vertical stress axis (σ_1) while reducing indirectly the relative difference between the magnitudes of σ_2 and σ_3 which, in turn, would reduce the stress ratio ("radial extension"). Consequently, the low stress ratio that characterises the rift-related regional stress field might be an indicator for active rifting. However, there is strong evidence against plume activity including the lack of an age-progressive volcanic track, pre-magmatic subsidence instead of uplift (deposition of Asker Group sediments), low to moderate ^{3}He/^{4}He values, the absence of a large igneous province, and normal or only slightly elevated mantle temperatures (Heeremans, 2005). Furthermore, the clear predominance of N-S-trending extensional structures in the area argues for a far field tensional stress field which would correspond to passive rifting. A possible scenario might comprise early passive rifting that later triggered active asthenospheric upwelling (Heeremans et al., 1996).

Oblique stress states

A very special outcome of the fault-slip analysis in the Oslo Graben area concerns the large number of oblique stress states. Integrating all available information on these atypical stress configurations which obviously postdated the tensional stress field, the question arises concerning the mechanism(s) that could be regarded responsible for the apparent failure of Andersonian principles.

Similar to folding or tilting of rock masses, the rotation of individual fault-bounded blocks can retroactively change the orientations of fault-slip data. This rotation, of course, would result in altered orientations of associated principal axes. In fact, there is evidence for intensive fault block rotations in the Oslo Graben area which are supposed to have occurred during the climax stage of rifting (Neumann et al., 1992). In this context, lavas are described to locally show 10-30° dips (Oftedahl, 1952). Furthermore, the syn-rift deposits of the Brumund Formation which correspond to the *Rotliegend* deposits in the Northern Permian Basin are recorded to dip even up to 60° (Lothe et al., 1999). However, many sites in the Oslo Graben area reveal both fault-slip data related to oblique stress states and fault-slip data related to pure compressional or tensional stress states. Since the compressional and the tensional stress fields have predated the oblique stress states, any fault block rotation causing oblique stress axes should have equally affected the compression- and tension-related fault-slip data. However, the latter do not give evidence for a greater shift of principal axes away from the vertical or horizontal.

Excluding thus a retroactive rotation of fault-slip data as the main cause for the abundance of oblique stress states in the Oslo Graben, while assuming Andersonian stress states to be an ever holding requisite of the crust close to the Earth's surface, the applicability of fault-slip analysis to the concerning portion of oblique data must be reconsidered. There are certain situations in the crust known to suspend simple (Andersonian or Wallace-Bott-) relationships between observed brittle fault kinematics and the associated tectonic stress field. In zones of transpression or transtension, for instance, the deformation pattern is not only controlled by tectonic stress, but to a large degree imposed by the boundary conditions (Dewey et al., 1998). Such boundary conditions may be provided by large pre-existing planes of weakness within a rock mass along which transpression or transtension may occur (e.g. *Case study 8*, Chapter 4). In the Oslo Graben area, the early rift stages produced numerous roughly N-S-striking fractures and faults (e.g. Ramberg et al., 1977). Slip along pre-existing planes of weakness usually requires less energy than stress release by the formation of new faults. Assuming a tensional stress field with a σ_3 not striking perpendicular to the main trend of the N-S-striking

planes, these pre-existing discontinuities would respond by movement with a component of strike slip supplemented to the dip slip component. The abundance of the resulting oblique-slip faults thus could potentially result in the estimation of oblique (transtensional) stress states though the overall controlling stress field might have been an Andersonian one.
While non-coaxial strain patterns induced by transpression or transtension might reflect a special manifestation (and potential misinterpretation) of actual Andersonian stress states, other mechanisms are plausible candidates for indeed inducing oblique stress states. As already mentioned in the context of extension, the intensive magmatic activity in the Oslo Graben area is likely to have affected the regional stress field. A magma chamber, for example, may function as a pressurised hole surrounded by a somehow-shaped fluid-solid interface that can support no shear stresses (Suppe, 1985). A near-surface magma chamber would thus add a radial stress component to the regional stress field. By implication, the resulting directions of principal stress axes may deviate from the vertical respectively the horizontal. Furthermore, the cumulative stress states detectable would be strongly dependent on the position relative to the magma chamber. This might explain the inconsistency of oblique paleostress states in the Oslo Graben area. On the other hand, the numerous calderas described for the area (Ramber & Larsen, 1978) are indicative of rapid pressure changes within the magma sources – changes that might have further complicated the associated stress and strain patterns. Shallow magmatism, volcanism and caldera development are supposed to have generated local transient stresses that strongly altered the regional (tensional) stress fields also in other regions such as the Yucca Flat (Nevada; Minor, 1995) or the Canary Islands (Fernández et al., 2002).
Finally, oblique stress states may locally be related to stress perturbations in the vicinity of large discontinuities within a rock mass. Such perturbations have been characterised by 2D distinct-element models (Homberg et al., 1997) as well as 3D finite-element models (Maniatis, 2008), which consistently have shown that the strongest perturbations occur at the tips of such discontinuities. At these particular positions, deviations in the directions of principal axes as well as changes of the relative magnitudes of stresses are strongest. These deviations depend on the far-field stress tensor, the strike of the discontinuity relative to the far-field stress, and the coefficient of friction on the discontinuity. Accordingly, though being complexly regulated, these stress perturbations respond to definable rules. On the contrary, the reconstructed oblique stress states in the Oslo Graben area do not show any evident regularity which could be related to the pattern of faults; oblique stress states have been derived from fault-slip data far from as well as close to large discontinuities such as faults or caldera structures. However, a systematic investigation would be required to certainly exclude any relationship between the characteristics of oblique stress states and the geometry and orientation of pre-existing faults in the area.
A definite explanation for the abundance of oblique paleostress states in the Oslo Graben area thus will not be provided by the present study. These atypical stress states are a graben-wide phenomenon with various local specifications. In light of this, the diverse effects of intensive magmatism in the area seem to be the most probable solution for the occurrence of oblique stress states. While the tensional stress field can be correlated with the eruption of rhomb-porphyry lavas from mainly N-S-striking fissures (*rift stage 3*), the oblique stress states might be associated to the formation of central volcanoes and calderas (*rift stage 4*) or the emplacement of batholiths and granitic intrusions (*rift stages 5* and *6*). However, the different suggested causes for non-Andersonian stresses might have also interacted to produce the complex fault-slip patterns that are presently observable.

Strike-slip faulting

The regional strike-slip Stress field Z with a roughly N-S-striking σ_1 is associated with the weakest constraints on any absolute timing. Most probably it postdated the Permo-Carboniferous phase of rifting.

The configuration of the strike-slip stress field is representative only for part of the whole number of estimated strike-slip stress states. The smaller part of strike-slip stress states reveals completely different σ_1-axes trending around E-W. Since the latter are only a local phenomenon restricted mainly to the accommodation zone between the Akershus and Vestfold Graben segments, it has been desisted from deducing a regional paleostress field from these stress states. This restricted occurrence of particular stress states might reflect the frequent observation that strain within accommodation zones between rift-related graben segments may not be representative for the overall tectonic stress controlling the formation of the respective rift system (Maler, 1990; Younes & McClay, 2002). Thus, the smaller group of strike-slip stress states might be related to a compensation of movements within the opposing half grabens north and south of the accommodation zone during the Permo-Carboniferous phase of rifting.

5.4 Conclusions

The fault-slip analysis performed for the Oslo Graben area yields three regional stress fields that affected the area in the following chronological order:

- A compressional stress field with a vertical σ_3 and a NW-SE-directed maximum compression (σ_1) characterises the Caledonian imprint. The temporal status of this stress field is based on the absence of corresponding fault-slip data in rocks younger than Silurian and the consistency in kinematics between fault-slip patterns and the folding of Cambro-Silurian sediments.
- The most prominent regional stress field detected in the area is tensional in character (vertical σ_1) and characterised by a WNW-ESE-directed minimum compression (σ_3). This stress field best corresponds with the climax stage of Permo-Carboniferous rifting in the course of which main extension along the graben segmenting master faults has taken place.
- A large number of reconstructed oblique stress states cannot be integrated into a common regional stress field due to a large degree of inconsistency in terms of reduced stress tensors. Altogether, these non-Andersonian stress states reveal mean directions of principal stress axes that roughly comply with the Permo-Carboniferous tensional stress field. Most probably oblique stress states are related to the intense magmatic activity during the phase of rifting.
- The youngest stress states detected correspond to a wrench regime (vertical σ_2) with a roughly N-S-directed σ_1 and a maximum age of Permian. The absolute timing of this stress field is poorly constrained because of the lack of any exposed rocks younger than Permian. Part of the locally derived strike-slip stress states might be related to a pre-rift (Variscan) stress field that initiated rifting in the area.

Further conclusions regard the mechanisms of deformation:

- The Permo-Carboniferous tensional stress field is characterised by a low stress ratio (radial extension) which indicates that rifting might at least partly have been thermally controlled (active rifting).
- Stress states inferred from the accommodation zone between the Akerhus and Vestfold Graben segments partly deviate from the general trends of paleostress states in the rest of the area.

- Finally, in contrast to the findings from the southern margin of the CEBS, no complete Mesozoic or Cenozoic reprogramming of observable fault-slip patterns has occurred in the Oslo Graben area.

6 Synthesis

The Central European Basin System (CEBS) is known as a complex intracontinental basin system that has developed through different geodynamic phases since latest Carboniferous times. Considering the configuration and development of individual sub-basins, questions arise concerning the mechanisms that controlled their changeful history. The present study has provided some new perceptions on the evolution and effects of paleostress fields in different parts of the basin system.

Evolution of paleostress fields

After having performed a fault-slip analysis separately for the Elbe Fault System (EFS) area and the Oslo Graben area, the deduced paleostress fields can now be set in relation to the evolution of stress states in other parts of the CEBS (Fig. 70, Fig. 71). This synthesis integrates results from the southern margin of the CEBS, from more central parts of the basin system (Lohr, 2007; van Gent et al., in press), from the Sorgenfrei-Tornquist Zone (Bergerat et al., 2007), from the Teisseyre-Tornquist Zone (Lamarche et al., 2002), and from parts north of the Tornquist Zone (Oslo Graben area).

The NW-SE compressional stress field detected in the Oslo Graben area has been demonstrated to correlate with Caledonian signs of deformation. Thus, this stress field is insignificant for the development of the CEBS which was initiated not until the latest Carboniferous. The tensional stress field, however, does correlate with the *initial rift phase* that has governed the CEBS during Permo-Carboniferous times. Along with the large number of oblique stress states, this tensional stress field documents that the phase of rifting exerted the most dominant imprint in the Oslo Graben area. Tensional stress fields of corresponding ages are found along the Sorgenfrei-Tornquist Zone (Bergerat et al., 2007) and also north of the Elbe Fault System (Lohr, 2007; van Gent et al., in press). Within the Elbe Fault System area, however, there are no signs of Permo-Carboniferous tensional stress fields documented by fault-slip data, despite the presence of Permo-Carboniferous rocks.

Due to a lack of Mesozoic and Cenozoic rocks in the Oslo Graben area, the temporal role of the strike-slip stress field (with NNW-SSE-directed σ_1) is not well constrained. Considering the directions of principal axes, however, it corresponds well with a transtensional stress field that affected parts of the Sorgenfrei-Tornquist Zone during the Permian (Fig. 70; Bergerat, et al., 2007). Thus, it is possible that the Oslo Graben area has remained widely unaffected by any major tectonic activity for much of the Mesozoic and Cenozoic. Such a tectonic quiescence agrees with findings from the Skagerrak Graben of which the Mesozoic and Cenozoic cover sediments do not show any significant signs of deformation (Ro et al., 1990; Lie & Anderson, 1998). In any case, post Paleozoic deformation events have not been intense enough to overprint much of the older signs of deformation in the Oslo Graben area.

A completely different story is archived by the rocks exposed along the Elbe Fault System: the oldest signs of faulting preserved by the Permo-Carboniferous volcanics of the Flechtingen High area, for instance, are related to the *Late Cretaceous–Early Tertiary phase of inversion*. The inversion-related compressional and strike-slip stress fields with N-S- to NE-SW-directed σ_1 are the most significant imprints along the southern margin of the CEBS while other regional stress fields have been demonstrated to postdate the phase of inversion. These observations argue for an extensive “reprogramming” of observable signs of deformation along the Elbe Fault System since Late Cretaceous times. This is in contrast to the more central parts of the basin such as the Groningen Block (van Gent et al., in press) or the Allertal Fault Zone area (AFZ; Lohr, 2007) where Late Cretaceous and Tertiary deformation patterns have successfully been distinguished from Permian tensional stress fields. Likewise, at the Sorgenfrei-Tornquist Zone signs of compressional and strike-slip stress states related to the phase of inversion are found as well as signs of a Permian tensional stress field (Bergerat et al., 2007). And finally, inversion-related strike-slip stress states have not completely overprinted the signs of Variscan compressional tectonics at the Teisseyre-Tornquist Zone (Holy Cross Mountains; Lamarche, 2002).

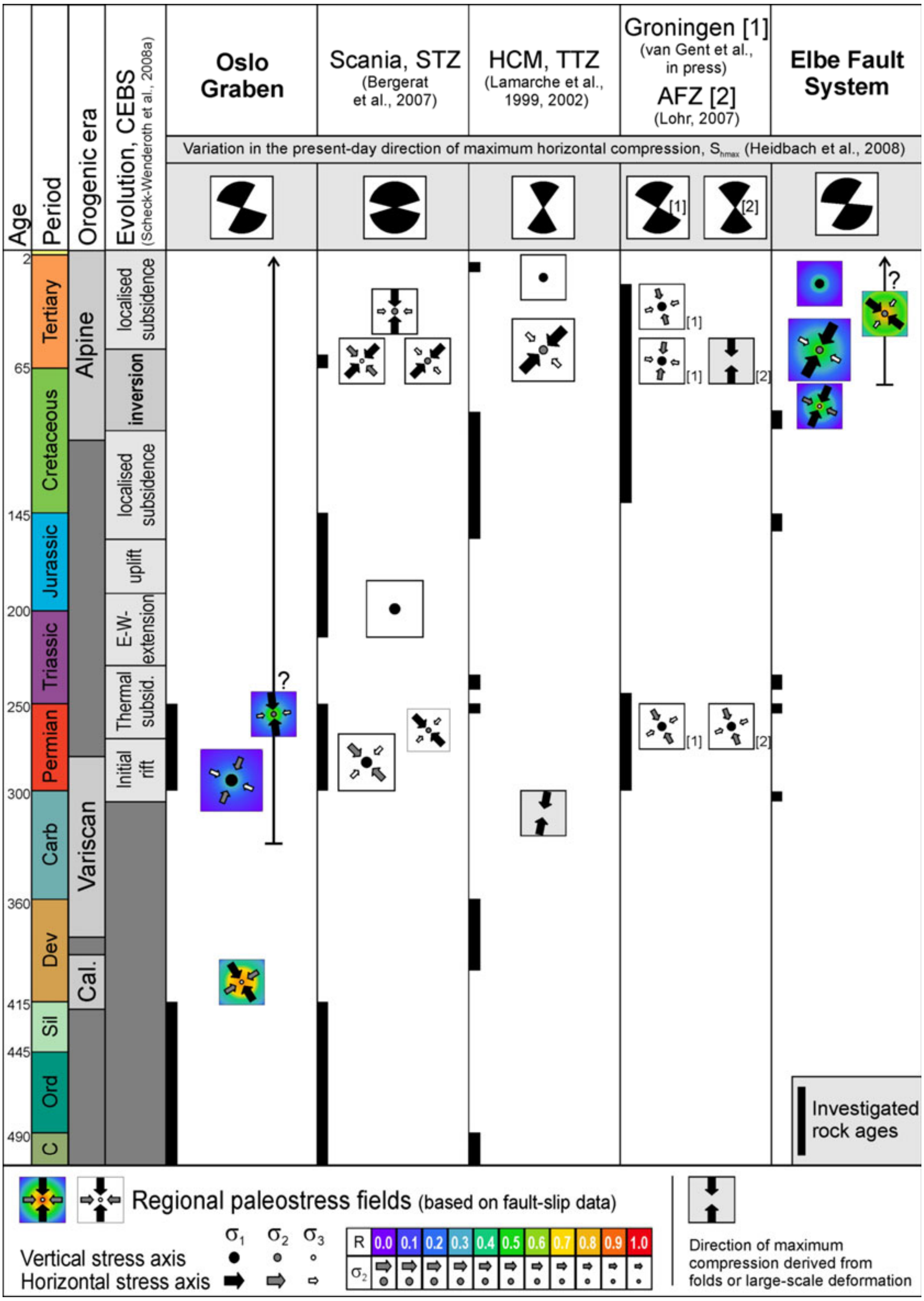

Figure 70: Compilation of paleostress and recent stress from different areas of the CEBS. Paleostress fields derived from fault-slip data are shown in chronological order (for locations see Fig. 71). Black parts of the symbols for recent stresses indicate the range of azimuths of directions of maximum compression (S_{Hmax}) taken from the World Stress Map (Fig. 71; Heidbach et al., 2008).
AFZ – Allertal Fault Zone; HCM – Holy Cross Mountains; STZ – Sorgenfrei-Tornquist Zone; TTZ – Teisseyre-Tornquist Zone

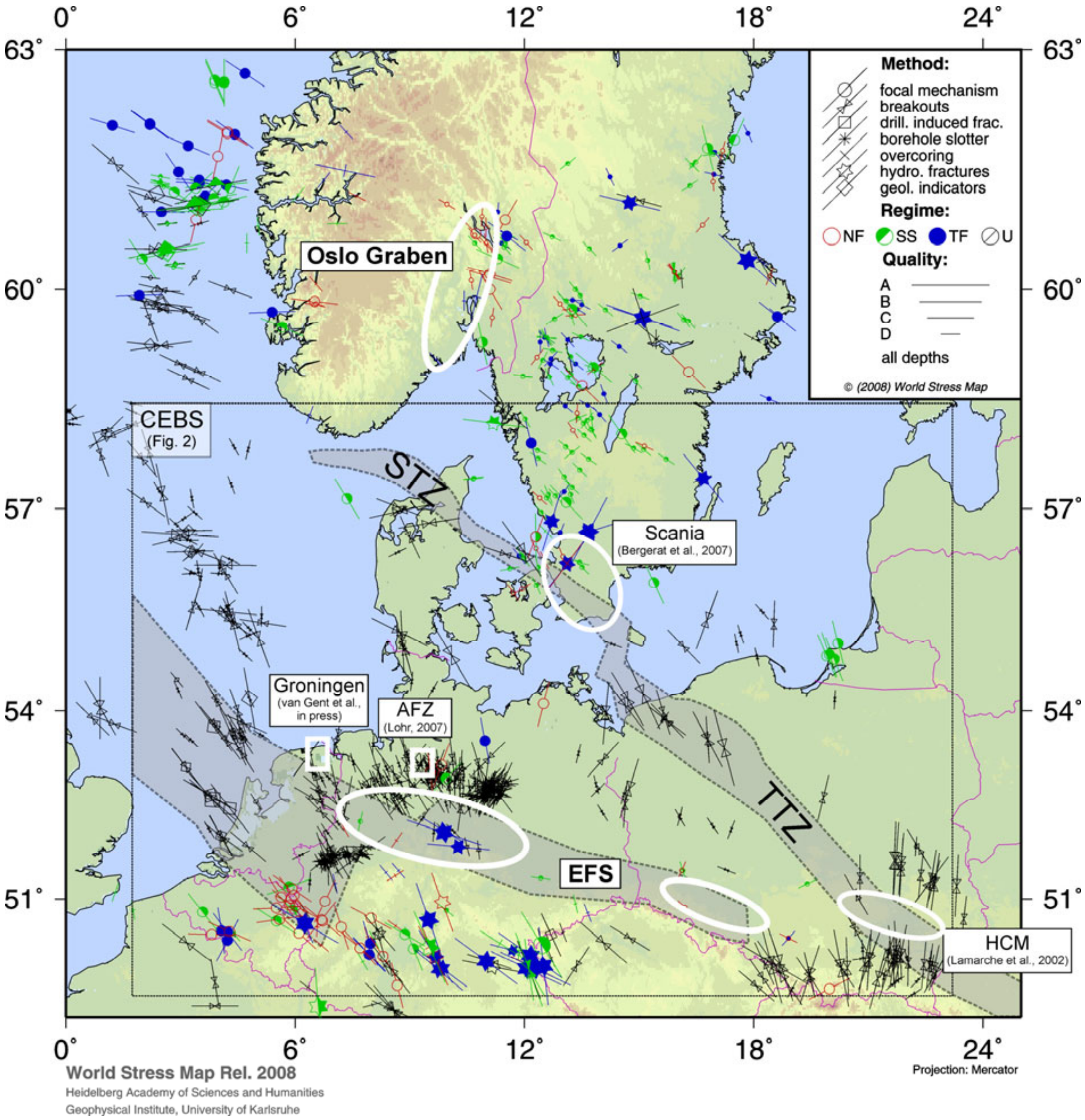

Figure 71: Present-day directions of maximum horizontal stress (S_{Hmax}) in North Central Europe (modified after Heidbach et al., 2008). Areas for which a fault-slip analysis has been performed are indicated (AFZ – Allertal Fault Zone area; EFS – Elbe Fault System area; HCM – Holy Cross Mountains).

The role of zones of crustal weakness

Though it is possible to trace large-scale deformation patterns and related regional stress fields across much of the CEBS, the results of this paleostress study argue for a recurrence of localised deformation. The *Late Cretaceous - Early Tertiary phase of inversion* has most strongly affected the area of the Elbe Fault System. The localised reprogramming of observable strain along this pre-existing fault system correlates with a stress-sensitive zone in the lower crust which has been described to have repeatedly supported strain localisation since Late Carboniferous times (Scheck et al., 2002a).

Likewise, the different segments of the Tornquist Zone show signs of intense inversion (Berthelsen, 1992). Both the Tornquist Zone and the Elbe Fault System reveal a prominent

WNW-ESE-trend. On the contrary, the sedimentary fill of the N-S-trending Glücksstadt Graben does not document any inversion-related signs of deformation (Maystrenko et al., 2005). Similarly, the Groningen Block - also bounded by roughly N-S striking faults – reveals fault patterns that document Late Cretaceous extension while the inversion is only manifest as uplift of this rigid block as a whole (van Gent et al., in press). Accordingly, the lack of any signs of inversion which is certain for the Skagerrak Graben and probable also for the Oslo Graben might be a result of the NNE-orientation of these structural domains which is parallel to the NNE-direction of maximum compression during the CEBS-wide inversion.
An alternative explanation for the inversion not to have affected the Oslo Graben area could be given by the Tornquist Zone which is supposed to largely correspond with the boundary between the stable Baltic Shield and the rheologically weaker accreted parts of Phanerozoic Europe. This rheological contrast is primarily explained by a deeper lithosphere-asthenosphere boundary and a deeper Moho beneath the Baltic Shield with respect to domains to the southwest (Gregersen et al., 2002; Ziegler & Dèzes, 2006). Accordingly, the Sorgenfrei-Tornquist Zone has been described as a weak crustal lineament which has been acting as a "buffer zone" whenever changes in the regional stress field have occurred (Mogensen, 1994, 1995). During the Mid Jurassic, for example, strain localisation along this zone has led to a decoupling of the Skagerrak Graben from extensional tectonics occurring along the Sorgenfrei-Tornquist Zone (Ro et al., 1990). In a similar way, stresses related to the *Late Cretaceous – Early Tertiary inversion* might have been released along the Tornquist Zone which thus protected areas to the north as the Skagerrak Graben and the Oslo Graben. Respective indications for the Tornquist Zone to act as a great stress barrier also come from 3D numeric modelling: These models predict the Tornquist Zone to form a region of localised deformation separating domains which are different in the style of horizontal deformation (Cacace et al., 2008). Accordingly, the special role of the Tornquist Zone emanates from the uneven distribution of sediments, crustal thickness variations, lateral depth variations in the lithosphere-asthenosphere isothermal boundary, and lateral rheological heterogeneities observed along this zone.

Paleostress and recent stress patterns

The present-day stress pattern in North Central Europe is characterised by a predominant NNW-SSE-direction of maximum horizontal stress (S_{Hmax}; Fig. 71). Though the predominance of this trend reflects some homogeneity of stresses in the area, there is a great variation in the local directions of S_{Hmax} when considering the total number of available data for a single subarea (upper row in Fig. 70). These local perturbations of stresses are supposed to be related, for instance, to rheological contrasts, salt movements, or the ongoing isostatic response to deglaciation (Roth & Fleckenstein, 2001; Kaiser et al., 2005; Cacace et al., 2008). Furthermore, differences in the patterns of S_{Hmax} between subsaline and suprasaline formations of the North German Basin argue for a decoupling of the regional stress field due to the *Zechstein* salt layer while only the stress states in the subsaline formations have been shown to represent the regional stress field (Roth & Fleckenstein, 2001).
Given all these complexities characterising the present-day stress pattern in North Central Europe, it is surprising how consistent the reconstructed paleostress states from different locations in the CEBS are. These consistencies are all the more remarkable as the signs of deformation underlying paleostress states are supposed to partly date back to hundreds of millions of years, while data bases for present-day stresses span not more than about the last hundred years. Moreover, many of the paleostress states from the southern margin of the CEBS have been derived from suprasaline formations and still could well be correlated with stress states elsewhere.
An explanation for the relatively small variations among reconstructed paleostresses might be given by the type of interpreted stress indicators. Crystal fibres are the most frequently used

paleostress indicators. Their growth requires a certain duration and continuity of movement along a fault plane which is best given under a constant stress field. In contrast, earthquakes, borehole breakouts, or artificially induced fractures which are widely used as indicators for recent stresses might occasionally represent short-lived responses to more locally restricted changes or modifications of the regional stress field.

Paleostress inversion – potentials and limitations

For reconstructing paleostress states, the present study makes use of an approach the principles of which can be traced back to the studies of Anderson (1942) and Wallace (1951) while its practical applicability has been improved gradually with the ever-growing capacities of computers since the 1970s: the technique of fault-slip analysis.

After having performed first field campaigns in the CEBS, it soon became obvious that a technique would be required which allows extracting paleostress states from heterogeneous or mixed sets of fault-slip data. To analyse this kind of data sets which mostly result from polyphase deformation the Stress Inversion Via Simulation (SVS) has been developed.

SVS is a stepwise technique that integrates different approaches towards fault-slip analysis and stress inversion. The PBT-Method (PBT; Sperner et al., 1993) incorporated in SVS corresponds to a graphical construction of strain axes for a single fault-slip datum according to Mohr-Coulomb principles of fracturing. PBT allows a fast and straightforward separation of fault-slip data according to consistencies in fault kinematics. It has been demonstrated that for sets of fault-slip data prominent trends of kinematic PBT-axes are preliminary indicators for the potential trends of associated stress axes. Thus, the orientation of clusters of PBT-axes might directly identify sets of fault-slip data as being related to non-Andersonian stress states. Such data sets, in turn, might document that folding or tilting of the respective rock mass has postdated faulting and back-tilting is required before stress inversion.

While PBT essentially constructs strain axes, the Multiple Inverse Method (MIM; Yamaji, 2000) relates fault kinematics to states of stress by following the Wallace-Bott hypothesis. Despite fundamental differences in the approaches of PBT and MIM, the orientations of kinematic and stress axes frequently reveal consistencies that provide significant constraints for determining the best-fitting stress tensor for a set of fault-slip data. Starting from these consistent results, a forward modelling procedure – the simulation – is performed which finally allows estimating the parameters of the best-fitting reduced stress tensor. Such an interactive stress simulation provides direct visual control on the misfit angle distribution of a set of fault-slip data while testing different stress states. Thus, one main advantage of SVS is that it does not work as a “black-box”. Another benefit concerns the quality of results: Stress states estimated according to SVS best fit the associated fault-slip data in terms of both misfit angles and shear-to-normal-stress ratios.

SVS has successfully been applied to fault-slip data from different subareas of the CEBS. The reliability of estimated stress states is confirmed by the fact that irrespective of (i) the number of fault-slip data from an outcrop, (ii) the number of subsets they represent and (iii) the proportion of newly formed and reactivated faults, very consistent reduced stress tensors are obtained from different outcrops within variously aged rocks. Such significant consistencies in the results have been demonstrated to allow regional correlations of locally estimated paleostress states.

The principles of paleostress stratigraphy are among the most reliable tools for estimating the relative timing of regional stress fields. Accordingly, a group of consistent paleostress states reconstructed exclusively from pre-Permian rocks in the Oslo Graben area has been demonstrated to date back to pre-Permian times due to correlations with Caledonian signs of deformation. Conclusions on the timing of other paleostress fields in this area, on the contrary, are impeded by the fact that all of these stress fields are indicated by faults in

Permian rocks while rocks younger than Permian are not exposed. In the area of the Elbe Fault System temporal constraints are similarly limited: Despite a great variety of investigated rock ages (from Late Carboniferous to Late Cretaceous), the regional stress fields are consistently derived from fault patterns in rocks of all ages. Thus, stratigraphic ages in the Elbe Fault System only argue for the regional stress fields to consistently be (post-) Late Cretaceous in age.
Alternative constraints on the relative timing of stress states are locally derived directly from field observations. Despite the diversity of stress states reconstructed at many sites, the number of chronological indicators on the relative timing of fault-slip data is remarkably low. Complementary constraints have been found at sites where phases of faulting have alternated with phases of folding and a reconstruction of the horizontality of bedding planes provides a deformation-time model.
After all, the relative and absolute dating of estimated paleostress states is one of the greatest problems in the CEBS. Available chronological constraints such as those derived from field observations have been considered, but most of the temporal arrangements of stress fields are based on correlations with the developments of large-scale deformation patterns which are well-established in both the Elbe Fault System and the Oslo Graben area.

Outlook

Up to the present, fault-slip analysis according to the strategy of SVS requires operating with several different software packages and tools. These programmes, in turn, operate based on different data formats. Moreover, the simulation tool allows interactively checking only the misfit angle distribution of fault-slip data, but not the shear-to-normal-stress ratios which have to be calculated separately. For these reasons, continuative work should aim on integrating all aspects of SVS into one software package.
Some potential solutions for the problem of absolute dating of paleostress states might be provided by the techniques of isotope geochemistry. The geochemical properties of minerals grown along a fault plane during movement of the fault (such as crystal fibres) may reflect the absolute date of mineral growth or indicate pressure and temperature conditions during precipitation. For calcite which is the most frequently observed fault-related mineral in the study areas, the scarcity of radiogenic elements impedes radiometric dating, but the abundance of the stable isotopes $^{\delta 13}C$ and $^{\delta 18}O$ may provide the possibility to find out more about p-T conditions during faulting. Theoretically, these conditions could then be related to stages in the subsidence and uplift history of the rocks.

Final conclusion

The Stress Inversion Via Simulation provides an adequate strategy for fault-slip analysis and paleostress inversion in a complex system of sedimentary basins. However, the strategy should be complemented by techniques that aim on determining the absolute age of faulting events to better constrain the ages of related paleostress states. The present study provides insight into the evolution of paleostress fields for the areas of the Elbe Fault System in the south and the Oslo Graben in the north. As a major zone of crustal weakness, the Elbe Fault System has experienced an almost complete reprogramming of observable strain since Late Cretaceous times. The Oslo Graben area, on the contrary, has widely been unaffected by major tectonic activity since Permian times, which is possibly due to localised deformation along the Tornquist Zone that acted as a stress barrier. Consequently, a temporal correlation of paleostresses from the two study areas is not possible and conclusions on the Permo-Carboniferous to recent evolution of stress fields affecting the entire Central European Basin System are very limited.

7 References

Anderson, E.M., 1942. The Dynamics of Faulting, Olivier and Boyd, Edinburgh, 266 pp.

Angelier, J., 1979. Determination of the mean principal directions of stresses for a given fault population. Tectonophysics, 56(3-4): T17-T26.

Angelier, J. and Goguel, J., 1979. Sur une méthode simple de détermination des axes principaux des contraintes pour une population de failles. Les Comptes Rendus de l'Académie des Sciences, Paris, 288: 307-310.

Angelier, J., 1984. Tectonic analysis of fault slip data sets, Special section; Fault behavior and the earthquake generation process. American Geophysical Union, Washington, DC, United States, pp. 5835-5848.

Angelier, J., 1989. From orientation to magnitudes in paleostress determinations using fault slip data. Journal of structural geology, 11(1/2): 37-50.

Angelier, J., 1990. Inversion of field data in fault tectonics to obtain the regional stress; Part 3, A new rapid direct inversion method by analytical means. Geophysical Journal International, 103(2): 363-376.

Angelier, J., 1994. Fault slip analysis and palaeostress reconstruction. In: P.L. Hancock (Editor), Continental deformation. Pergamon Press, Oxford, pp. 53-101.

Angelier, J., Bergerat, F., Stefansson, R. and Bellou, M., 2008. Seismotectonics of a newly formed transform zone near a hotspot: Earthquake mechanisms and regional stress in the South Iceland Seismic Zone. Tectonophysics, 447: 95-116.

Apperson, K.D. and Frohlich, C., 1988. Sums of moment tensors for earthquakes near subduction zones. EOS, Transactions of the American Geophysical Union, 69: 1438.

Arthaud, F. and Matte, P., 1977. Late Paleozoic strike-slip faulting in southern Europe and northern Africa: Result of a right-lateral shear zone between the Appalachians and the Urals. Geological Society of America Bulletin, 88: 1305-1320.

Babuska, V. and Plomerova, J., 2004. The Sorgenfrei-Tornquist Zone as the mantle edge of Baltica lithosphere: new evidence from three-dimensional seismic anisotropy. Terra Nova, 16: 243-249.

Bachmann, G.H. and Hoffmann, N., 1997. Development of the Rotliegend Basin in Northern Germany. Geologisches Jahrbuch, D103: 9-31.

Badley, M.E., Price, J.D. and Backshall, L.C., 1993. Inversion, reactivated faults and related structures: seismic examples from the southern North Sea. In: M.A. Cooper and G.D. Williams (Editors), Inversion Tectonics. Geological Society of London, Special Publications, London, pp. 201-217.

Baldschuhn, R. et al., 1996. Subcrop Map of Formations beneath Tertiary or Quarternary. In: R. Baldschuhn and F. Kockel (Editors), Tectonic Atlas of NW-Germany - part 2. Federal Institute for Geosciences and Natural Resources, Hannover.

Baldschuhn, R., Binot, F., Fleig, S. and Kockel, F., 2001. Geotektonischer Atlas von Nordwest-Deutschland und dem deutschen Nordsee-Sektor. Geologisches Jahrbuch, 153(A): 3-95.

Benek, R. et al., 1996. Permo-Carboniferous magmatism of the Northeast German Basin. Tectonophysics, 266: 379-404.

Bergerat, F., 1987. Stress fields in the European Platform at the time of Africa-Eurasia collision. Tectonics, 6(2): 99-132.

Bergerat, F., Angelier, J. and Andreasson, P.-G., 2007. Evolution of paleostress fields and brittle deformation of the Tornquist Zone in Scania (Sweden) during Permo-Mesozoic and Cenozoic times. Tectonophysics, 444: 93-110.

Berthelsen, A., 1980. Towards a palinspastic tectonic analysis of the Baltic Shield. In: J. Cogné and M. Slansky (Editors), Geology of Europe from Precambrian to the post-Hercynian sedimentary basins (Proceedings of the 26th International Geological Congress). Memoirs of the Bureau de Recherches Géologique et Miniéres, Paris, pp. 5-21.

Berthelsen, A., 1992. From Precambrian to Variscan Europe. In: D. Blundell, R. Freeman and S. Mueller (Editors), A continent revealed. The European Geotraverse. Cambridge University Press, Cambridge, pp. 153-163.

Betz, D., Fuehrer, F., Greiner, G. and Plein, E., 1987. Evolution of the Lower Saxony Basin, Compressional intra-plate deformations in the Alpine Foreland. Elsevier, Amsterdam, Netherlands, pp. 127-170.

Bingham, C., 1964. Distributions on a sphere and the projective plane. Dissertation Thesis, Yale University, New Haven, 93 pp.

Bishop, A., 1966. The strength of solids as engineering materials. Geotechnique, 16: 91-130.

Bjørlykke, K., 1983. Subsidence and tectonics in Late Precambrian and Paleozoic sedimentary basins of southern Norway. Norges Geologisk Undersökelse, 380: 159-172.

Bockelie, J.F. and Nystuen, J.P., 1985. The southeastern part of the Scandinavian Caledonides. In: D.G. Gee and B.A. Sturt (Editors), The Caledonide Orogen - Scandinavia and Related Areas. John Wiley, New York, pp. 69-88.

Bott, M.H.P., 1959. The mechanics of oblique slip faulting. Geological Magazine, 96(2): 109-117.

Breitkreuz, C. and Kennedy, A., 1999. Magmatic flare-up at the Carboniferous-Permian boundary in the NE German Basin revealed by SHRIMP zircon ages. Tectonophysics, 302: 307-326.

Buchanan, P.G., Bishop, D.J. and Hood, D.N., 1996. Development of salt related structures in the Central North Sea: results from section balancing. In: G.I. Alsop and I. Davison (Editors), Salt tectonics. Geological Society of London, Special Publications, London, pp. 111-128.

Byerlee, J.D., 1968. Brittle-ductile transition in rocks. Journal of Geophysical Research, 73(B14): 4741-4750.

Cacace, M., Bayer, U. and Marotta, A.M., 2008. Strain localization due to structural in-homogeneities in the Central European Basin System. International Journal of Earth Sciences, 97: 899-913.

Capote, R., Munoz, J.A., Simón, J.L., Liesa, C.-L. and Arlegui, L.E., 2002. Alpine tectonics I: the Alpine system north of the Betic Cordillera. In: W. Gibbons and T. Moreno (Editors), Geology of Spain. The Geological Society of London, London, pp. 319-338.

Carey, E. and Brunier, B., 1974. Analyse theorique et numerique d'un modele mecanique elementaire applique a l'etude d'une population de failles. Comptes Rendus Hebdomadaires des Seances de l'Academie des Sciences, Serie D: Sciences Naturelles, 279(11): 891-894.

Carlé, W., 1938. Die saxonische Tektonik westlich und nordwestlich des Harzes (Gittelder Graben und Lutterer Sattel). Geotektonische Forschungen, 3: 33-72.

Célérier, B., 1988. How much does slip on a reactivated fault plane constrain the stress tensor? Tectonics, 7(6): 1257-1278.

Clausen, O.R. and Pedersen, P.K., 1999. Late Triassic structural evolution of the southern margin of the Ringkobing-Fyn High, Denmark. Marine and Petroleum Geology, 16(7): 653-665.

Corfu, F. and Dahlgren, S., 2007. Pervoskite U-Pb ages and the Pb isotopic composition of alkaline volcanism initiating the Permo-Carboniferous Oslo Rift. Earth and Planetary Science Letters, 265: 256-269.

Coulomb, C.A., 1776. Essai sur une application des règles des maximis et minimis à quelques problemes de statique relatifs à l'architecture. Mémoires Academie Royale Présentes Par Divers Savants, 7: 343-382.

Coward, M.P., Dewey, J., Hempton, M. and Holroyd, J., 2003. Tectonic evolution. In: D. Evans, C. Graham, A. Armour and P. Brathust (Editors), The Millenium Atlas: Petroleum Geology of the Central and Northern North Sea. Geological Society of London, London, pp. 2.1-2.17.

Dadlez, R., Narkiewicz, M., Stephenson, R.A., Visser, M.T.M. and Wees, J.-D.v., 1995. Tectonic evolution of the Mid-Polish Trough: modelling implications and significance for central European geology. Tectonophysics, 252: 179-195.

Dadlez, R., Marek, S. and Pokorski, J., 1998. Palaeogeographic Atlas of Epicontinental Permian and Mesozoic in Poland (1:2 500 000). Polish Geological Institute, Warszawa.

Dadlez, R., Marek, S. and Pokorski, J., 2000. Geological Map of Poland without Cainozoic deposits 1:1 000 000. Polish Geological Institute, Warsaw.

Decourt, J. et al., 2000. Atlas Peri-Tethys. Commission de la Carte Géologique du Monde, Paris.

DeLugt, I.R., VanWees, J.D. and Wong, T.E., 2003. The tectonic evolution of the southern Dutch North Sea during the Paleogene: basin inversion in distinct pulses. Tectonophysics, 373(1-4): 141-159.

Dewey, J.F., Holdsworth, R.E. and Strachan, R.A., 1998. Transpression and transtension zones. In: R.E. Holdsworth, R.A. Strachan and J.F. Dewey (Editors), Continental Transpressional and Trantensional Tectonics. Geological Society, London, Special Publications, London, pp. 1-14.

Doblas, M., 1998. Slickenside kinematic indicators, Rock deformation; the Logan volume. Elsevier, Amsterdam, Netherlands, pp. 187-197.

Drozdzewski, G., 1988. Die Wurzel der Osning-Überschiebung und der Mechanismus herzynischer Inversionsstörungen in Mitteleuropa. Geologische Rundschau, 77(1): 127-141.

Dupin, J.-M., Sassi, W. and Angelier, J., 1993. Homogeneous stress hypothesis and actual fault slip: a distinct element analysis. Journal of Structural Geology, 15(8): 1033-1043.

Erlström, M., Thomas, S.A., Deeks, N. and Sivheda, U., 1997. Structure and tectonic evolution of the Tornquist Zone and adjacent sedimentary basins in Scania and the southern Baltic Sea area. Tectonophysics, 271(3-4): 191-251.

Etchecopar, A., Vasseur, G. and Daignieres, M., 1981. An inverse problem in microtectonics for the determination of stress tensors from fault striation analysis. Journal of Structural Geology, 3(1): 51-65.

EUGENO-SWorkingGroup, 1988. Crustal structure and tectonic evolution of the transition between the Baltic Shield and the North German Caledonides. Tectonophysics, 150: 253-348.

Evans, D., Graham, C., Armour, A., Bathurst, P. and compilers), e.a., 2003. The Millennium Atlas: Petroleum Geology of the Central and Northern North Sea. Geological Society of London, London, Bath, 389 pp.

Fernández, C., de la Nuez, J., Casillas, R. and García Navarro, E., 2002. Stress fields associated with the growth of a large shield volcano (La Palma, Canary Islands). Tectonics, 21(4): pp.18.

Fiedler, K., 1984. Tektonik (Baugeschichte). In: H. Klassen (Editor), Geologie des Osnabrücker Berglandes. Naturwissenschaftliches Museum Osnabrück, Osnabrück, pp. 519-565.

Fleuty, M.J., 1974. Slickensides and slickenlines. Geological Magazine, 112(3): 319-322.

Franzke, H.J., Voigt, T., Eynatten, H.v., Brix, M.R. and Burmeister, G., 2004. Geometrie und Kinematik der Harznordrandstörung, erläutert an Profilen aus dem Gebiet von Blankenburg. Geologische Mitteilungen von Thüringen, 11: 39-63.

Franzke, H.J., Müller, R., Voigt, T. and Eynatten, H.v., 2007. Paleo-Stress Paths in the Harz Mountains and surrounding areas (Germany) between the Triassic and the Upper Cretaceous. Zeitschrift für geologische Wissenschaften, Berlin, 35(3): 141-156.

Frohlich, C., 1992. Triangle diagrams: ternary graphs to display similarity and diversity of earthquake focal mechanisms. Physics of the Earth and Planetary Interiors, 75: 193-198.

Gephart, J.W. and Forsyth, D.W., 1984. An improved method for determining the regional stress tensor using earthquake focal mechanism data; application to the San Fernando earthquake sequence. Journal of Geophysical Research. B 89(11): 9305-9320.

Gephart, J.W., 1990. Stress and the direction of slip on fault planes. Tectonics, 9(4): 845-858.

Giner-Robles, J.L., Gonzáles-Casado, J.M., Gumiel, P. and García-Cuevas, C., 2003. Changes in stress trajectories in three different types of plate tectonic boundary deduced from earthquake focal mechanisms. Tectonophysics, 372: 179-191.

Glennie, K.W., 1984. The structural framework and the Pre-Permian history of the North Sea. In: K.W. Glennie (Editor), Introduction to the Petroleum Geology of the North Sea. Blackwell Scientific Publication, pp. 17-60.

Goes, S., Loohuis, J.J.P., Wortel, M.J.R. and Govers, R., 2000. The effect of plate stresses and shallow mantle temperature on tectonics of northwestern Europe. Global and Planetary Change, 27: 23-38.

Golonka, J., 2004. Plate tectonic evolution of the southern margin of Eurasia in the Mesozoic and Cenozoic. Tectonophysics, 381: 235-273.

Gölke, M. and Coblentz, D., 1996. Origins of the European regional stress field. Tectonophysics, 266: 11-24.

Gregersen, S., 1992. Crustal stress regime in Fennoscandia from focal mechanisms. Journal of Geophysical Research, 97(B8): 11821-11827.

Gregersen, S., Voss, P., Shomali, Z.H. and Group, T.W., 2002. Summary of Project T: delineation of a stepwise, sharp, deep lithosphere transition across Germany-Denmark-Sweden. Tectonophysics, 360: 61-73.

Grünthal, G. and Stromeyer, D., 1992. The recent crustal stress field in Central Europe: trajectories and finite element modeling. Journal of Geophysical Research - Solid Earth, 97(B8): 11805-11820.

Hancock, P.L., 1985. Brittle microtectonics: principles and practice. Journal of Structural Geology, 7(3/4): 437-457.

Hancock, P.L. and Barka, A.A., 1987. Kinematic indicators on active normal faults in western Turkey. Journal of Structural Geology, 9(5-6): 573-584.

Hansen, D.L., Nielsen, S.B. and Lykke, A.H., 2000. The post-Triassic evolution of the Sorgenfrei-Tornquist Zone; results from thermo-mechanical modelling. Tectonophysics, 328(3-4): 245-267.

Hansen, D.L., Blundell, D.J. and Nielsen, S.B., 2002. A model for the evolution of the Weald Basin. Bulletin of the Geological Soceity of Denmark, 49: 109-118.

Hansen, D.L. and Nielsen, S.B., 2003. Why rifts invert in compression. Tectonophysics, 373(1-4): 5-24.

Hecht, C.A., Lempp, C. and Scheck, M., 2003. Geomechanical model for the post-Variscan evolution of the Permocarboniferous-Mesozoic basins in Northeast Germany. Tectonophysics, 373(1-4): 125-139.

Heeremans, M., Larsen, B.T. and Stel, H., 1996. Paleostress reconstruction from kinematic indicators in the Oslo Graben, southern Norway: new constraints on the mode of rifting. Tectonophysics, 266(1-4): 55-79.

Heeremans, M. and Faleide, J.I., 2004. Late Carboniferous-Permian tectonics and magmatic activity in the Skagerrak, Kattegat and the North Sea. In: M. Wilson et al. (Editors), Permo-Carboniferous Magmatism and Rifting in Europe. Geological Society Special Publication, London, pp. 157-176.

Heeremans, M., 2005. A plume beneath the Oslo Graben?

Heidbach, O. et al., 2008. The 2008 release of the World Stress Map (available online at www.world-stress-map.org).

Hejl, E., Coyle, D., Lal, N., Haute, P.v.d. and Wagner, G.A., 1997. Fission-track dating of the western border of the Bohemian massif: thermochronology and tectonic implications. International Journal of Earth Sciences (Geologische Rundschau), 86: 210-219.

Hinzen, K.-G., 2003. Stress field in the Northern Rhine area, Central Europe, from earthquake fault plane solutions. Tectonophysics, 377: 325-356.

Hoeppener, R., 1955. Tektonik im Schiefergebirge; Eine Einführung. Geologische Rundschau.

Homberg, C., Hu, J.C., Angelier, J., Bergerat, F. and Lacombe, O., 1997. Characterization of stress perturbations near major fault zones: insights from 2-D distinct-element numerical modelling and field studies (Jura mountains). Journal of Structural Geology, 19(5): 703-718.

Homberg, C., Bergerat, F., Philippe, Y., Lacombe, O. and Angelier, J., 2002. Structural inheritance and Cenozoic stress fields in the Jura fold-and-thrust belt (France). Tectonophysics, 357: 137-158.

Hosseinidust, S.D., 1980. Klüfte und Stylolithen am nordwestlichen Harzrand und im Lutterer Sattel in ihrer Bedeutung für die tektonische Auflösung dieses Gebietes. Clausthaler Geologische Abhandlungen, 36, Clausthal-Zellerfeld, 61 pp.

Hu, J.-C. and Angelier, J., 2004. Stress permutations: Three-dimensional distinct element analysis accounts for a common phenomenon in brittle tectonics. Journal of Geophysical Research, 109(B09403): 1-20.

Huang, Q., 1988. Computer-based method to separate heterogeneous sets of fault-slip data into sub-sets. Journal of Structural Geology, 10(3): 297-299.

Hubbert, M.K., 1951. Mechanical basis for certain familiar geological structures. Geological Society American Bulletin, 62(4): 355-372.

Hudec, M.R. and Jackson, M.P.A., 2007. Terra infirma: Understanding salt tectonics. Earth-Science Reviews, 82: 1-28.

Jaeger, J.C. and Cook, N.G.W., 1979. Fundamentals of rock mechanics. Chapman & Hall, London, 593 pp.

Jaritz, W., 1987. The origin and development of salt structures in Northwest Germany. In: I. Lerche and J.J. O'Brien (Editors), Dynamical geology of salt and related structures. Academic Press, Orlando, pp. 479-493.

Kaiser, A., Reicherter, K., Hubscher, C. and Gajewski, D., 2005. Variation of the present-day stress field within the North German Basin - Insights from thin shell FE modeling based on residual GPS velocities. Tectonophysics, 397(1-2 SPEC. ISS.): 55-72.

Kiersnowski, H., Paul, J., Peryt, T.M. and Smith, D.B., 1995. Facies paleogeography and sedimetary history of the Southern Permian Basin in Europe. In: P. Scholle, T.M. Peryt and D. Ulmer-Scholle (Editors), The Permian of Northern Pangea. Springer, Berlin, Heidelberg, New York, pp. 119-136.

Klassen, H., 1984. Geologie des Osnabrücker Berglandes. Naturwissenschaftliches Museum Osnabrück, 672 pp.

Kleinspehn, K.L., Pershing, J. and Teyssier, C., 1989. Paleostress stratigraphy: A new technique for analyzing tectonic control on sediementary-basin subsidence. Geology, 17: 253-256.

Kley, J. and Voigt, T., 2008. Late Cretaceous intraplate thrusting in central Europe: effect of Africa-Iberia-Europe convergence, not Alpine collision. Geology, 36(11): 839-842.

Kockel, F., 2003. Inversion structures in Central Europe - Expressions and reasons, an open discussion. Netherlands Journal of Geosciences / Geologie en Mijnbouw, 82(4): 367-382.

Kossow, D., Krawczyk, C.M., McCann, T., Strecker, M. and Negendank, J.F.W., 2000. Style and evolution of salt pillows and related structures in the northern part of the Northeast German Basin. International Journal of Earth Sciences, 89(3): 652-664.

Kossow, D., Krawczyk, C.M., McCann, T., Negendank, J. and Strecker, M., 2001. Structural development of the inverted Northeast German Basin, EUG XI, 8-12 April 2001. Journal of Conference Abstracts, Strasbourg, France, pp. LS05:SUpo05:PO.

Kossow, D. and Krawczyk, C.M., 2002. Strcture and quantification of processes controlling the evolution of the inverted NE German Basin. Marine and Petroleum Geology, 19: 601-618.

Krzywiec, P., 2002. Mid-Polish Trough inversion - seismic examples, main mechanisms and the relationship to the Alpine-Carpathian collision. EGU Stephan Mueller Special Publication Series, 1: 151-165.

Krzywiec, P., Kramarska, R. and Zientara, P., 2003. Strike-slip tectonics within the SW Baltic Sea and its relationship to the inversion of the Mid-Polish Trough - evidence from high-resolution seismic data. Tectonophysics, 373(1-4): 93-105.

Kukla, P.A., Urai, J.L. and Mohr, M., 2008. Dynamics of salt structures. In: R. Littke, U. Bayer, D. Gajewski and S. Nelskamp (Editors), Dynamics of Complex Intracontinental Basins. The Central European Basin System. Springer.

Lacombe, O., Mouthereau, F., Kargar, S. and Meyer, B., 2006. Late Cenozoic and modern stress field in the western Fars (Iran) : implications for the tectonic and kinematic evolution of Central Zagros. Tectonics, 25(1): TC1003, pp. 27.

Lamarche, J. et al., 1999. Variscan tectonics in the Holy Cross Mountains (Poland) and the role of structural inheritance during Alpine tectonics., EUROPROBE GeoRift; Volume 2, Intraplate tectonics and basin dynamics of the Eastern European Craton and its margins. Elsevier, Amsterdam, Netherlands, pp. 171-186.

Lamarche, J. et al., 2002. Variscan to Alpine heterogeneous palaeo-stress field above a major Palaeozoic suture in the Carpathian foreland (southeastern Poland). Tectonophysics, 357(1-4): 55-80.

Lamarche, J., Scheck, M. and Lewerenz, B., 2003. Heterogeneous tectonic inversion of the Mid-Polish Trough related to crustal architecture, sedimentary patterns and structural inheritance. Tectonophysics, 373(1-4): 75-92.

Larsen, B.T., Olaussen, S., Sundvoll, B. and Heeremans, M., 2006 (English edition 2008). Vulkaner, forkastninger, og orkenklima. In: I.B. Ramberg, I. Bryhni and A. Nottvedt (Editors), Landet blir til. Norsk Geologisk Forening, pp. 284-32.

Larsen, B.T., Olaussen, S., Sundvoll, B. and Heeremans, M., 2008. The Permo-Carboniferous Oslo Rift through six stages and 65 million years. Episodes, 31(1): 52-58.

Letouzy, J., 1986. Cenozoic paleo-stress pattern in the Alpine Foreland and structural interpretation in a platform basin. Tectonophysics, 132: 215-231.

Lie, J.E. and Andersson, M., 1998. The deep-seismic image of the crustal structure of the Tornquist Zone beneath the Skagerrak Sea, northwestern Europe. Tectonophysics, 287: 139-155.

Liesa, C.L. and Lisle, R.J., 2004. Reliability of methods to separate stress tensors from heterogeneous fault-slip data. Journal of Structural Geology, 26(3): 559-572.

Lindholm, C.D., Bungum, H., Hicks, E. and Villagran, M., 2000. Crustal stress and tectonics in Norwegian regions determined from earthquake focal mechanisms. In: A. Nøttvedt (Editor), Dynamics of the Norwegian Margin. Geological Society of London, Special Publications, London, pp. 429-439.

Lisle, R.J. and Vandycke, S., 1996. Separation of multiple stress events by fault striation analysis: an example from Variscan and younger structures at Ogmore, South Wales. Journal of the Geological Society, 153(6): 945-953.

Lohr, T. et al., 2007. Strain partitioning due to salt: insights from interpretation of a 3D seismic data set in the NW German Basin. Basin Research, 19: 579-597.

Lohr, T., 2007. Seismic and sub-seismic deformation on different scales in the NW German Basin. Dissertation Thesis, Free University, Berlin, 89 pp.

Lokhorst, A., 1998. NW European Gas Atlas - Composition and Isotope Ratios of Natural Gases. GIS application on CD by the British Geological Survey, Bundesanstalt für Geowissenschaften und Rohstoffe, Danmarks og Gronlands Geologiske Undersogelse, Nederlands Instituut voor Toegepaste Geowetenschappen, Panstwowwy Instytut Geologiczny, European Union.

Lokhorst, A., 1998. NW European Gas Atlas - Composition and Isotope Ratios of Natural Gases. GIS application on CD by the British Geological Survey, Bundesanstalt für Geowissenschaften und Rohstoffe, Danmarks og Gronlands Geologiske Undersogelse, Nederlands Instituut voor Toegepaste Geowetenschappen, Panstwowwy Instytut Geologiczny, European Union.

Lothe, A.E. et al., 1999. Struktural and sedimentological aspects of the Early Permian Brumunddal Sandstone, northern Oslo Graben. Geonytt: 68.

Maler, M.O., 1990. Dead Horse Graben: A West Texas accomodation zone. Tectonics, 9(6): 1357-1368.

Maniatis, G. and Hampel, A., 2008. Along-strike variations of the slip direction on normal faults: Insights from three-dimensional finite-element models. Journal of Structural Geology, 30: 21-28.

Mansfield, C. and Cartwright, J., 2001. Fault growth by linkage; observations and implications from analogue models. Journal of Structural Geology, 23(5): 745-763.

Marchal, D., Guiraud, M. and Rivers, T., 2003. Geometric and morphologic evolution of normal fault planes and traces from 2D to 4D data. Journal of Structural Geology, 25(1): 135-158.

Marrett, R. and Peacock, D.C.P., 1999. Strain and stress. Journal of Structural Geology, 21: 1057-1063.

Mattern, F., 1996. The Elbe Zone at Dresden - a Late Paleozoic pull-apart intruded shear zone. Zeitschrift der deutschen geologischen Gesellschaft, 147(1): 57-80.

Maystrenko, Y., Bayer, U. and Scheck Wenderoth, M., 2005. The Glueckstadt Graben, a sedimentary record between the North and Baltic Sea in north Central Europe. Tectonophysics, 397(1-2 SPEC. ISS.): 113-126.

Maystrenko, Y., Bayer, U. and Scheck-Wenderoth, M., 2006. 3D reconstruction of salt movements within the deepest post-Permian structure of the Central European Basin System - the Glückstadt Graben. Netherlands Journal of Geosciences / Geologie en Mijnbouw, 85(3): 183-198.

McLeod, A.E., Dawers, N.H. and Underhill, J.R., 2000. The propagation and linkage of normal faults; insights from the Strathspey-Brent-Stratfjord fault array, northern North Sea. Basin Research, 12(3-4): 263-284.

Meissner, R., Sadowiakl, P. and Thomas, S.A., 1994. East Avalonia, the third partner in the Caledonian collisions: evidence from deep seismic reflection data. International Journal of Earth Sciences, 83(1): 186-196.

Meschede, M., 1994. Methoden der Strukturgeologie. Enke, Stuttgart, 169 pp.

Michael, A.J., 1984. Determination of Stress from Slip Data: Faults and Folds. Journal of Geophysical Research, 89: 11517-11526.

Minor, S.A., 1995. Superposed local and regional paleostress: Fault-slip analysis of Neogene extensional faulting near coeval caldera complexes, Yucca Flat, Nevada. Journal of Geophysical Research, 100(B6): 10507-10528.
Mogensen, T.E., 1994. Palaeozoic structural development along the Tornquist Zone, Kattegat area, Denmark. Tectonophysics, 240: 191-214.
Mogensen, T.E., 1995. Triassic and Jurassic structural developement along the Tornquist Zone, Denmark. Tectonophysics, 252: 197-220.
Mohr, O., 1900. Welche Umstände bedingen die Elastizitätsgrenze und den Bruch eines Materials? Zeitschrift des Vereins Deutscher Ingenieure, 44: 1524-1530, 1572-1577.
Mohr, K., 1982. Harzvorland. Westlicher Teil. Sammlung geologischer Führer. Gebrüder Borntraeger, Berlin, Stuttgart, 142 pp.
Mutterlose, J. and Böckel, B., 1998. The Barrêmian-Aptian interval in NW Germany: a review. Cretaceous Research, 19: 539-568.
Nalpas, T. and Brun, J.-P., 1993. Salt flow and diapirism related to extension at crustal scale. Tectonophysics, 228: 349-362.
Nalpas, T., Le, D.S., Brun, J.P., Unternehr, P. and Richert, J.P., 1995. Inversion of the Broad Fourteens Basin (offshore Netherlands), a small-scale model investigation. Sedimentary Geology, 95(3-4): 237-250.
Needham, T., Yielding, G. and Freeman, R., 1996. Analysis of fault geometry and displacement patterns. In: P.G. Buchanan and D.A. Nieuwland (Editors), Modern Developments in Structural Interpretation, Validation and Modelling. Geological Society of London, Special Publications, London, pp. 189-199.
Nemcok, M. and Lisle, R.J., 1995. A stress inversion procedure for polyphase fault/ slip data sets. Journal of Structural Geology, 17(10): 1445-1453.
Nemcok, M., Kovac, D. and Lisle, R.J., 1999. A stress inversion procedure for polyphase calcite twin and fault/slip data sets. Journal of Structural Geology, 21: 597-611.
Neumann, E.-R., Olsen, K.H., Baldridge, W.S. and Sundvoll, B., 1992. The Oslo Rift: a review. Tectonophysics, 208: 1-18.
Neumann, E.-R., 1994. The Oslo Rift: P-T relations and lithospheric structure. Tectonophysics, 240: 159-172.
Neumann, E.-R. et al., 2004. Carboniferous-Permian rifting and magmatism in southern Scandinavia, the North Sea and northern Germany. In: M. Wilson et al. (Editors), Permo-Carboniferous Magmatism and Rifting in Europe. Geological Society, Special Publications, London, pp. 11-40.
Nielsen, S.B., Thomsen, E., Hansen, D.L. and Clausen, O.R., 2005. Plate-wide stress relaxation explains European Palaeocene basin inversions. Nature, 435: 195-198.
Oftedahl, C., 1952. The lavas, Studies on the igneous rock complex of the Oslo Region, 12. Skrifter utgitt av Det Norske Videnskaps-Akademi 1, Oslo, pp. 64.
Olaussen, S., Larsen, B.T. and Steel, R., 1994. The Upper Carboniferous-Permian Oslo rift; Basin fill in relation to tectonic development. In: A.F. Embry, B. Beauchamp and D.J. Glass (Editors), Pangea, Global environments and resources. Canadian Society of Petroleum Geologists Memoirs, pp. 175-198.
Orife, T. and Lisle, R.J., 2006. Assessing the statistical significance of paleostress estimates: simulations using random fault-slips. Journal of Structural Geology, 28: 952-956.
Otto, V., 2003. Inversion-related features along the southeastern margin of the North German Basin (Elbe fault system), Dynamics of sedimentary basin inversion; observations and modelling. Elsevier, Amsterdam, Netherlands, pp. 107-123.
Pascal, C., Angelier, J., Seland, R.T. and Lepvrier, C., 2002. A simplified model of stress-slip relationship: application to the Frøy Field, northern North Sea. Tectonophysics, 357(1-4): 103-118.

Petit, J.P., 1987. Criteria for the sense of movement on fault surfaces in brittle rocks. Journal of Structural Geology, 9(5/6): 597-608.

Pfiffner, O.A., Schlunegger, F. and Buiter, S.H.J., 2002. The Swiss Alps and their peripheral foreland basin: Stratigraphic response to deep crustal processes. Tectonics, 21(2): 1009.

Pharaoh, T.C., 1999. Palaeozoic terranes and their lithospheric boundaries within the Trans-European Suture Zone (TESZ): a review. Tectonophysics, 314: 17-41.

Plein, E., 1995. Norddeutsches Rotliegendbecken, Rotliegend-Monographie Teil II. In: S.K. Deutschlands (Editor), Stratigraphie von Deutschland I. Courier Forschungsinstitut Senckenberg, Frankfurt (Main), pp. 193.

Pluijm, B.A.v.d. and Marshak, S., 2004. Earth Structure. W. W. Norton & Company, New York, London, 656 pp.

Pollard, D.D., Saltzer, S.D. and Rubin, A.M., 1993. Stress inversion methods: are they based on faulty assumptions? Journal of Structural Geology, 15(8): 1045-1054.

Ramberg, I.B., 1976. Gravity interpretation of the Oslo Graben and associated igneous rocks. Norsk Geologisk Tidsskrift, 325: pp. 193.

Ramberg, I.B., Gabrielsen, R.H., Larsen, B.T. and Solli, A., 1977. Analysis of frature patterns in southern Norway. Geologie en Mijnbouw, 56: 295-310.

Ramberg, I.B. and Larsen, B.T., 1978. Tectonomagmatic evoloution. In: J.A. Dons and B.T. Larsen (Editors), The Oslo Paleorift: a Review and Guide to Excursions. Norges Geologisk Undersökelse, pp. 55-73.

Ramsay, J.G. and Lisle, R.J., 2000. The Techniques of Modern Structural Geology, Volume 3: Applications of continuum mechanics in structural geology. Academic Press, London, pp. 701-1061.

Rasser, M.W. et al., 2008. Paleogene and Neogene. In: T. McCann (Editor), The Geology of Central Europe. Volume 2: Mesozoic and Cenozoic. Geological Society, London, pp. 1031-1039.

Reches, Z.e., 1987. Determination of the tectonic stress tensor from slip along faults that obey the Coulomb yield condition. Tectonics, 6(6): 849-861.

Reicherter, K.R. and Peters, G., 2005. Neotectonic evolution of the central Betic Cordilleras (southern Spain). Tectonophysics, 405(1-4): 191-212.

Reicherter, K., Kaiser, A. and Stackebrandt, W., 2005. The post-glacial landscape evolution of the North German Basin: Morphology, neotectonics and crustal deformation. International Journal of Earth Sciences, 94(5-6): 1083-1093.

Reicherter, K. et al., 2008. Alpine tectonics north of the Alps. In: T. McCann (Editor), The Geology of Central Europe, Volume 2: Mesozoic and Cenozoic. Geological Society of London, London.

Reiter, F. and Acs, P., 1996-2008. TectonicsFP - A computer program for structural geology. http://www.tectonicsfp.com/.

Remmelts, G., 1995. Fault-related salt tectonics in the southern North Sea, the Netherlands. In: M.P.A. Jackson, D.G. Roberts and S. Snelson (Editors), Salt Tectonics: A Global Perspective. American Association of Petroleum Geologists, Memoirs, pp. 261-272.

Ro, H.E., Stuevold, L.M., Faleide, J.I. and Myhre, A.M., 1990. Skagerrak Graben - the offshore continuation of the Oslo Graben. Tectonophysics, 178: 1-10.

Ro, H.E. and Faleide, J.I., 1992. A stretching model for the Oslo Rift. Tectonophysics, 208: 19-36.

Rohrmann, M., Beek, P.v.d., Andriessen, P. and Cloetingh, S., 1995. Meso-Cenozoic morphotectonic evolution of southern Norway: Neogene domal uplift inferred from apatite fission track thermochronology. Tectonics, 14(3): 704-718.

Rosenbaum, G., Lister, G.S. and Duboz, C., 2002. Relative motions of Africa, Iberia, and Europe during Alpine orogeny. Tectonophysics, 359: 117-129.

Roth, F. and Fleckenstein, P., 2001. Stress orientations found in North-East Germany differ from the West European trend. Terra Nova, 13(4): 289-296.

Russell, M.J. and Smythe, D.K., 1983. Origin of the Oslo Graben in relation to the Hercynian-Alleghian orogeny and lithospheric rifting in the North Atlantic. Tectonophysics, 94: 457-472.

Rüffer, T. and Zühlke, R., 1995. Sequence stratigraphy and sea-level changes in the Early and Middle Triassic of the Alps: a global comparison. In: B.U. Haq (Editor), Sequence Stratigraphy and Depositional Response to Eustatic, Tectonic, and Climatic Forcing. Kluwer, Amsterdam, pp. 161-207.

Scheck, M. and Bayer, U., 1999. Evolution of the Northeast German Basin - inferences from a 3D structural model and subsidence analysis. Tectonophysics, 313(1-2): 145-169.

Scheck, M. et al., 2002. The Elbe fault system in North Central Europe- a basement controlled zone of crustal weakness. Tectonophysics, 360(1-4): 281-299.

Scheck, M., Thybo, H., Lassen, A., Abramovitz, T. and Laigle, M., 2002. Basement structure in the southern North Sea, offshore Denmark, based on seismic interpretation. Geological Society Special Publication, -(201): 311-326.

Scheck, M., Bayer, U. and Lewerenz, B., 2003. Salt movement in the Northeast German Basin and its relation to major post-Permian tectonic phases - results from 3D structural modelling, backstripping and reflection seismic data. Tectonophysics, 361(3-4): 277-299.

Scheck, M., Bayer, U. and Lewerenz, B., 2003. Salt redistribution during extension and inversion inferred from 3D backstripping. Tectonophysics, 373(1-4): 55-73.

Scheck-Wenderoth, M. and Lamarche, J., 2005. Crustal memory and basin evolution in the Central European Basin System - New insights from a 3D structural model. Tectonophysics, 397(1-2 SPEC. ISS.): 143-165.

Scheck-Wenderoth, M., Krzywiec, P., Zühlke, R., Maystrenko, Y. and Froitzheim, N., 2008. Permian to Cretaceous Tectonics. In: T. McCann (Editor), The Geology of Central Europe. Volume 2: Mesozoic and Cenozoic. Geological Society of London, London.

Scheck-Wenderoth, M., Maystrenko, Y., Hübscher, C., Hansen, M. and Mazur, S., 2008. Dynamics of salt basins. In: R. Littke, U. Bayer, D. Gajewski and S. Nelskamp (Editors), Dynamics of Complex Intracontinental Basins. The Central European Basin System. Springer.

Scherneck, H.G., Johansson, J.M., Mitrovica, J.X. and Davis, J.L., 1998. The BIFROST project: GPS determined 3-D displacement rates in Fennoscandia from 800 days of continuous observations in the SWEPO network. Tectonophysics, 294: 305-321.

Schmid, S.M., Pfiffner, O.A., Froitzheim, N., Schönborn, G. and Kissling, E., 1996. Geophysical-geological transect and tectonic evolution of the Swiss-Italian Alps. Tectonics, 15: 1036-1064.

Schreiber, U. and Rotsch, S., 1998. Cenozoic block rotation according to a conjugate shear system in central Europe - indications from paleomagnetic measurements. Tectonophysics, 299: 111-142.

Senglaub, Y., Brix, M.R., Adriasola, A.C. and Littke, R., 2005. New information on the thermal history of the southwestern Lower Saxony Basin, northern Germany, based on fission track analysis. International Journal of Earth Sciences, 94: 876-896.

Senglaub, Y., Littke, R. and Brix, M.R., 2006. Numerical modelling of burial and temperature history as an approach for an alternative interpretation of the Bramsche anomaly, Lower Saxony Basin. International Journal of Earth Sciences (Geologische Rundschau), 95: 204-224.

Senglaub, Y., Littke, R. and Brix, M.R., 2006. Numerical modelling of burial and temperature history as an approach for an alternative interpretation of the Bramsche anomaly, Lower Saxony Basin. International Journal of Earth Sciences (Geologische Rundschau), 95: 204-224.

Shan, Y., Suen, H. and Lin, G., 2003. Separation of polyphase fault/slip data: an objective-function algorithm based on hard division. Journal of Structural Geology, 25: 829-840.

Shan, Y., Lin, G. and Li, Z., 2004. An inverse method to determine the optimal stress from imperfect fault data. Tectonophysics, 387: 205-215.

Sippel, J., Scheck-Wenderoth, M., Reicherter, K. and Mazur, S., in press. Paleostress states at the south-western margin of the Central European Basin System - application of fault-slip analysis to unravel a polyphase deformation pattern. Submitted to Tectonophysics, available online since April 2008., DOI: 10.1016/j.tecto.2008.04.010; Available online 18 April 2008.

Skjernaa, L. and Pedersen, S., 1982. The effects of penetrative Sveconorwegian deformations on Rb–Sr isotope systems in the Römskog-Aurskog-Höland ara, SE Norway. Precambrian Research, 17: 215-243.

Skjeseth, S., 1963. Contribution to geology of the Mjosa District and the classical Sparagmite area in southern Norway. Norges Geologisk Undersökelse, 220, 226 pp.

Spang, J.H., 1972. Numerical Method for dynamic Analysis of Calcite Twin Lamellae. Geological Society American Bulletin, 83(1): 467-472.

Sperner, B., Ratschbacher, L. and Ott, R., 1993. Fault-striae analysis: a turbo pascal program package for graphical presentation and reduced stress tensor calculation. Computers & Geosciences, 19: 1361-1388.

Sperner, B., 1993. FLUMO - Fluctuation histogram and Mohr circle diagram. Institut für Geologie, Tübingen.

Sperner, B., 1996. Computer programs for the kinematic analysis of brittle deformation structures and the Tertiary tectonic evolution of the Western Carpathians (Slovakia). Tübinger Geowissenschaftliche Arbeiten (TGA), Institut und Museum für Geologie und Paläontologie der Universität Tübingen., 27: 120.

Sperner, B., 1996. Computer programs for the kinematic analysis of brittle deformation structures and the Tertiary tectonic evolution of the Western Carpathians (Slovakia). Tübinger Geowissenschaftliche Arbeiten (TGA), Institut und Museum für Geologie und Paläontologie der Universität Tübingen., 27: 120.

Sperner, B. and Zweigel, P., unpublished manuscript. A plea for more caution in kinematic fault-slip analysis, pp. 32.

Stampfli, G.M., Mosar, J., Favre, P., Pillevuit, A. and Vannay, J.-C., 2001. Permo-Mesozoic evolution of the western Tethys realm: the Neo-Tethys east Mediterranean basin connection. In: P.A. Ziegler, W. Cavazza, A.H.F. Robertson and S. Crasquin-Soleau (Editors), Peri-Tethys Memoir 6: Peri-Tethyan Rift/Wrench Basins and Passive Margins. Mémoires du Muséum National d'Histoire Naturelle, pp. 51-108.

Stampfli, G.M. and Borel, G.D., 2002. A plate tectonic model for the Paleozoic and Mesozoic constrained by dynamic plate boundaries and restored synthetic oceanic isochrons. Earth and Planetary Science Letters(196): 17-33.

Stampfli, G.M. and Borel, G.D., 2004. The TRANSMED transects in space and time: constraints on the paleotectonic evolution of the Mediterranean domain. In: W. Cavazza, F.M. Roure, W. Spakman, G.M. Stampfli and P.A. Ziegler (Editors), The TRANSMED Atlas. The Mediterranean Region from Crust to Mantle. Springer, Heidelberg, pp. 53-80.

Steiner, C.W., Hobson, A., Favre, P., Stampfli, G.M. and Hernandez, J., 1998. Mesozoic sequence of Fuerteventura (Canary Islands); witness of Early Jurassic sea-floor spreading in the central Atlantic. The Geological Society of America Bulletin, 110(10): 1304-1317.

Sundvoll, B., Neumann, E.-R., Larsen, B.T. and Tuen, E., 1990. Age relations among Oslo Rift magmatic rocks: implications for tectonic and magmatic modelling. Tectonophysics, 178: 67-87.

Sundvoll, B., Larsen, B.T. and Wandaas, B., 1992. Early magmatic phase in the Oslo Rift and its related stress regime. Tectonophysics, 208: 37-54.

Sundvoll, B. and Larsen, B.T., 1994. Architecture and early evolution of the Oslo Rift. Tectonophysics, 240: 173-189.

Suppe, J., 1985. Principles of Structural Geology. Prentice-Hall, Inc., Englewood Cliffs, New Jersey, 537 pp.

Surlyk, F., 2003. The Jurassic of East Greenland: a sedimentary record of thermal subsidence, onset and culmination of rifting. In: J.R. Ineson and F. Surlyk (Editors), The Jurassic of Denmark and Greenland. Geological Survey of Denmark and Greenland Ministry of the Environment, Copenhagen, pp. 659-722.

Swensson, E., 1990. Cataclastic rocks along the Nesodden Fault, Oslo Region, Norway: a reactivated Precambrian shear zone. Tectonophysics, 178: 51-65.

Thomson, S.N., Brix, M. and Carter, A., 1997. Late Cretaceous denudation of the Harz Massif assessed by apatite fission track analysis, Regionale Geologie von Mitteleuropa; geodynamische Prozesse zwischen Alpen und Nordatlantik; 149 Hauptversammlung der Deutschen Geologischen Gesellschaft und Jahreshauptversammlung der Fachsektion Geoinformatik; Kurzfassung der Vortraege und Poster. Deutsche Geologische Gesellschaft, Hanover, Federal Republic of Germany, pp. 115.

Thomson, S.N., Brix, M. and Carter, A., 1997. Late Cretaceous denudation of the Harz Massif assessed by apatite fission track analysis, Regionale Geologie von Mitteleuropa; geodynamische Prozesse zwischen Alpen und Nordatlantik; 149 Hauptversammlung der Deutschen Geologischen Gesellschaft und Jahreshauptversammlung der Fachsektion Geoinformatik; Kurzfassung der Vortraege und Poster. Deutsche Geologische Gesellschaft, Hanover, Federal Republic of Germany, pp. 115.

Thomson, S.N. and Zeh, A., 2000. Fission-track thermochronology of the Ruhla Crystalline Complex: new constraints on the post-Variscan thermal evolution of the NW Saxo-Bohemian Massif. Tectonophysics, 324: 17-35.

Torsvik, T.H., Eide, E.A., Meert, J.G., Smethurst, M.A. and Walderhaug, H.J., 1998. The Oslo Rift; new paleomagnetic and 40Ar/39Ar age constraints. Geophysical Journal International, 135: 1045-1059.

Torsvik, T.H., Carlos, D., Mosar, J., Cocks, L.R.M. and Malme, T.N.M., 2002. Global reconstructions and North Atlantic paleogeography 440 Ma to recent. In: E.A. Eide (Editor), Batlas - Mid Norway Plate Reconstruction Atlas with Global and Atlantic Perspectives. Geological Survey of Norway, Trondheim, pp. 18-39.

Turner, F.J., 1953. Nature and dynamic interpretation of deformation lamellae in calcite of three marbles. American Journal of Sciences, 251(4): 276-298.

Twiss, R.J. and Gefell, M.J., 1990. Curved slickenfibers; a new brittle shear sense indicator with application to a sheared serpentinite. Journal of Structural Geology, 12(4): 471-481.

Twiss, R.J. and Moores, E.M., 1992. Structural Geology. W.H. Freeman, New York.

Twiss, R.J. and Unruh, J.R., 1998. Analysis of fault slip inversions; do they constrain stress or strain rate? Journal of Geophysical Research, B, Solid Earth and Planets, 103(6): 12,205-12,222.

Underhill, J.R. and Partington, M.A., 1993. Jurassic thermal doming and deflation in the North Sea: implications of the sequence stratigraphic evidence. In: J.R. Parker (Editor), Petroloeum Geology of Northwest Europe: Proceedings of the 4th Conference. The Geological Society of London, London, pp. 337-345.

van Gent, H., Back, S., Urai, J.L., Kukla, P.A. and Reicherter, K., in press. Paleostresses of the Groningen area, the Netherlands - results of a seismic based structural reconstruction. Tectonophysics: doi: 10.1016/j.tecto.2008.09.038; Available online 7 October 2008.

van Wees, J.D. and Beekman, F., 2000. Lithosphere rheology during intraplate basin extension and inversion - inferences from automated modeling of four basins in Western Europe. Tectonophysics, 320: 219-242.

Vandycke, S., 1997. Post-Herzynian brittle tectonics and paleostress analysis in Carboniferous limestones, Belgian Symposium on Structural Geology and Tectonics, Aardk. Mededel., pp. 193-196.

Vandycke, S., 2002. Palaeostress records in Cretaceous formations in NW Europe: Extensional and strike-slip events in relationships with Cretaceous-Tertiary inversion tectonics. Tectonophysics, 357(1-4): 119-136.

Veevers, J.J., Clare, A. and Wopfner, H., 1994. Neocratonic magmatic-sedimentary basins of post-Variscan Europe and post-Kanimblan eastern Australia generated by right lateral transtension of Permo-Carboniferous Pangea. Basin Research, 6(2-3): 141-157.

Vejbaek, O.V., 1990. The Horn Graben, and its relationship to the Oslo Graben and the Danish Basin. Tectonophysics, 178: 29-49.

Vejbaek, O. and Andersen, C., 2002. Post mid-Cretaceous inversion tectonics in the Danish Central Graben - regionally synchronous tectonic events? Bulletin of the Geological Soceity of Denmark, 49: 129-144.

Voigt, E., 1962. Über Randtröge vor Schollenrändern und ihre Bedeutung im Gebiet der Mitteleuropäischen Senke und angrenzender Gebiete. Zeitschrift der Deutschen Geologischen Gesellschaft, 114: 378-418.

Voigt, T., Eynatten, H.v. and Franzke, H.J., 2004. Late Cretaceous unconformities in the Subhercynian Cretaceous Basin (Germany). Acta Geologica Polonica, 54: 673-694.

Voigt, T., Wiese, F., Eynatten, H.v. and Franzke, H.-J., 2006. Facies evolution of syntectonic Upper Cretaceous Deposits in the Subhercynian Cretaceous Basin and adjoining areas (Germany). Zeitschrift der deutschen Gesellschaft für Geowissenschaften, 15(2): 203-244.

Wallace, R.E., 1951. Geometry of shearing stress and relation to faulting. Journal of Geology, 59(2): 118-130.

Wallbrecher, 1986. Tektonische und gefügeanalytische Arbeitsweisen. Enke-Verlag, Stuttgart, 244 pp.

Walsh, J.J., Watterson, J., Bailey, W.R. and Childs, C., 1999. Fault relays, bends, and branch-lines. Journal of Structural Geology, 21(8-9): 1019-1026.

Walter, R., Giese, P., Walther, H.W. and Dill, F., 1995. Geologie von Mitteleuropa. E. Schweizerbart'sche Verlagsbuchhandlung (Nägele und Obermiller), Stuttgart, 566 pp.

Worsley, D. et al., 1982. The Silurian succession of the Olso Region. Norges Geologisk Undersökelse, 384: 57pp.

Wrede, V., 1988. Der nördliche Harzrand - flache Abscherbahn oder wrench-fault-system? Geologische Rundschau, 77(1): 101-114.

Yamaji, A., 2000. The multiple inverse method; a new technique to separate stresses from heterogeneous fault-slip data. Journal of Structural Geology, 22(4): 441-452.

Yamaji, A., Sato, K. and Otsubo, M., 2005. Multiple Inverse Method Main Processor, Version 5.31. Division of Earth and Planetary Sciences, Kyoto University., Kyoto.

Yamaji, A. and Sato, K., 2005. MI Viewer, Version 4.10. Division of Earth and Planetary Sciences, Kyoto University., Kyoto.

Yin, Z.M. and Ranalli, G., 1992. Critical stress difference, fault orientation, and slip direction in anisotropic rocks under non-Andersonian stress system. Journal of Structural Geology, 14: 237-244.

Younes, A.I. and McClay, K., 2002. Development of accommodation zones in the Gulf of Suez–Red Sea rift, Egypt. AAPG Bulletin, 86(6): 1003-1026.

Zalohar, J. and Vrabec, M., 2007. Paleostress analysis of heterogeneous fault-slip data: The Gauss method. Journal of Structural Geology, 29: 1798-1810.

Ziegler, P.A., 1988. Evolution of the Arctic-North Atlantic and the Western Tethys - A visual presentation of a series of paleotectonic maps., 43. AAPG Memoirs, Tulsa, 197 pp.

Ziegler, P.A., 1990. Geological Atlas of Western and Central Europe. Shell Internationale Petroleum Maatschappij B. V., New York, 239 pp.

Ziegler, P.A., Cloetingh, S. and Wees, J.-D.v., 1995. Dynamics of intra-plate compressionla deformation: the Alpine foreland and other examples. Tectonophysics, 252: 7-59.

Ziegler, P.A. and Dèzes, P., 2006. Crustal evolution of Western and Central Europe. In: D.G. Gee and R.A. Stephenson (Editors), European lithosphere dynamics. Geological Society of London Memoirs, London, pp. 43-56.

Zühlke, R., Bouaouda, M.-S., Ouajhain, B., Bechstädt, T. and Leinfelder, R., 2004. Quantitative Meso-/Cenozoic development of the eastern Central Atlantic continental shelf, onshore Agadir Basin, Morocco. Marine and Petroleum Geology, 21(225-276).

8 Acknowledgements

The present study was conducted in sections 4.3 and 4.4 of the Helmholtz Centre Potsdam, GFZ, German Research Centre for Geosciences. Financial support from the German Research Council is acknowledged which has been provided within the DFG-SPP 1135 “Dynamics of sedimentary systems under varying stress conditions by example of the Central European Basin System”.

I would like to express gratitude to my supervisors Prof. Onno Oncken and Prof. Klaus Reicherter for rendering an expert opinion on this Ph.D. thesis and for many fruitful discussions. Thank you, Klaus, for inducting me in the world of slickensides and paleostress.

I especially wish to thank Leni Scheck-Wenderoth for valuable guidance throughout my studies on paleostresses and during the final dissertation writing. Thank you, Leni, you have encouraged me to follow new ideas and esteem my own work. Thank you also for giving me the possibility to meet people from all over the (geosciences) world.

Gratitude is extended to Stanislaw Mazur who guided me through the outcrops of southwestern Poland and was one of my first teachers in fault-slip analysis. Thank you, Stachu, for introducing to me the difference between measuring structures in the “German” and the “British” way.

I’m grateful to Aline Saintot (NGU, Norway) and Michel Heeremans (University of Oslo) who provided the great amount of fault-slip data from the Oslo Graben area. Aline has sampled the data within the GEOS (Geology of Oslo Region) academic programme. I want to thank both of you for the markedly uncomplicated collaboration, for many interesting discussions, for your warm hospitality and the fun we have had during the field trips.

This work benefited greatly from free usage of the MIM software package courtesy of Prof. Atsushi Yamaji (Kyoto University) and the software FLUMO courtesy of Blanka Sperner (University of Freiberg). I thank both of you for answering patiently any questions concerning the programmes and for giving some very helpful advices on fault-slip analysis and stress inversion in general.

I’m grateful to Bernard Celerier for interesting discussions on fault-slip analysis and paleostress inversion and for providing his software for plotting triangle diagrams.

The tectonomagmatic map of the Oslo Graben area has been plotted using GMT 4.0 (http://gmt.soest.hawaii.edu/).

The present study is based on field work. - Identifying geological structures often requires someone to open one’s eyes while bad weather requires someone to make one keep up. So, thanks to all my companions in the field: Prof. Hans-Joachim Franzke, Rainer Müller, Pierre-Olivier Bruna, Birgit Plessen, and the SPP-group of book chapter 3.3 (Strain and Stress).

Special thanks go to Volker Lüders and the „Mädels“ who made field trips and long car rides much more comfortable. But always pay attention to Pepi’s lights: fuel may be low!

Thanks go also to Björn Lewerenz who helped greatly in solving some fundamental problems on data transformations – he did it as elegant as a “pitchy-plunge”.

My gratitude to GFZ sections 4.3 and 4.4 and the entire floor C4 for the good working atmosphere. I would especially like to thank Denis Gröpler and Alexandra Wille for supporting me in handling the large amounts of data and Yuriy Maystrenko for helping patiently with some computer programmes.

What would I have done without my office mates and companions on the long roads of a Ph.D.? Thank you, Mauro, for taking care of me after lunch and whenever there was too much stress around me. And thank you, my precious “Schatz” Katja, for your understanding and for infusing our office with your great sense of humour and your enormous talent for making music.

Ganz herzlich danken möchte ich schließlich meinen Eltern, meinen Geschwistern, Jörg, Jutta, sowie all denen „zu Hause“, die mich in den letzten Jahren liebevoll unterstützt haben. Danke, Jörg, für Deine Geduld und Dein Verständnis während der letzten Monate und dafür, dass Du immer für mich da bist.

Appendix A

Raw data and estimated stress tensors from the area of the Elbe Fault System

Part 1: Fault-slip data.

Lat: Latitude [°N] – Long [°E] - DipDir/Dip: dip direction and dip of fault plane – Azimuth/Plunge: azimuth and plunge of striae – Sense: 1-reverse, 2-normal, 3-dextral, 4-sinistral – Quality of kinematic indicators: 1-excellent, 2-good, 3-poor – Kinematic indicators: 1-crystal fibres, 2-slickolites, 3-non-specified steps, 4-non-specified striations, 5-offsets of structures. Mineral coatings: cc-calcite, chl-chlorite, hem-hematite, qz-quartz.

Part 2: Reduced stress tensors.

az/pl: Azimuth and plunge of the principal stress axes σ_1, σ_2, σ_3 ($\sigma_1 \geq \sigma_2 \geq \sigma_3$).

R: Stress ratio, $R=(\sigma_2-\sigma_3)/(\sigma_1-\sigma_3)$.

Part 3: Bedding planes and veins. DipDir/Dip: dip direction and dip of plane – Rock ages: Ctu-Late Cretaceous, Jru-Late Jurassic, Trm-Mid Triassic, Pru-Late Permian – Minerals: cc-calcite, CaF2-fluorite, CuFeS2-chalcopyrite, qz-quartz.

1 Wettringen — Lat 52.218 — Long 7.321

Data #	DipDir	Dip	Azimuth	Plunge	Sense	Quality	Indicators + mineral coatings
1	170	57	122	50	2	3	3, 4
2	206	89	116	5	3	2	1(cc)
3	210	65	210	65	2	3	5
4	134	89	223	7	4	1	1(cc)
5	293	45	219	15	4	1	1(cc),2
6	254	89	350	2	4	1	3, 4
7	146	85	59	14	3	1	3, 4
8	254	81	168	1	4	2	1(cc)
9	352	57	74	9	4	1	1(cc)
10	281	66	198	6	4	1	1(cc)
11	240	39	240	39	2	3	3
12	240	39	304	20	3	1	1(cc)
13	229	75	316	18	3	3	1(cc)
14	100	87	184	24	3	2	1(cc)
15	355	74	84	7	4	3	4
16	156	70	72	15	3	1	1(cc)

2 Rheine — Lat 52.262 — Long 7.402

Data #	DipDir	Dip	Azimuth	Plunge	Sense	Quality	Indicators + mineral coatings
1	280	78	230	72	2	2	3, 4
2	128	53	120	49	2	2	4
3	88	83	156	71	2	2	4
4	90	57	90	57	2	1	1(cc)
5	112	64	79	57	2	1	1(cc)
6	340	79	67	21	4	2	3, 4
7	105	40	105	40	2	3	3, 5
8	70	50	160	1	3	2	4
9	78	57	42	55	2	2	1(cc)
10	88	76	175	7	3	1	1(cc)
11	81	75	353	23	3	2	1(cc)
12	265	54	265	54	2	1	1(cc),2
13	264	44	209	36	3	1	1(cc)
14	276	60	260	55	2	1	1(cc)
15	246	69	158	8	3	1	1(cc),2
16	56	88	328	15	3	1	1(cc)
17	61	75	326	1	3	1	1(cc),2
18	61	75	342	32	3	1	1(cc),4
19	272	49	272	49	2	1	1(cc)
20	294	64	206	9	4	1	1(cc)
21	48	66	321	9	3	1	1(cc)

3 Middel — Lat 52.256 — Long 7.438

Data #	DipDir	Dip	Azimuth	Plunge	Sense	Quality	Indicators + mineral coatings
1	358	80	281	20	4	1	1(cc)
2	356	62	356	62	1	1	1(cc)
3	200	82	114	15	3	2	1(cc)
4	345	87	76	1	4	2	4, 3, 1(cc)
5	14	89	100	30	4	2	1(cc)
6	24	88	110	25	3	2	4, 3
7	104	68	16	4	3	1	4, 3
8	81	71	145	53	2	1	1(cc)
9	91	85	178	7	3	2	4
10	71	58	86	55	2	1	1(cc)
11	186	87	276	23	4	1	1(cc)
12	36	67	308	1	3	3	1(cc)
13	132	60	222	4	4	1	1(cc)
14	356	69	70	28	4	1	1(cc)
15	114	65	27	7	4	2	1(cc), 3
16	359	60	91	4	4	3	1(cc)
17	18	55	342	47	2	1	1(cc), 5
18	33	66	305	25	3	2	4, 3
19	106	58	106	58	2	1	4, 3
20	125	54	161	47	2	1	1(cc)
21	123	56	209	9	4	1	1(cc)
22	178	59	124	31	2	1	1(cc)
23	165	55	182	53	2	3	4
24	168	42	97	30	1	1	1(cc)
25	306	51	31	12	3	1	1(cc)
26	10	89	274	4	4	3	1(cc)
27	272	89	359	24	3	3	4, 3
28	86	83	178	12	3	2	2
29	94	77	8	16	3	1	1(cc)
30	285	50	264	47	2	1	1(cc)
31	238	59	148	1	3	2	2
32	226	52	316	6	3	1	1(cc)
33	236	57	309	34	3	3	1(cc)
34	3	52	3	52	1	1	1(cc)
35	356	73	313	62	1	1	5
36	93	52	177	17	3	1	4
37	143	52	116	42	2	1	1(cc)
38	174	65	254	21	4	3	1(cc)
39	160	80	242	6	4	1	1(cc)
40	169	79	82	2	4	1	1(cc)

4 Dörenthe — Lat 52.227 — Long 7.673

Data #	DipDir	Dip	Azimuth	Plunge	Sense	Quality	Indicators + mineral coatings
1	203	60	151	45	1	1	1(cc)
2	213	70	152	48	1	1	1(cc)
3	215	55	149	34	1	1	1(cc)
4	169	48	93	10	3	2	1(cc)
5	236	80	149	9	3	1	1(cc)
6	242	88	144	4	3	1	1(cc)
7	72	87	338	5	3	1	3

5 Lengerich — Lat 52.182 — Long 7.896

Data #	DipDir	Dip	Azimuth	Plunge	Sense	Quality	Indicators + mineral coatings
1	200	45	200	45	1	2	1(cc)
2	292	80	192	80	1	1	1(cc)
3	218	40	258	36	1	1	1(cc)
4	71	40	335	1	2	2	1(cc)
5	343	81	71	1	3	1	1(cc)
6	182	46	182	46	2	2	1(cc)
7	176	50	102	18	3	2	1(cc)
8	178	40	214	38	2	1	1(cc)
9	85	22	46	20	1	0	1(cc)
10	85	22	16	10	1	2	1(cc)
11	204	79	220	78	1	1	1(cc)
12	210	66	210	66	2	1	1(cc)
13	210	70	222	69	1	1	1(cc)
14	211	70	282	29	3	1	1(cc)
15	140	79	216	45	2	2	1(cc)
16	12	10	12	10	1	1	1(cc)
17	356	83	264	26	4	1	1(cc)
18	184	79	154	74	2	1	1(cc)
19	163	83	252	5	4	3	1(cc)
20	170	84	256	15	4	3	1(cc), 3
21	162	76	190	74	2	2	1(cc)
22	209	43	212	42	2	2	1(cc)
23	198	65	236	63	1	1	1(cc), 3
24	216	85	156	82	1	1	1(cc)
25	213	87	294	56	1	1	1(cc)
26	172	65	262	1	4	1	1(cc)
27	198	82	296	5	4	1	1(cc)
28	179	73	200	67	2	1	1(cc)
29	220	72	273	67	1	1	1(cc)
30	200	81	174	79	1	1	1(cc)
31	200	81	274	52	1	1	1(cc)
32	204	65	204	65	1	1	1(cc)
33	214	74	169	58	1	1	1(cc)
34	212	80	170	75	1	1	1(cc)
35	218	79	190	74	1	1	1(cc)
36	205	60	236	56	1	1	1(cc)
37	40	55	40	55	2	1	1(cc)
38	240	70	185	48	1	2	1(cc)

6 Höste — Lat 52.167 — Long 7.938

Data #	DipDir	Dip	Azimuth	Plunge	Sense	Quality	Indicators + mineral coatings
1	333	89	244	23	4	1	2
2	153	81	243	18	4	1	1(cc)
3	150	85	250	10	3	2	1(cc)
4	164	76	240	44	4	3	1(cc)
5	280	46	315	40	2	1	1(cc)
6	157	65	244	9	3	2	1(cc)
7	120	29	132	21	2	2	1(cc)
8	133	65	60	25	4	2	1(cc)
9	124	27	124	27	2	1	1(cc)
10	140	55	56	1	4	1	1(cc)
11	157	81	246	2	4	1	2
12	276	61	351	30	3	2	1(cc)
13	322	30	242	2	4	2	1(cc)
14	175	83	268	18	3	2	1(cc), 3
15	178	71	236	44	1	2	1(cc)
16	280	46	300	45	2	1	1(cc)
17	280	42	260	37	2	1	1(cc)
18	310	46	255	33	4	1	1(cc)
19	306	50	242	29	4	1	1(cc)
20	98	73	182	12	3	1	1(cc)
21	62	67	344	15	4	1	1(cc)
22	76	57	18	35	4	1	1(cc)

8 Holsten — Lat 52.228 — Long 8.128

Data #	DipDir	Dip	Azimuth	Plunge	Sense	Quality	Indicators + mineral coatings
1	80	85	348	4	3	3	1(cc)
2	264	89	176	5	3	3	1(cc)
3	268	87	1	14	3	3	4
4	186	80	102	2	4	1	1(cc)
5	350	85	77	3	3	1	1(cc)
6	190	39	206	35	1	3	1(cc)
7	218	71	301	6	3	3	1(cc)
8	86	89	356	4	3	1	1(cc)
9	304	75	210	6	4	1	2
10	216	89	125	9	4	3	1(cc)
11	302	85	214	4	3	3	1(cc)
12	232	73	318	15	4	3	4
13	238	42	154	5	4	3	1(cc)
14	43	89	320	45	3	3	1(cc), 3, 4

7 Lienen — Lat 52.164 — Long 7.942

Data #	DipDir	Dip	Azimuth	Plunge	Sense	Quality	Indicators + mineral coatings
1	262	85	342	5	3	1	1(cc)
2	184	10	240	4	1	1	1(cc)
3	346	76	78	10	4	3	1(cc)
4	86	52	150	29	2	1	1(cc)
5	321	79	50	30	1	1	1(cc)
6	1	32	26	30	1	1	1(cc)
7	15	50	15	50	1	1	4
8	40	45	40	45	1	1	4
9	22	35	22	35	1	1	1(cc)
10	357	52	32	42	1	1	1(cc)
11	357	52	78	6	4	3	1(cc)
12	135	60	60	26	2	1	1(cc)
13	166	80	78	10	4	1	1(cc)
14	340	66	250	7	4	3	1(cc)
15	170	80	264	1	4	1	1(cc)
16	340	45	250	2	4	2	1(cc)
17	164	64	72	1	4	1	1(cc)
18	114	19	26	1	1	1	1(cc)
19	162	68	254	1	4	1	1(cc)
20	186	4	218	1	2	1	4
21	34	32	24	30	1	1	3
22	42	30	40	29	1	1	1(cc)
23	170	12	220	5	1	2	1(cc)
24	57	70	325	3	4	1	1(cc)
25	62	26	12	20	1	1	1(cc)
26	19	23	19	23	1	1	1(cc)
27	71	54	160	3	3	1	1(cc)
28	92	70	173	11	3	1	1(cc)
29	68	39	18	20	1	1	1(cc)
30	186	3	203	2	1	1	1(cc)
31	77	32	8	10	1	1	1(cc)
32	84	57	355	5	3	1	1(cc)
33	50	50	350	40	1	3	1(cc)
34	8	20	8	20	2	2	1(cc)
35	8	49	8	49	2	1	1(cc)

9 Hilter — Lat 52.161 — Long 8.149

Data #	DipDir	Dip	Azimuth	Plunge	Sense	Quality	Indicators + mineral coatings
1	32	78	32	78	2	1	1(cc)
2	211	35	205	34	2	1	1(cc)
3	220	20	196	12	2	1	1(cc)
4	332	24	30	9	1	1	1(cc)
5	320	18	21	2	1	1	1(cc)
6	31	40	31	40	1	1	1(cc)
7	359	70	85	35	2	2	1(cc)
8	15	40	40	32	1	2	1(cc)
9	15	40	306	19	1	2	1(cc)
10	50	80	340	40	2	1	1(cc)

10 Bissendorf — Lat 52.231 — Long 8.15

Data #	DipDir	Dip	Azimuth	Plunge	Sense	Quality	Indicators + mineral coatings
1	182	82	94	2	3	1	1(cc)
2	9	86	278	6	3	3	1(cc)
3	249	88	339	9	3	1	1(cc)
4	182	76	275	6	3	3	1(cc)
5	162	87	76	15	3	1	1(cc)
6	217	80	125	6	4	1	1(cc)
7	246	81	336	8	3	1	1(cc)
8	195	88	119	16	3	3	1(cc)
9	236	75	146	2	3	1	1(cc)
10	240	78	329	12	3	1	1(cc)
11	242	85	154	7	3	1	1(cc)

11 Halle — Lat 52.074 — Long 8.345

Data #	DipDir	Dip	Azimuth	Plunge	Sense	Quality	Indicators + mineral coatings
1	30	79	96	75	2	1	1(cc)
2	11	35	40	31	2	3	1(cc)
3	11	35	94	3	3	1	1(cc)
4	214	80	105	78	1	1	1(cc)
5	38	86	38	86	2	1	1(cc)
6	47	89	47	89	2	1	1(cc)
7	232	83	225	80	1	1	3
8	51	76	42	73	2	1	1(cc)
9	270	84	336	2	3	1	1(cc)
10	26	81	26	81	1	1	1(cc)
11	39	71	44	69	1	1	1(cc)
12	359	77	286	16	3	1	1(cc)
13	70	86	140	80	2	1	1(cc)
14	218	81	225	78	1	1	1(cc)
15	240	86	165	75	1	1	1(cc)
16	65	53	358	35	3	1	1(cc)
17	84	54	352	16	3	1	1(cc)
18	68	75	150	40	3	1	1(cc)
19	68	75	160	4	3	1	1(cc)
20	24	77	24	77	1	1	1(cc)
21	60	36	64	35	1	1	1(cc)
22	20	29	20	29	1	1	1(cc)
23	45	82	340	74	1	1	1(cc)
24	62	78	341	2	3	1	1(cc)
25	19	66	350	63	2	1	1(cc)
26	359	82	323	80	2	1	1(cc)
27	36	76	343	64	2	1	1(cc)
28	31	61	31	61	2	1	1(cc)
29	36	67	23	66	2	1	1(cc)
30	220	83	181	80	1	1	1(cc)
31	195	85	110	77	1	1	1(cc)

12 Künsebeck Lat 52.04 Long 8.404

Data #	DipDir	Dip	Azimuth	Plunge	Sense	Quality	Indicators + mineral coatings
1	319	72	42	19	4	3	4, 3
2	208	81	296	2	3	1	1(cc)
3	353	88	94	5	3	1	1(cc)
4	282	86	190	21	4	1	3
5	310	36	328	34	1	1	3
6	1	62	86	2	3	3	1(cc)
7	114	76	204	9	3	0	1(cc)
8	116	83	207	14	3	0	1(cc)
9	356	89	270	6	4	2	4, 3
10	335	77	249	21	4	1	1(cc)
11	220	85	306	6	3	1	1(cc)
12	222	31	235	29	2	2	1(cc)
13	338	44	303	40	2	1	1(cc)
14	327	35	266	19	4	1	1(cc)
15	318	45	20	15	2	1	3, 4
16	342	39	26	31	2	1	1(cc)
17	332	49	12	39	2	1	1(cc)
18	348	80	352	78	2	1	1(cc)
19	355	81	262	43	3	3	4
20	144	88	232	71	2	3	3, 4
21	326	78	257	61	1	2	1(cc)
22	338	45	338	45	2	1	1(cc)
23	8	76	275	23	4	3	1(cc)
24	280	70	3	17	4	1	3
25	270	75	260	74	2	3	4
26	114	69	29	6	4	1	1(cc)
27	322	85	239	4	3	3	3, 4
28	126	79	216	1	4	1	1(cc)
29	188	61	172	59	1	1	1(cc)
30	188	61	100	11	3	1	4
31	118	84	206	8	3	1	1(cc)
32	156	68	232	39	2	2	1(cc)
33	155	35	155	35	2	1	1(cc), 3
34	152	34	268	16	3	3	4
35	320	83	227	25	4	1	1(cc), 3
36	158	75	227	51	4	1	1(cc), 3
37	117	85	211	10	4	3	1(cc)
38	238	87	317	9	4	2	2
39	300	87	208	10	4	3	4
40	249	85	166	40	3	1	1(cc), 2
41	195	60	108	10	3	1	1(cc), 2
42	198	65	166	59	1	2	3
43	234	81	152	65	1	2	3
44	295	89	204	12	4	2	1(cc), 4
45	113	71	202	1	4	1	1(cc)
46	168	74	77	4	3	3	1(cc)
47	152	59	220	41	2	2	4

13 Steinbergen Lat 52.217 Long 9.137

Data #	DipDir	Dip	Azimuth	Plunge	Sense	Quality	Indicators + mineral coatings
1	195	50	195	50	1	3	4
2	205	34	192	33	1	2	1(cc)
3	202	16	202	16	1	1	1(cc)
4	274	30	270	28	1	1	1(cc)
5	172	31	210	25	1	1	1(cc)
6	222	49	190	44	1	1	1(cc)
7	196	53	196	53	1	1	1(cc)
8	356	37	62	14	4	2	1(cc)
9	240	22	203	16	1	1	1(cc)
10	238	31	198	27	1	1	1(cc)
11	225	25	212	24	2	2	1(cc)

14 Barntrup Lat 51.996 Long 9.154

Data #	DipDir	Dip	Azimuth	Plunge	Sense	Quality	Indicators + mineral coatings
1	198	59	134	37	3	1	1(cc)
2	288	84	200	16	3	3	4
3	293	89	204	4	3	2	1(cc)
4	209	47	220	45	3	2	4
5	110	88	205	1	4	1	1(cc)
6	112	88	26	12	4	1	1(cc)
7	31	81	120	9	4	1	1(cc)
8	112	88	200	3	3	3	4
9	212	85	292	12	3	2	4, 3
10	202	84	121	7	3	1	1(cc)

15 Rohden Lat 52.206 Long 9.234

Data #	DipDir	Dip	Azimuth	Plunge	Sense	Quality	Indicators + mineral coatings
1	54	22	54	22	1	1	1(cc)
2	40	45	58	26	1	1	1(cc)
3	30	41	59	40	1	1	1(cc)
4	3	49	37	44	1	1	1(cc)

16 Hamelspringe Lat 52.194 Long 9.537

Data #	DipDir	Dip	Azimuth	Plunge	Sense	Quality	Indicators + mineral coatings
1	65	70	340	10	4	3	4
2	76	77	348	6	4	3	4
3	204	78	238	75	1	1	1(cc)
4	214	89	123	72	1	1	1(cc)
5	198	79	270	55	1	1	1(cc)
6	144	56	47	10	3	3	1(cc)
7	312	75	221	14	3	2	4

17 Lauenstein Lat 52.068 Long 9.543

Data #	DipDir	Dip	Azimuth	Plunge	Sense	Quality	Indicators + mineral coatings
1	60	70	17	63	N	1	1(cc)
2	222	51	230	49	N	2	1(cc)
3	220	47	229	46	N	1	1(cc)
4	330	77	236	5	D	1	1(cc)
5	318	80	48	1	D	1	1(cc)
6	314	75	48	1	D	1	1(cc)
7	319	74	54	14	D	1	1(cc)
8	265	60	174	5	S	1	1(cc)
9	52	68	11	62	N	1	4
10	45	74	343	59	N	1	4
11	51	70	354	56	N	1	4
12	134	57	73	37	N	1	4
13	243	63	258	62	N	1	4

18 Marienhagen Lat 52.021 Long 9.704

Data #	DipDir	Dip	Azimuth	Plunge	Sense	Quality	Indicators + mineral coatings
1	208	84	300	15	4	1	1(cc)
2	206	80	293	4	4	3	1(cc)
3	332	80	264	50	2	2	4
4	145	74	207	59	2	1	4
5	320	85	338	84	2	1	2
6	330	86	330	86	2	1	2
7	322	88	340	85	2	1	2
8	336	87	336	87	2	3	1(cc)
9	236	64	149	5	4	1	1(cc)

19 Avendshausen Lat 51.851 Long 9.791

Data #	DipDir	Dip	Azimuth	Plunge	Sense	Quality	Indicators + mineral coatings
1	288	72	13	20	3	1	1(cc)
2	186	57	186	57	2	2	1(cc)
3	192	87	104	18	4	3	4
4	314	77	47	7	4	2	1(cc)
5	237	79	152	9	3	3	4
6	342	84	256	3	4	1	1(cc)

20 Emmenhausen — Lat 51.576 — Long 9.835

Data #	DipDir	Dip	Azimuth	Plunge	Sense	Quality	Indicators + mineral coatings
1	186	85	95	2	4	1	1(cc)
2	18	86	100	10	4	3	1(cc)
3	259	82	166	4	4	2	1(cc)
4	246	85	158	32	4	2	1(cc)
5	253	84	344	3	4	1	1(cc)
6	240	84	156	9	4	1	1(cc)
7	318	66	307	64	1	3	1(cc)
8	178	85	270	3	3	3	1(cc)
9	252	65	346	4	3	3	1(cc)
10	69	75	346	11	3	2	1(cc)
11	355	80	260	5	4	1	1(cc)
12	268	76	359	5	4	1	1(cc)
13	285	80	14	1	4	2	1(cc)
14	252	70	168	4	4	1	1(cc)

21 Hardegsen — Lat 51.66 — Long 9.836

Data #	DipDir	Dip	Azimuth	Plunge	Sense	Quality	Indicators + mineral coatings
1	306	70	38	3	4	3	1(cc), 4
2	210	85	114	20	4	1	1(cc)
3	272	70	180	5	4	1	1(cc), 3
4	262	72	171	3	3	1	1(cc), 3
5	326	68	50	19	4	3	1(cc)
6	265	58	184	34	3	2	2
7	274	68	196	26	3	3	4
8	18	24	18	24	1	1	4
9	214	76	140	2	4	1	1(cc)
10	346	85	78	11	4	2	4
11	140	60	55	10	4	3	1(cc), 3
12	142	89	232	9	4	1	1(cc)
13	294	74	12	6	4	2	1(cc), 3, 5

22 Misburg — Lat 52.384 — Long 9.884

Data #	DipDir	Dip	Azimuth	Plunge	Sense	Quality	Indicators + mineral coatings
1	348	34	318	33	2	2	4
2	296	45	296	45	2	3	3
3	214	50	238	47	2	2	4
4	285	50	310	39	2	2	4
5	285	87	285	87	2	2	3
6	312	85	228	60	2	3	4
7	73	85	150	49	2	2	4
8	280	70	285	66	2	2	4
9	285	58	314	53	2	3	4
10	242	63	264	60	2	3	4
11	262	64	246	63	2	3	4
12	260	70	243	69	2	3	4
13	295	63	283	59	2	1	3
14	68	80	156	10	4	1	4
15	64	76	152	8	3	2	4
16	128	71	104	70	2	3	4
17	272	79	230	76	2	3	3
18	220	76	250	71	2	3	3
19	270	58	270	58	2	3	3
20	276	68	263	62	2	3	4
21	254	68	226	65	2	3	4
22	230	58	225	57	2	3	4
23	220	50	216	49	2	3	4
24	274	52	280	51	2	3	4
25	270	84	194	57	2	3	4
26	286	54	298	53	2	3	4
27	276	46	276	46	2	3	4
28	292	59	252	56	2	3	3
29	290	41	283	40	2	1	3
30	230	45	245	42	2	3	3
31	280	64	280	64	2	3	3
32	290	65	290	65	2	2	4
33	216	60	216	60	2	2	4
34	230	44	230	44	2	1	3
35	66	77	153	32	3	3	3
36	296	60	296	60	2	2	4
37	245	55	245	55	2	3	4
38	346	52	346	52	2	1	4
39	148	72	148	72	2	3	1(cc)
40	308	74	278	72	2	3	4
41	206	65	256	50	1	2	3
42	256	58	337	26	2	3	1(cc)
43	246	81	330	30	2	3	4
44	267	79	358	5	3	3	4
45	258	78	324	57	2	3	4
46	250	57	231	56	2	3	3
47	266	51	266	51	2	3	3
48	246	63	276	59	2	3	3
49	286	88	184	10	4	1	3
50	64	74	347	42	2	1	3
51	144	83	210	76	2	1	3
52	256	58	166	17	4	3	4
53	280	51	200	11	4	1	3
54	284	47	284	47	2	3	4
55	91	89	91	89	2	2	4

23 Elvese — Lat 51.674 — Long 9.938

Data #	DipDir	Dip	Azimuth	Plunge	Sense	Quality	Indicators + mineral coatings
1	72	47	10	22	4	3	1(cc)
2	282	63	226	40	2	1	1(cc)
3	282	61	208	30	3	2	1(cc)
4	107	44	197	5	3	3	1(cc)
5	66	60	59	59	2	1	1(cc)
6	50	50	46	45	2	2	1(cc)
7	76	51	358	24	2	1	1(cc)
8	308	89	215	15	3	1	1(cc)
9	128	74	218	20	3	1	1(cc)
10	117	86	207	13	3	2	1(cc)
11	225	74	192	65	1	2	1(cc)
12	258	62	230	49	2	2	1(cc)
13	258	62	194	38	1	2	1(cc)
14	252	51	209	46	2	0	1(cc)
15	93	16	62	10	1	1	1(cc)
16	285	40	20	2	3	3	1(cc)
17	114	10	40	2	1	2	1(cc)
18	101	14	46	9	1	2	1(cc)
19	270	56	195	25	3	3	1(cc)
20	84	36	56	30	1	1	1(cc)
21	78	31	51	20	1	1	1(cc)
22	64	36	38	33	1	1	1(cc)
23	270	30	212	15	2	0	4
24	100	53	72	48	1	1	1(cc)
25	88	48	50	42	1	1	1(cc)
26	292	34	218	15	1	1	1(cc)
27	100	50	78	49	2	2	1(cc)
28	92	86	359	20	3	1	1(cc)
29	8	21	8	21	1	3	1(cc)
30	252	25	223	19	1	1	1(cc)
31	284	65	10	4	3	3	1(cc)
32	286	65	12	6	3	1	1(cc)
33	285	65	206	40	1	2	1(cc)
34	295	45	22	6	3	1	1(cc)
35	276	57	200	25	4	3	1(cc)
36	194	89	92	9	3	3	1(cc)
37	48	42	104	24	2	1	1(cc)
38	266	89	163	84	2	3	1(cc)
39	288	52	206	11	3	3	4
40	8	65	80	25	2	3	1(cc)
41	114	76	114	76	2	3	4
42	110	69	40	26	3	3	1(cc)
43	110	69	120	64	2	2	1(cc)
44	105	39	10	1	3	1	1(cc)
45	101	40	55	30	1	2	1(cc)
46	101	40	25	10	3	1	1(cc)
47	104	40	132	35	1	3	1(cc)
48	104	39	39	19	2	1	1(cc)
49	104	39	39	19	1	3	1(cc)
50	102	36	8	1	3	1	1(cc)
51	98	39	55	28	3	1	1(cc)
52	90	34	49	37	2	1	1(cc)
53	92	42	50	35	4	2	1(cc)
54	92	42	134	35	2	2	1(cc)
55	104	45	192	4	3	1	1(cc)
56	104	45	101	44	2	3	1(cc)
57	87	46	42	37	1	1	1(cc)
58	110	72	32	27	3	3	1(cc)
59	118	86	26	14	3	1	1(cc)
60	118	82	34	20	3	1	1(cc)

23 Elvese — Lat 51.674 — Long 9.938

Data #	DipDir	Dip	Azimuth	Plunge	Sense	Quality	Indicators + mineral coatings
61	102	69	29	35	1	1	1(cc)
62	108	89	134	74	2	3	1(cc)
63	285	47	234	33	3	1	1(cc)
64	268	60	194	25	3	2	1(cc)
65	268	60	179	11	3	1	1(cc)
66	264	69	173	1	3	1	1(cc)
67	98	54	46	37	3	1	1(cc)
68	101	57	38	35	3	1	1(cc)
69	118	55	43	24	3	1	1(cc)
70	124	60	41	19	3	1	1(cc)
71	88	57	74	55	1	1	1(cc)
72	83	89	354	1	3	3	1(cc)
73	86	20	30	10	2	1	1(cc)
74	272	72	3	3	3	2	1(cc)
75	259	58	358	27	3	1	1(cc)
76	276	69	356	6	3	2	1(cc)
77	298	47	243	30	2	2	1(cc)
78	297	35	250	34	1	2	1(cc)
79	336	75	251	9	4	1	1(cc)
80	282	54	251	50	2	1	4
81	285	54	256	49	2	1	4
82	106	48	78	45	2	3	4
83	333	81	244	6	4	1	1(cc)
84	283	80	19	8	3	1	1(cc)
85	290	80	215	19	3	1	1(cc)
86	280	88	190	18	3	1	1(cc)
87	282	70	240	64	2	2	4
88	118	89	206	10	3	1	1(cc)
89	30	80	30	80	2	3	1(cc)
90	208	19	214	15	1	2	1(cc)
91	269	25	205	11	2	3	1(cc)
92	236	77	340	10	4	3	1(cc)
93	218	80	128	14	3	2	1(cc)
94	52	60	100	47	2	3	1(cc)
95	47	56	66	47	1	2	1(cc)
96	54	71	331	7	3	1	1(cc)
97	62	81	332	2	3	1	1(cc)
98	248	70	160	9	3	1	1(cc)
99	46	71	335	36	3	3	1(cc)
100	242	81	334	10	3	2	1(cc)
101	66	76	78	75	1	3	1(cc)
102	86	83	116	76	1	1	1(cc)
103	66	87	100	85	1	1	1(cc)
104	280	74	192	8	3	2	1(cc)
105	282	70	192	9	3	2	1(cc)
106	62	81	329	4	3	1	1(cc)
107	225	26	224	24	2	1	1(cc)
108	28	85	130	29	4	1	1(cc)
109	114	55	84	50	1	1	1(cc)
110	102	72	40	48	3	2	1(cc)
111	97	56	63	36	3	1	1(cc)
112	42	60	82	45	3	1	1(cc)
113	243	70	337	12	3	1	4
114	253	79	342	11	3	1	4
115	25	80	25	80	2	2	1(cc)
116	65	80	42	79	2	1	1(cc)
117	108	57	26	36	3	3	1(cc)
118	110	54	85	52	2	0	4
119	205	89	290	71	2	0	4
120	38	50	6	45	2	0	1(cc)

24 Vogelbeck — Lat 51.775 — Long 9.95

Data #	DipDir	Dip	Azimuth	Plunge	Sense	Quality	Indicators + mineral coatings
1	262	50	262	50	1	3	1(cc)
2	99	88	13	74	1	1	1(cc)
3	68	89	150	3	4	3	1(cc)
4	82	78	30	74	2	0	4, 5
5	330	83	60	10	4	2	1(cc)
6	335	84	64	30	3	2	1(cc)
7	335	79	62	1	4	3	2
8	297	60	205	5	4	2	1(cc)
9	21	75	109	20	4	1	1(cc)
10	136	88	220	36	4	3	1(cc), 2
11	152	89	244	14	4	2	1(cc)
12	134	66	170	63	3	3	4
13	128	59	111	58	2	3	1(cc)

25 Papenberg — Lat 51.643 — Long 9.961

Data #	DipDir	Dip	Azimuth	Plunge	Sense	Quality	Indicators + mineral coatings
1	113	34	186	13	1	1	1(cc)
2	104	36	178	12	1	1	1(cc)
3	120	34	188	13	1	2	1(cc)
4	128	27	190	12	1	1	1(cc)
5	145	46	216	26	1	1	1(cc)
6	106	27	195	6	1	2	1(cc)
7	164	17	215	13	1	1	1(cc)
8	188	56	206	54	1	3	1(cc)
9	192	44	201	43	1	1	1(cc)
10	173	32	173	32	1	1	1(cc)
11	200	36	200	36	1	1	1(cc)
12	61	30	155	5	4	1	1(cc)

26 Upstedt — Lat 52.042 — Long 10.059

Data #	DipDir	Dip	Azimuth	Plunge	Sense	Quality	Indicators + mineral coatings
1	320	89	240	14	3	1	4
2	328	78	51	12	3	3	4
3	146	86	245	11	3	1	4
4	322	82	59	5	3	1	4, 1(cc)
5	152	87	242	10	4	3	4
6	319	87	235	6	3	1	4
7	337	77	328	76	2	1	4
8	152	85	237	9	4	3	4
9	149	89	244	10	3	3	4
10	314	83	227	14	3	3	4
11	340	70	325	67	2	3	4
12	308	78	35	21	3	3	4
13	310	71	220	1	3	3	4
14	321	75	238	23	3	3	4
15	304	84	34	12	3	3	4
16	322	76	340	75	2	2	4
17	136	84	48	8	3	3	4
18	323	72	337	66	2	1	4
19	323	72	54	23	3	1	4
20	144	84	230	7	3	3	4
21	142	81	235	7	3	3	4
22	335	74	335	74	2	3	4
23	310	88	222	35	4	3	4
24	336	80	282	75	2	3	4
25	324	89	52	3	3	3	4
26	14	54	341	46	2	3	4
27	308	58	5	40	2	3	4
28	318	69	7	61	2	1	4
29	318	62	37	25	3	1	4
30	128	88	219	35	3	3	4
31	309	74	283	68	2	3	4
32	324	56	320	53	2	3	4
33	352	86	322	72	2	1	4, 1(cc)
34	312	77	286	74	2	3	4
35	302	72	290	67	2	3	4
36	180	89	94	3	4	2	4, 3
37	320	74	46	4	3	1	1(cc), 2
38	338	77	338	77	2	2	1(cc), 2
39	346	85	253	20	4	1	1(cc), 2
40	335	80	335	80	2	2	2
41	166	35	150	33	2	2	2
42	162	65	162	65	2	2	2
43	156	56	146	53	2	2	2
44	162	86	69	10	4	2	2
45	165	84	76	21	4	2	2
46	145	80	80	62	2	2	2
47	152	81	67	6	4	2	2
48	156	72	138	68	2	2	2
49	160	44	144	38	2	1	2
50	161	66	161	66	2	2	2
51	324	80	237	18	3	2	2
52	148	88	148	88	2	2	4
53	314	89	224	9	3	2	2
54	314	86	46	2	3	1	2
55	324	68	324	68	2	1	2

27 Baddeckenstedt Lat 52.092 Long 10.23

Data #	DipDir	Dip	Azimuth	Plunge	Sense	Quality	Indicators + mineral coatings
1	296	55	254	49	2	1	4, 2
2	310	56	280	51	2	1	4, 2
3	291	60	266	54	2	1	4, 2
4	280	46	280	46	2	1	4, 2
5	300	51	288	40	2	1	4, 2
6	286	55	348	31	2	1	4, 2
7	314	44	352	34	2	2	4, 3
8	316	68	285	60	2	2	4, 3
9	126	74	214	6	4	3	4, 3
10	126	74	184	61	2	3	4, 3
11	332	85	245	10	3	3	4, 3
12	195	85	256	70	2	3	4, 3
13	268	55	295	51	2	1	4, 7
14	158	82	242	67	2	3	4
15	306	43	320	40	2	2	4, 1(cc)
16	170	71	230	58	2	1	4, 1(cc)
17	156	52	196	45	2	1	4, 5
18	135	70	84	54	2	1	4, 3

28 Söhlde Lat 52.182 Long 10.2453

Data #	DipDir	Dip	Azimuth	Plunge	Sense	Quality	Indicators + mineral coatings
1	121	74	100	72	2	3	4, 2
2	42	56	42	56	2	1	2, 1(cc)
3	266	70	216	62	2	2	4
4	271	79	209	71	2	2	4
5	31	47	31	47	2	2	4, 3
6	18	50	53	37	2	3	4, 3
7	104	60	100	55	2	2	4, 3
8	115	69	88	65	2	2	4, 3
9	125	72	93	65	2	2	4, 3
10	263	72	306	68	2	3	4, 3
11	263	72	176	7	4	3	4, 3
12	80	45	80	45	2	2	4, 3
13	1	59	348	57	2	2	4, 3
14	25	46	25	46	2	3	4, 5
15	122	65	122	65	2	3	4, 3
16	328	55	328	55	2	3	4
17	130	72	111	70	2	3	4
18	151	68	178	66	2	3	4
19	69	50	10	25	2	1	4, 3
20	270	48	270	48	2	1	4, 3
21	272	46	272	46	2	1	4, 3
22	150	65	150	65	2	1	5

58 Górazdze Lat 50.526 Long 18.029

Data #	DipDir	Dip	Azimuth	Plunge	Sense	Quality	Indicators + mineral coatings
1	305	65	305	65	2	1	4
2	320	60	295	50	2	1	4
3	305	75	220	30	3	3	4
4	310	65	320	63	2	1	4
5	320	85	280	75	2	2	4
6	320	65	300	63	2	0	4
7	310	70	0	55	2	1	4
8	300	85	300	85	2	3	4

29 Langelsheim Lat 51.939 Long 10.352

Data #	DipDir	Dip	Azimuth	Plunge	Sense	Quality	Indicators + mineral coatings
1	36	76	106	51	4	1	2, 1(cc)
2	22	76	101	35	4	2	2, 1(cc)
3	27	78	109	38	4	2	2, 1(cc)
4	14	74	88	46	4	1	2, 1(cc)
5	9	89	101	34	4	2	2, 1(cc)
6	232	78	326	3	3	2	1(cc)
7	17	80	92	51	4	1	1(cc), 2
8	355	89	81	45	4	1	1(cc), 2
9	18	78	87	43	4	1	1(cc), 2
10	268	81	355	1	3	1	1(cc), 2
11	260	42	192	17	3	1	4
12	340	80	65	34	4	1	1(cc), 2
13	245	35	194	26	1	2	2, 1(cc)
14	245	29	206	20	1	1	2
15	164	80	250	19	4	3	1(cc), 2
16	220	56	308	6	4	2	2
17	54	82	320	10	3	1	1(cc)
18	202	73	119	20	4	1	1(cc), 2
19	35	65	124	23	4	1	1(cc), 2
20	200	65	118	25	4	1	1(cc), 2
21	182	79	89	9	4	1	1(cc), 2
22	1	63	89	9	4	1	1(cc), 2
23	24	55	56	47	1	1	1(cc), 2
24	14	72	74	58	1	1	1(cc), 2
25	336	83	56	48	1	1	1(cc), 2
26	6	65	6	65	2	1	1(cc)
27	15	73	15	73	2	1	1(cc), 2
28	28	85	108	43	4	1	1(cc), 2
29	10	70	68	47	4	1	1(cc), 2
30	6	37	6	37	1	1	1(cc)
31	348	70	265	9	4	1	1(cc), 2
32	346	68	260	2	4	1	1(cc), 2
33	346	80	258	1	4	1	1(cc), 2
34	350	73	12	65	1	1	1(cc), 2
35	344	75	318	71	1	1	1(cc), 2
36	357	70	357	70	1	1	1(cc), 2

30 Scharzfeld Lat 51.619 Long 10.391

Data #	DipDir	Dip	Azimuth	Plunge	Sense	Quality	Indicators + mineral coatings
1	84	87	178	10	4	1	1(cc), 3
2	310	82	222	6	4	1	2
3	110	76	198	6	3	1	3
4	85	81	2	1	3	1	2
5	324	89	234	5	4	1	2

31 Wendessen Lat 52.161 Long 10.568

Data #	DipDir	Dip	Azimuth	Plunge	Sense	Quality	Indicators + mineral coatings
1	61	76	330	1	3	3	4
2	61	76	17	71	2	3	4
3	157	49	124	43	1	1	4
4	190	36	149	30	1	1	4
5	163	53	146	50	1	1	4
6	291	40	2	20	4	2	4, 3

32 Bodendorf Lat 52.28 Long 11.21

Data #	DipDir	Dip	Azimuth	Plunge	Sense	Quality	Indicators + mineral coatings
1	8	62	53	52	2	1	1(cc)
2	18	70	63	61	2	1	1(cc)
3	67	77	342	24	3	1	1(cc), hem
4	350	45	22	39	2	1	1(cc), hem
5	340	53	26	42	2	1	4, hem
6	358	80	270	5	3	1	1(cc), hem
7	8	85	282	24	3	1	1(cc), hem
8	352	86	266	18	3	1	1(cc), hem
9	8	77	292	40	1	3	1(cc), hem
10	18	77	318	65	1	1	1(cc), hem
11	22	76	295	9	3	2	1(cc)
12	17	84	289	10	3	1	1(cc)
13	191	82	282	20	3	1	1(cc), hem
14	191	82	182	74	2	3	4
15	93	80	185	1	3	3	4, hem
16	107	35	107	35	2	2	4, hem
17	270	83	188	30	4	1	1(cc), hem
18	272	88	3	65	2	1	4
19	5	65	41	50	2	2	1(cc), hem
20	145	88	236	22	4	2	1(cc)
21	330	89	57	45	2	1	4, hem
22	358	60	47	50	1	2	4, hem
23	342	84	65	10	4	1	4
24	304	69	21	28	4	3	4, hem
25	310	58	28	30	4	3	4
26	12	76	12	76	2	2	4, hem
27	325	52	31	29	4	3	4, hem
28	338	62	242	23	4	1	4, hem
29	359	75	16	75	2	3	4, hem
30	20	75	105	15	3	1	4, hem
31	355	73	78	22	3	1	1(cc), hem
32	347	77	74	12	3	1	4, hem
33	331	85	245	6	4	1	1(cc), hem
34	339	75	249	1	4	1	1(cc), hem
35	336	77	68	2	4	1	1(cc), hem
36	336	84	247	4	4	3	4
37	52	89	320	15	4	3	1(cc)
38	205	74	236	73	2	1	1(cc)
39	198	77	287	17	3	3	4
40	195	89	264	58	2	2	1(cc)
41	198	84	285	28	4	2	1(cc)
42	228	56	228	56	2	1	1(cc), hem
43	212	78	298	18	3	1	1(cc), hem
44	2	89	265	1	3	1	1(cc), hem
45	64	36	64	36	1	1	1(cc)

33 Flechtingen — Lat 52.315 — Long 11.21

Data #	DipDir	Dip	Azimuth	Plunge	Sense	Quality	Indicators + mineral coatings
1	44	80	315	11	3	3	1(cc)
2	48	76	320	5	3	1	1(cc)
3	50	82	138	25	3	3	1(cc)
4	82	78	172	2	3	1	4
5	66	37	29	31	1	1	1(cc)
6	94	67	8	1	3	2	1(cc)
7	58	47	2	29	3	2	4
8	40	70	44	69	2	3	1(cc)
9	1	53	82	14	4	1	1(cc)
10	50	74	322	9	2	3	1(cc)
11	194	59	193	58	1	3	1(cc), 4
12	194	59	96	2	3	3	1(cc)
13	183	60	235	47	1	1	1(cc), 4
14	175	75	256	35	3	1	1(cc)
15	179	74	257	38	3	1	1(cc)
16	33	75	320	46	4	3	1(cc)
17	33	77	320	49	2	1	1(cc)
18	243	74	325	20	3	2	4
19	164	61	230	40	3	1	1(cc)
20	55	73	320	6	3	1	1(cc), chl
21	31	81	300	4	3	1	1(cc), chl
22	76	74	130	25	3	1	1(cc)
23	40	87	344	73	1	1	1(cc), chl
24	52	75	347	8	4	1	1(cc)
25	57	70	346	39	4	2	1(qz)
26	64	65	348	28	4	1	1(qz)
27	42	69	2	70	4	1	1(qz)
28	215	35	177	26	1	1	1(cc)
29	52	80	322	6	4	2	1(cc)

34 Kroppenstedt — Lat 51.915 — Long 11.29

Data #	DipDir	Dip	Azimuth	Plunge	Sense	Quality	Indicators + mineral coatings
1	165	86	78	20	4	3	4
2	165	86	70	5	4	3	4
3	10	89	282	73	2	2	4
4	115	80	14	5	4	2	4
5	271	81	1	1	3	2	1(cc)
6	284	85	186	5	3	2	4
7	86	88	174	1	3	2	4
8	260	87	352	2	3	2	4

37 Förderstedt — Lat 51.875 — Long 11.629

Data #	DipDir	Dip	Azimuth	Plunge	Sense	Quality	Indicators + mineral coatings
1	240	40	252	38	2	2	4
2	238	42	247	20	2	2	4
3	248	40	174	8	4	1	4
4	266	80	286	52	2	3	4
5	218	54	218	54	2	1	4

35 Dönstedt — Lat 52.259 — Long 11.333

Data #	DipDir	Dip	Azimuth	Plunge	Sense	Quality	Indicators + mineral coatings
1	63	81	154	9	3	2	1(cc), hem
2	60	72	147	4	4	2	4, hem
3	54	78	142	5	4	1	1(cc), hem
4	50	76	140	6	4	1	1(cc), hem
5	50	75	136	20	4	1	1(cc), hem
6	43	73	127	21	4	1	1(cc), hem
7	34	85	120	40	4	1	1(cc)
8	188	84	99	23	4	1	1(cc)
9	116	60	32	15	3	1	1(cc)
10	104	81	17	13	3	1	1(cc)
11	288	89	19	20	3	1	1(cc)
12	354	78	288	23	4	1	1(cc)
13	61	69	338	22	3	2	1(cc)
14	66	77	340	11	3	2	1(cc)
15	154	87	81	50	2	1	1(cc)
16	154	65	65	8	4	1	1(cc)
17	160	59	73	5	4	1	1(cc)
18	175	70	255	1	4	1	1(cc)
19	70	36	29	29	3	3	4, hem
20	21	87	108	28	4	1	1(cc)
21	172	83	84	16	4	1	1(cc)
22	166	83	77	20	4	1	1(cc)
23	160	79	254	4	4	1	1(cc)
24	169	85	84	35	4	1	1(cc)
25	191	86	101	30	4	1	1(cc), 4
26	68	40	20	35	1	2	1(cc)
27	114	40	23	3	3	1	1(cc)
28	70	82	348	20	3	1	1(cc)
29	140	76	55	3	4	1	1(cc)
30	144	66	59	10	4	1	1(cc)

57 Folwark — Lat 50.612 — Long 17.909

Data #	DipDir	Dip	Azimuth	Plunge	Sense	Quality	Indicators + mineral coatings
1	260	65	275	60	2	1	4
2	250	55	260	53	2	1	4
3	250	60	265	55	2	1	4
4	266	40	270	38	2	1	4
5	157	40	157	40	2	1	4
6	144	45	144	45	2	1	4
7	120	52	112	50	2	1	4
8	160	50	155	45	2	1	4
9	178	53	148	50	2	2	4
10	135	42	135	42	2	3	4
11	192	35	193	34	2	1	4
12	144	59	118	56	2	1	4
13	195	62	195	62	2	1	4
14	184	60	161	58	2	1	4
15	190	50	182	49	2	1	4
16	166	45	150	40	2	1	4

36 Mammendorf — Lat 52.178 — Long 11.435

Data #	DipDir	Dip	Azimuth	Plunge	Sense	Quality	Indicators + mineral coatings
1	60	85	331	1	3	2	4, hem
2	72	62	160	2	3	2	4, hem
3	60	70	148	4	3	1	1(cc)
4	43	81	134	1	3	1	1(cc)
5	48	85	319	6	3	1	4, hem
6	233	85	144	15	3	2	1(cc)
7	32	84	119	19	4	1	4
8	250	86	156	6	3	1	1(cc)
9	250	86	160	4	3	1	1(cc)
10	254	87	157	2	3	1	1(cc), hem
11	246	85	160	9	3	1	1(cc)
12	262	86	175	14	3	2	4
13	262	75	185	21	3	1	1(cc)
14	265	87	173	9	3	1	1(cc)
15	301	63	26	12	3	2	4
16	305	55	12	27	3	3	4, hem
17	52	85	322	8	4	1	4
18	53	83	323	2	4	1	1(cc)
19	116	75	200	27	4	1	1(cc)
20	116	78	199	32	4	1	1(cc)
21	83	86	160	19	4	1	1(cc)
22	145	73	236	2	3	1	4
23	310	86	220	3	4	1	1(cc), hem
24	303	78	215	12	4	1	1(cc), hem
25	35	88	126	5	4	1	1(cc)
26	314	80	46	24	3	1	1(cc)
27	70	70	348	25	3	3	1(cc)
28	104	70	16	8	4	1	1(cc)
29	106	69	185	24	4	2	1(cc), 4
30	121	80	208	24	4	1	1(qz), 1(cc)
31	227	88	138	28	3	1	1(cc)
32	228	86	142	21	3	1	1(cc)
33	112	80	202	7	3	3	1(cc)
34	108	85	190	63	1	1	1(cc)
35	113	86	196	61	1	3	4, hem
36	115	87	206	4	4	1	1(cc)

56 Raciborovice — Lat 51.192 — Long 15.709

Data #	DipDir	Dip	Azimuth	Plunge	Sense	Quality	Indicators + mineral coatings
1	42	50	42	50	1	1	1(cc)
2	41	49	41	49	1	1	1(cc)
3	42	53	32	52	1	1	1(cc)
4	156	72	245	4	3	3	1(cc)
5	128	83	45	38	3	2	4
6	204	61	238	57	1	2	1(cc)
7	51	34	78	27	1	1	1(cc)
8	42	85	40	80	2	3	1(cc)

Site	Rock age	Stress state	Type	n	σ_1-az	σ_1-pl	σ_2-az	σ_2-pl	σ_3-az	σ_3-pl	R	Rest
1	Cretaceous	WET1	Strike-slip	5	205	10	330	73	113	14	0.1	
1	Cretaceous	WET2	Strike-slip	7	149	1	247	83	59	7	0.6	4
2	Cretaceous	RHE1	Strike-slip	4	34	1	299	78	124	12	0	
2	Cretaceous	RHE2	Strike-slip	7	181	2	80	80	271	10	0.1	
2	Cretaceous	RHE3	Tensional	10	157	89	5	1	275	1	0.3	0
3	Cretaceous	MID1	Strike-slip	15	227	1	119	87	317	3	0.2	
3	Cretaceous	MID2	Strike-slip	13	348	6	222	80	79	8	0.5	
3	Cretaceous	MID3	Tensional	8	211	82	17	8	107	2	0	4
4	Cretaceous	DÖR	Strike-slip	6	14	1	277	82	104	8	0.3	1
5	Cretaceous	LEN1	Compressional	6	230	6	138	13	344	75	0.1	
5	Cretaceous	LEN2	Compressional	15	24	0	294	4	114	86	0.1	
5	Cretaceous	LEN3	Strike-slip	6	236	5	124	77	327	12	0.5	
5	Cretaceous	LEN4	Tensional	7	0	90	130	0	193	0	0.0-0.1	4
6	Cretaceous	HÖS1	Strike-slip	12	201	11	51	77	293	6	0.3	
6	Cretaceous	HÖS2	Strike-slip	5	308	6	83	81	217	6	0.8	
6	Cretaceous	HÖS3	Tensional	5	0	90	200	0	290	0	0.5-0.6	0
7	Cretaceous	LIE1	Compressional	15	21	0	111	4	291	86	0.0-0.1	
7	Cretaceous	LIE2	Strike-slip	14	28	3	208	87	118	0	0.5	6
8	Triassic	HOL1	Strike-slip	9	23	12	235	76	115	7	0.2-0.4	
8	Triassic	HOL2	Strike-slip	5	108	0	0	90	18	0	0.4	0
9	Cretaceous	HIL	Compressional	7	202	14	294	10	58	73	0.3-0.4	3
10	Triassic	BIS1	Strike-slip	5	2	8	219	80	93	6	0.4	
10	Triassic	BIS2	Strike-slip	6	110	0	21	89	200	1	0.0-0.2	0
11	Cretaceous	HAL1	Compressional	5	13	9	282	8	151	78	0.0-0.1	
11	Cretaceous	HAL2	Compressional	16	208	1	298	20	115	70	0.1-0.2	
11	Cretaceous	HAL3	Strike-slip	6	196	4	91	74	287	15	0.1	4
12	Cretaceous	KÜN1	Strike-slip	9	231	8	18	81	140	5	0.3	
12	Cretaceous	KÜN2	Strike-slip	12	359	1	95	80	269	10	0.3-0.4	
12	Cretaceous	KÜN3	Strike-slip	12	318	2	218	79	48	11	0.2-0.3	
12	Cretaceous	KÜN4	Tensional	8	111	75	257	13	349	8	0.9-1.0	6
13	Jurassic	STE	Compressional	9	201	4	291	4	66	84	0.3	2
14	Triassic	BAR1	Strike-slip	4	241	0	331	80	151	10	0.3-0.4	
14	Triassic	BAR2	Strike-slip	5	339	1	244	79	69	11	0.2-0.4	1
15	Jurassic	ROH	Compressional	4	46	0	316	4	137	86	0.5	0
16	Jurassic	HAM	Strike-slip	4	293	6	147	83	24	4	0.6	3
17	Jurassic	LAU1	Strike-slip	4	259	2	79	88	169	0	0.0-0.5	
17	Jurassic	LAU2	Tensional	7	317	85	136	5	46	0	0.2	2
18	Jurassic	MAR	Tensional	6	173	80	58	4	327	9	0.3-0.4	3
19	Triassic	AVE	Strike-slip	5	211	0	0	90	121	0	0.1-0.2	1
20	Triassic	EMM1	Strike-slip	5	220	0	0	90	310	0	0.6	
20	Triassic	EMM2	Strike-slip	9	312	0	0	90	222	0	0.4-0.6	0
21	Triassic	HAR	Strike-slip	10	201	2	301	79	111	11	0	3
22	Cretaceous	MIS1	Strike-slip	6	183	2	318	87	93	2	0.4	
22	Cretaceous	MIS2	Tensional	43	308	89	189	0	99	1	0	6
23	Triassic	ELV1	Tensional	22	0	90	167	0	77	0	0	
23	Triassic	ELV2	Oblique	32	65	0	155	34	335	65	0.1	
23	Triassic	ELV3	Strike-slip	30	39	0	0	90	309	0	0.2	
23	Triassic	ELV4	Strike-slip	15	7	10	187	80	97	0	0.2-0.4	21
24	Triassic	VOG	Strike-slip	5	202	12	3	77	111	4	0	8
25	Triassic	PAP	Compressional	11	6	4	279	1	161	84	0.3	1
26	Triassic	UPS1	Tensional	24	62	87	242	3	152	0	0.0-0.1	
26	Triassic	UPS2	Strike-slip	26	247	6	67	84	337	0	0.2	
26	Triassic	UPS3	Strike-slip	4	29	4	153	83	299	6	0.7	1
27	Cretaceous	BAD1	Tensional	4	276	78	90	12	180	1	0.0-0.1	
27	Cretaceous	BAD2	Tensional	10	311	83	210	1	120	7	0.1	4

Site	Rock age	Stress state	Type	n	σ_1-az	σ_1-pl	σ_2-az	σ_2-pl	σ_3-az	σ_3-pl	R	Rest
28	Cretaceous	SÖH	Tensional	20	14	86	182	4	272	1	0.0-0.1	2
29	Cretaceous	LAN1	Oblique	15	58	12	319	35	164	52	0.4	
29	Cretaceous	LAN2	Compressional	8	28	9	295	15	147	72	0.4	
29	Cretaceous	LAN3	Strike-slip	8	226	2	328	81	136	9	0.4	5
30	Permian	SAR	Strike-slip	4	207	7	73	80	298	7	0.0-0.1	1
31	Cretaceous	WEN	Compressional	5	160	5	251	7	35	82	0.0-0.1	1
32	Carboniferous	BOD1	Strike-slip	11	227	2	128	78	317	12	0.2	
32	Carboniferous	BOD2	Strike-slip	16	319	1	184	89	49	1	0.6	
32	Carboniferous	BOD3	Tensional	13	83	83	298	6	208	4	0.2	5
33	Carboniferous	FLE1	Strike-slip	8	212	4	32	86	302	0	0.0-0.1	
33	Carboniferous	FLE2	Strike-slip	6	177	4	283	75	86	14	0.4-0.5	
33	Carboniferous	FLE3	Strike-slip	10	292	8	92	81	202	3	0.7-0.9	5
34	Triassic	KRO	Strike-slip	7	16	8	262	71	109	17	0.1	1
35	Carboniferous	DÖN1	Strike-slip	20	44	6	154	73	312	16	0.2	
35	Carboniferous	DÖN2	Strike-slip	6	109	2	13	71	200	19	0.3-0.9	4
36	Carboniferous	MAM1	Strike-slip	24	185	10	348	80	94	3	0	
36	Carboniferous	MAM2	Strike-slip	9	270	0	0	90	180	0	0.5-0.6	3
37	Triassic	FÖR	Tensional	4	278	90	154	0	64	0	0	1
56	Triassic	RAC	Compressional	5	47	8	135	1	235	81	0.6-0.9	3
57	Cretaceous	FOL1	Tensional	12	164	86	255	0	345	4	0.2	
57	Cretaceous	FOL2	Tensional	4	306	83	170	5	80	5	0.5	0
58	Triassic	GOR	Tensional	7	133	80	42	0	312	10	0.1-0.2	1

Bedding planes

Site	Data#	DipDir	Dip	rock age
1	1	124	17	Ctu
1	2	131	6	Ctu
1	3	70	20	Ctu
1	4	110	15	Ctu
1	5	94	21	Ctu
2	1	300	18	Ctu
3	1	70	22	Ctu
4	1	195	52	Ctu
4	2	208	53	Ctu
4	3	208	65	Ctu
5	1	200	45	Ctu
5	2	195	40	Ctu
5	3	192	80	Ctu
5	4	195	81	Ctu
5	5	192	80	Ctu
5	6	210	40	Ctu
5	7	221	40	Ctu
5	8	195	35	Ctu
5	9	195	40	Ctu
5	10	218	40	Ctu
5	11	204	79	Ctu
5	12	214	74	Ctu
5	13	212	80	Ctu
5	14	218	79	Ctu
5	15	205	60	Ctu
5	16	185	41	Ctu
6	1	170	13	Ctu
6	2	224	13	Ctu
6	3	178	19	Ctu
6	4	212	20	Ctu
6	5	212	21	Ctu
7	1	190	19	Ctu
7	2	204	13	Ctu
7	3	190	16	Ctu
7	4	170	24	Ctu
7	5	189	3	Ctu
7	6	170	12	Ctu
7	7	20	12	Ctu
7	8	28	7	Ctu
8	1	31	8	Trm
8	2	40	8	Trm
8	3	90	12	Trm
8	4	105	9	Trm
8	5	163	18	Trm
8	6	180	19	Trm
8	7	195	25	Trm
8	8	198	39	Trm
8	9	196	35	Trm
8	10	190	39	Trm
8	11	188	14	Trm
8	12	180	10	Trm
8	13	248	2	Trm
8	14	160	5	Trm
8	15	176	17	Trm
8	16	181	10	Trm
8	17	180	22	Trm
8	18	230	12	Trm
8	19	356	5	Trm

Bedding planes

Site	Data#	DipDir	Dip	rock age
8	20	355	9	Trm
8	21	40	34	Trm
8	22	35	15	Trm
8	23	140	10	Trm
8	24	198	11	Trm
8	25	354	35	Trm
8	26	300	10	Trm
9	1	196	35	Ctu
9	2	203	30	Ctu
9	3	201	24	Ctu
9	4	198	50	Ctu
10	1	46	35	Trm
10	2	356	18	Trm
10	3	100	8	Trm
10	4	150	6	Trm
10	5	37	10	Trm
10	6	19	14	Trm
10	7	162	13	Trm
10	8	230	3	Trm
10	9	357	17	Trm
10	10	351	24	Trm
10	11	346	19	Trm
11	1	10	49	Ctu
11	2	11	35	Ctu
11	3	30	43	Ctu
11	4	26	49	Ctu
11	5	24	41	Ctu
11	6	24	46	Ctu
11	7	26	44	Ctu
11	8	26	45	Ctu
11	9	11	32	Ctu
12	1	226	44	Ctu
12	2	209	21	Ctu
12	3	222	31	Ctu
12	4	219	32	Ctu
12	5	230	24	Ctu
12	6	238	23	Ctu
12	7	230	8	Ctu
13	1	350	15	Jru
13	2	35	12	Jru
13	3	24	20	Jru
13	4	350	16	Jru
13	5	333	19	Jru
13	6	22	20	Jru
13	7	32	19	Jru
13	8	355	32	Jru
13	9	359	39	Jru
13	10	178	39	Jru
13	11	215	38	Jru
13	12	226	4	Jru
13	13	4	30	Jru
13	14	238	13	Jru
14	1	205	18	Trm
14	2	206	12	Trm
14	3	208	17	Trm
14	4	205	12	Trm
14	5	62	4	Trm
14	6	235	3	Trm

Bedding planes

Site	Data#	DipDir	Dip	rock age
14	7	254	7	Trm
14	8	182	10	Trm
14	9	290	10	Trm
14	10	339	4	Trm
14	11	185	15	Trm
14	12	204	24	Trm
14	13	200	10	Trm
14	14	214	14	Trm
14	15	148	8	Trm
14	16	72	1	Trm
14	17	122	3	Trm
14	18	290	20	Trm
16	1	292	1	Jru
16	2	292	7	Jru
17	1	95	11	Jru
18	1	228	23	Jru
19	1	78	19	Trm
19	2	42	6	Trm
19	3	128	17	Trm
19	4	174	36	Trm
19	5	172	46	Trm
19	6	186	57	Trm
19	7	146	30	Trm
19	8	204	34	Trm
19	9	82	25	Trm
20	1	228	10	Trm
20	2	178	11	Trm
20	3	270	11	Trm
20	4	68	7	Trm
21	1	113	15	Trm
21	2	18	21	Trm
21	3	137	8	Trm
21	4	18	24	Trm
21	5	92	13	Trm
22	1	58	16	Ctu
23	1	76	6	Trm
23	2	142	6	Trm
23	3	172	9	Trm
23	4	152	6	Trm
23	5	265	4	Trm
23	6	188	11	Trm
23	7	342	4	Trm
23	8	283	4	Trm
23	9	345	10	Trm
23	10	48	4	Trm
23	11	257	9	Trm
23	12	246	19	Trm
23	13	291	13	Trm
23	14	334	5	Trm
23	15	302	19	Trm
23	16	262	6	Trm
23	17	251	12	Trm
23	18	70	10	Trm
23	19	92	15	Trm
23	20	131	10	Trm
23	21	108	8	Trm
23	22	101	6	Trm
23	23	78	6	Trm

Bedding planes

Site	Data#	DipDir	Dip	rock age
23	24	70	40	Trm
23	25	84	41	Trm
23	26	113	22	Trm
23	27	79	20	Trm
23	28	38	31	Trm
23	29	77	27	Trm
23	30	96	11	Trm
23	31	73	26	Trm
23	32	50	10	Trm
23	33	316	9	Trm
23	34	78	25	Trm
23	35	10	70	Trm
23	36	130	16	Trm
23	37	135	5	Trm
23	38	316	9	Trm
23	39	291	5	Trm
23	40	70	88	Trm
23	41	66	84	Trm
23	42	48	55	Trm
23	43	95	22	Trm
23	44	38	4	Trm
23	45	32	37	Trm
23	46	76	1	Trm
24	1	155	26	Trm
25	1	76	32	Trm
25	2	106	43	Trm
25	3	119	30	Trm
25	4	110	25	Trm
25	5	92	24	Trm
25	6	74	26	Trm
25	7	80	27	Trm
25	8	60	35	Trm
25	9	25	40	Trm
25	10	88	29	Trm
25	11	101	28	Trm
25	12	72	19	Trm
25	13	55	24	Trm
25	14	66	19	Trm
25	15	71	26	Trm
25	16	38	15	Trm
25	17	100	18	Trm
25	18	113	34	Trm
25	19	134	28	Trm
25	20	23	38	Trm
25	21	152	17	Trm
25	22	148	19	Trm
25	23	164	17	Trm
25	24	76	14	Trm
25	25	34	21	Trm
25	26	65	10	Trm
25	27	32	15	Trm
25	28	118	15	Trm
25	29	131	19	Trm
25	30	138	24	Trm
25	31	139	34	Trm
25	32	185	45	Trm
25	33	189	45	Trm
25	34	72	7	Trm

Bedding planes

Site	Data#	DipDir	Dip	rock age
25	35	173	32	Trm
25	36	200	36	Trm
25	37	61	30	Trm
25	38	51	22	Trm
25	39	59	30	Trm
25	40	154	7	Trm
25	41	98	24	Trm
25	42	286	3	Trm
25	43	70	29	Trm
25	44	102	27	Trm
25	45	133	28	Trm
25	46	162	37	Trm
25	47	147	41	Trm
25	48	111	31	Trm
25	49	92	32	Trm
25	50	100	34	Trm
25	51	20	80	Trm
25	52	34	65	Trm
26	1	103	3	Trm
26	2	200	1	Trm
26	3	308	15	Trm
26	4	284	24	Trm
27	1	135	12	Ctu
28	1	138	15	Ctu
28	2	125	20	Ctu
28	3	105	11	Ctu
28	4	84	15	Ctu
29	1	43	18	Ctu
29	2	46	17	Ctu
29	3	26	15	Ctu
29	4	12	34	Ctu
29	5	66	23	Ctu
29	6	12	34	Ctu
34	1	296	13	Trm
37	1	50	5	Trm
38	1	150	50	Pru
38	2	352	31	Pru
38	3	63	26	Pru
38	4	92	9	Pru
38	5	300	6	Pru
40	1	352	17	Trm
40	2	332	20	Trm
41	1	68	12	Trm
41	2	40	20	Trm
41	3	51	4	Trm
41	4	218	27	Trm
41	5	38	32	Trm
41	6	16	16	Trm
41	7	43	20	Trm
41	8	42	10	Trm
41	9	238	12	Trm
41	10	175	28	Trm
41	11	195	36	Trm
41	12	182	32	Trm
41	13	16	28	Trm
43	1	57	15	Jru
43	2	12	30	Jru
43	3	18	15	Jru

Bedding planes

Site	Data#	DipDir	Dip	rock age
43	4	338	12	Jru
45	1	6	27	Trm
45	2	20	20	Trm
46	1	209	10	Trm
46	2	203	7	Trm
48	1	286	4	Jru
48	2	60	4	Jru
50	1	31	34	Jru
52	1	12	65	Ctu
52	2	25	71	Ctu
52	3	28	70	Ctu
52	4	24	66	Ctu
53	1	107	20	Trm
53	2	86	17	Trm
53	3	98	16	Trm
53	4	98	25	Trm
53	5	115	8	Trm
53	6	88	5	Trm
54	1	125	6	Trm
54	2	136	9	Trm
54	3	125	4	Trm
54	4	188	6	Trm
54	5	196	15	Trm
54	6	199	16	Trm
54	7	198	19	Trm
54	8	68	14	Trm
54	9	42	12	Trm
54	10	220	13	Trm
54	11	182	20	Trm
54	12	220	10	Trm
55	1	42	3	Trm
55	2	46	9	Trm
55	3	270	3	Trm
55	4	30	11	Trm
55	5	24	15	Trm
55	6	21	20	Trm
55	7	16	10	Trm
55	8	14	10	Trm
55	9	164	4	Trm
56	1	22	6	Trm
56	2	350	20	Trm
56	3	50	63	Trm
56	4	28	55	Trm
56	5	24	60	Trm
56	6	256	35	Trm
56	7	66	47	Trm
56	8	103	31	Trm
56	9	116	14	Trm
56	10	221	50	Trm
56	11	30	55	Trm
56	12	230	70	Trm
56	13	228	75	Trm
56	14	40	30	Trm
56	15	28	54	Trm
56	16	193	63	Trm
56	17	15	30	Trm
56	18	206	37	Trm
56	19	251	25	Trm

Bedding planes

Site	Data#	DipDir	Dip	rock age
56	20	42	39	Trm
56	21	25	12	Trm
56	22	39	50	Trm
56	23	217	20	Trm
56	24	28	42	Trm
56	25	285	25	Trm
56	26	43	34	Trm
56	27	78	80	Trm
56	28	5	23	Trm
56	29	48	50	Trm
56	30	210	27	Trm
56	31	211	34	Trm
56	32	30	30	Trm
56	33	246	55	Trm
56	34	80	78	Trm
56	35	260	60	Trm
56	36	20	25	Trm
56	37	22	40	Trm
56	38	228	45	Trm
56	39	70	40	Trm
56	40	30	55	Trm

Veins

Site	Data#	DipDir	Dip	Mineral
4	1	118	88	cc
8	1	186	80	cc
8	2	350	85	cc
8	3	6	83	cc
10	1	176	86	cc
10	2	217	80	cc
10	3	236	75	cc
11	1	133	82	cc
11	2	34	88	cc
12	1	114	76	cc
12	2	116	83	cc
12	3	92	86	cc
14	1	292	74	cc
17	1	318	83	cc
17	2	205	72	cc
21	1	266	81	cc
21	2	288	68	cc
21	3	357	82	cc
21	4	9	86	cc
23	1	247	82	cc
23	2	270	90	cc
23	3	222	84	cc
23	4	210	85	cc
23	5	200	80	cc
23	6	202	88	cc
23	7	200	20	cc
23	8	244	65	cc
23	9	65	70	cc
23	10	345	75	cc
23	11	70	84	cc
23	12	52	72	cc
23	13	205	89	cc
25	1	160	82	cc
25	2	179	75	cc
32	1	344	66	cc
32	2	44	85	cc
32	3	340	80	cc
32	4	356	73	cc
32	5	352	85	cc
33	1	54	78	cc
33	2	44	80	cc
33	3	65	70	CaF2
33	4	20	87	cc, CuFeS2
33	5	37	84	cc
33	6	44	73	cc, Qz
33	7	62	57	cc
33	8	22	75	cc, CaF2
33	9	50	67	qz, CaF2
35	1	66	65	cc
35	2	21	87	cc
35	3	68	75	cc
35	4	90	20	cc
36	1	259	81	cc
36	2	64	88	qz, cc
36	3	83	86	cc
51	1	118	89	cc

Appendix B

Raw data and estimated stress tensors from the Oslo Graben area

Part 1: Fault-slip data.

Lat: Latitude [°N] – Long: Longitude [°E] - DipDir/Dip: dip direction and dip of fault plane – Azimuth/Plunge: azimuth and plunge of striae – Sense: 1-reverse, 2-normal, 3-dextral, 4-sinistral – Quality of kinematic indicators: 1-excellent, 2-good, 3-poor.

Part 2: Reduced stress tensors.

az/pl: Azimuth and plunge of the principal stress axes σ_1, σ_2, σ_3 ($\sigma_1 \geq \sigma_2 \geq \sigma_3$).

R: Stress ratio, $R=(\sigma_2-\sigma_3)/(\sigma_1-\sigma_3)$.

Part 3: Bedding planes, dykes, and veins. DipDir/Dip: dip direction and dip of plane.

1 Torunstad Mælum — Lat 60.947 — Long 11.000

Data #	DipDir	Dip	Azimuth	Plunge	Sense	Quality	Source
1	332	39	297	34	2	2	M. Heeremans
2	335	65	283	53	2	1	M. Heeremans
3	340	54	304	48	2	1	M. Heeremans
4	349	59	287	38	2	1	M. Heeremans
5	320	36	290	32	2	3	M. Heeremans
6	328	75	256	49	2	2	M. Heeremans
7	293	29	262	25	2	1	M. Heeremans
8	301	40	274	37	2	1	M. Heeremans
9	93	89	181	61	2	3	M. Heeremans
10	278	80	210	65	2	1	M. Heeremans
11	273	75	238	72	2	1	M. Heeremans
12	268	83	258	83	2	3	M. Heeremans
13	291	82	213	56	2	2	M. Heeremans
14	285	58	238	48	2	3	M. Heeremans
15	345	53	277	26	2	1	M. Heeremans
16	347	50	272	17	2	3	M. Heeremans
17	358	71	277	23	2	3	M. Heeremans
18	325	38	269	23	2	3	M. Heeremans
19	351	63	283	36	2	3	M. Heeremans
20	343	38	259	5	4	3	M. Heeremans
21	307	34	267	27	2	3	M. Heeremans
22	106	60	102	60	2	1	M. Heeremans
23	83	79	157	55	2	3	M. Heeremans
24	95	73	178	21	4	3	M. Heeremans
25	271	85	193	67	0	0	M. Heeremans
26	57	81	134	55	0	0	M. Heeremans

2 Brummunddal — Lat 60.933 — Long 10.998

Data #	DipDir	Dip	Azimuth	Plunge	Sense	Quality	Source
1	233	44	293	26	2	1	M. Heeremans
2	291	27	298	27	2	3	M. Heeremans
3	280	35	306	32	2	3	M. Heeremans
4	295	60	288	60	2	3	M. Heeremans
5	268	39	268	39	2	1	M. Heeremans
6	294	40	275	38	2	3	M. Heeremans
7	293	35	261	31	2	3	M. Heeremans
8	281	20	271	20	2	3	M. Heeremans
9	285	49	285	49	2	1	M. Heeremans
10	293	71	349	58	2	3	M. Heeremans
11	266	44	297	40	2	3	M. Heeremans
12	239	55	300	34	2	3	M. Heeremans
13	329	36	306	34	2	2	M. Heeremans
14	248	43	322	15	2	3	M. Heeremans
15	308	44	341	39	2	3	M. Heeremans
16	280	48	303	46	2	1	M. Heeremans
17	264	62	258	62	2	1	M. Heeremans
18	356	44	323	39	2	3	M. Heeremans
19	328	45	328	45	2	3	M. Heeremans
20	327	46	6	39	2	3	M. Heeremans
21	277	51	277	51	2	3	M. Heeremans
22	281	50	281	50	2	3	M. Heeremans
23	40	65	89	55	0	0	M. Heeremans

3 Hellerud — Lat 60.818 — Long 10.803

Data #	DipDir	Dip	Azimuth	Plunge	Sense	Quality	Source
1	250	66	170	21	2	1	M. Heeremans
2	207	69	147	53	2	2	M. Heeremans
3	229	62	184	53	2	2	M. Heeremans
4	231	57	177	42	1	2	M. Heeremans
5	230	70	155	35	2	2	M. Heeremans
6	222	66	169	53	2	2	M. Heeremans
7	230	63	230	63	2	3	M. Heeremans
8	291	29	291	29	2	2	M. Heeremans
9	265	67	183	19	3	3	M. Heeremans
10	278	47	318	39	2	2	M. Heeremans
11	248	74	171	38	2	2	M. Heeremans
12	273	69	198	33	2	2	M. Heeremans
13	229	85	146	53	2	1	M. Heeremans
14	255	50	255	50	2	1	M. Heeremans
15	225	52	225	52	2	1	M. Heeremans
16	221	59	246	57	2	2	M. Heeremans
17	226	59	255	56	2	2	M. Heeremans
18	230	77	165	61	1	1	M. Heeremans
19	271	69	205	47	2	2	M. Heeremans
20	212	63	136	25	1	1	M. Heeremans
21	219	67	144	31	1	1	M. Heeremans
22	245	79	160	26	1	2	M. Heeremans
23	280	77	203	44	2	1	M. Heeremans
24	272	87	193	75	2	2	M. Heeremans
25	254	71	207	63	2	2	M. Heeremans
26	285	50	249	44	2	2	M. Heeremans
27	303	55	269	50	2	3	M. Heeremans
28	253	55	202	42	2	1	M. Heeremans
29	253	89	253	89	2	1	M. Heeremans
30	152	81	226	59	1	2	M. Heeremans
31	354	62	296	45	2	1	M. Heeremans
32	232	66	215	65	2	2	M. Heeremans
33	96	88	186	6	3	3	M. Heeremans
34	281	80	208	58	2	3	M. Heeremans
35	91	86	171	69	2	3	M. Heeremans

4 Gorum — Lat 60.799 — Long 10.860

Data #	DipDir	Dip	Azimuth	Plunge	Sense	Quality	Source
1	154	49	154	49	2	1	M. Heeremans
2	12	77	307	61	2	1	M. Heeremans
3	186	58	202	57	2	1	M. Heeremans
4	148	61	193	52	2	1	M. Heeremans
5	356	77	293	63	2	1	M. Heeremans
6	160	55	160	55	2	1	M. Heeremans
7	147	60	161	59	2	1	M. Heeremans
8	160	75	116	69	2	1	M. Heeremans
9	160	64	160	64	2	1	M. Heeremans
10	173	49	169	49	2	1	M. Heeremans
11	165	76	165	76	2	1	M. Heeremans
12	178	66	178	66	2	1	M. Heeremans
13	159	69	214	56	2	1	M. Heeremans

5 Bøverbu — Lat 60.664 — Long 10.654

Data #	DipDir	Dip	Azimuth	Plunge	Sense	Quality	Source
1	185	78	210	77	1	1	M. Heeremans
2	350	72	299	63	2	1	M. Heeremans
3	193	55	142	42	2	3	M. Heeremans
4	175	54	216	46	2	1	M. Heeremans
5	44	71	11	68	2	1	M. Heeremans
6	177	50	210	45	2	1	M. Heeremans
7	290	86	290	86	2	1	M. Heeremans
8	240	80	326	23	3	2	M. Heeremans
9	114	86	198	58	1	1	M. Heeremans
10	272	89	288	89	1	1	M. Heeremans
11	183	87	266	66	2	2	M. Heeremans
12	347	86	347	86	2	1	M. Heeremans
13	196	68	283	8	3	1	M. Heeremans
14	206	76	286	35	2	3	M. Heeremans
15	199	64	282	13	3	1	M. Heeremans
16	199	80	127	61	1	2	M. Heeremans
17	351	70	56	49	2	1	M. Heeremans
18	200	74	133	53	1	3	M. Heeremans
19	360	81	72	63	2	2	M. Heeremans
20	193	70	269	34	2	1	M. Heeremans
21	129	61	102	58	2	1	M. Heeremans
22	128	54	79	42	2	2	M. Heeremans
23	140	55	87	41	2	1	M. Heeremans
24	177	78	95	33	1	1	M. Heeremans
25	181	79	250	61	2	1	M. Heeremans
26	4	81	303	72	2	1	M. Heeremans

6	Korslia			Lat 60.575		Long 10.717	
Data #	DipDir	Dip	Azimuth	Plunge	Sense	Quality	Source
1	118	20	157	16	2	2	M. Heeremans
2	160	28	160	28	2	1	M. Heeremans
3	163	85	163	85	2	1	M. Heeremans
4	184	65	141	57	2	1	M. Heeremans
5	142	47	179	41	2	2	M. Heeremans
6	160	48	160	48	2	2	M. Heeremans
7	99	73	40	59	2	1	M. Heeremans
8	175	87	87	38	2	2	M. Heeremans
9	177	89	177	89	2	3	M. Heeremans
10	103	46	107	46	2	1	M. Heeremans
11	91	39	104	38	2	2	M. Heeremans
12	185	75	130	65	2	3	M. Heeremans
13	39	82	119	51	2	3	M. Heeremans
14	172	89	172	89	2	1	M. Heeremans
15	166	62	160	62	2	2	M. Heeremans
16	87	58	54	53	2	3	M. Heeremans
17	121	60	157	54	2	3	M. Heeremans
18	109	52	61	40	2	2	M. Heeremans
19	110	75	39	50	2	1	M. Heeremans
20	89	86	0	15	4	1	M. Heeremans
21	96	63	13	13	3	3	M. Heeremans
22	298	80	24	19	4	3	M. Heeremans
23	230	72	148	24	2	1	M. Heeremans
24	137	50	67	22	2	2	M. Heeremans
25	26	84	298	17	3	2	M. Heeremans
26	240	88	150	0	3	1	M. Heeremans
27	53	46	143	0	4	2	M. Heeremans
28	140	48	61	12	4	1	M. Heeremans
29	79	83	351	17	4	1	M. Heeremans

7	Skari			Lat 60.456		Long 10.471	
Data #	DipDir	Dip	Azimuth	Plunge	Sense	Quality	Source
1	64	54	20	45	2	1	M. Heeremans
2	118	43	68	31	2	2	M. Heeremans
3	240	83	152	16	3	3	M. Heeremans
4	4	50	293	21	2	3	M. Heeremans
5	320	80	26	67	2	3	M. Heeremans
6	279	80	342	69	2	3	M. Heeremans
7	280	85	280	85	2	2	M. Heeremans
8	282	89	9	70	2	2	M. Heeremans
9	62	50	8	35	2	1	M. Heeremans
10	307	74	249	61	2	3	M. Heeremans
11	80	81	80	81	2	3	M. Heeremans
12	245	70	214	67	2	2	M. Heeremans
13	338	65	272	41	2	3	M. Heeremans
14	46	75	1	69	2	2	M. Heeremans
15	338	74	354	73	2	2	M. Heeremans
16	244	83	320	64	2	1	M. Heeremans
17	287	64	242	56	2	2	M. Heeremans
18	277	84	277	84	2	3	M. Heeremans
19	309	72	309	72	2	3	M. Heeremans
20	324	59	300	57	2	1	M. Heeremans
21	305	58	338	53	2	1	M. Heeremans
22	290	46	290	46	2	2	M. Heeremans
23	295	74	245	66	2	2	M. Heeremans
24	332	64	269	43	2	2	M. Heeremans
25	300	60	300	60	2	1	M. Heeremans
26	236	66	281	58	2	1	M. Heeremans
27	356	39	310	29	2	1	M. Heeremans

8	Moen			Lat 60.419		Long 10.560	
Data #	DipDir	Dip	Azimuth	Plunge	Sense	Quality	Source
1	306	44	291	43	2	1	M. Heeremans
2	310	40	310	40	2	1	M. Heeremans
3	328	72	31	54	2	3	M. Heeremans
4	92	89	6	77	2	2	M. Heeremans
5	81	84	81	84	2	3	M. Heeremans
6	343	68	268	32	2	1	M. Heeremans
7	82	75	355	10	4	1	M. Heeremans
8	29	40	339	28	2	1	M. Heeremans
9	359	36	336	34	2	3	M. Heeremans
10	358	60	56	43	2	3	M. Heeremans
11	6	56	6	56	2	3	M. Heeremans
12	290	82	13	42	2	2	M. Heeremans
13	14	38	14	38	2	1	M. Heeremans
14	9	40	352	39	2	1	M. Heeremans
15	45	34	59	33	2	1	M. Heeremans
16	24	41	65	33	2	1	M. Heeremans
17	52	77	331	33	2	1	M. Heeremans
18	60	43	5	28	2	1	M. Heeremans
19	24	42	8	41	2	1	M. Heeremans
20	194	87	278	62	2	1	M. Heeremans
21	319	77	232	11	3	1	M. Heeremans
22	5	38	5	38	2	1	M. Heeremans
23	3	44	62	26	2	1	M. Heeremans
24	75	38	2	13	2	2	M. Heeremans
25	83	60	5	20	1	2	M. Heeremans
26	208	34	182	31	2	3	M. Heeremans
27	163	73	243	29	2	2	M. Heeremans
28	1	51	45	41	2	3	M. Heeremans
29	302	61	316	60	2	3	M. Heeremans
30	307	39	265	31	2	1	M. Heeremans

9	Brandbu			Lat 60.413		Long 10.502	
Data #	DipDir	Dip	Azimuth	Plunge	Sense	Quality	Source
1	335	51	295	43	2	1	M. Heeremans
2	336	66	50	32	2	1	M. Heeremans
3	333	63	43	33	2	1	M. Heeremans
4	335	55	43	28	2	1	M. Heeremans
5	340	59	44	36	2	1	M. Heeremans
6	336	68	52	31	2	1	M. Heeremans
7	341	65	52	35	2	1	M. Heeremans
8	350	49	324	46	2	1	M. Heeremans
9	305	38	305	38	1	3	M. Heeremans
10	290	64	238	52	2	2	M. Heeremans
11	343	46	308	40	1	2	M. Heeremans
12	306	61	235	30	2	1	M. Heeremans
13	345	49	15	45	2	1	M. Heeremans
14	345	52	19	47	2	1	M. Heeremans
15	35	60	67	56	2	1	M. Heeremans
16	13	88	101	41	2	1	M. Heeremans
17	325	61	307	60	1	2	M. Heeremans
18	252	76	169	26	2	1	M. Heeremans
19	197	86	114	60	1	2	M. Heeremans
20	196	84	125	72	1	2	M. Heeremans
21	324	56	17	42	2	2	M. Heeremans
22	28	88	111	73	2	1	M. Heeremans
23	13	84	95	55	2	1	M. Heeremans
24	326	57	30	34	2	3	M. Heeremans
25	336	76	49	50	2	1	M. Heeremans
26	333	68	38	47	2	1	M. Heeremans
27	2	60	50	49	2	1	M. Heeremans
28	1	51	36	45	2	1	M. Heeremans
29	349	47	45	31	2	1	M. Heeremans
30	13	60	68	45	2	3	M. Heeremans
31	349	59	19	55	2	1	M. Heeremans
32	350	60	350	60	2	1	M. Heeremans
33	23	70	83	54	2	1	M. Heeremans
34	338	68	338	68	2	1	M. Heeremans
35	338	68	40	49	2	1	M. Heeremans
36	324	64	324	64	2	1	M. Heeremans
37	341	75	62	31	1	1	M. Heeremans
38	328	40	265	21	1	2	M. Heeremans
39	310	40	242	18	2	2	M. Heeremans
40	327	61	289	55	2	1	M. Heeremans
41	326	67	285	61	2	1	M. Heeremans
42	290	77	210	36	2	3	M. Heeremans
43	17	89	106	45	2	1	M. Heeremans
44	337	44	2	41	2	1	M. Heeremans
45	341	50	20	43	2	1	M. Heeremans
46	4	80	70	67	2	1	M. Heeremans
47	360	70	46	62	2	1	M. Heeremans
48	352	60	42	48	2	1	M. Heeremans
49	139	63	79	44	2	2	M. Heeremans
50	317	62	293	60	2	2	M. Heeremans
51	326	53	277	41	1	2	M. Heeremans
52	325	56	276	44	1	2	M. Heeremans
53	340	38	340	38	1	2	M. Heeremans
54	319	88	235	70	2	2	M. Heeremans
55	344	33	344	33	1	2	M. Heeremans
56	340	30	340	30	1	2	M. Heeremans
57	323	62	336	61	2	2	M. Heeremans
58	332	36	332	36	1	2	M. Heeremans
59	324	48	277	37	1	2	M. Heeremans
60	347	86	263	55	2	2	M. Heeremans

9 Brandbu — Lat 60.413 — Long 10.502

Data #	DipDir	Dip	Azimuth	Plunge	Sense	Quality	Source
61	329	39	310	37	1	2	M. Heeremans
62	322	73	274	66	2	2	M. Heeremans
63	326	68	281	60	2	2	M. Heeremans
64	348	62	348	62	2	1	M. Heeremans
65	164	84	164	84	1	1	M. Heeremans
66	114	71	31	19	4	1	M. Heeremans
67	167	77	128	74	2	2	M. Heeremans
68	354	82	37	79	2	1	M. Heeremans
69	352	89	352	89	2	1	M. Heeremans
70	304	84	32	16	4	1	M. Heeremans
71	121	82	37	37	2	1	M. Heeremans
72	311	68	229	20	4	1	M. Heeremans
73	320	81	231	8	4	1	M. Heeremans
74	305	81	220	31	2	1	M. Heeremans
75	342	89	342	89	2	1	M. Heeremans
76	130	66	48	18	4	3	M. Heeremans
77	244	83	244	83	2	3	M. Heeremans
78	343	56	343	56	2	1	M. Heeremans
79	330	56	330	56	2	3	M. Heeremans
80	159	89	244	79	1	1	M. Heeremans
81	338	78	309	76	2	2	M. Heeremans
82	338	33	338	33	2	3	M. Heeremans
83	337	60	337	60	2	3	M. Heeremans
84	340	74	303	70	2	1	M. Heeremans
85	344	50	344	50	2	2	M. Heeremans
86	67	89	340	69	1	1	M. Heeremans
87	331	75	331	75	2	3	M. Heeremans
88	346	75	346	75	2	1	M. Heeremans
89	350	85	350	85	2	1	M. Heeremans
90	343	70	343	70	2	1	M. Heeremans
91	293	37	272	35	2	1	M. Heeremans
92	305	40	267	33	2	3	M. Heeremans
93	304	66	242	47	2	2	M. Heeremans
94	297	40	262	34	2	1	M. Heeremans
95	343	70	307	66	2	3	M. Heeremans
96	355	62	328	59	2	1	M. Heeremans
97	337	75	337	75	2	1	M. Heeremans
98	349	84	295	80	2	1	M. Heeremans
99	347	75	347	75	2	1	M. Heeremans
100	357	84	298	78	2	1	M. Heeremans
101	344	88	260	70	2	3	M. Heeremans
102	238	53	271	48	2	1	M. Heeremans
103	304	55	343	48	1	1	M. Heeremans
104	268	52	250	51	2	3	M. Heeremans
105	92	45	36	29	2	1	M. Heeremans
106	121	58	46	23	2	1	M. Heeremans
107	107	48	49	31	2	1	M. Heeremans
108	63	77	335	10	4	1	M. Heeremans
109	230	88	147	74	1	1	M. Heeremans
110	15	48	74	30	2	3	M. Heeremans
111	32	77	111	39	2	1	M. Heeremans

10 Tingelstad — Lat 60.394 — Long 10.473

Data #	DipDir	Dip	Azimuth	Plunge	Sense	Quality	Source
1	348	62	348	62	2	1	M. Heeremans
2	164	84	164	84	1	1	M. Heeremans
3	114	71	31	19	4	1	M. Heeremans
4	167	77	128	74	2	2	M. Heeremans
5	354	82	37	79	2	1	M. Heeremans
6	352	89	352	89	2	1	M. Heeremans
7	304	84	32	16	4	1	M. Heeremans
8	121	82	37	37	2	1	M. Heeremans
9	311	68	229	20	4	1	M. Heeremans
10	320	81	231	8	4	1	M. Heeremans
11	305	81	220	31	2	1	M. Heeremans
12	342	89	342	89	2	1	M. Heeremans
13	130	66	48	18	4	3	M. Heeremans
14	244	83	244	83	2	3	M. Heeremans
15	343	56	343	56	2	1	M. Heeremans
16	330	56	330	56	2	3	M. Heeremans
17	159	89	244	79	1	1	M. Heeremans
18	338	78	309	76	2	2	M. Heeremans
19	338	33	338	33	2	3	M. Heeremans
20	337	60	337	60	2	3	M. Heeremans
21	340	74	303	70	2	1	M. Heeremans
22	344	50	344	50	2	2	M. Heeremans
23	67	89	340	69	1	1	M. Heeremans
24	331	75	331	75	2	3	M. Heeremans
25	346	75	346	75	2	1	M. Heeremans
26	350	85	350	85	2	1	M. Heeremans
27	343	70	343	70	2	1	M. Heeremans
28	293	37	272	35	2	1	M. Heeremans
29	305	40	267	33	2	3	M. Heeremans
30	304	66	242	47	2	2	M. Heeremans
31	297	40	262	34	2	1	M. Heeremans
32	343	70	307	66	2	3	M. Heeremans
33	355	62	328	59	2	1	M. Heeremans
34	337	75	337	75	2	1	M. Heeremans
35	349	84	295	80	2	1	M. Heeremans
36	347	75	347	75	2	1	M. Heeremans
37	357	84	298	78	2	1	M. Heeremans
38	344	88	260	70	2	3	M. Heeremans
39	238	53	271	48	2	1	M. Heeremans
40	304	55	343	48	1	1	M. Heeremans
41	268	52	250	51	2	3	M. Heeremans
42	92	45	36	29	2	1	M. Heeremans
43	121	58	46	23	2	1	M. Heeremans
44	107	48	49	31	2	1	M. Heeremans
45	63	77	335	10	4	1	M. Heeremans
46	230	88	147	74	1	1	M. Heeremans
47	15	48	74	30	2	3	M. Heeremans
48	32	77	111	39	2	1	M. Heeremans

11 Engnes — Lat 60.384 — Long 10.360

Data #	DipDir	Dip	Azimuth	Plunge	Sense	Quality	Source
1	111	47	124	46	2	2	M. Heeremans
2	98	38	90	38	2	2	M. Heeremans
3	115	32	96	31	2	2	M. Heeremans
4	97	58	76	56	2	2	M. Heeremans
5	320	71	45	13	4	2	M. Heeremans
6	100	43	100	43	2	2	M. Heeremans
7	128	46	95	41	2	2	M. Heeremans
8	110	46	110	46	2	2	M. Heeremans
9	106	48	106	48	2	2	M. Heeremans
10	120	48	79	40	2	2	M. Heeremans

12 Jaren — Lat 60.375 — Long 10.565

Data #	DipDir	Dip	Azimuth	Plunge	Sense	Quality	Source
1	257	88	346	17	3	2	M. Heeremans
2	299	68	221	27	2	2	M. Heeremans
3	264	85	324	80	2	1	M. Heeremans
4	90	77	44	72	2	2	M. Heeremans
5	63	67	93	64	2	2	M. Heeremans
6	79	71	79	71	2	1	M. Heeremans
7	244	89	333	43	2	2	M. Heeremans
8	240	83	240	83	1	1	M. Heeremans
9	106	84	16	4	4	1	M. Heeremans
10	87	69	7	24	2	1	M. Heeremans
11	82	75	357	19	4	2	M. Heeremans
12	55	80	347	65	2	1	M. Heeremans
13	55	80	327	11	4	1	M. Heeremans
14	56	80	329	19	4	3	M. Heeremans
15	96	88	186	3	4	1	M. Heeremans
16	102	73	60	68	2	1	M. Heeremans
17	70	84	360	73	2	2	M. Heeremans
18	49	71	340	46	2	1	M. Heeremans
19	83	45	53	41	2	1	M. Heeremans
20	75	70	39	66	2	1	M. Heeremans
21	108	58	80	55	2	1	M. Heeremans

13 Råholt — Lat 60.280 — Long 11.146

Data #	DipDir	Dip	Azimuth	Plunge	Sense	Quality	Source
1	33	57	326	31	2	2	M. Heeremans
2	95	74	159	57	2	3	M. Heeremans
3	82	70	145	51	2	1	M. Heeremans
4	83	57	133	45	2	2	M. Heeremans
5	76	71	152	36	1	1	M. Heeremans
6	108	82	193	32	2	2	M. Heeremans
7	45	49	55	49	2	3	M. Heeremans
8	49	48	360	36	2	1	M. Heeremans
9	55	54	15	46	2	3	M. Heeremans
10	114	62	136	60	2	1	M. Heeremans
11	114	74	149	71	2	1	M. Heeremans
12	75	58	144	30	2	1	M. Heeremans
13	99	81	175	58	2	2	M. Heeremans
14	64	58	347	20	1	3	M. Heeremans

14 Roa — Lat 60.277 — Long 10.601

Data #	DipDir	Dip	Azimuth	Plunge	Sense	Quality	Source
1	100	74	34	55	2	1	M. Heeremans
2	260	80	220	77	2	1	M. Heeremans
3	260	75	202	63	2	1	M. Heeremans
4	117	80	207	0	4	1	M. Heeremans
5	148	44	108	36	2	3	M. Heeremans
6	156	41	109	31	2	2	M. Heeremans
7	138	45	102	39	2	2	M. Heeremans
8	148	44	89	27	2	2	M. Heeremans
9	229	42	229	42	2	2	M. Heeremans
10	165	85	77	25	4	1	M. Heeremans
11	304	68	248	54	2	1	M. Heeremans
12	168	40	101	18	2	2	M. Heeremans
13	190	48	107	7	4	2	M. Heeremans
14	140	65	93	56	2	1	M. Heeremans
15	57	78	327	2	3	2	M. Heeremans
16	55	80	327	12	3	2	M. Heeremans

16 Jevnaker — Lat 60.263 — Long 10.379

Data #	DipDir	Dip	Azimuth	Plunge	Sense	Quality	Source
1	70	39	97	36	2	2	M. Heeremans
2	93	54	62	50	2	2	M. Heeremans
3	77	51	103	48	2	2	M. Heeremans
4	78	60	115	54	2	2	M. Heeremans
5	61	51	103	42	2	2	M. Heeremans
6	174	51	118	35	2	2	M. Heeremans
7	56	55	116	36	2	2	M. Heeremans
8	33	63	305	4	4	2	M. Heeremans
9	46	51	105	33	1	2	M. Heeremans
10	71	55	91	53	2	2	M. Heeremans
11	71	52	90	50	2	2	M. Heeremans
12	52	50	102	38	2	2	M. Heeremans

18 Stubdalskampen — Lat 60.115 — Long 10.384

Data #	DipDir	Dip	Azimuth	Plunge	Sense	Quality	Source
1	235	80	235	80	2	2	M. Heeremans
2	239	60	313	25	2	2	M. Heeremans
3	60	62	89	59	2	2	M. Heeremans
4	135	71	91	64	2	2	M. Heeremans
5	226	66	300	32	2	2	M. Heeremans
6	52	46	72	44	2	2	M. Heeremans
7	95	79	95	79	2	2	M. Heeremans

19 Åsaveien — 60.0977 — 10.3466

Data #	DipDir	Dip	Azimuth	Plunge	Sense	Quality	Source
1	95	89	5	22	4	1	A. Saintot
2	68	84	345	48	1	1	A. Saintot
3	237	72	184	62	2	1	A. Saintot

15 Grymyr — Lat 60.273 — Long 10.417

Data #	DipDir	Dip	Azimuth	Plunge	Sense	Quality	Source
1	68	81	68	81	2	2	M. Heeremans
2	113	78	40	54	2	2	M. Heeremans
3	271	86	271	86	2	2	M. Heeremans
4	98	67	27	38	2	2	M. Heeremans
5	351	58	351	58	1	1	M. Heeremans
6	354	65	354	65	1	1	M. Heeremans
7	162	84	79	51	2	3	M. Heeremans
8	57	78	98	74	2	2	M. Heeremans
9	165	81	125	78	2	3	M. Heeremans
10	155	89	67	67	2	2	M. Heeremans
11	166	85	85	62	2	3	M. Heeremans
12	163	84	93	73	2	2	M. Heeremans
13	344	83	50	73	2	2	M. Heeremans
14	171	84	171	84	2	2	M. Heeremans
15	171	85	171	85	2	2	M. Heeremans
16	254	69	254	69	2	3	M. Heeremans
17	166	87	166	87	2	3	M. Heeremans
18	352	79	61	61	2	3	M. Heeremans
19	340	47	340	47	2	1	M. Heeremans
20	351	83	295	78	1	1	M. Heeremans
21	316	84	26	73	2	3	M. Heeremans
22	337	43	2	40	2	1	M. Heeremans
23	356	86	267	8	4	3	M. Heeremans
24	357	88	357	88	2	1	M. Heeremans
25	354	76	354	76	2	1	M. Heeremans
26	360	84	280	58	1	1	M. Heeremans
27	349	82	59	68	1	3	M. Heeremans
28	350	76	260	2	4	2	M. Heeremans
29	159	72	223	53	2	2	M. Heeremans
30	348	82	55	70	2	3	M. Heeremans
31	168	84	168	84	2	1	M. Heeremans
32	335	64	19	56	1	1	M. Heeremans
33	137	68	69	43	2	3	M. Heeremans
34	273	69	310	64	2	1	M. Heeremans
35	175	58	156	57	1	2	M. Heeremans
36	123	82	206	39	2	1	M. Heeremans
37	178	74	115	58	1	3	M. Heeremans
38	177	72	177	72	1	1	M. Heeremans
39	178	74	251	46	1	1	M. Heeremans
40	182	28	182	28	2	3	M. Heeremans
41	180	66	180	66	2	1	M. Heeremans
42	180	66	132	56	2	2	M. Heeremans
43	176	71	118	57	1	1	M. Heeremans
44	261	82	261	82	2	1	M. Heeremans
45	42	51	323	14	4	1	M. Heeremans
46	74	68	159	12	3	1	M. Heeremans
47	191	66	141	55	1	1	M. Heeremans
48	251	83	339	17	3	1	M. Heeremans
49	190	60	259	31	2	3	M. Heeremans
50	196	60	266	30	1	3	M. Heeremans
51	346	86	72	48	1	2	M. Heeremans

17 Åsa — Lat 60.132 — Long 10.310

Data #	DipDir	Dip	Azimuth	Plunge	Sense	Quality	Source
1	144	40	144	40	2	1	M. Heeremans
2	82	69	19	50	2	1	M. Heeremans
3	84	85	172	20	4	1	M. Heeremans
4	145	36	138	36	1	1	M. Heeremans
5	129	30	129	30	1	1	M. Heeremans
6	268	74	356	6	4	1	M. Heeremans
7	76	87	347	25	4	1	M. Heeremans
8	239	70	274	66	1	2	M. Heeremans
9	256	88	167	20	4	1	M. Heeremans
10	67	89	157	18	4	1	M. Heeremans
11	89	87	178	14	4	1	M. Heeremans
12	67	79	156	6	4	1	M. Heeremans
13	70	70	7	52	2	1	M. Heeremans
14	75	72	352	21	4	1	M. Heeremans
15	73	89	163	9	4	3	M. Heeremans
16	285	89	195	4	4	1	M. Heeremans
17	77	89	348	44	2	1	M. Heeremans
18	83	84	359	45	2	2	M. Heeremans
19	77	85	356	60	2	3	M. Heeremans
20	252	74	316	56	1	1	M. Heeremans
21	50	70	344	48	2	2	M. Heeremans
22	235	60	302	34	2	1	M. Heeremans
23	75	71	6	46	2	1	M. Heeremans
24	77	83	350	24	3	2	M. Heeremans
25	77	83	348	11	3	2	M. Heeremans
26	146	19	146	19	1	3	M. Heeremans
27	73	81	354	51	2	1	M. Heeremans
28	75	70	0	36	2	1	M. Heeremans
29	81	63	13	36	2	1	M. Heeremans
30	79	65	5	31	2	1	M. Heeremans
31	62	77	335	11	3	1	M. Heeremans
32	70	55	60	55	2	1	M. Heeremans
33	90	55	66	53	2	1	M. Heeremans
34	79	49	54	46	2	1	M. Heeremans
35	80	79	353	16	4	3	M. Heeremans
36	80	79	4	51	2	3	M. Heeremans
37	80	79	144	66	1	3	M. Heeremans
38	71	76	54	75	2	1	M. Heeremans
39	73	59	73	59	2	1	M. Heeremans
40	69	78	13	69	2	1	M. Heeremans
41	87	72	21	51	2	1	M. Heeremans
42	84	86	171	35	1	1	M. Heeremans
43	88	72	6	24	2	1	M. Heeremans
44	88	72	88	72	2	2	M. Heeremans
45	81	88	355	60	2	2	M. Heeremans
46	85	61	55	57	2	1	M. Heeremans
47	82	73	26	61	2	1	M. Heeremans
48	268	87	184	62	2	1	M. Heeremans
49	75	72	33	66	2	1	M. Heeremans
50	72	61	14	44	2	1	M. Heeremans
51	72	61	352	18	4	2	M. Heeremans
52	151	39	151	39	1	1	M. Heeremans
53	16	59	334	51	2	2	M. Heeremans
54	167	36	146	34	1	1	M. Heeremans
55	59	85	148	16	4	1	M. Heeremans
56	81	85	158	69	2	1	M. Heeremans
57	81	85	358	55	2	3	M. Heeremans
58	78	42	36	34	2	1	M. Heeremans
59	73	65	3	37	2	1	M. Heeremans
60	58	89	148	14	4	2	M. Heeremans

20 Kroksund — Lat 60.069 — Long 10.300

Data #	DipDir	Dip	Azimuth	Plunge	Sense	Quality	Source
1	274	85	197	68	1	1	M. Heeremans
2	266	71	237	69	2	1	M. Heeremans
3	259	54	312	40	2	1	M. Heeremans
4	268	78	310	74	2	1	M. Heeremans
5	257	75	332	44	1	1	M. Heeremans
6	227	52	293	28	2	1	M. Heeremans
7	120	89	32	58	2	1	M. Heeremans
8	262	60	299	54	1	1	M. Heeremans
9	127	74	96	72	2	1	M. Heeremans
10	252	77	295	72	1	1	M. Heeremans
11	100	76	52	70	2	1	M. Heeremans
12	297	35	297	35	2	1	M. Heeremans
13	266	30	310	23	2	1	M. Heeremans
14	259	70	326	47	2	1	M. Heeremans
15	271	72	309	68	1	1	M. Heeremans
16	117	80	37	45	2	1	M. Heeremans
17	90	70	40	61	2	1	M. Heeremans
18	89	60	58	56	2	1	M. Heeremans
19	113	70	68	63	2	1	M. Heeremans
20	98	77	46	70	2	1	M. Heeremans
21	95	87	16	75	2	1	M. Heeremans
22	47	57	322	8	4	1	M. Heeremans
23	126	65	85	58	2	1	M. Heeremans
24	322	72	15	62	1	1	M. Heeremans
25	317	80	30	59	1	1	M. Heeremans
26	135	79	69	64	2	1	M. Heeremans
27	40	72	118	32	2	1	M. Heeremans

22 Sundvollen 2 — Lat 60.055 — Long 10.328

Data #	DipDir	Dip	Azimuth	Plunge	Sense	Quality	Source
1	65	89	335	6	4	1	A. Saintot
2	70	84	160	2	4	1	A. Saintot
3	230	80	295	68	2	1	A. Saintot
4	220	87	305	58	2	1	A. Saintot
5	223	63	266	55	2	3	A. Saintot
6	58	63	14	54	2	1	A. Saintot
7	48	72	344	54	2	1	A. Saintot
8	212	54	261	42	2	1	A. Saintot

23 Sundvollen 1 — Lat 60.053 — Long 10.322

Data #	DipDir	Dip	Azimuth	Plunge	Sense	Quality	Source
1	240	82	158	46	2	1	A. Saintot
2	260	58	256	58	2	1	A. Saintot
3	280	57	300	55	2	1	A. Saintot
4	96	86	96	86	2	1	A. Saintot
5	273	50	279	50	2	1	A. Saintot
6	286	60	292	60	2	1	A. Saintot
7	305	62	294	62	2	1	A. Saintot
8	296	52	290	52	2	1	A. Saintot
9	93	89	3	20	4	3	A. Saintot
10	288	82	15	18	4	2	A. Saintot
11	110	89	20	10	4	1	A. Saintot
12	300	82	27	18	4	1	A. Saintot
13	107	84	19	22	4	1	A. Saintot
14	285	48	323	41	2	1	A. Saintot
15	278	48	335	31	2	1	A. Saintot
16	230	80	318	11	4	3	A. Saintot

21 Sundvollen 3 — Lat 60.056 — Long 10.295

Data #	DipDir	Dip	Azimuth	Plunge	Sense	Quality	Source
1	286	59	305	58	2	1	M. Heeremans
2	116	83	49	73	1	1	M. Heeremans
3	110	70	76	66	2	1	M. Heeremans
4	110	70	158	61	2	1	M. Heeremans
5	110	70	39	42	2	1	M. Heeremans
6	267	43	289	41	2	1	M. Heeremans
7	260	66	292	62	2	1	M. Heeremans
8	255	21	267	21	2	1	M. Heeremans
9	255	51	278	49	2	1	M. Heeremans
10	273	61	284	61	2	1	M. Heeremans
11	264	57	293	53	2	1	M. Heeremans
12	272	85	358	38	1	1	M. Heeremans
13	100	73	90	73	2	1	M. Heeremans
14	268	67	268	67	2	1	M. Heeremans
15	271	69	341	42	2	1	M. Heeremans
16	280	69	259	68	2	1	M. Heeremans
17	266	45	301	39	2	1	M. Heeremans
18	99	84	14	38	2	3	M. Heeremans
19	264	87	264	87	1	2	M. Heeremans
20	265	88	348	73	1	2	M. Heeremans
21	266	76	313	70	2	1	M. Heeremans
22	265	70	320	58	2	1	M. Heeremans
23	262	73	322	59	2	1	M. Heeremans
24	86	85	86	85	2	2	M. Heeremans
25	262	74	319	62	2	1	M. Heeremans
26	273	40	273	40	2	1	M. Heeremans
27	257	84	341	46	2	1	M. Heeremans
28	257	84	257	84	2	1	M. Heeremans
29	270	66	321	55	2	1	M. Heeremans
30	270	67	322	56	1	1	M. Heeremans
31	5	79	49	75	1	1	M. Heeremans
32	273	70	273	70	2	1	M. Heeremans
33	266	65	309	57	2	1	M. Heeremans
34	261	77	317	68	2	2	M. Heeremans
35	281	79	281	79	2	1	M. Heeremans
36	295	65	273	63	2	2	M. Heeremans
37	288	67	313	65	2	1	M. Heeremans
38	295	70	295	70	2	3	M. Heeremans
39	293	88	20	60	1	1	M. Heeremans
40	145	82	64	48	2	1	M. Heeremans
41	120	89	31	55	2	2	M. Heeremans
42	298	82	346	78	2	3	M. Heeremans
43	278	67	255	65	2	1	M. Heeremans
44	289	64	267	62	2	3	M. Heeremans
45	291	60	259	56	2	1	M. Heeremans
46	286	58	267	57	2	1	M. Heeremans
47	278	53	278	53	2	3	M. Heeremans
48	290	55	261	51	2	3	M. Heeremans
49	297	50	297	50	2	1	M. Heeremans
50	297	61	297	61	2	1	M. Heeremans
51	288	63	288	63	2	1	M. Heeremans
52	287	66	200	8	3	1	M. Heeremans
53	287	64	323	59	2	1	M. Heeremans
54	274	75	274	75	1	1	M. Heeremans
55	278	58	296	57	2	1	M. Heeremans
56	289	62	272	61	2	1	M. Heeremans
57	283	66	227	52	2	1	M. Heeremans

24 Sørkedal — Lat 60.010 — Long 10.615

Data #	DipDir	Dip	Azimuth	Plunge	Sense	Quality	Source
1	115	79	199	29	1	1	A. Saintot
2	180	40	170	40	1	1	A. Saintot
3	116	79	27	3	4	2	A. Saintot
4	118	78	194	49	1	2	A. Saintot
5	181	35	171	35	2	2	A. Saintot
6	180	68	164	67	2	2	A. Saintot
7	179	73	125	62	2	2	A. Saintot
8	180	43	154	40	2	3	A. Saintot
9	125	69	197	39	1	2	A. Saintot
10	120	70	185	49	1	2	A. Saintot
11	113	73	187	42	1	2	A. Saintot
12	240	83	156	42	1	2	A. Saintot
13	250	74	173	38	1	2	A. Saintot
14	120	66	168	57	1	2	A. Saintot
15	115	73	190	40	1	2	A. Saintot
16	242	66	180	46	1	2	A. Saintot
17	122	72	184	55	1	2	A. Saintot
18	272	79	199	56	2	2	A. Saintot
19	200	60	188	59	1	1	A. Saintot
20	272	74	219	65	2	2	A. Saintot
21	120	66	183	46	1	2	A. Saintot
22	275	80	211	68	2	1	A. Saintot
23	80	78	126	73	1	1	A. Saintot
24	270	85	189	60	2	2	A. Saintot

25 Holmenkollen — Lat 59.979 — Long 10.660

Data #	DipDir	Dip	Azimuth	Plunge	Sense	Quality	Source
1	305	57	287	56	2	1	A. Saintot
2	303	65	262	58	2	1	A. Saintot
3	306	60	278	57	2	1	A. Saintot
4	320	78	260	67	2	2	A. Saintot

26 Frognerseteren — Lat 59.978 — Long 10.674

Data #	DipDir	Dip	Azimuth	Plunge	Sense	Quality	Source
1	220	55	147	23	2	2	A. Saintot
2	320	80	8	75	2	2	A. Saintot
3	50	80	124	57	2	1	A. Saintot
4	48	85	129	62	2	1	A. Saintot
5	54	89	142	58	2	1	A. Saintot
6	245	50	233	49	2	1	A. Saintot
7	249	56	209	49	2	2	A. Saintot
8	350	64	301	53	1	2	A. Saintot
9	60	63	87	60	2	1	A. Saintot
10	74	82	163	10	4	1	A. Saintot
11	230	78	180	72	2	1	A. Saintot
12	358	73	85	10	4	1	A. Saintot
13	50	82	126	59	1	1	A. Saintot
14	30	80	81	74	2	1	A. Saintot
15	29	83	70	81	2	1	A. Saintot
16	30	83	90	76	2	1	A. Saintot
17	35	84	101	76	2	1	A. Saintot
18	54	80	102	75	2	1	A. Saintot
19	216	75	170	69	2	1	A. Saintot
20	220	78	168	71	2	1	A. Saintot

27 Bogstad Lat 59.971 Long 10.635

Data #	DipDir	Dip	Azimuth	Plunge	Sense	Quality	Source
1	15	80	324	74	2	2	A. Saintot
2	38	85	312	42	1	2	A. Saintot
3	54	80	136	39	1	1	A. Saintot
4	1	79	313	74	2	1	A. Saintot
5	86	79	2	26	2	1	A. Saintot
6	84	80	358	20	4	1	A. Saintot
7	84	89	354	15	4	2	A. Saintot
8	255	68	252	68	2	1	A. Saintot
9	46	80	29	80	2	2	A. Saintot
10	30	70	358	67	2	2	A. Saintot
11	213	80	240	79	2	2	A. Saintot
12	202	78	130	55	2	1	A. Saintot
13	74	89	344	6	4	2	A. Saintot

28 Burudveien Lat 59.960 Long 10.497

Data #	DipDir	Dip	Azimuth	Plunge	Sense	Quality	Source
1	230	69	174	56	2	2	A. Saintot
2	112	60	22	0	4	1	A. Saintot
3	112	60	158	51	2	1	A. Saintot
4	118	85	207	7	3	1	A. Saintot
5	175	89	265	11	4	1	A. Saintot
6	225	50	190	44	2	2	A. Saintot
7	210	50	183	47	2	2	A. Saintot
8	220	57	181	50	2	2	A. Saintot
9	210	53	172	46	2	2	A. Saintot
10	223	40	198	37	2	2	A. Saintot
11	290	80	206	30	2	1	A. Saintot
12	235	40	210	37	2	3	A. Saintot
13	236	74	323	11	4	1	A. Saintot

29 Grinibru Lat 59.952 Long 10.631

Data #	DipDir	Dip	Azimuth	Plunge	Sense	Quality	Source
1	214	80	141	59	2	1	A. Saintot
2	160	77	102	66	2	1	A. Saintot
3	174	89	86	64	2	1	A. Saintot
4	115	60	79	54	2	1	A. Saintot
5	114	59	88	56	2	1	A. Saintot
6	114	60	95	59	2	1	A. Saintot
7	116	57	79	51	2	1	A. Saintot
8	310	89	226	80	2	1	A. Saintot
9	303	89	240	88	2	1	A. Saintot
10	310	80	283	79	2	1	A. Saintot
11	315	79	262	72	2	1	A. Saintot
12	305	82	253	77	2	1	A. Saintot
13	314	80	269	76	2	1	A. Saintot
14	140	78	86	70	2	2	A. Saintot

30 Skollerudveien Lat 59.944 Long 10.509

Data #	DipDir	Dip	Azimuth	Plunge	Sense	Quality	Source
1	190	64	233	56	2	1	A. Saintot
2	214	58	259	48	2	1	A. Saintot
3	213	78	156	68	2	1	A. Saintot
4	210	84	137	70	2	1	A. Saintot
5	215	54	195	52	2	1	A. Saintot
6	40	64	40	64	2	3	A. Saintot
7	42	70	69	68	2	3	A. Saintot
8	215	78	301	20	4	2	A. Saintot
9	270	83	270	83	2	3	A. Saintot
10	268	76	268	76	2	2	A. Saintot
11	268	76	212	66	2	1	A. Saintot
12	262	82	352	3	4	3	A. Saintot
13	252	80	341	4	4	1	A. Saintot
14	250	79	339	4	4	1	A. Saintot
15	254	77	165	3	4	1	A. Saintot
16	246	80	335	5	4	1	A. Saintot
17	262	83	352	2	4	1	A. Saintot
18	254	82	344	1	4	1	A. Saintot
19	193	60	183	60	2	1	A. Saintot
20	118	79	180	67	2	1	A. Saintot
21	189	64	207	63	2	1	A. Saintot
22	178	62	178	62	2	1	A. Saintot

31 Bærums Verk Lat 59.941 Long 10.513

Data #	DipDir	Dip	Azimuth	Plunge	Sense	Quality	Source
1	28	74	10	73	2	2	A. Saintot
2	198	69	120	28	1	2	A. Saintot
3	190	72	115	38	1	2	A. Saintot
4	57	68	49	68	2	2	A. Saintot
5	195	85	120	71	2	1	A. Saintot
6	80	89	359	84	2	1	A. Saintot
7	70	78	16	70	2	1	A. Saintot
8	60	73	355	54	2	1	A. Saintot
9	56	86	337	70	2	2	A. Saintot
10	290	75	290	75	2	1	A. Saintot
11	72	80	0	60	2	1	A. Saintot
12	224	78	215	78	2	1	A. Saintot
13	235	60	207	57	2	1	A. Saintot

32 Gamle Ringeriksvei Lat 59.940 Long 10.533

Data #	DipDir	Dip	Azimuth	Plunge	Sense	Quality	Source
1	240	75	153	12	4	1	A. Saintot
2	230	65	186	57	2	1	A. Saintot
3	272	80	199	59	2	1	A. Saintot
4	245	76	193	68	2	1	A. Saintot
5	144	70	55	2	4	2	A. Saintot
6	130	85	130	85	2	1	A. Saintot
7	280	89	192	60	2	1	A. Saintot
8	120	60	171	47	2	1	A. Saintot
9	125	65	197	34	2	1	A. Saintot
10	90	89	180	24	4	2	A. Saintot
11	185	70	185	70	2	1	A. Saintot
12	200	80	245	76	2	2	A. Saintot
13	170	80	170	80	2	1	A. Saintot
14	190	70	168	69	2	1	A. Saintot
15	195	78	209	78	2	1	A. Saintot
16	190	70	100	0	4	1	A. Saintot
17	205	65	115	0	4	1	A. Saintot
18	190	65	100	0	4	1	A. Saintot

33 Hvile Lat 59.938 Long 10.425

Data #	DipDir	Dip	Azimuth	Plunge	Sense	Quality	Source
1	9	70	72	52	1	1	M. Heeremans
2	186	76	157	74	2	1	M. Heeremans
3	15	76	88	49	1	1	M. Heeremans
4	177	54	177	54	2	1	M. Heeremans
5	204	64	148	49	2	1	M. Heeremans
6	199	89	112	70	1	1	M. Heeremans
7	196	75	196	75	1	1	M. Heeremans
8	214	78	135	43	1	1	M. Heeremans
9	219	52	187	47	2	1	M. Heeremans
10	217	72	156	56	2	1	M. Heeremans
11	240	75	161	34	2	1	M. Heeremans
12	190	74	130	60	2	3	M. Heeremans
13	211	86	123	25	3	3	M. Heeremans
14	194	82	109	32	1	3	M. Heeremans
15	201	85	114	27	1	3	M. Heeremans
16	212	82	125	18	3	1	M. Heeremans
17	173	61	97	24	1	3	M. Heeremans
18	183	75	106	40	2	1	M. Heeremans
19	190	61	190	61	2	3	M. Heeremans
20	201	69	118	17	3	1	M. Heeremans
21	254	74	166	8	3	2	M. Heeremans
22	140	33	112	30	2	3	M. Heeremans
23	169	51	112	34	2	3	M. Heeremans
24	214	84	304	1	4	1	M. Heeremans
25	157	43	157	43	2	2	M. Heeremans
26	118	80	204	22	3	1	M. Heeremans
27	131	76	131	76	2	1	M. Heeremans
28	180	63	267	6	3	3	M. Heeremans
29	159	58	212	44	2	3	M. Heeremans
30	152	42	196	33	2	3	M. Heeremans
31	162	89	249	71	1	1	M. Heeremans
32	6	85	277	15	3	1	M. Heeremans
33	358	85	269	15	3	1	M. Heeremans
34	15	53	82	27	2	1	M. Heeremans
35	15	53	300	20	1	1	M. Heeremans
36	357	56	273	9	3	1	M. Heeremans
37	243	71	177	50	2	1	M. Heeremans
38	192	66	273	20	3	1	M. Heeremans
39	346	73	265	26	1	1	M. Heeremans
40	37	78	309	11	3	3	M. Heeremans
41	2	89	272	1	3	1	M. Heeremans
42	355	89	355	89	2	3	M. Heeremans
43	311	83	245	73	2	2	M. Heeremans
44	327	70	270	56	1	2	M. Heeremans
45	157	64	157	64	2	3	M. Heeremans
46	154	61	160	61	2	3	M. Heeremans
47	262	77	182	37	2	1	M. Heeremans
48	72	88	160	51	2	1	M. Heeremans
49	158	77	109	70	2	2	M. Heeremans
50	46	69	114	45	2	1	M. Heeremans
51	195	88	277	75	2	3	M. Heeremans
52	175	70	95	26	2	0	M. Heeremans
53	184	60	184	60	2	0	M. Heeremans

34	Rykkinn			Lat 59.933		Long 10.485	
Data #	DipDir	Dip	Azimuth	Plunge	Sense	Quality	Source
1	265	68	229	64	2	1	A. Saintot
2	270	72	243	70	2	1	A. Saintot
3	258	79	258	79	2	1	A. Saintot
4	263	75	221	70	2	2	A. Saintot
5	240	59	223	58	2	3	A. Saintot
6	192	42	175	41	1	3	A. Saintot
7	256	72	181	38	2	1	A. Saintot
8	250	59	173	20	2	1	A. Saintot
9	247	43	160	3	4	1	A. Saintot
10	275	89	187	68	2	1	A. Saintot
11	260	70	173	9	4	2	A. Saintot
12	74	62	140	38	2	1	A. Saintot
13	80	70	155	35	2	1	A. Saintot
14	270	70	253	69	2	1	A. Saintot
15	260	79	180	42	2	1	A. Saintot

35	Sinsen			Lat 59.917		Long 10.812	
Data #	DipDir	Dip	Azimuth	Plunge	Sense	Quality	Source
1	290	89	201	31	2	2	M. Heeremans
2	106	87	193	40	2	1	M. Heeremans
3	103	80	188	28	2	1	M. Heeremans
4	97	38	97	38	2	1	M. Heeremans
5	100	39	110	39	2	1	M. Heeremans
6	106	38	130	35	2	1	M. Heeremans
7	103	35	111	35	2	1	M. Heeremans
8	221	64	294	31	2	1	M. Heeremans
9	258	86	344	44	1	2	M. Heeremans
10	351	54	291	34	2	2	M. Heeremans
11	345	48	284	28	2	2	M. Heeremans
12	293	58	227	33	1	3	M. Heeremans
13	229	57	319	1	4	2	M. Heeremans
14	113	64	61	52	1	1	M. Heeremans
15	60	72	150	1	3	3	M. Heeremans
16	250	72	331	26	2	1	M. Heeremans
17	248	70	331	18	3	1	M. Heeremans
18	313	69	234	26	2	1	M. Heeremans
19	310	67	233	27	2	1	M. Heeremans

36	Vækerø			Lat 59.909		Long 10.650	
Data #	DipDir	Dip	Azimuth	Plunge	Sense	Quality	Source
1	75	34	75	34	2	1	M. Heeremans
2	74	31	97	29	2	1	M. Heeremans
3	88	45	88	45	2	1	M. Heeremans
4	76	40	76	40	2	1	M. Heeremans
5	151	56	68	10	4	2	M. Heeremans
6	82	38	82	38	2	1	M. Heeremans
7	65	54	65	54	2	1	M. Heeremans
8	86	35	120	30	2	1	M. Heeremans
9	40	38	116	10	3	1	M. Heeremans
10	42	52	118	17	2	1	M. Heeremans
11	264	54	248	53	2	1	M. Heeremans
12	337	83	250	25	4	1	M. Heeremans
13	337	89	248	52	2	1	M. Heeremans
14	74	58	116	50	2	1	M. Heeremans
15	75	70	126	60	2	1	M. Heeremans
16	299	62	318	61	2	2	M. Heeremans
17	300	28	300	28	1	1	M. Heeremans
18	315	40	291	37	1	1	M. Heeremans
19	293	37	323	33	1	1	M. Heeremans
20	298	30	298	30	1	1	M. Heeremans
21	294	36	309	35	1	1	M. Heeremans
22	303	64	330	61	2	1	M. Heeremans
23	292	54	292	54	2	1	M. Heeremans
24	299	50	299	50	2	2	M. Heeremans
25	298	51	315	50	2	1	M. Heeremans
26	295	58	324	55	2	2	M. Heeremans
27	298	56	309	56	2	1	M. Heeremans
28	313	64	313	64	2	2	M. Heeremans
29	310	70	310	70	2	1	M. Heeremans
30	322	80	256	67	2	1	M. Heeremans
31	317	84	268	81	2	1	M. Heeremans
32	325	84	237	22	4	2	M. Heeremans
33	156	88	245	24	4	1	M. Heeremans
34	162	57	239	19	1	1	M. Heeremans
35	158	86	248	7	4	2	M. Heeremans
36	116	87	204	28	1	2	M. Heeremans
37	160	70	238	30	1	1	M. Heeremans
38	153	73	201	66	1	1	M. Heeremans
39	339	78	259	40	2	1	M. Heeremans
40	170	75	260	1	4	1	M. Heeremans
41	150	66	68	18	4	1	M. Heeremans
42	153	66	243	0	4	1	M. Heeremans
43	312	84	359	81	2	3	M. Heeremans
44	294	79	274	78	2	1	M. Heeremans
45	131	68	51	23	2	1	M. Heeremans
46	315	64	315	64	2	3	M. Heeremans
47	93	84	4	7	3	3	M. Heeremans
48	293	55	236	38	2	0	M. Heeremans

37	Ekeberg			Lat 59.900		Long 10.770	
Data #	DipDir	Dip	Azimuth	Plunge	Sense	Quality	Source
1	103	67	181	27	2	2	M. Heeremans
2	257	57	270	56	2	2	M. Heeremans
3	217	62	291	28	2	2	M. Heeremans
4	100	87	10	8	4	2	M. Heeremans
5	355	62	303	49	2	3	M. Heeremans
6	355	62	58	41	2	1	M. Heeremans
7	360	62	63	41	1	1	M. Heeremans
8	360	62	310	50	2	1	M. Heeremans
9	23	48	35	47	1	1	M. Heeremans
10	8	60	51	52	2	1	M. Heeremans
11	340	70	54	38	2	3	M. Heeremans
12	18	60	73	45	2	3	M. Heeremans
13	321	80	242	47	2	2	M. Heeremans
14	310	85	225	46	2	1	M. Heeremans
15	211	89	121	20	3	1	M. Heeremans
16	349	69	292	55	1	2	M. Heeremans
17	302	76	302	76	2	1	M. Heeremans
18	354	56	301	42	2	2	M. Heeremans
19	54	56	86	52	1	2	M. Heeremans
20	90	52	28	31	2	2	M. Heeremans
21	344	58	298	48	1	1	M. Heeremans
22	343	60	299	51	1	1	M. Heeremans
23	260	86	334	76	2	3	M. Heeremans
24	315	85	228	27	2	2	M. Heeremans
25	221	59	173	48	2	2	M. Heeremans
26	216	65	158	49	1	1	M. Heeremans
27	261	57	203	39	2	1	M. Heeremans
28	210	47	152	30	2	1	M. Heeremans
29	195	60	155	53	1	1	M. Heeremans
30	242	37	180	19	2	1	M. Heeremans
31	214	44	295	8	3	2	M. Heeremans
32	260	30	284	28	2	1	M. Heeremans
33	352	81	13	80	2	1	M. Heeremans
34	236	42	236	42	2	1	M. Heeremans
35	238	36	259	34	2	1	M. Heeremans
36	234	37	234	37	2	1	M. Heeremans
37	298	69	246	58	2	3	M. Heeremans
38	349	72	50	56	2	1	M. Heeremans
39	301	70	281	69	2	1	M. Heeremans
40	337	85	64	33	2	3	M. Heeremans
41	7	70	85	29	2	1	M. Heeremans
42	68	89	158	26	3	3	M. Heeremans
43	188	66	113	31	2	3	M. Heeremans
44	221	63	141	18	3	1	M. Heeremans
45	222	44	151	17	1	1	M. Heeremans
46	224	80	139	25	2	3	M. Heeremans
47	271	61	193	20	2	3	M. Heeremans
48	272	79	352	41	2	3	M. Heeremans
49	309	65	272	60	1	2	M. Heeremans
50	308	82	226	46	2	1	M. Heeremans
51	117	67	192	31	2	1	M. Heeremans
52	106	74	184	36	2	3	M. Heeremans
53	282	65	218	43	2	3	M. Heeremans
54	307	82	31	35	2	3	M. Heeremans
55	306	69	29	17	3	3	M. Heeremans
56	138	75	61	39	1	3	M. Heeremans
57	314	67	38	14	4	2	M. Heeremans
58	91	63	147	47	2	1	M. Heeremans
59	95	80	95	80	2	2	M. Heeremans
60	77	70	44	66	2	1	M. Heeremans

37 Ekeberg — Lat 59.900 — Long 10.770

Data #	DipDir	Dip	Azimuth	Plunge	Sense	Quality	Source
61	90	59	76	58	2	1	M. Heeremans
62	89	87	175	53	1	1	M. Heeremans
63	105	82	182	59	1	3	M. Heeremans
64	117	65	117	65	2	1	M. Heeremans
65	301	74	222	34	2	3	M. Heeremans
66	275	84	191	45	2	1	M. Heeremans
67	127	81	213	22	4	3	M. Heeremans
68	60	88	338	76	2	1	M. Heeremans
69	61	40	47	39	2	1	M. Heeremans
70	116	44	52	23	2	1	M. Heeremans
71	284	86	197	38	2	1	M. Heeremans
72	97	75	16	31	2	2	M. Heeremans
73	310	89	221	40	2	2	M. Heeremans
74	117	85	202	47	2	3	M. Heeremans
75	354	54	291	32	2	1	M. Heeremans
76	320	35	307	34	2	3	M. Heeremans
77	313	88	35	76	2	2	M. Heeremans
78	305	51	284	49	2	1	M. Heeremans
79	329	83	242	24	4	3	M. Heeremans
80	313	67	233	23	2	2	M. Heeremans
81	138	66	194	51	1	1	M. Heeremans
82	360	72	280	27	2	3	M. Heeremans

38 Hovedøya — Lat 59.895 — Long 10.728

Data #	DipDir	Dip	Azimuth	Plunge	Sense	Quality	Source
1	67	60	49	59	2	2	M. Heeremans
2	313	45	309	45	2	2	M. Heeremans
3	205	72	232	70	2	2	M. Heeremans
4	289	60	295	60	2	2	M. Heeremans
5	302	46	280	44	2	2	M. Heeremans
6	259	85	289	84	1	3	M. Heeremans
7	259	65	283	63	2	2	M. Heeremans
8	141	72	112	70	2	2	M. Heeremans
9	320	32	320	32	2	2	M. Heeremans

38 Hovedøya — Lat 59.895 — Long 10.728

Data #	DipDir	Dip	Azimuth	Plunge	Sense	Quality	Source
1	67	60	49	59	2	2	M. Heeremans
2	313	45	309	45	2	2	M. Heeremans
3	205	72	232	70	2	2	M. Heeremans
4	289	60	295	60	2	2	M. Heeremans
5	302	46	280	44	2	2	M. Heeremans
6	259	85	289	84	1	3	M. Heeremans
7	259	65	283	63	2	2	M. Heeremans
8	141	72	112	70	2	2	M. Heeremans
9	320	32	320	32	2	2	M. Heeremans

40 Sandvika — Lat 59.888 — Long 10.522

Data #	DipDir	Dip	Azimuth	Plunge	Sense	Quality	Source
1	95	50	84	50	2	0	M. Heeremans
2	76	66	9	41	2	2	M. Heeremans
3	256	42	324	19	1	1	M. Heeremans
4	335	68	248	7	4	3	M. Heeremans
5	85	88	85	88	1	2	M. Heeremans
6	82	89	19	88	1	1	M. Heeremans
7	65	33	65	33	2	1	M. Heeremans
8	239	60	220	59	2	2	M. Heeremans
9	330	64	15	55	1	2	M. Heeremans
10	330	66	258	34	2	2	M. Heeremans
11	130	70	53	32	2	2	M. Heeremans
12	125	70	38	9	4	2	M. Heeremans
13	335	50	297	43	2	2	M. Heeremans
14	79	85	9	76	2	2	M. Heeremans
15	75	83	163	18	3	0	M. Heeremans
16	30	55	36	55	2	0	M. Heeremans
17	62	84	349	70	1	2	M. Heeremans
18	86	73	128	67	2	2	M. Heeremans
19	79	52	99	50	2	2	M. Heeremans
20	255	82	178	58	2	2	M. Heeremans
21	89	56	42	46	2	2	M. Heeremans
22	84	43	62	41	2	2	M. Heeremans
23	239	86	324	53	2	2	M. Heeremans
24	230	80	308	49	2	2	M. Heeremans
25	52	39	62	39	1	2	M. Heeremans
26	284	68	241	61	2	2	M. Heeremans
27	306	66	230	28	2	2	M. Heeremans
28	355	89	84	32	2	2	M. Heeremans
29	60	62	118	45	2	2	M. Heeremans
30	334	72	262	43	1	2	M. Heeremans
31	12	85	282	1	3	1	M. Heeremans
32	319	10	319	10	1	2	M. Heeremans
33	216	76	132	24	1	2	M. Heeremans
34	216	76	298	29	1	2	M. Heeremans
35	231	89	143	63	2	2	M. Heeremans
36	282	82	250	81	2	2	M. Heeremans
37	75	64	158	14	4	1	M. Heeremans
38	72	34	72	34	2	2	M. Heeremans
39	187	86	116	78	2	2	M. Heeremans
40	198	86	124	76	2	2	M. Heeremans
41	188	74	188	74	2	2	M. Heeremans
42	37	65	71	61	2	2	M. Heeremans
43	289	55	264	52	2	2	M. Heeremans

41 Fornebru — 59.8875 — 10.6261

Data #	DipDir	Dip	Azimuth	Plunge	Sense	Quality	Source
1	270	67	197	35	2	1	M. Heeremans
2	289	62	290	62	2	1	M. Heeremans
3	323	64	240	14	3	2	M. Heeremans
4	322	72	48	11	4	1	M. Heeremans
5	302	42	320	41	1	2	M. Heeremans
6	324	67	50	9	3	1	M. Heeremans
7	310	40	307	40	1	1	M. Heeremans
8	305	42	282	40	1	1	M. Heeremans
9	147	64	76	33	2	2	M. Heeremans
10	309	63	323	62	1	2	M. Heeremans
11	323	75	242	29	2	1	M. Heeremans
12	148	72	233	15	4	2	M. Heeremans
13	332	60	249	12	4	1	M. Heeremans
14	333	86	244	14	4	1	M. Heeremans
15	330	55	264	31	2	1	M. Heeremans
16	230	54	237	54	2	2	M. Heeremans
17	154	62	242	3	4	2	M. Heeremans
18	337	67	348	67	1	2	M. Heeremans
19	333	72	246	9	4	1	M. Heeremans
20	321	33	303	32	1	1	M. Heeremans
21	307	42	263	33	2	1	M. Heeremans
22	337	48	267	21	1	1	M. Heeremans
23	261	52	254	52	2	1	M. Heeremans
24	285	79	210	54	2	1	M. Heeremans
25	303	39	304	39	2	1	M. Heeremans
26	170	46	123	35	1	1	M. Heeremans
27	137	34	143	34	1	1	M. Heeremans
28	75	71	54	70	2	1	M. Heeremans
29	47	74	51	74	1	1	M. Heeremans
30	199	88	123	82	2	1	M. Heeremans
31	319	55	308	54	1	2	M. Heeremans
32	290	40	288	40	2	2	M. Heeremans
33	311	40	295	39	1	2	M. Heeremans
34	74	32	83	32	2	2	M. Heeremans
35	136	45	51	4	4	1	M. Heeremans
36	135	25	70	11	2	1	M. Heeremans
37	160	54	118	46	1	2	M. Heeremans
38	315	40	273	32	2	1	M. Heeremans
39	319	48	275	39	2	1	M. Heeremans
40	328	50	279	38	2	1	M. Heeremans
41	280	64	238	57	2	1	M. Heeremans
42	325	59	275	47	2	1	M. Heeremans
43	335	72	263	43	2	1	M. Heeremans
44	335	72	258	35	2	1	M. Heeremans
45	320	40	285	34	1	1	M. Heeremans
46	326	28	286	22	1	2	M. Heeremans
47	258	88	170	47	1	2	M. Heeremans
48	72	54	100	51	2	1	M. Heeremans
49	72	54	73	54	2	1	M. Heeremans
50	163	70	112	60	2	1	M. Heeremans
51	158	89	248	1	4	1	M. Heeremans

42 Gryssestad Lat 59.881 Long 10.503

Data #	DipDir	Dip	Azimuth	Plunge	Sense	Quality	Source
1	101	82	165	72	1	2	M. Heeremans
2	108	85	66	83	2	2	M. Heeremans
3	230	67	170	50	1	1	M. Heeremans
4	74	67	123	57	1	3	M. Heeremans
5	79	80	156	52	1	3	M. Heeremans
6	113	82	185	65	2	3	M. Heeremans
7	269	54	240	50	2	1	M. Heeremans
8	79	65	140	46	1	2	M. Heeremans
9	254	63	203	51	1	2	M. Heeremans
10	283	70	208	35	2	3	M. Heeremans
11	58	72	123	52	2	2	M. Heeremans
12	60	70	123	51	1	3	M. Heeremans
13	160	34	160	34	2	2	M. Heeremans
14	59	84	147	16	3	2	M. Heeremans
15	249	85	164	45	2	2	M. Heeremans

43 Malmøya Lat 59.880 Long 10.764

Data #	DipDir	Dip	Azimuth	Plunge	Sense	Quality	Source
1	115	72	102	72	1	2	M. Heeremans
2	128	79	52	52	1	2	M. Heeremans
3	248	32	310	17	2	2	M. Heeremans
4	226	30	296	11	2	3	M. Heeremans
5	225	31	293	13	2	3	M. Heeremans
6	149	33	60	0	2	2	M. Heeremans
7	304	28	285	27	2	2	M. Heeremans
8	105	32	75	28	2	2	M. Heeremans

44 Nesoddtangen Lat 59.870 Long 10.656

Data #	DipDir	Dip	Azimuth	Plunge	Sense	Quality	Source
1	94	78	180	20	3	2	A. Saintot
2	312	57	301	57	2	1	A. Saintot
3	74	66	142	40	2	1	A. Saintot
4	40	60	114	26	2	1	A. Saintot
5	38	49	95	32	2	1	A. Saintot
6	86	60	125	53	2	1	A. Saintot
7	80	70	145	49	2	1	A. Saintot
8	80	66	140	48	2	1	A. Saintot
9	75	62	142	36	2	1	A. Saintot
10	68	60	142	26	2	1	A. Saintot
11	20	89	290	0	4	1	A. Saintot
12	170	89	80	0	4	1	A. Saintot
13	230	70	143	9	4	1	A. Saintot
14	220	80	130	0	4	1	A. Saintot

47 Bjørnemyr Lat 59.832 Long 10.637

Data #	DipDir	Dip	Azimuth	Plunge	Sense	Quality	Source
1	120	80	120	80	2	1	

45 Ostøya Lat 59.862 Long 10.568

Data #	DipDir	Dip	Azimuth	Plunge	Sense	Quality	Source
1	137	55	89	44	2	2	M. Heeremans
2	231	81	149	40	2	2	M. Heeremans
3	116	46	135	44	2	2	M. Heeremans
4	94	56	162	29	1	2	M. Heeremans
5	252	36	252	36	2	1	M. Heeremans
6	104	86	120	86	2	2	M. Heeremans
7	290	32	290	32	2	1	M. Heeremans
8	97	75	171	46	2	1	M. Heeremans
9	109	63	109	63	1	1	M. Heeremans
10	124	21	51	7	2	1	M. Heeremans
11	242	80	332	1	4	2	M. Heeremans
12	107	56	136	52	2	2	M. Heeremans
13	44	80	128	30	2	2	M. Heeremans
14	347	77	24	74	2	1	M. Heeremans
15	253	76	168	20	3	3	M. Heeremans
16	254	73	254	73	1	1	M. Heeremans
17	144	40	169	37	1	1	M. Heeremans
18	269	81	269	81	2	1	M. Heeremans
19	120	69	120	69	2	3	M. Heeremans
20	66	84	150	46	2	2	M. Heeremans
21	232	70	157	36	1	1	M. Heeremans
22	249	63	196	50	2	1	M. Heeremans
23	300	60	280	58	2	1	M. Heeremans
24	271	85	184	32	1	1	M. Heeremans
25	76	86	351	52	1	1	M. Heeremans
26	251	57	190	37	2	1	M. Heeremans
27	251	57	270	55	2	1	M. Heeremans
28	82	75	82	75	2	1	M. Heeremans
29	249	80	169	44	1	2	M. Heeremans
30	155	37	128	34	2	3	M. Heeremans
31	258	71	215	65	2	2	M. Heeremans
32	258	71	312	60	2	1	M. Heeremans
33	263	80	339	53	2	2	M. Heeremans
34	263	80	263	80	2	3	M. Heeremans
35	90	83	170	56	2	1	M. Heeremans
36	85	62	85	62	2	1	M. Heeremans
37	107	58	138	54	2	1	M. Heeremans
38	84	80	146	69	2	3	M. Heeremans
39	267	62	267	62	2	3	M. Heeremans
40	292	89	204	61	2	2	M. Heeremans
41	62	89	150	64	2	2	M. Heeremans
42	277	80	208	64	2	1	M. Heeremans
43	298	63	259	57	2	1	M. Heeremans
44	267	57	267	57	2	3	M. Heeremans
45	97	80	47	75	2	1	M. Heeremans
46	167	33	237	12	2	2	M. Heeremans
47	82	49	82	49	2	1	M. Heeremans
48	275	70	310	66	2	3	M. Heeremans
49	326	84	241	40	2	2	M. Heeremans
50	75	82	159	36	1	2	M. Heeremans

46 Hvalstad Lat 59.856 Long 10.481

Data #	DipDir	Dip	Azimuth	Plunge	Sense	Quality	Source
1	210	77	182	75	2	2	M. Heeremans
2	139	74	193	64	2	2	M. Heeremans
3	139	74	227	8	3	2	M. Heeremans
4	202	79	126	50	2	2	M. Heeremans
5	217	87	131	54	2	2	M. Heeremans
6	160	28	145	27	1	1	M. Heeremans
7	39	40	71	36	1	2	M. Heeremans
8	175	20	156	19	1	2	M. Heeremans
9	329	36	317	35	1	2	M. Heeremans
10	159	45	127	40	2	1	M. Heeremans
11	143	48	121	46	2	1	M. Heeremans
12	147	89	60	68	2	1	M. Heeremans
13	101	50	151	38	2	3	M. Heeremans
14	112	66	183	37	1	3	M. Heeremans
15	153	65	101	53	2	2	M. Heeremans

48/49 Alværn Brygge 1/2 Lat 59.821 Long 10.623

Data #	DipDir	Dip	Azimuth	Plunge	Sense	Quality	Source
1	90	88	179	20	3	1	A. Saintot
2	275	68	200	33	2	2	A. Saintot
3	78	64	144	39	2	2	A. Saintot
4	85	69	137	58	2	2	A. Saintot
5	85	63	7	23	1	2	A. Saintot
6	85	40	355	0	4	2	A. Saintot
7	250	60	160	0	4	1	A. Saintot
8	120	40	30	0	4	1	A. Saintot
9	120	50	30	0	4	1	A. Saintot
10	110	40	110	40	1	1	A. Saintot
11	290	85	312	85	2	2	A. Saintot
12	95	32	102	32	2	1	A. Saintot
13	100	75	100	75	2	1	A. Saintot
14	114	72	95	71	2	1	A. Saintot
15	90	50	95	50	2	1	A. Saintot
16	120	70	120	70	2	1	A. Saintot
17	111	66	111	66	2	1	A. Saintot
18	114	70	150	66	2	1	A. Saintot

50 Blakstad Lat 59.816 Long 10.471

Data #	DipDir	Dip	Azimuth	Plunge	Sense	Quality	Source
1	250	60	299	49	2	1	A. Saintot
2	250	60	177	27	2	1	A. Saintot
3	248	55	188	35	2	1	A. Saintot
4	255	58	189	33	2	1	A. Saintot
5	80	60	90	60	2	1	A. Saintot
6	150	68	83	44	2	3	A. Saintot
7	160	60	111	49	2	1	A. Saintot
8	235	60	182	46	2	1	A. Saintot
9	99	64	134	59	2	1	A. Saintot

51 Hauger Lat 59.806 Long 10.412

Data #	DipDir	Dip	Azimuth	Plunge	Sense	Quality	Source
1	196	66	106	0	4	2	A. Saintot
2	201	74	201	74	2	1	A. Saintot
3	203	75	245	70	2	1	A. Saintot
4	248	82	159	8	4	1	A. Saintot
5	197	80	135	69	2	1	A. Saintot
6	216	86	128	28	2	1	A. Saintot
7	220	80	137	35	2	1	A. Saintot
8	199	70	155	63	2	1	A. Saintot
9	136	82	217	49	2	1	A. Saintot
10	144	77	221	44	2	1	A. Saintot
11	194	83	107	20	4	1	A. Saintot
12	195	68	281	9	4	1	A. Saintot
13	118	75	175	64	2	2	A. Saintot

53 Utsikten Lat 59.791 Long 10.276

Data #	DipDir	Dip	Azimuth	Plunge	Sense	Quality	Source
1	80	68	135	55	2	1	A. Saintot
2	75	72	140	53	2	1	A. Saintot
3	215	64	156	47	2	3	A. Saintot
4	260	84	175	40	1	3	A. Saintot
5	60	89	149	51	2	3	A. Saintot
6	215	80	297	37	1	2	A. Saintot
7	185	57	203	56	2	2	A. Saintot

55 Reistad Lat 59.783 Long 10.280

Data #	DipDir	Dip	Azimuth	Plunge	Sense	Quality	Source
1	248	82	160	16	4	2	A. Saintot
2	229	84	142	26	2	2	A. Saintot
3	249	64	168	18	4	1	A. Saintot
4	222	81	134	10	4	1	A. Saintot
5	219	79	171	74	2	2	A. Saintot
6	222	79	134	10	4	1	A. Saintot
7	224	83	179	80	2	2	A. Saintot
8	238	89	328	2	4	1	A. Saintot
9	223	80	144	48	2	1	A. Saintot

56 Bøveien Lat 59.772 Long 10.439

Data #	DipDir	Dip	Azimuth	Plunge	Sense	Quality	Source
1	300	50	280	48	2	2	A. Saintot
2	330	52	274	36	2	1	A. Saintot
3	310	83	5	78	2	1	A. Saintot
4	310	83	38	13	3	1	A. Saintot
5	345	36	298	26	2	1	A. Saintot
6	336	35	301	30	2	1	A. Saintot
7	312	47	311	47	2	1	A. Saintot
8	314	38	306	38	2	1	A. Saintot
9	261	67	343	18	3	2	A. Saintot
10	288	78	215	54	2	2	A. Saintot
11	300	70	231	44	2	1	A. Saintot
12	280	66	225	52	2	2	A. Saintot
13	294	70	247	62	2	1	A. Saintot
14	294	39	285	39	2	1	A. Saintot
15	308	40	295	39	2	1	A. Saintot
16	160	68	119	62	2	2	A. Saintot

52 Fjellstrand Lat 59.803 Long 10.619

Data #	DipDir	Dip	Azimuth	Plunge	Sense	Quality	Source
1	137	87	225	35	1	2	A. Saintot
2	310	80	228	39	2	1	A. Saintot
3	310	88	222	38	2	2	A. Saintot
4	126	89	215	42	1	1	A. Saintot
5	122	89	211	38	1	1	A. Saintot
6	115	70	162	62	2	1	A. Saintot
7	314	85	230	52	1	1	A. Saintot
8	314	82	260	76	1	1	A. Saintot
9	188	85	143	83	1	1	A. Saintot
10	174	82	261	20	3	1	A. Saintot
11	180	86	102	72	1	1	A. Saintot
12	124	89	211	70	1	1	A. Saintot
13	256	76	182	48	2	1	A. Saintot
14	191	80	127	68	1	1	A. Saintot
15	130	85	44	36	1	1	A. Saintot
16	290	85	16	40	2	1	A. Saintot
17	312	74	238	44	2	2	A. Saintot
18	122	85	204	58	1	2	A. Saintot
19	295	88	208	60	2	1	A. Saintot
20	295	88	210	70	2	1	A. Saintot
21	120	89	208	59	1	1	A. Saintot
22	200	79	128	58	1	2	A. Saintot
23	122	89	210	60	1	1	A. Saintot
24	127	89	214	70	1	1	A. Saintot
25	110	84	191	57	1	1	A. Saintot
26	100	60	84	59	1	2	A. Saintot
27	110	85	190	64	2	1	A. Saintot
28	114	76	188	48	2	1	A. Saintot
29	120	89	208	60	1	2	A. Saintot
30	110	89	199	28	1	1	A. Saintot
31	180	80	267	18	4	2	A. Saintot
32	190	78	144	73	2	1	A. Saintot
33	95	50	70	47	1	1	A. Saintot
34	320	58	273	47	2	1	A. Saintot
35	320	62	299	60	2	1	A. Saintot
36	295	58	261	53	2	1	A. Saintot
37	130	89	216	76	1	1	A. Saintot
38	110	70	169	54	1	1	A. Saintot
39	110	85	185	71	1	1	A. Saintot
40	125	89	214	45	1	1	A. Saintot
41	300	87	215	59	2	1	A. Saintot
42	120	83	202	49	1	1	A. Saintot
43	320	82	241	53	2	1	A. Saintot
44	180	80	268	10	4	2	A. Saintot
45	115	89	115	89	1	1	A. Saintot
46	290	85	213	69	2	1	A. Saintot
47	115	85	198	53	1	1	A. Saintot
48	294	88	211	74	2	1	A. Saintot
49	112	89	200	58	1	1	A. Saintot
50	120	89	209	42	1	1	A. Saintot

57 Hasle Lat 59.771 Long 10.691

Data #	DipDir	Dip	Azimuth	Plunge	Sense	Quality	Source
1	280	22	243	18	2	3	A. Saintot
2	270	28	244	26	2	1	A. Saintot
3	262	20	246	19	2	2	A. Saintot
4	260	40	248	39	2	2	A. Saintot
5	255	65	180	29	2	1	A. Saintot
6	260	58	187	25	2	1	A. Saintot
7	266	76	185	31	2	1	A. Saintot
8	270	66	197	33	2	1	A. Saintot
9	260	58	269	58	2	1	A. Saintot
10	257	72	181	36	2	1	A. Saintot
11	257	72	270	72	2	2	A. Saintot
12	255	84	171	46	2	1	A. Saintot
13	255	84	295	82	2	2	A. Saintot
14	278	30	250	27	2	2	A. Saintot
15	280	40	212	18	2	3	A. Saintot
16	277	45	236	37	2	2	A. Saintot
17	278	40	263	39	2	1	A. Saintot
18	260	68	189	38	2	3	A. Saintot
19	264	76	180	24	2	1	A. Saintot
20	260	69	271	69	2	1	A. Saintot
21	254	70	174	26	2	1	A. Saintot
22	262	69	180	20	4	1	A. Saintot
23	265	72	185	28	2	1	A. Saintot
24	265	72	259	72	2	2	A. Saintot
25	266	64	191	28	2	1	A. Saintot
26	270	30	254	29	2	1	A. Saintot
27	277	30	246	26	2	1	A. Saintot

58 Mølleveien 59.7651 10.4377

Data #	DipDir	Dip	Azimuth	Plunge	Sense	Quality	Source
1	310	58	286	56	2	1	A. Saintot
2	310	30	235	8	2	1	A. Saintot
3	320	60	284	54	2	1	A. Saintot
4	92	58	150	41	2	1	A. Saintot
5	92	54	129	48	2	1	A. Saintot
6	95	60	145	48	2	1	A. Saintot
7	160	56	186	53	2	2	A. Saintot
8	174	68	149	66	2	1	A. Saintot
9	250	67	185	45	2	1	A. Saintot
10	251	65	181	36	2	1	A. Saintot
11	260	62	202	45	2	1	A. Saintot
12	216	58	216	58	2	1	A. Saintot
13	234	79	234	79	2	1	A. Saintot
14	28	60	346	52	2	1	A. Saintot
15	260	78	180	38	2	1	A. Saintot
16	260	66	194	43	2	1	A. Saintot
17	266	30	232	26	2	1	A. Saintot
18	272	78	182	0	4	1	A. Saintot
19	20	89	290	0	4	1	A. Saintot
20	260	76	170	0	4	1	A. Saintot
21	275	83	190	38	2	3	A. Saintot
22	188	72	175	72	2	3	A. Saintot
23	260	78	177	31	2	3	A. Saintot
24	264	68	179	12	3	2	A. Saintot
25	279	60	279	60	2	2	A. Saintot
26	260	58	187	25	2	2	A. Saintot
27	254	64	207	55	2	1	A. Saintot

59 Spro — Lat 59.764 — Long 10.585

Data #	DipDir	Dip	Azimuth	Plunge	Sense	Quality	Source
1	355	85	84	7	3	2	A. Saintot
2	40	72	40	72	2	2	A. Saintot
3	100	70	29	42	2	1	A. Saintot
4	205	87	115	5	4	2	A. Saintot
5	220	85	306	40	2	2	A. Saintot
6	50	52	15	47	1	1	A. Saintot
7	275	82	4	6	3	1	A. Saintot
8	275	83	186	10	3	1	A. Saintot
9	275	84	186	10	3	1	A. Saintot
10	40	82	331	69	2	1	A. Saintot
11	130	79	212	34	1	1	A. Saintot
12	188	24	242	15	1	1	A. Saintot
13	200	69	184	68	2	1	A. Saintot
14	90	87	178	35	2	2	A. Saintot
15	270	60	270	60	2	1	A. Saintot
16	270	89	270	89	2	1	A. Saintot

60 Nærsnes — Lat 59.763 — Long 10.496

Data #	DipDir	Dip	Azimuth	Plunge	Sense	Quality	Source
1	135	55	45	0	4	1	A. Saintot
2	135	53	133	53	2	1	A. Saintot
3	143	48	142	48	2	1	A. Saintot
4	150	63	60	0	4	1	A. Saintot
5	135	55	45	0	4	1	A. Saintot
6	315	70	288	68	1	1	A. Saintot
7	304	80	304	80	1	1	A. Saintot
8	330	80	21	74	1	1	A. Saintot
9	100	45	81	43	2	1	A. Saintot
10	248	85	161	32	2	1	A. Saintot
11	90	80	171	41	2	1	A. Saintot
12	60	76	149	4	3	1	A. Saintot
13	72	48	343	1	3	1	A. Saintot
14	115	84	203	16	4	1	A. Saintot
15	75	64	347	4	3	1	A. Saintot
16	40	84	125	38	2	2	A. Saintot
17	60	89	149	28	2	2	A. Saintot
18	92	80	6	20	3	3	A. Saintot
19	210	55	147	33	2	3	A. Saintot
20	155	88	67	48	2	1	A. Saintot

62 Brevik — Lat 59.752 — Long 10.715

Data #	DipDir	Dip	Azimuth	Plunge	Sense	Quality	Source
1	240	75	150	0	3	1	A. Saintot
2	62	89	332	0	3	1	A. Saintot
3	138	89	48	0	4	1	A. Saintot
4	150	40	60	0	3	1	A. Saintot
5	156	50	200	41	2	1	A. Saintot
6	236	75	150	14	3	1	A. Saintot
7	28	89	298	0	3	1	A. Saintot
8	202	72	112	0	3	1	A. Saintot
9	90	62	172	14	4	3	A. Saintot
10	312	65	25	32	1	1	A. Saintot
11	185	70	113	40	1	3	A. Saintot
12	258	75	198	62	2	1	A. Saintot

61 Slemmestadveien — Lat 59.757 — Long 10.456

Data #	DipDir	Dip	Azimuth	Plunge	Sense	Quality	Source
1	292	76	233	64	2	2	A. Saintot
2	195	74	263	53	2	1	A. Saintot
3	268	86	185	60	2	3	A. Saintot
4	318	68	252	45	2	1	A. Saintot
5	334	72	272	55	2	1	A. Saintot
6	80	35	350	0	1	1	A. Saintot
7	50	40	320	0	3	1	A. Saintot
8	295	64	271	62	2	1	A. Saintot
9	308	70	253	58	2	1	A. Saintot
10	300	58	300	58	2	1	A. Saintot
11	328	72	256	43	2	1	A. Saintot
12	92	82	169	58	2	1	A. Saintot
13	92	84	171	60	2	1	A. Saintot
14	95	84	169	69	2	1	A. Saintot
15	108	38	145	32	1	2	A. Saintot
16	230	24	225	24	1	3	A. Saintot
17	110	80	184	57	2	1	A. Saintot
18	98	82	173	62	2	1	A. Saintot
19	100	74	163	58	2	1	A. Saintot

63 Brynsholmen — Lat 59.751 — Long 10.441

Data #	DipDir	Dip	Azimuth	Plunge	Sense	Quality	Source
1	105	68	84	67	2	1	A. Saintot
2	84	74	159	43	2	1	A. Saintot
3	108	78	191	28	1	1	A. Saintot
4	110	80	192	37	1	1	A. Saintot
5	260	87	174	50	2	1	A. Saintot
6	257	85	196	80	2	1	A. Saintot
7	270	79	190	43	2	1	A. Saintot
8	110	74	178	53	1	1	A. Saintot
9	344	82	68	35	2	1	A. Saintot
10	60	78	130	58	2	1	A. Saintot
11	44	79	122	47	1	1	A. Saintot
12	43	76	118	45	1	1	A. Saintot
13	292	77	231	65	2	1	A. Saintot
14	70	80	142	60	1	1	A. Saintot
15	282	84	202	59	2	1	A. Saintot
16	104	80	178	57	1	1	A. Saintot
17	274	80	205	64	2	1	A. Saintot
18	103	80	148	76	2	1	A. Saintot
19	192	83	108	42	1	1	A. Saintot
20	115	80	198	35	1	1	A. Saintot
21	116	82	197	47	1	1	A. Saintot
22	8	80	92	31	2	1	A. Saintot
23	88	82	175	18	4	1	A. Saintot

64 Dalbanen — Lat 59.750 — Long 10.710

Data #	DipDir	Dip	Azimuth	Plunge	Sense	Quality	Source
1	273	54	195	16	4	1	A. Saintot
2	240	52	291	39	1	1	A. Saintot
3	275	78	206	60	2	2	A. Saintot
4	288	88	14	66	1	3	A. Saintot
5	100	85	20	64	2	3	A. Saintot
6	154	60	239	9	3	3	A. Saintot
7	112	76	197	20	4	1	A. Saintot
8	277	60	227	48	2	1	A. Saintot
9	248	75	175	48	2	3	A. Saintot
10	240	40	235	40	2	3	A. Saintot
11	257	76	180	42	2	1	A. Saintot
12	257	76	176	31	2	1	A. Saintot
13	264	84	178	35	2	1	A. Saintot
14	288	44	247	36	2	2	A. Saintot
15	290	48	237	34	2	1	A. Saintot
16	262	66	192	38	2	3	A. Saintot
17	306	36	256	25	2	1	A. Saintot
18	288	58	228	39	2	1	A. Saintot
19	156	80	238	39	2	1	A. Saintot
20	164	72	242	33	2	1	A. Saintot
21	148	80	232	30	2	1	A. Saintot
22	330	48	360	44	1	2	A. Saintot
23	345	55	60	20	2	2	A. Saintot

65 Røyken — 59.7488 — 10.4023

Data #	DipDir	Dip	Azimuth	Plunge	Sense	Quality	Source
1	44	89	314	19	3	3	A. Saintot
2	48	83	320	17	3	2	A. Saintot
3	94	80	129	78	2	2	A. Saintot
4	288	60	288	60	2	2	A. Saintot
5	82	79	138	71	2	2	A. Saintot
6	36	84	313	50	2	2	A. Saintot
7	110	70	184	37	2	3	A. Saintot
8	110	70	176	48	2	1	A. Saintot
9	110	67	173	47	2	1	A. Saintot
10	110	70	174	50	2	1	A. Saintot
11	190	72	190	72	2	1	A. Saintot
12	200	68	195	68	2	1	A. Saintot
13	194	64	210	63	2	1	A. Saintot

67 Alværn Brygge 3 — Lat 59.747 — Long 10.614

Data #	DipDir	Dip	Azimuth	Plunge	Sense	Quality	Source
1	202	85	260	81	2	1	A. Saintot
2	11	72	11	72	2	1	A. Saintot
3	30	58	52	56	2	1	A. Saintot
4	68	10	55	10	1	2	A. Saintot
5	24	57	49	54	2	1	A. Saintot
6	22	82	91	69	2	1	A. Saintot
7	20	68	59	62	2	1	A. Saintot
8	212	48	180	43	2	3	A. Saintot
9	200	72	170	69	2	1	A. Saintot
10	35	60	63	57	2	3	A. Saintot
11	315	70	225	0	3	2	A. Saintot
12	350	72	29	67	2	2	A. Saintot
13	60	70	8	59	2	1	A. Saintot
14	35	70	18	69	2	1	A. Saintot

66 Nordre Dal — Lat 59.748 — Long 10.697

Data #	DipDir	Dip	Azimuth	Plunge	Sense	Quality	Source
1	155	88	234	80	1	1	A. Saintot
2	82	57	139	40	1	1	A. Saintot
3	5	58	29	56	2	1	A. Saintot
4	53	80	140	18	3	1	A. Saintot
5	334	50	342	50	2	1	A. Saintot
6	329	62	244	9	4	1	A. Saintot
7	125	58	61	35	2	1	A. Saintot
8	343	73	57	43	1	1	A. Saintot
9	147	72	211	54	2	1	A. Saintot
10	20	80	100	43	1	1	A. Saintot
11	340	76	67	13	4	1	A. Saintot
12	278	33	290	32	2	1	A. Saintot
13	240	64	175	41	2	1	A. Saintot
14	248	75	181	55	2	1	A. Saintot
15	210	85	133	69	1	1	A. Saintot
16	215	74	157	61	1	1	A. Saintot
17	105	84	17	20	3	1	A. Saintot
18	264	87	353	20	3	1	A. Saintot
19	242	70	190	59	1	1	A. Saintot
20	320	44	320	44	2	1	A. Saintot
21	250	52	245	52	2	1	A. Saintot
22	290	75	202	8	4	1	A. Saintot
23	240	34	314	10	1	1	A. Saintot
24	318	40	330	39	2	1	A. Saintot
25	310	52	334	50	2	1	A. Saintot
26	310	45	229	9	4	1	A. Saintot
27	320	50	323	50	2	1	A. Saintot
28	300	55	7	30	2	1	A. Saintot
29	294	53	357	31	2	1	A. Saintot
30	237	65	321	14	3	1	A. Saintot
31	47	73	47	73	2	1	A. Saintot
32	237	85	305	77	1	1	A. Saintot
33	240	87	153	40	1	1	A. Saintot
34	314	51	250	29	2	2	A. Saintot

68 Gunnerud — Lat 59.745 — Long 10.455

Data #	DipDir	Dip	Azimuth	Plunge	Sense	Quality	Source
1	228	45	247	43	2	1	A. Saintot

69 Mjøndalen — Lat 59.744 — Long 10.022

Data #	DipDir	Dip	Azimuth	Plunge	Sense	Quality	Source
61	19	76	328	68	2	1	M. Heeremans
62	280	68	319	62	2	1	M. Heeremans
63	143	78	69	52	1	1	M. Heeremans
64	274	62	319	53	2	2	M. Heeremans
65	160	40	160	40	2	1	M. Heeremans

69 Mjøndalen — Lat 59.744 — Long 10.022

Data #	DipDir	Dip	Azimuth	Plunge	Sense	Quality	Source
1	1	83	1	83	2	1	M. Heeremans
2	12	76	324	70	2	1	M. Heeremans
3	160	68	179	67	2	1	M. Heeremans
4	10	60	10	60	2	1	M. Heeremans
5	35	59	35	59	2	1	M. Heeremans
6	192	64	143	54	2	1	M. Heeremans
7	3	80	3	80	2	1	M. Heeremans
8	359	78	314	73	2	3	M. Heeremans
9	175	60	175	60	1	1	M. Heeremans
10	175	72	160	71	2	1	M. Heeremans
11	93	86	175	63	2	1	M. Heeremans
12	356	60	356	60	2	1	M. Heeremans
13	355	80	68	58	2	1	M. Heeremans
14	352	86	78	47	2	1	M. Heeremans
15	360	81	69	66	2	1	M. Heeremans
16	190	87	103	46	2	2	M. Heeremans
17	340	86	250	4	3	1	M. Heeremans
18	346	84	260	36	1	2	M. Heeremans
19	340	85	251	7	3	2	M. Heeremans
20	336	87	246	4	3	2	M. Heeremans
21	200	87	110	5	4	1	M. Heeremans
22	16	74	287	4	4	1	M. Heeremans
23	219	79	307	10	4	1	M. Heeremans
24	339	82	66	18	3	1	M. Heeremans
25	16	86	287	14	4	2	M. Heeremans
26	336	86	66	2	3	1	M. Heeremans
27	353	86	82	9	3	2	M. Heeremans
28	148	86	238	0	4	1	M. Heeremans
29	159	80	71	11	4	1	M. Heeremans
30	161	75	248	12	4	1	M. Heeremans
31	179	76	267	8	4	3	M. Heeremans
32	179	76	102	42	2	1	M. Heeremans
33	139	76	229	0	4	1	M. Heeremans
34	152	54	209	37	1	1	M. Heeremans
35	350	80	79	4	3	2	M. Heeremans
36	342	86	71	10	3	2	M. Heeremans
37	196	89	107	48	2	1	M. Heeremans
38	164	88	77	54	1	1	M. Heeremans
39	194	76	116	39	2	1	M. Heeremans
40	183	74	110	45	2	1	M. Heeremans
41	193	70	115	30	2	1	M. Heeremans
42	169	76	93	44	2	1	M. Heeremans
43	188	82	107	49	2	1	M. Heeremans
44	337	89	66	32	2	1	M. Heeremans
45	159	89	70	50	1	1	M. Heeremans
46	337	87	65	30	2	1	M. Heeremans
47	158	89	69	42	1	1	M. Heeremans
48	160	57	160	57	1	1	M. Heeremans
49	156	44	156	44	1	1	M. Heeremans
50	165	53	165	53	2	1	M. Heeremans
51	165	63	136	60	1	1	M. Heeremans
52	166	89	78	61	1	1	M. Heeremans
53	167	66	114	53	2	1	M. Heeremans
54	352	86	352	86	2	1	M. Heeremans
55	336	85	65	17	3	1	M. Heeremans
56	338	89	68	20	3	1	M. Heeremans
57	169	87	82	44	2	2	M. Heeremans
58	161	89	73	59	2	1	M. Heeremans
59	136	72	65	45	1	1	M. Heeremans
60	8	80	291	52	2	1	M. Heeremans

70 Gullaugfjellet — Lat 59.741 — Long 10.304

Data #	DipDir	Dip	Azimuth	Plunge	Sense	Quality	Source
1	216	68	304	5	4	1	A. Saintot
2	200	75	111	5	4	1	A. Saintot
3	210	84	183	83	2	1	A. Saintot
4	78	89	78	89	3	2	A. Saintot
5	237	76	325	8	3	2	A. Saintot
6	135	74	47	8	4	1	A. Saintot
7	130	84	40	4	4	1	A. Saintot
8	100	89	10	20	4	1	A. Saintot
9	104	89	192	58	1	2	A. Saintot
10	108	88	198	3	4	2	A. Saintot

71 Søndre Dal — Lat 59.740 — Long 10.693

Data #	DipDir	Dip	Azimuth	Plunge	Sense	Quality	Source
1	66	89	337	46	1	2	A. Saintot
2	247	53	181	29	1	1	A. Saintot
3	100	82	178	55	2	1	A. Saintot
4	335	30	328	30	2	2	A. Saintot
5	308	59	260	48	2	1	A. Saintot
6	296	70	226	43	2	1	A. Saintot
7	290	45	277	44	2	1	A. Saintot
8	285	68	233	56	2	1	A. Saintot
9	84	84	161	64	2	1	A. Saintot
10	80	89	168	67	2	1	A. Saintot
11	78	89	166	62	2	1	A. Saintot
12	288	71	9	24	2	2	A. Saintot
13	262	80	187	56	2	3	A. Saintot
14	260	70	201	54	2	3	A. Saintot
15	145	70	80	49	1	1	A. Saintot
16	55	82	338	57	2	1	A. Saintot
17	295	75	13	38	2	1	A. Saintot

72 Ovnerudveien — Lat 59.738 — Long 10.335

Data #	DipDir	Dip	Azimuth	Plunge	Sense	Quality	Source
1	130	65	135	65	2	1	A. Saintot
2	138	63	153	62	2	1	A. Saintot
3	265	89	180	78	2	1	A. Saintot
4	180	78	199	77	2	2	A. Saintot
5	172	67	201	64	2	1	A. Saintot
6	30	80	355	78	2	1	A. Saintot
7	186	60	101	8	4	1	A. Saintot
8	192	64	103	3	4	1	A. Saintot
9	189	72	101	8	4	1	A. Saintot

73 Tusse — Lat 59.727 — Long 10.690

Data #	DipDir	Dip	Azimuth	Plunge	Sense	Quality	Source
1	286	44	252	39	1	1	A. Saintot

74 Krokodden — Lat 59.726 — Long 10.449

Data #	DipDir	Dip	Azimuth	Plunge	Sense	Quality	Source
1	280	70	208	40	2	1	A. Saintot
2	113	83	200	23	3	1	A. Saintot
3	295	50	15	11	3	1	A. Saintot
4	132	72	70	55	2	1	A. Saintot
5	112	82	37	62	2	1	A. Saintot
6	110	89	20	0	4	1	A. Saintot

75 Fagerstrandveien Lat 59.722 Long 10.676

Data #	DipDir	Dip	Azimuth	Plunge	Sense	Quality	Source
1	355	54	355	54	1	3	A. Saintot
2	108	89	197	46	1	1	A. Saintot
3	125	89	215	26	4	1	A. Saintot
4	128	75	201	48	1	1	A. Saintot
5	295	71	223	42	2	1	A. Saintot
6	296	85	241	81	2	1	A. Saintot
7	315	44	300	43	1	3	A. Saintot
8	320	50	320	50	1	3	A. Saintot
9	320	47	320	47	1	3	A. Saintot
10	325	48	235	0	3	3	A. Saintot
11	340	44	250	0	3	3	A. Saintot
12	350	40	260	0	3	3	A. Saintot
13	346	40	256	0	3	3	A. Saintot
14	355	54	355	54	1	3	A. Saintot
15	310	40	242	18	1	3	A. Saintot

76 Konnerud Lat 59.721 Long 10.147

Data #	DipDir	Dip	Azimuth	Plunge	Sense	Quality	Source
1	303	80	213	0	4	1	M. Heeremans
2	8	84	81	70	2	1	M. Heeremans
3	258	72	347	2	4	1	M. Heeremans
4	274	86	193	65	2	3	M. Heeremans
5	333	54	354	52	2	1	M. Heeremans
6	59	73	59	73	2	1	M. Heeremans
7	347	74	260	10	3	3	M. Heeremans
8	236	89	148	68	2	3	M. Heeremans
9	108	89	197	51	2	1	M. Heeremans
10	68	83	68	83	2	1	M. Heeremans
11	21	70	106	14	3	3	M. Heeremans
12	125	78	215	2	4	3	M. Heeremans
13	172	81	82	1	3	3	M. Heeremans
14	5	84	275	4	3	3	M. Heeremans

78 Holtbråten 1 Lat 59.720 Long 10.666

Data #	DipDir	Dip	Azimuth	Plunge	Sense	Quality	Source
1	290	84	207	50	2	3	A. Saintot
2	94	89	183	35	1	3	A. Saintot
3	305	65	244	46	2	1	A. Saintot
4	296	58	233	36	2	1	A. Saintot
5	246	88	158	48	2	3	A. Saintot
6	110	56	164	41	2	1	A. Saintot
7	80	48	123	39	2	1	A. Saintot
8	96	42	128	37	2	1	A. Saintot
9	72	60	146	26	2	1	A. Saintot
10	107	57	164	40	2	1	A. Saintot
11	260	85	176	50	2	1	A. Saintot
12	285	55	208	18	2	1	A. Saintot
13	303	60	221	13	4	1	A. Saintot

77 Holtbråten 3 Lat 59.720 Long 10.664

Data #	DipDir	Dip	Azimuth	Plunge	Sense	Quality	Source
1	286	85	200	40	2	1	M. Heeremans
2	276	88	188	51	2	2	M. Heeremans
3	279	81	195	34	2	1	M. Heeremans
4	258	81	211	77	2	2	M. Heeremans
5	82	62	136	48	2	1	M. Heeremans
6	288	67	237	56	2	2	M. Heeremans
7	306	85	221	46	2	1	M. Heeremans
8	281	51	245	45	2	1	M. Heeremans
9	315	65	249	41	2	1	M. Heeremans
10	288	64	230	47	2	1	M. Heeremans
11	290	69	223	46	2	1	M. Heeremans
12	88	45	133	35	2	1	M. Heeremans
13	86	70	356	0	4	2	M. Heeremans
14	256	70	166	1	4	2	M. Heeremans
15	100	76	182	30	1	3	M. Heeremans
16	88	82	177	5	4	3	M. Heeremans
17	85	43	135	31	2	1	M. Heeremans
18	347	77	273	50	2	1	M. Heeremans
19	69	80	151	38	1	1	M. Heeremans
20	316	78	13	69	2	3	M. Heeremans
21	269	56	199	27	2	2	M. Heeremans
22	249	89	160	46	2	1	M. Heeremans
23	283	58	209	24	2	1	M. Heeremans
24	308	69	223	12	4	2	M. Heeremans
25	304	79	33	6	4	1	M. Heeremans
26	321	57	241	15	3	1	M. Heeremans
27	236	67	158	26	2	2	M. Heeremans
28	236	82	150	29	2	2	M. Heeremans
29	246	67	181	45	2	1	M. Heeremans
30	255	70	173	20	4	1	M. Heeremans
31	242	85	154	24	4	3	M. Heeremans
32	234	84	147	26	2	1	M. Heeremans
33	250	86	161	11	4	1	M. Heeremans
34	260	63	187	30	2	2	M. Heeremans
35	239	81	156	37	2	2	M. Heeremans

79 Holtbråten 2 Lat 59.719 Long 10.663

Data #	DipDir	Dip	Azimuth	Plunge	Sense	Quality	Source
1	1	81	292	66	2	1	A. Saintot
2	350	78	285	63	2	1	A. Saintot
3	30	54	30	54	2	1	A. Saintot
4	11	45	5	45	2	2	A. Saintot
5	10	44	7	44	2	1	A. Saintot
6	338	71	299	66	2	1	A. Saintot
7	223	70	271	61	1	1	A. Saintot
8	18	57	18	57	2	1	A. Saintot
9	1	50	315	39	2	1	A. Saintot
10	15	44	41	41	2	1	A. Saintot
11	15	44	325	32	2	1	A. Saintot
12	10	75	297	48	2	1	A. Saintot
13	18	75	302	42	2	1	A. Saintot
14	5	87	306	84	1	1	A. Saintot
15	13	62	312	43	2	1	A. Saintot
16	308	64	234	30	2	1	A. Saintot
17	345	83	260	38	2	1	A. Saintot
18	340	86	253	38	2	1	A. Saintot
19	169	89	165	89	2	1	A. Saintot
20	112	73	160	65	2	1	A. Saintot
21	112	73	188	39	2	1	A. Saintot
22	320	68	246	34	2	1	A. Saintot

80 Hallangshagen Lat 59.716 Long 10.645

Data #	DipDir	Dip	Azimuth	Plunge	Sense	Quality	Source
1	195	84	108	25	3	1	A. Saintot
2	186	79	268	37	2	2	A. Saintot
3	195	82	105	3	3	3	A. Saintot
4	180	75	96	20	3	1	A. Saintot
5	182	76	95	12	3	1	A. Saintot
6	42	89	131	42	2	3	A. Saintot
7	203	85	117	40	1	3	A. Saintot
8	8	75	81	48	2	1	A. Saintot

81 Hyggen Lat 59.716 Long 10.370

Data #	DipDir	Dip	Azimuth	Plunge	Sense	Quality	Source
1	291	73	204	8	4	2	M. Heeremans
2	108	83	32	64	2	2	M. Heeremans
3	107	85	26	60	2	2	M. Heeremans
4	200	80	111	6	3	2	M. Heeremans
5	106	83	22	39	2	2	M. Heeremans
6	93	78	5	8	4	2	M. Heeremans
7	108	83	21	21	4	2	M. Heeremans
8	207	74	295	8	3	2	M. Heeremans
9	32	77	120	7	3	2	M. Heeremans
10	31	89	121	24	3	2	M. Heeremans
11	313	89	225	58	2	2	M. Heeremans
12	280	75	227	66	2	2	M. Heeremans
13	10	74	59	66	2	2	M. Heeremans
14	39	78	112	54	2	2	M. Heeremans
15	220	85	307	30	2	2	M. Heeremans
16	133	64	85	54	2	2	M. Heeremans
17	97	78	46	71	2	2	M. Heeremans

82 Hallangen Lat 59.699 Long 10.613

Data #	DipDir	Dip	Azimuth	Plunge	Sense	Quality	Source
1	285	55	202	10	4	2	M. Heeremans
2	260	63	311	51	2	1	M. Heeremans
3	252	79	315	66	2	1	M. Heeremans
4	259	87	174	56	2	2	M. Heeremans
5	290	67	208	18	4	3	M. Heeremans
6	264	70	190	38	2	2	M. Heeremans
7	274	71	204	45	2	2	M. Heeremans
8	19	72	350	70	2	3	M. Heeremans
9	272	68	219	56	2	1	M. Heeremans
10	256	67	203	55	2	3	M. Heeremans
11	287	43	231	28	2	3	M. Heeremans
12	287	87	199	32	2	3	M. Heeremans
13	161	45	196	39	2	2	M. Heeremans
14	257	71	220	67	2	1	M. Heeremans
15	279	68	211	43	2	2	M. Heeremans
16	213	87	134	75	2	2	M. Heeremans
17	185	40	185	40	2	3	M. Heeremans
18	261	61	327	36	2	1	M. Heeremans
19	217	89	307	10	3	1	M. Heeremans
20	210	88	300	8	3	2	M. Heeremans
21	256	64	329	30	2	1	M. Heeremans
22	222	82	312	0	3	2	M. Heeremans
23	275	62	205	33	2	2	M. Heeremans
24	271	79	196	53	2	3	M. Heeremans
25	286	52	224	31	2	3	M. Heeremans
26	34	80	315	48	2	1	M. Heeremans
27	109	74	109	74	2	1	M. Heeremans
28	100	61	138	55	2	2	M. Heeremans
29	27	62	27	62	2	2	M. Heeremans

83 Selvik Lat 59.640 Long 10.449

Data #	DipDir	Dip	Azimuth	Plunge	Sense	Quality	Source
1	189	66	252	46	2	2	M. Heeremans
2	266	48	266	48	2	2	M. Heeremans
3	294	78	313	77	2	2	M. Heeremans
4	197	80	268	62	2	2	M. Heeremans
5	240	80	221	79	2	2	M. Heeremans
6	243	60	243	60	2	2	M. Heeremans
7	177	84	265	21	3	2	M. Heeremans
8	282	50	282	50	2	2	M. Heeremans
9	255	83	332	62	2	2	M. Heeremans
10	51	73	37	73	2	2	M. Heeremans
11	272	89	1	40	2	2	M. Heeremans
12	197	89	197	89	2	2	M. Heeremans
13	213	82	129	39	1	2	M. Heeremans
14	275	66	306	62	2	2	M. Heeremans
15	289	70	254	66	2	2	M. Heeremans

84 Heistadmoen Lat 59.600 Long 9.663

Data #	DipDir	Dip	Azimuth	Plunge	Sense	Quality	Source
1	291	61	249	53	2	1	M. Heeremans
2	286	70	255	67	2	1	M. Heeremans
3	221	70	252	67	2	1	M. Heeremans
4	247	80	247	80	2	1	M. Heeremans
5	279	70	246	66	2	1	M. Heeremans
6	75	64	75	64	2	1	M. Heeremans
7	248	72	248	72	2	1	M. Heeremans
8	135	80	80	73	2	1	M. Heeremans
9	106	80	28	50	2	1	M. Heeremans

85 Tofte Tronstad Lat 59.551 Long 10.497

Data #	DipDir	Dip	Azimuth	Plunge	Sense	Quality	Source
1	256	74	192	57	2	2	M. Heeremans
2	253	74	182	49	2	2	M. Heeremans
3	315	89	227	60	2	2	M. Heeremans
4	307	61	239	34	2	2	M. Heeremans
5	280	85	353	74	2	2	M. Heeremans
6	94	76	172	39	1	2	M. Heeremans
7	139	63	133	63	2	2	M. Heeremans
8	220	72	295	38	2	2	M. Heeremans
9	181	85	266	45	2	2	M. Heeremans
10	265	70	213	60	2	2	M. Heeremans
11	255	71	206	62	2	2	M. Heeremans
12	263	87	174	17	3	2	M. Heeremans
13	315	60	251	37	1	2	M. Heeremans

86-88 Jeløya 2 Lat 59.489 Long 10.642

Data #	DipDir	Dip	Azimuth	Plunge	Sense	Quality	Source
1	50	77	9	73	2	1	A. Saintot
2	52	68	25	66	2	1	A. Saintot
3	60	89	330	0	4	1	A. Saintot
4	64	80	360	68	2	1	A. Saintot
5	45	70	15	67	2	1	A. Saintot
6	20	76	350	74	2	1	A. Saintot
7	42	60	0	52	2	1	A. Saintot
8	70	62	46	60	2	1	A. Saintot
9	30	62	117	5	3	1	A. Saintot
10	30	62	9	60	2	1	A. Saintot
11	58	38	71	37	2	1	A. Saintot
12	290	75	10	33	1	1	A. Saintot
13	230	40	292	22	2	1	A. Saintot
14	320	60	31	30	1	1	A. Saintot
15	222	32	294	11	1	1	A. Saintot

89 Jeløya 4 Lat 59.448 Long 10.623

Data #	DipDir	Dip	Azimuth	Plunge	Sense	Quality	Source
1	255	75	319	59	2	3	M. Heeremans
2	262	89	351	49	2	3	M. Heeremans
3	66	71	359	48	1	3	M. Heeremans
4	275	73	349	42	2	3	M. Heeremans
5	76	84	359	64	1	3	M. Heeremans
6	259	86	333	76	2	3	M. Heeremans
7	265	89	182	82	2	3	M. Heeremans
8	271	85	355	52	2	3	M. Heeremans
9	263	89	347	80	2	3	M. Heeremans
10	269	76	287	75	2	3	M. Heeremans
11	95	83	19	62	1	3	M. Heeremans
12	267	83	314	80	2	3	M. Heeremans
13	250	87	323	80	2	3	M. Heeremans
14	240	76	292	68	2	3	M. Heeremans
15	278	78	260	77	2	3	M. Heeremans
16	237	71	267	68	2	3	M. Heeremans
17	278	76	307	74	2	3	M. Heeremans
18	79	89	352	72	1	3	M. Heeremans
19	90	82	6	38	1	3	M. Heeremans
20	231	29	142	0	2	3	M. Heeremans
21	93	79	183	1	4	3	M. Heeremans
22	67	80	131	68	2	2	M. Heeremans
23	245	68	192	56	2	3	M. Heeremans
24	217	70	279	53	2	3	M. Heeremans
25	242	89	153	35	1	3	M. Heeremans
26	245	86	158	38	1	3	M. Heeremans
27	231	48	165	25	1	2	M. Heeremans

91 Steinholt Lat 59.409 Long 10.408

Data #	DipDir	Dip	Azimuth	Plunge	Sense	Quality	Source
1	91	85	42	82	2	2	M. Heeremans
2	79	67	79	67	2	2	M. Heeremans
3	119	48	119	48	2	3	M. Heeremans
4	136	85	214	67	2	1	M. Heeremans
5	142	70	187	63	2	1	M. Heeremans
6	172	70	195	68	2	1	M. Heeremans
7	164	53	164	53	2	1	M. Heeremans
8	153	84	230	65	2	1	M. Heeremans
9	137	78	96	74	2	3	M. Heeremans
10	287	85	206	60	2	3	M. Heeremans

90 Horten Lat 59.433 Long 10.454

Data #	DipDir	Dip	Azimuth	Plunge	Sense	Quality	Source
1	80	70	102	69	1	2	M. Heeremans
2	77	78	151	53	2	2	M. Heeremans
3	21	85	106	46	1	2	M. Heeremans
4	43	66	101	50	1	2	M. Heeremans
5	100	79	44	71	1	2	M. Heeremans
6	110	85	34	70	1	2	M. Heeremans
7	111	84	57	80	1	2	M. Heeremans
8	28	73	76	65	1	2	M. Heeremans
9	103	77	54	70	2	2	M. Heeremans
10	266	67	278	67	2	2	M. Heeremans
11	88	72	103	71	2	2	M. Heeremans
12	296	73	300	73	2	2	M. Heeremans
13	339	78	339	78	2	2	M. Heeremans
14	305	60	312	60	2	2	M. Heeremans
15	337	77	313	76	2	2	M. Heeremans
16	341	72	357	71	2	2	M. Heeremans
17	307	60	277	56	2	2	M. Heeremans
18	102	80	143	77	2	2	M. Heeremans
19	165	89	79	75	2	2	M. Heeremans
20	176	86	102	75	2	2	M. Heeremans
21	121	61	55	36	2	2	M. Heeremans
22	302	57	10	30	2	2	M. Heeremans
23	157	89	76	83	2	2	M. Heeremans
24	302	49	354	36	2	2	M. Heeremans
25	290	52	349	33	2	2	M. Heeremans
26	100	83	46	78	2	2	M. Heeremans
27	104	87	30	80	2	2	M. Heeremans
28	280	67	349	40	2	2	M. Heeremans
29	339	59	14	54	2	2	M. Heeremans
30	203	89	119	80	2	2	M. Heeremans
31	290	89	201	32	2	2	M. Heeremans
32	359	80	309	75	2	2	M. Heeremans
33	98	46	71	43	2	2	M. Heeremans
34	235	78	285	72	2	2	M. Heeremans
35	260	85	260	85	2	2	M. Heeremans
36	240	85	321	60	2	2	M. Heeremans
37	333	38	18	29	1	2	M. Heeremans
38	265	70	265	70	2	2	M. Heeremans
39	237	66	264	64	2	2	M. Heeremans
40	249	48	313	26	2	2	M. Heeremans
41	220	80	220	80	2	2	M. Heeremans
42	46	82	332	63	2	2	M. Heeremans
43	267	83	310	80	2	2	M. Heeremans
44	90	70	90	70	2	2	M. Heeremans
45	237	82	313	59	2	2	M. Heeremans
46	84	56	41	47	2	2	M. Heeremans
47	272	76	237	73	2	2	M. Heeremans
48	246	73	291	67	2	2	M. Heeremans
49	256	89	342	76	2	2	M. Heeremans
50	18	80	100	38	2	2	M. Heeremans
51	89	87	89	87	2	2	M. Heeremans
52	88	68	21	44	2	2	M. Heeremans
53	77	77	21	68	2	2	M. Heeremans
54	82	66	82	66	2	2	M. Heeremans
55	86	78	86	78	2	2	M. Heeremans
56	82	74	157	43	2	2	M. Heeremans

92 Himberg Lat 59.325 Long 10.296

Data #	DipDir	Dip	Azimuth	Plunge	Sense	Quality	Source
1	138	54	176	47	2	2	M. Heeremans
2	38	69	38	69	2	3	M. Heeremans
3	57	56	57	56	2	2	M. Heeremans
4	109	81	37	62	2	2	M. Heeremans
5	54	58	26	55	2	3	M. Heeremans
6	29	61	4	58	2	2	M. Heeremans
7	122	58	122	58	2	3	M. Heeremans
8	123	60	123	60	2	3	M. Heeremans
9	135	49	107	45	2	3	M. Heeremans
10	74	68	74	68	2	3	M. Heeremans
11	110	79	110	79	2	3	M. Heeremans
12	167	60	115	47	2	1	M. Heeremans
13	140	62	88	49	2	3	M. Heeremans
14	280	56	305	53	2	3	M. Heeremans
15	282	73	282	73	2	2	M. Heeremans
16	264	65	249	64	2	2	M. Heeremans
17	97	79	173	51	2	3	M. Heeremans
18	87	73	21	53	2	1	M. Heeremans
19	5	61	5	61	2	1	M. Heeremans
20	14	72	71	59	2	3	M. Heeremans
21	41	38	60	36	2	2	M. Heeremans
22	56	58	56	58	2	1	M. Heeremans
23	77	71	37	66	2	1	M. Heeremans
24	357	68	22	66	2	1	M. Heeremans
25	256	85	340	51	2	3	M. Heeremans
26	332	89	332	89	2	2	M. Heeremans
27	328	51	328	51	2	3	M. Heeremans
28	340	77	255	21	4	3	M. Heeremans
29	289	74	13	19	4	2	M. Heeremans
30	200	80	273	59	1	2	M. Heeremans
31	276	53	346	25	1	2	M. Heeremans
32	307	83	24	61	2	1	M. Heeremans
33	292	83	8	64	2	1	M. Heeremans
34	38	86	312	47	2	1	M. Heeremans
35	93	88	181	47	2	1	M. Heeremans
36	41	86	41	86	2	2	M. Heeremans
37	13	40	13	40	2	2	M. Heeremans
38	44	71	18	69	1	1	M. Heeremans
39	70	75	12	63	2	3	M. Heeremans
40	164	88	164	88	2	1	M. Heeremans
41	134	89	224	13	4	1	M. Heeremans
42	134	85	222	22	4	3	M. Heeremans
43	124	54	200	18	2	3	M. Heeremans
44	135	82	223	17	4	1	M. Heeremans
45	147	82	97	78	2	1	M. Heeremans
46	124	76	190	58	2	1	M. Heeremans
47	71	70	71	70	2	1	M. Heeremans
48	73	88	159	65	2	1	M. Heeremans
49	305	70	241	50	2	1	M. Heeremans
50	308	63	308	63	2	1	M. Heeremans
51	300	79	210	0	4	1	M. Heeremans
52	302	79	216	21	4	1	M. Heeremans
53	248	87	160	28	1	2	M. Heeremans
54	222	84	133	13	3	1	M. Heeremans
55	68	89	157	34	2	1	M. Heeremans
56	249	84	167	53	1	1	M. Heeremans
57	242	89	153	54	1	1	M. Heeremans
58	230	80	320	0	3	2	M. Heeremans
59	247	81	160	20	3	1	M. Heeremans
60	260	81	170	3	4	1	M. Heeremans

92 Himberg Lat 59.325 Long 10.296

Data #	DipDir	Dip	Azimuth	Plunge	Sense	Quality	Source
61	225	80	141	32	1	2	M. Heeremans
62	225	80	314	7	3	1	M. Heeremans
63	272	79	2	0	4	2	M. Heeremans
64	41	80	127	23	3	1	M. Heeremans
65	75	80	353	39	2	1	M. Heeremans
66	75	80	165	0	4	1	M. Heeremans
67	285	63	195	0	4	1	M. Heeremans
68	202	51	123	13	3	1	M. Heeremans
69	33	87	123	0	3	3	M. Heeremans
70	207	46	141	23	1	3	M. Heeremans
71	245	82	156	8	3	1	M. Heeremans
72	245	82	159	27	1	1	M. Heeremans

93 Lakstjen Lat 59.325 Long 10.068

Data #	DipDir	Dip	Azimuth	Plunge	Sense	Quality	Source
1	153	89	241	67	2	3	M. Heeremans
2	180	55	196	54	2	3	M. Heeremans
3	243	54	243	54	2	3	M. Heeremans
4	161	76	229	57	2	3	M. Heeremans
5	158	70	182	68	2	1	M. Heeremans
6	152	30	185	26	2	2	M. Heeremans
7	312	83	240	68	1	2	M. Heeremans
8	346	78	346	78	1	2	M. Heeremans
9	324	77	276	71	1	1	M. Heeremans
10	294	77	204	0	3	2	M. Heeremans
11	99	82	24	62	2	1	M. Heeremans
12	108	67	50	51	1	1	M. Heeremans
13	331	77	264	59	1	1	M. Heeremans
14	20	65	59	59	1	1	M. Heeremans
15	103	64	103	64	2	2	M. Heeremans
16	143	53	143	53	2	2	M. Heeremans
17	113	66	95	65	2	2	M. Heeremans
18	295	87	20	60	2	2	M. Heeremans

94 Skoppum Lat 59.238 Long 9.656

Data #	DipDir	Dip	Azimuth	Plunge	Sense	Quality	Source
1	89	87	89	87	2	2	M. Heeremans
2	88	68	21	44	2	2	M. Heeremans
3	77	77	21	68	2	2	M. Heeremans
4	82	66	82	66	2	2	M. Heeremans
5	86	78	86	78	2	2	M. Heeremans
6	82	74	157	43	2	2	M. Heeremans

95 Eidanger Lat 59.118 Long 9.706

Data #	DipDir	Dip	Azimuth	Plunge	Sense	Quality	Source
1	24	80	106	39	1	1	M. Heeremans
2	320	69	33	37	2	1	M. Heeremans
3	140	61	107	56	2	2	M. Heeremans
4	118	55	106	54	2	1	M. Heeremans
5	275	70	193	21	3	1	M. Heeremans
6	259	72	178	27	1	1	M. Heeremans
7	273	63	273	63	2	2	M. Heeremans
8	236	78	152	25	1	1	M. Heeremans
9	237	69	165	39	2	3	M. Heeremans
10	356	87	85	18	4	1	M. Heeremans
11	207	78	127	38	2	2	M. Heeremans
12	311	67	17	43	2	1	M. Heeremans
13	349	85	263	36	2	1	M. Heeremans
14	315	70	271	63	2	1	M. Heeremans
15	169	51	215	41	2	1	M. Heeremans
16	315	72	315	72	2	1	M. Heeremans
17	189	86	100	14	4	1	M. Heeremans
18	272	64	337	41	2	1	M. Heeremans
19	312	72	245	50	2	1	M. Heeremans
20	324	77	254	56	2	1	M. Heeremans
21	226	78	190	75	1	1	M. Heeremans
22	308	73	308	73	2	1	M. Heeremans
23	276	55	201	20	1	1	M. Heeremans
24	274	71	338	51	2	1	M. Heeremans
25	265	42	200	21	2	3	M. Heeremans
26	280	57	218	36	2	1	M. Heeremans
27	280	57	347	31	1	1	M. Heeremans
28	277	77	189	9	4	1	M. Heeremans
29	60	87	342	76	2	1	M. Heeremans
30	280	52	247	47	2	1	M. Heeremans
31	281	64	223	48	2	1	M. Heeremans
32	291	61	221	32	2	1	M. Heeremans
33	274	58	226	47	1	1	M. Heeremans
34	235	85	316	62	1	1	M. Heeremans
35	321	75	31	52	2	1	M. Heeremans
36	280	66	280	66	2	1	M. Heeremans
37	6	76	322	71	2	1	M. Heeremans
38	276	57	276	57	2	1	M. Heeremans
39	282	42	282	42	2	1	M. Heeremans
40	8	84	294	69	2	1	M. Heeremans
41	297	60	342	51	2	3	M. Heeremans
42	6	83	95	5	3	2	M. Heeremans
43	289	69	247	63	2	2	M. Heeremans
44	286	55	242	46	2	1	M. Heeremans
45	327	79	38	59	2	1	M. Heeremans
46	272	70	316	63	2	2	M. Heeremans
47	288	65	308	64	2	1	M. Heeremans
48	143	78	219	49	2	2	M. Heeremans
49	285	67	310	65	1	1	M. Heeremans
50	188	82	265	57	2	1	M. Heeremans
51	126	84	126	84	2	2	M. Heeremans
52	319	77	319	77	2	3	M. Heeremans
53	333	79	28	71	2	1	M. Heeremans
54	275	57	290	56	1	1	M. Heeremans
55	283	82	355	66	2	1	M. Heeremans
56	288	74	288	74	1	1	M. Heeremans
57	310	69	259	58	1	1	M. Heeremans
58	205	85	117	25	3	2	M. Heeremans
59	255	70	180	35	2	2	M. Heeremans

96 North of Brevik Lat 59.056 Long 9.703

Data #	DipDir	Dip	Azimuth	Plunge	Sense	Quality	Source
1	228	76	287	64	1	1	A. Saintot
2	25	85	308	69	2	1	A. Saintot
3	250	70	280	67	1	1	A. Saintot
4	50	42	80	38	2	2	A. Saintot
5	40	55	79	48	2	1	A. Saintot
6	263	78	303	74	2	1	A. Saintot
7	80	78	137	68	2	1	A. Saintot
8	42	40	42	40	1	1	A. Saintot
9	275	84	320	82	2	1	A. Saintot
10	30	52	91	32	2	1	A. Saintot
11	278	88	359	77	2	1	A. Saintot
12	277	85	349	74	2	1	A. Saintot
13	75	42	94	40	2	2	A. Saintot
14	295	78	290	78	2	2	A. Saintot
15	75	85	7	77	1	1	A. Saintot
16	85	80	34	74	1	1	A. Saintot
17	50	52	102	38	2	1	A. Saintot
18	85	54	121	48	2	1	A. Saintot
19	88	85	30	81	1	2	A. Saintot
20	92	80	39	74	1	2	A. Saintot
21	290	80	263	79	2	1	A. Saintot
22	95	86	31	81	1	1	A. Saintot
23	90	84	154	77	1	1	A. Saintot
24	280	81	322	78	2	1	A. Saintot
25	60	78	138	45	2	1	A. Saintot
26	69	83	152	45	1	1	A. Saintot
27	57	46	114	29	2	3	A. Saintot
28	88	86	32	83	1	1	A. Saintot
29	20	38	297	6	3	1	A. Saintot

97 Tveidalen Lat 59.034 Long 9.849

Data #	DipDir	Dip	Azimuth	Plunge	Sense	Quality	Source
1	160	88	92	85	1	1	A. Saintot
2	135	75	196	61	2	1	A. Saintot
3	70	78	343	15	4	1	A. Saintot
4	80	80	352	10	4	1	A. Saintot
5	145	85	55	0	3	1	A. Saintot
6	320	72	279	67	1	1	A. Saintot
7	265	60	184	16	4	1	A. Saintot
8	254	58	176	19	2	1	A. Saintot

98 NW-Nevlunghavn Lat 58.996 Long 9.855

Data #	DipDir	Dip	Azimuth	Plunge	Sense	Quality	Source
1	180	80	264	30	2	2	A. Saintot

99-101 Nevlunghavn 1-3 Lat 58.968 Long 9.869

Data #	DipDir	Dip	Azimuth	Plunge	Sense	Quality	Source
1	290	70	2	41	2	2	A. Saintot
2	270	63	249	61	2	1	A. Saintot
3	265	60	235	56	2	1	A. Saintot
4	245	58	245	58	2	1	A. Saintot

Site	Rock age	Stress state	Type	n	σ_1-az	σ_1-pl	σ_2-az	σ_2-pl	σ_3-az	σ_3-pl	R	Rest
1	Silurian	TORU1	Tensional	6	170	78	1	12	271	2	0.3	
1	Silurian	TORU2	Oblique	17	243	52	26	32	128	19	0.1	1
2	Permian	BRUM1	Tensional	6	350	78	237	5	146	11	0.3	
2	Permian	BRUM2	Oblique	14	302	69	192	8	99	19	0.4	2
3	Prec.	HELL1	Tensional	11	253	77	349	1	79	13	0	
3	Prec.	HELL2	Oblique	12	142	65	310	24	42	5	0.3	
3	Prec.	HELL3	Strike-slip	6	192	12	317	70	99	16	0.1	6
4	L. Ord.	GORU	Tensional	13	255	82	76	8	346	0	0.2	0
5	Cam.-Sil.	BOVR1	Oblique	7	245	67	111	16	16	16	0.1	
5	Cam.-Sil.	BOVR2	Oblique	5	58	68	203	18	297	12	0.1	
5	Cam.-Sil.	BOVR3	Oblique	7	160	35	47	30	287	41	0.2	
5	Cam.-Sil.	BOVR4	Strike-slip	4	312	15	132	75	42	0	0.2	3
6	Ord.-Sil.	KORS1	Tensional	11	2	77	262	2	171	13	0.6	
6	Ord.-Sil.	KORS2	Oblique	9	358	30	200	58	94	10	0.8	
6	Ord.-Sil.	KORS3	Strike-slip	5	338	12	173	78	69	3	0.2-0.4	4
7	Prec.	SKAR1	Tensional	13	114	80	24	0	294	10	0.3	
7	Prec.	SKAR2	Tensional	8	335	74	148	16	239	2	0	
7	Prec.	SKAR3	Tensional	6	245	75	51	15	142	4	0.9	0
8	Prec.	MOEN1	Tensional	6	325	73	183	13	91	10	0.3	
8	Prec.	MOEN2	Oblique	11	339	65	98	13	193	21	0.2-0.3	
8	Prec.	MOEN3	Oblique	7	86	58	309	25	210	19	0.1	6
9	Ord.-Sil.	BRAN1	Compressional	12	319	12	50	5	162	77	0.3	
9	Ord.-Sil.	BRAN2	Tensional	42	193	77	65	8	334	10	0	
9	Ord.-Sil.	BRAN3	Oblique	30	128	60	299	30	31	4	0.3	
9	Ord.-Sil.	BRAN4	Oblique	11	195	40	3	49	100	6	0.6	
9	Ord.-Sil.	BRAN5	Oblique	8	9	38	167	50	270	11	0.3	8
10	Ord.-Sil.	TING1	Tensional	24	178	74	72	4	341	15	0.2	
10	Ord.-Sil.	TING2	Oblique	7	231	65	6	18	101	17	0.2	
10	Ord.-Sil.	TING3	Strike-slip	9	10	9	184	81	280	1	0.6	8
11	Prec.	ENGN	Tensional	9	83	73	193	6	285	16	0.0-0.3	1
12	Permian	JARE1	Tensional	10	346	81	166	9	256	0	0	
12	Permian	JARE2	Oblique	4	125	29	293	60	32	5	0.6	
12	Permian	JARE3	Strike-slip	6	350	15	138	72	258	9	0.0-0.1	1
13	Prec.	RAHO	Oblique	8	210	60	19	30	112	5	0.3-0.7	3
14	Ord.-Sil.	ROAX1	Tensional	5	161	83	348	7	258	1	0.3-0.4	
14	Ord.-Sil.	ROAX2	Oblique	7	73	53	211	29	313	21	0.6-0.7	4
15	Ord.-Sil.	GRYM1	Compressional	11	354	2	84	7	248	83	0.3	
15	Ord.-Sil.	GRYM2	Tensional	13	356	85	175	5	265	0	0	
15	Ord.-Sil.	GRYM3	Oblique	16	347	68	254	1	163	22	0.5	11
16	Prec.	JEVN	Oblique	10	140	68	353	19	259	11	0.5	2
17	U. Sil.	ASAX1	Oblique	28	320	61	157	28	63	7	0.2	
17	U. Sil.	ASAX2	Oblique	9	322	26	135	64	231	3	0.0-0.4	
17	U. Sil.	ASAX3	Strike-slip	11	136	10	352	78	227	7	0.4	12
18	Ord.-Sil.	STUB	Tensional	5	94	85	339	2	249	5	0	2
19	Cam.-Sil.											3
20	Silurian	KROK1	Oblique	19	340	60	199	24	101	17	0.2	
20	Silurian	KROK2	Oblique	6	279	39	178	13	74	48	0.1-0.2	2
21	Silurian	SUN31	Tensional	39	11	85	191	5	281	0	0.1	
21	Silurian	SUN32	Oblique	10	352	48	196	39	96	12	0	
21	Silurian	SUN33	Oblique	5	280	48	179	10	81	40	0.7	3
22	Cam.-Sil.	SUN2	Oblique	8	335	65	134	23	227	8	0.6	0
23	Permian	SUN11	Tensional	8	293	78	193	2	103	12	0	
23	Permian	SUN12	Strike-slip	5	346	14	203	73	79	10	0.0-0.6	3
24	Permian	SORK1	Tensional	4	109	77	262	12	353	6	0.2	
24	Permian	SORK2	Oblique	14	156	34	28	42	268	29	0.3	
24	Permian	SORK3	Oblique	4	181	32	308	44	71	29	0.1	2

Site	Rock age	Stress state	Type	n	σ_1-az	σ_1-pl	σ_2-az	σ_2-pl	σ_3-az	σ_3-pl	R	Rest
25	Permian	HOLM	Tensional	4	198	74	32	16	301	4	0.0-0.3	0
26	Permian	FROG	Tensional	15	141	71	321	19	51	0	0	5
27	Permian	BOGS1	Tensional	7	281	87	100	3	10	0	0.1	
27	Permian	BOGS2	Strike-slip	5	327	14	110	73	235	10	0.0-0.2	1
28	Permian	BURU	Tensional	8	47	81	278	6	187	7	0.5	5
29	L. Sil.	GRIN1	Tensional	8	30	74	242	14	150	8	0.1	
29	L. Sil.	GRIN2	Oblique	6	148	65	39	9	305	23	0.0-0.9	0
30	Permian	SKOL1	Tensional	14	128	88	311	2	221	0	0.1	
30	Permian	SKOL2	Strike-slip	8	108	12	235	71	15	15	0.5-0.7	0
31	Permian	BAER	Tensional	11	218	86	99	2	9	4	0.1	2
32	Permian	GAML1	Tensional	10	0	90	99	0	9	0	0	
32	Permian	GAML2	Strike-slip	4	77	12	222	75	345	8	0.2	4
33	Permian	HVIL1	Tensional	11	357	84	247	1	166	6	0.0-0.1	
33	Permian	HVIL2	Oblique	13	184	61	92	1	1	29	0	
33	Permian	HVIL3	Oblique	6	152	37	311	51	54	10	0.6	
33	Permian	HVIL4	Oblique	7	61	16	309	52	162	33	0.6	
33	Permian	HVIL5	Strike-slip	12	301	5	121	85	31	0	0.1	4
34	U. Sil.	RYKK1	Tensional	7	118	77	348	8	257	10	0.1-0.3	
34	U. Sil.	RYKK2	Oblique	5	129	32	280	54	30	14	0.3	3
35	Cam.-Sil.	SINS1	Oblique	6	225	41	24	47	126	11	0.0-0.2	
35	Cam.-Sil.	SINS2	Strike-slip	4	358	6	138	82	268	5	0.4-0.5	9
36	Cam.-Sil.	VAEK1	Compressional	6	303	3	213	1	103	87	0.1-0.3	
36	Cam.-Sil.	VAEK2	Tensional	24	22	86	215	4	125	1	0.2	
36	Cam.-Sil.	VAEK3	Strike-slip	13	216	1	123	74	306	16	0.5-0.6	5
37	Prec.	EKEB1	Tensional	15	235	82	4	5	94	5	0.0-0.1	
37	Prec.	EKEB2	Oblique	10	173	10	279	57	77	31	0.1-0.2	
37	Prec.	EKEB3	Oblique	12	196	37	32	52	292	8	0.2	
37	Prec.	EKEB4	Oblique	9	239	49	131	15	29	37	0.3	
37	Prec.	EKEB5	Oblique	17	137	55	298	34	34	9	0.5-0.7	
37	Prec.	EKEB6	Oblique	6	50	30	296	35	169	40	0.2	13
38	Cam.-Sil.	HOVE	Tensional	9	310	78	202	4	111	11	0	0
39	Prec.	KONG	Tensional	15	61	84	153	0	243	6	0	0
40	Cam.-Sil.	SAND1	Tensional	20	85	77	355	0	265	13	0.1-0.6	
40	Cam.-Sil.	SAND2	Oblique	6	94	68	306	19	212	11	0.1	
40	Cam.-Sil.	SAND3	Oblique	5	130	0	220	21	40	69	0.1	12
41	Cam.-Sil.	FORN1	Compressional	12	308	6	38	0	129	84	0.4	
41	Cam.-Sil.	FORN2	Tensional	14	126	83	346	5	256	4	0.3-0.4	
41	Cam.-Sil.	FORN3	Oblique	10	227	51	25	37	123	11	0.2-0.4	
41	Cam.-Sil.	FORN4	Oblique	5	103	29	9	7	267	61	0.5	
41	Cam.-Sil.	FORN5	Strike-slip	10	32	2	292	79	122	11	0.1	1
42	Permian	GRYS1	Tensional	4	329	80	174	9	83	4	0.9-1.0	
42	Permian	GRYS2	Oblique	6	109	33	352	35	229	38	0.0-0.1	5
43	Cam.-Sil.	MALM	Oblique	4	309	45	200	18	94	39	0.2-0.6	3
44	Prec.	NESO1	Oblique	9	183	54	7	36	276	2	0.9	
44	Prec.	NESO2	Strike-slip	4	255	13	75	77	165	0	0.9-1.0	1
45	Ord.-Sil.	OSTO1	Tensional	25	232	86	6	3	96	3	0	
45	Ord.-Sil.	OSTO2	Oblique	10	208	41	357	44	103	16	0.3	
45	Ord.-Sil.	OSTO3	Oblique	6	34	51	175	32	278	19	0.4	
45	Ord.-Sil.	OSTO4	Oblique	5	139	31	325	59	230	3	0.1	4
46	Cam.-Sil.	HVAL1	Compressional	6	329	6	239	1	140	84	0.7	
46	Cam.-Sil.	HVAL2	Tensional	8	89	74	238	14	330	8	0.2	1
47	Prec.											1
48/49	Ordovician	ALVA1	Tensional	9	183	87	18	3	287	1	0.1	
48/49	Ordovician	ALVA2	Strike-slip	5	183	4	326	85	93	3	0.2	4
50	Ordovician	BLAK1	Tensional	4	205	80	22	10	112	1	0.4-0.5	
50	Ordovician	BLAK2	Oblique	5	163	57	307	28	46	16	0.3-0.5	0

Site	Rock age	Stress state	Type	n	σ_1-az	σ_1-pl	σ_2-az	σ_2-pl	σ_3-az	σ_3-pl	R	Rest
51	Permian	HAUG1	Tensional	7	292	79	91	10	182	4	0.3	
51	Permian	HAUG2	Strike-slip	6	84	14	264	76	354	0	0.3	0
52	Prec.	FJEL1	Compressional	4	311	3	42	20	213	70	0.7	
52	Prec.	FJEL2	Tensional	7	232	73	34	16	125	5	0.1	
52	Prec.	FJEL3	Oblique	31	170	55	20	31	281	14	0.3	
52	Prec.	FJEL4	Oblique	4	68	14	194	67	333	18	0.6-1.0	4
53	Permian	UTSI	Oblique	4	198	49	351	38	92	14	0.3-0.5	3
54	Permian											0
55	Permian	REIS	Strike-slip	6	116	17	279	72	25	5	0.6	3
56	Ordovician	BOVE1	Tensional	10	222	85	42	5	132	0	0.4	
56	Ordovician	BOVE2	Oblique	4	173	60	10	29	276	7	0.2-0.4	2
57	Prec.	HASL1	Tensional	14	153	80	348	10	257	2	0.6	
57	Prec.	HASL2	Oblique	13	148	38	322	52	56	3	0.3	0
58	Cambrian	MOLL1	Tensional	7	145	74	24	8	292	14	0.5	
58	Cambrian	MOLL2	Tensional	6	321	83	94	4	180	2	0.2	
58	Cambrian	MOLL3	Oblique	9	148	48	328	42	238	0	0.3	5
59	Prec.	SPRO1	Tensional	6	103	79	303	10	212	4	0.2	
59	Prec.	SPRO2	Strike-slip	7	41	0	311	79	131	11	0.5-0.7	3
60	Prec.	NAER1	Tensional	6	318	79	215	3	124	11	0.7	
60	Prec.	NAER2	Strike-slip	9	194	9	63	76	286	10	0.3	0
61	Ordovician	SLEM	Oblique	13	216	63	22	26	116	5	0.1-0.2	6
62	Prec.	BREV1	Strike-slip	5	3	3	261	76	94	14	0.0-0.1	
62	Prec.	BREV2	Strike-slip	4	145	3	266	84	55	5	0.2	3
63	Prec.	BRYN1	Tensional	5	246	76	5	7	96	12	0.8	
63	Prec.	BRYN2	Oblique	16	125	64	334	23	239	12	0.4	2
64	Prec.	DALB1	Oblique	14	151	65	318	24	49	5	0.3	
64	Prec.	DALB2	Strike-slip	6	268	12	35	71	175	15	0.2	3
65	Permian	ROYK	Oblique	11	254	67	103	20	9	10	0.4	2
66	Prec.	NORD1	Tensional	8	11	70	237	14	143	14	0.8-1.0	
66	Prec.	NORD2	Tensional	7	0	90	128	0	218	0	0.3	
66	Prec.	NORD3	Strike-slip	12	207	6	81	80	298	8	0.2	7
67	Prec.	ALVA3	Tensional	12	133	83	294	7	24	2	0.1-0.2	2
68	Prec.											1
69	Ord.-Sil.	MJON1	Tensional	16	160	80	266	3	357	10	0.3	
69	Ord.-Sil.	MJON2	Oblique	4	160	26	252	4	349	64	0.3-0.6	
69	Ord.-Sil.	MJON3	Oblique	11	59	44	263	43	161	12	0.1-0.4	
69	Ord.-Sil.	MJON4	Oblique	8	111	39	243	40	358	27	0.3	
69	Ord.-Sil.	MJON5	Strike-slip	16	97	7	261	83	7	2	0.3	
69	Ord.-Sil.	MJON6	Strike-slip	6	27	1	120	72	297	18	0	4
70	Permian	GULL	Strike-slip	5	3	0	0	90	93	0	0.4-0.9	5
71	Prec.	SOND1	Tensional	6	219	80	83	7	352	7	0.6	
71	Prec.	SOND2	Oblique	8	214	60	5	26	101	13	0.1	3
72	Permian	OVNE	Tensional	6	283	89	77	1	167	0	0	3
73	Prec.											1
74	Permian											6
75	Prec.	FAGE1	Compressional	5	349	13	79	1	174	77	0.7-0.9	
75	Prec.	FAGE2	Oblique	5	163	56	359	33	264	7	0.2	
75	Prec.	FAGE3	Strike-slip	5	89	15	318	70	183	15	0..	0
76	Cam.-Sil.	KONN1	Tensional	6	139	77	312	13	42	2	0.1	3
76	Cam.-Sil.	KONN2	Strike-slip	5	124	5	315	85	214	1	0.2-0.3	
77	Prec.	HOL3	Oblique	13	167	51	347	39	77	0	0.1	0
78	Prec.	HOL11	Oblique	16	167	49	3	40	266	8	0.1	
78	Prec.	HOL12	Oblique	10	120	34	319	55	216	9	0.0-0.1	
78	Prec.	HOL13	Strike-slip	7	143	10	350	79	234	5	0.3	2

Site	Rock age	Stress state	Type	n	σ_1-az	σ_1-pl	σ_2-az	σ_2-pl	σ_3-az	σ_3-pl	R	Rest
79	Permian	HOL21	Tensional	7	17	74	111	1	201	16	0.1	
79	Permian	HOL22	Oblique	12	242	62	62	28	333	0	0.4	3
80	Prec.	HAHA	Strike-slip	7	139	5	247	74	48	15	0.7	1
81	Permian	HYGG1	Tensional	4	150	78	359	11	268	6	0.2	
81	Permian	HYGG2	Oblique	5	338	63	195	22	99	15	0.1-0.6	
81	Permian	HYGG3	Strike-slip	8	334	0	0	90	244	0	0.6	0
82	Prec.	HALL1	Tensional	6	213	76	102	5	11	13	0.1-0.3	
82	Prec.	HALL2	Oblique	14	164	50	344	40	74	0	0.4-0.6	
82	Prec.	HALL3	Strike-slip	6	184	0	94	71	274	19	0.3	3
83	Permian	SELV	Tensional	11	104	88	355	1	265	2	0	4
84	Prec.	HEIS	Tensional	9	6	85	204	5	294	2	0.2	0
85	Permian	TOFT1	Tensional	4	303	70	170	14	76	14	0.3	
85	Permian	TOFT2	Oblique	6	136	62	338	26	244	9	0.0-0.6	1
86/88	Cam.-Sil.	JEL11	Strike-slip	5	325	0	0	90	55	0	0.2	
86/88	Cam.-Sil.	JEL12	Tensional	8	278	75	132	13	40	8	0.1	2
89	Permian	JEL4	Oblique	17	46	60	174	19	272	22	0	11
90	Permian	HORT1	Tensional	28	354	78	174	12	264	0	0.1	
90	Permian	HORT2	Oblique	14	25	58	244	26	145	17	0.0-0.1	
90	Permian	HORT3	Oblique	7	108	47	203	5	298	43	0.7	7
91	Permian	STEI	Tensional	9	291	77	60	8	151	10	0.2	1
92	Permian	HIMB1	Tensional	30	354	82	174	8	84	0	0.1	
92	Permian	HIMB2	Oblique	12	222	49	38	41	130	2	0.2	
92	Permian	HIMB3	Strike-slip	22	170	9	298	76	78	11	0.1	8
93	Permian	LAKS1	Tensional	7	276	85	127	4	37	3	0.0-0.1	
93	Permian	LAKS2	Oblique	6	295	49	163	30	57	25	0	5
94	Permian	SKOP	Tensional	5	296	70	171	12	78	16	0	1
95	Ord.-Sil.	EIDA1	Tensional	22	152	86	21	3	291	3	0	
95	Ord.-Sil.	EIDA2	Oblique	8	78	46	258	44	168	0	0.0-0.2	
95	Ord.-Sil.	EIDA3	Oblique	8	212	67	320	7	53	22	0.2	
95	Ord.-Sil.	EIDA4	Oblique	6	214	5	313	60	121	29	0.4-0.5	
95	Ord.-Sil.	EIDA5	Strike-slip	5	144	8	261	73	52	15	0.4	10
96	Ordovician	NBRE	Oblique	22	75	64	181	7	274	25	0.2	7
97	Permian	TVEI	Strike-slip	6	317	5	137	85	47	0	0.6	2
98	Permian											1
99-101	Permian	NEVL	Tensional	4	59	72	152	1	242	19	0	0

Bedding planes

Site	Data #	DipDir	Dip	Source
19	1	60	8	A. Saintot
19	2	102	6	A. Saintot
19	3	50	8	A. Saintot
19	4	50	7	A. Saintot
19	5	48	11	A. Saintot
22	1	110	22	A. Saintot
29	1	226	14	A. Saintot
29	2	320	80	A. Saintot
29	3	298	50	A. Saintot
29	4	306	85	A. Saintot
34	1	14	5	A. Saintot
34	2	22	12	A. Saintot
34	3	40	5	A. Saintot
34	4	33	11	A. Saintot
34	5	335	4	A. Saintot
34	6	15	16	A. Saintot
38	1	144	87	M. Heeremans
50	1	150	30	A. Saintot
50	2	180	30	A. Saintot
56	1	350	60	A. Saintot
61	1	352	40	A. Saintot
88	1	120	18	A. Saintot

Dykes

Site	Data#	DipDir	Dip	Source
5	1	268	61	M. Heeremans
5	2	77	85	M. Heeremans
5	3	250	75	M. Heeremans
5	4	259	50	M. Heeremans
5	5	126	87	M. Heeremans
5	6	283	65	M. Heeremans
5	7	331	20	M. Heeremans
9	1	268	61	M. Heeremans
9	2	77	85	M. Heeremans
9	3	250	75	M. Heeremans
9	4	259	50	M. Heeremans
9	5	126	87	M. Heeremans
9	6	283	65	M. Heeremans
9	7	331	20	M. Heeremans
10	1	268	61	M. Heeremans
10	2	77	85	M. Heeremans
10	3	283	65	M. Heeremans
10	4	331	20	M. Heeremans
17	1	77	89	M. Heeremans
17	2	74	74	M. Heeremans
17	3	262	81	M. Heeremans
17	4	253	78	M. Heeremans
17	5	81	85	M. Heeremans
24	1	202	65	A. Saintot
24	2	198	60	A. Saintot
24	3	198	79	A. Saintot
24	4	195	84	A. Saintot
26	1	350	30	A. Saintot
27	1	85	80	A. Saintot
27	2	95	90	A. Saintot
27	3	85	80	A. Saintot
27	1	70	90	A. Saintot
28	1	280	65	A. Saintot
29	1	30	80	A. Saintot
29	2	130	90	A. Saintot
29	3	128	81	A. Saintot
29	4	120	82	A. Saintot
29	5	110	90	A. Saintot
29	6	94	65	A. Saintot
29	7	92	62	A. Saintot
29	8	90	60	A. Saintot
29	9	102	60	A. Saintot
29	10	90	65	A. Saintot
31	1	70	70	A. Saintot
31	2	50	70	A. Saintot
31	3	70	70	A. Saintot
31	4	50	90	A. Saintot
31	5	44	90	A. Saintot
31	6	300	64	A. Saintot
31	7	108	85	A. Saintot
31	8	109	81	A. Saintot
31	9	110	90	A. Saintot
31	10	340	80	A. Saintot
31	11	300	80	A. Saintot
31	12	290	80	A. Saintot
34	1	70	80	A. Saintot
34	2	280	80	A. Saintot
34	3	278	70	A. Saintot

Dykes

Site	Data#	DipDir	Dip	Source
34	4	100	90	A. Saintot
38	1	255	70	M. Heeremans
38	2	49	68	M. Heeremans
38	3	73	85	M. Heeremans
38	4	80	60	M. Heeremans
38	5	64	85	M. Heeremans
38	6	237	76	M. Heeremans
38	7	144	87	M. Heeremans
41	1	71	76	M. Heeremans
41	2	78	80	M. Heeremans
41	3	255	86	M. Heeremans
41	4	73	68	M. Heeremans
42	1	60	84	M. Heeremans
44	1	80	90	A. Saintot
44	2	75	90	A. Saintot
44	3	110	90	A. Saintot
44	4	100	90	A. Saintot
44	5	90	90	A. Saintot
44	6	85	65	A. Saintot
45	1	161	45	M. Heeremans
45	2	260	80	M. Heeremans
45	3	151	75	M. Heeremans
45	4	50	75	M. Heeremans
46	1	80	70	M. Heeremans
46	2	67	86	M. Heeremans
48/49	1	330	70	A. Saintot
48/49	2	315	70	A. Saintot
50	1	95	70	A. Saintot
50	2	110	70	A. Saintot
51	1	102	82	A. Saintot
51	2	103	82	A. Saintot
51	3	100	81	A. Saintot
51	4	110	80	A. Saintot
54	1	115	90	A. Saintot
55	1	120	85	A. Saintot
55	2	125	82	A. Saintot
55	3	120	85	A. Saintot
55	4	265	85	A. Saintot
59	1	90	90	A. Saintot
60	1	40	80	A. Saintot
64	1	80	50	A. Saintot
64	2	82	60	A. Saintot
67	1	315	70	A. Saintot
69	1	277	68	M. Heeremans
70	1	114	90	A. Saintot
70	2	120	90	A. Saintot
70	3	115	70	A. Saintot
70	4	112	70	A. Saintot
70	5	112	72	A. Saintot
70	6	120	35	A. Saintot
70	7	105	80	A. Saintot
70	8	128	90	A. Saintot
70	9	122	90	A. Saintot
70	10	120	90	A. Saintot
70	11	110	80	A. Saintot
70	12	105	74	A. Saintot
70	13	115	80	A. Saintot
70	14	310	86	A. Saintot

Dykes

Site	Data#	DipDir	Dip	Source
72	1	74	80	A. Saintot
72	2	88	86	A. Saintot
72	3	0	74	A. Saintot
72	4	0	30	A. Saintot
72	5	10	80	A. Saintot
72	6	4	65	A. Saintot
72	7	20	55	A. Saintot
72	8	114	80	A. Saintot
72	9	114	83	A. Saintot
72	10	114	90	A. Saintot
74	1	110	90	A. Saintot
74	2	10	90	A. Saintot
74	3	110	90	A. Saintot
79	1	15	38	A. Saintot
80	1	275	46	A. Saintot
80	2	273	42	A. Saintot
86-88	1	44	90	A. Saintot
86-88	2	70	90	A. Saintot
86-88	3	48	90	A. Saintot
86-88	4	60	90	A. Saintot
86-88	5	50	90	A. Saintot
86-88	6	45	90	A. Saintot
86-88	7	54	65	A. Saintot
86-88	8	95	38	A. Saintot
86-88	9	80	70	A. Saintot
86-88	10	70	60	A. Saintot
86-88	11	40	60	A. Saintot
86-88	12	90	25	A. Saintot
86-88	13	290	65	A. Saintot
95	1	185	80	M. Heeremans
95	2	267	56	M. Heeremans
97	3	138	80	A. Saintot
97	4	90	90	A. Saintot
97	5	110	85	A. Saintot
97	6	245	65	A. Saintot
97	7	265	60	A. Saintot
97	8	145	85	A. Saintot
97	9	320	80	A. Saintot
97	10	265	60	A. Saintot
99-101	1	60	90	A. Saintot
99-101	2	130	90	A. Saintot

Veins

Site	Data#	DipDir	Dip	Source
19	1	286	72	A. Saintot
19	2	274	78	A. Saintot
19	3	260	72	A. Saintot
19	4	256	70	A. Saintot
19	5	262	71	A. Saintot
19	6	263	77	A. Saintot
19	7	264	78	A. Saintot
19	8	252	72	A. Saintot
19	9	240	85	A. Saintot
19	10	252	70	A. Saintot
19	11	248	74	A. Saintot
19	12	240	78	A. Saintot
19	13	248	69	A. Saintot
19	14	264	72	A. Saintot
28	1	210	30	A. Saintot
28	2	120	58	A. Saintot
28	3	250	80	A. Saintot
28	4	348	85	A. Saintot
28	5	212	68	A. Saintot
28	6	160	73	A. Saintot
28	7	30	88	A. Saintot
28	8	200	55	A. Saintot
28	9	210	52	A. Saintot
28	10	140	60	A. Saintot
28	11	220	80	A. Saintot
28	12	114	72	A. Saintot
28	13	120	90	A. Saintot
28	14	248	78	A. Saintot
28	15	98	85	A. Saintot
28	16	210	80	A. Saintot
29	1	114	90	A. Saintot
29	2	30	85	A. Saintot
29	3	180	72	A. Saintot
29	4	130	72	A. Saintot
29	5	220	82	A. Saintot
29	6	50	80	A. Saintot
29	7	230	70	A. Saintot
29	8	50	76	A. Saintot
29	9	70	84	A. Saintot
29	10	260	84	A. Saintot
29	11	87	90	A. Saintot
29	12	40	68	A. Saintot
29	13	84	90	A. Saintot
29	14	65	85	A. Saintot
29	15	218	76	A. Saintot
29	16	75	65	A. Saintot
29	17	70	62	A. Saintot
29	18	87	63	A. Saintot
29	19	203	84	A. Saintot
29	20	210	86	A. Saintot
29	21	60	78	A. Saintot
29	22	90	79	A. Saintot
29	23	190	67	A. Saintot
29	24	95	63	A. Saintot
29	25	195	70	A. Saintot
29	26	70	90	A. Saintot
29	27	210	84	A. Saintot
29	28	90	64	A. Saintot

Veins

Site		DipDir	Dip	Source
29	29	86	64	A. Saintot
29	30	195	64	A. Saintot
29	31	195	70	A. Saintot
29	32	100	70	A. Saintot
29	33	193	75	A. Saintot
29	34	115	70	A. Saintot
29	35	130	68	A. Saintot
29	36	190	63	A. Saintot
29	37	170	62	A. Saintot
29	38	30	60	A. Saintot
29	39	130	70	A. Saintot
29	40	126	76	A. Saintot
29	41	181	67	A. Saintot
29	42	144	79	A. Saintot
29	43	80	65	A. Saintot
30	1	55	60	A. Saintot
30	2	12	36	A. Saintot
30	3	64	81	A. Saintot
30	4	60	78	A. Saintot
30	5	60	79	A. Saintot
30	6	220	66	A. Saintot
30	7	13	50	A. Saintot
30	8	230	62	A. Saintot
30	9	14	37	A. Saintot
30	10	214	80	A. Saintot
30	11	263	78	A. Saintot
30	12	230	69	A. Saintot
30	13	222	66	A. Saintot
30	14	226	56	A. Saintot
30	15	212	84	A. Saintot
30	16	215	78	A. Saintot
30	17	102	68	A. Saintot
30	18	154	80	A. Saintot
30	19	108	83	A. Saintot
30	20	228	67	A. Saintot
30	21	270	83	A. Saintot
30	22	235	72	A. Saintot
30	23	214	80	A. Saintot
30	24	252	80	A. Saintot
30	25	250	79	A. Saintot
30	26	254	77	A. Saintot
30	27	246	80	A. Saintot
30	28	262	83	A. Saintot
30	29	254	82	A. Saintot
30	30	196	66	A. Saintot
30	31	189	64	A. Saintot
32	1	179	48	A. Saintot
32	2	126	60	A. Saintot
32	3	220	55	A. Saintot
32	4	149	85	A. Saintot
32	5	185	58	A. Saintot
32	6	102	80	A. Saintot
34	1	80	84	A. Saintot
34	2	80	83	A. Saintot
34	3	210	79	A. Saintot
34	4	236	58	A. Saintot
34	5	181	64	A. Saintot
34	6	240	73	A. Saintot

Veins

Site		DipDir	Dip	Source
34	7	179	70	A. Saintot
34	8	220	77	A. Saintot
34	9	152	80	A. Saintot
45	1	267	80	M. Heeremans
48/49	1	80	55	A. Saintot
48/49	2	76	60	A. Saintot
48/49	3	100	45	A. Saintot
50	1	240	85	A. Saintot
51	1	200	85	A. Saintot
53	1	100	85	A. Saintot
53	2	115	90	A. Saintot
53	3	295	85	A. Saintot
53	4	120	85	A. Saintot
53	5	125	85	A. Saintot
53	6	126	90	A. Saintot
53	7	120	85	A. Saintot
54	1	114	90	A. Saintot
54	2	115	84	A. Saintot
54	3	300	89	A. Saintot
54	4	114	85	A. Saintot
54	5	295	82	A. Saintot
55	1	117	86	A. Saintot
58	1	35	80	A. Saintot
58	2	58	70	A. Saintot
58	3	330	77	A. Saintot
58	4	116	82	A. Saintot
58	5	258	68	A. Saintot
58	6	48	50	A. Saintot
58	7	263	53	A. Saintot
58	8	10	82	A. Saintot
58	9	68	67	A. Saintot
58	10	65	73	A. Saintot
58	11	57	70	A. Saintot
58	12	260	78	A. Saintot
58	13	268	82	A. Saintot
58	14	264	68	A. Saintot
58	15	279	60	A. Saintot
58	16	260	58	A. Saintot
59	1	40	72	A. Saintot
60	1	18	90	A. Saintot
60	2	190	80	A. Saintot
60	3	42	75	A. Saintot
60	4	140	80	A. Saintot
60	5	0	75	A. Saintot
60	6	55	85	A. Saintot
60	7	230	80	A. Saintot
60	8	238	72	A. Saintot
61	1	160	74	A. Saintot
62	1	90	90	A. Saintot
63	1	70	90	A. Saintot
63	2	230	84	A. Saintot
63	3	244	85	A. Saintot
63	4	230	80	A. Saintot
63	5	220	84	A. Saintot
63	6	45	80	A. Saintot
63	7	40	78	A. Saintot
63	8	84	74	A. Saintot
63	9	48	85	A. Saintot

Veins

Site		DipDir	Dip	Source
63	10	50	80	A. Saintot
63	11	75	76	A. Saintot
63	12	246	85	A. Saintot
63	13	60	78	A. Saintot
63	14	40	90	A. Saintot
63	15	50	75	A. Saintot
63	16	64	62	A. Saintot
63	17	118	90	A. Saintot
63	18	44	72	A. Saintot
63	19	50	65	A. Saintot
63	20	34	79	A. Saintot
63	21	62	80	A. Saintot
64	1	241	81	A. Saintot
64	2	42	85	A. Saintot
64	3	36	90	A. Saintot
64	4	14	78	A. Saintot
65	1	80	83	A. Saintot
65	2	243	80	A. Saintot
65	3	58	76	A. Saintot
66	1	280	50	A. Saintot
66	2	280	60	A. Saintot
66	3	285	55	A. Saintot
66	4	290	50	A. Saintot
66	5	290	60	A. Saintot
70	1	10	90	A. Saintot
70	2	30	90	A. Saintot
70	3	26	90	A. Saintot
70	4	210	70	A. Saintot
70	5	210	84	A. Saintot
70	6	38	90	A. Saintot
71	1	110	90	A. Saintot
71	2	290	62	A. Saintot
71	3	268	55	A. Saintot
71	4	276	60	A. Saintot
71	5	270	58	A. Saintot
71	6	273	50	A. Saintot
71	7	270	45	A. Saintot
71	8	270	85	A. Saintot
72	1	80	80	A. Saintot
72	2	148	80	A. Saintot
72	3	244	85	A. Saintot
72	4	115	87	A. Saintot
72	5	113	90	A. Saintot
72	6	104	85	A. Saintot
72	7	94	78	A. Saintot
74	1	230	80	A. Saintot
74	2	303	67	A. Saintot
74	3	244	66	A. Saintot
74	4	80	90	A. Saintot
77	1	70	70	M. Heeremans
77	2	110	78	M. Heeremans
86-88	1	0	90	A. Saintot
91	1	179	48	M. Heeremans
91	2	126	60	M. Heeremans
91	3	220	55	M. Heeremans
91	4	149	85	M. Heeremans
91	5	185	58	M. Heeremans
91	6	102	80	M. Heeremans